Aero-Thermal Performance of Transonic High-Pressure Turbine Blade Tips

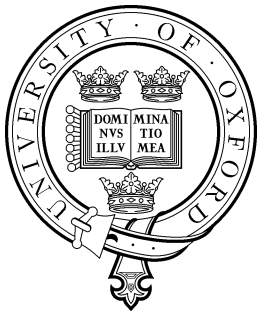

Devin Owen O'Dowd
St John's College

A thesis submitted in partial fulfillment of the requirements for the degree of

Doctor of Philosophy

Michaelmas Term, 2010

Department of Engineering Science
University of Oxford

Aero-Thermal Performance of Transonic High-Pressure Turbine Blade Tips

Devin Owen O'Dowd
St John's College

A thesis submitted in partial fulfilment of the requirements for the degree of Doctor of Philosophy, University of Oxford, Michaelmas Term, 2010.

Abstract

This thesis presents an experimental and theoretical study of unshrouded tips on gas turbine blades with and without winglets. The goal of the winglet tip design is to reduce over-tip leakage flow. To assess the potential use of winglets, their effectiveness in reducing loss and the cooling scheme's effectiveness must be determined under engine-realistic flow conditions. An aero-thermal investigation was performed to answer these questions.

A high-speed linear cascade was commissioned for use under transonic conditions. Once realistic inlet and exit conditions were established, the heat transfer measurement technique used was qualified. An infrared thermography technique was used to obtain a detailed time history of the surface temperature, which was used to reconstruct heat flux and calculate heat transfer coefficients. Several processing techniques were compared to determine that a technique using an impulse response digital filter in the frequency domain has the smallest uncertainty, is the most consistent and is the most computationally efficient.

Heat transfer tests were then performed on a flat blade tip under transonic and low-speed flow conditions, and results showed both qualitative and quantitative differences, highlighting the need for testing at engine-realistic conditions. A heat transfer tip gap survey was then performed on a flat tip, and this agreed well with an independent computational study. Uncooled and cooled winglet tip heat transfer was also examined, showing that the uncooled winglet has nearly 3.2 times the area-averaged heat load of a flat tip and the cooled winglet has nearly 3.4 times the area-averaged heat load of a flat tip. Cooled winglet heat transfer results showed enhanced heat transfer compared to the uncooled winglet and an increase in film cooling effectiveness with a smaller tip gap. Reflecting the complexity of testing at high-speed conditions, these are the first detailed, spatially-resolved heat transfer results on the blade tip under transonic conditions.

Aerodynamic loss measurements were obtained using a specially-designed three-hole probe and a single-hole probe to resolve the near-casing region. The flat tip experimental and computational results agree well. The winglet results showed a decrease in loss with coolant injection.

Finally, a numerical study is carried out to investigate the influence of 2-D corner conduction on the accuracy of heat transfer measurements when using the conventional semi-infinite 1-D assumption. The errors in the conventionally processed heat transfer coefficient are shown to be very high around the corner. A relatively simple and efficient new correction method has been developed and shown to be effective.

Dedication

For my Heavenly Father,
who through my Lord and Saviour, Jesus Christ,
and by the power of His Holy Spirit,
enabled this work.

Acknowledgements

I am deeply grateful for all of the support and encouragement from the academic and support staff, technicians and fellow researchers at the Osney Lab. Professors He and Oldfield, who stepped in to supervise me during difficult times, were always available for technical advice and greatly improved my writing.

A special thank you must go out to Dr Qiang Zhang, my fellow researcher and friend. He really pushed this project and gave timely advice. His CFD processing provided the necessary tools to help our research team understand not only the experimental data, but the nature of the problem as well. Most of the CAD drawings were originally produced by Dr Zhang and his computational efforts form a strong basis for the understanding obtained through this work.

Others in the lab helped me with advice, encouragement and support: Brian, Richard, Adam, James, Chris, Salva, Dave, Gerald, Trevor and Rex.

I'm very thankful for Rolls-Royce support. I'd especially like to thank Brian Cheong, Ed Romero and Stefan Friedrichs for their technical feedback.

Dr. Ian Sobey, Professor Richard Compton and the other staff at St John's College provided excellent support. Professor Fionn Dunne, Mr. Chris Scotcher and the other staff at the Department of Engineering Science were invaluable, helping ensure I had the support I needed to complete my experiments.

Many thanks go out to the U.S. Air Force Academy, who provided not only financial support, but encouragement along the way. I'd specifically like to thank Brigadier General Dana Born, Dean of the Faculty; Colonel D. Neal Barlow, Permanent Professor and Head, Department of Aeronautics; Professor Aaron Byerley (Merton College/Osney Lab '89); and Colonel Keith Boyer, AFIT Dean of Students, mentor and friend. Thanks also to the DFAN family for your continued friendship during this challenging program.

Thanks to my fellow Air Force friends, Ian, Mario, Nick, Andrew and Vic, who provided professional examples of the warrior-scholar ethos. Thanks also to friends at St Ebbe's Church who helped me to remember my priorities in life.

To my parents who have always been a source of support, advice and encouragement. I'd like to thank my brothers Brendon and Ryan (along with their respective families) for the Christ-like example they set. Appreciation goes out to Jenna for her helpful proofreading.

Finally and foremost, my most sincere love and affection go out to my wife, Andrea, and our three wonderful children, Austin, Teagan and Bailey. They bring great job to my life. Thank you for your patience and encouragement. I love you!

"The views expressed in this work are those of the author and do not necessarily reflect the official policy or position of the United States Air Force, Department of Defense or the United States Government."

Contents

List of Figures

LIST OF FIGURES

List of Tables

Nomenclature

Roman

C	chord, probe calibration coefficient [mm]
C_{ax}	axial chord [mm]
C_p	coefficient of pressure, specific heat capacity for constant pressure [J/kg K]
Cp_0	aerodynamic loss coefficient
E	excitation voltage (hot-wire) [V]
G	greyscale value
g	tip clearance [mm]
h	heat transfer coefficient [W/m^{2}K], enthalpy [J/kg]
$h(t)$	impulse response function
k	thermal conductivity [W/m K]
I	current [A]
L	location
m	total number of data points
M	Mach number
n	numerical integration variable
Nu	Nusselt number = $\frac{hC_{ax}}{k_{\text{local}}}$
P	pressure [kPa (or psi)], blade pitch [mm]
$\dot{q}$	heat flux [W/m^2]
r	recovery factor
R	gas constant [J/kg K], span-wise radial distance [mm]
R/S	Radius-wise location normalised by blade span
Re	Reynolds number
S	blade span [mm]
s	entropy [J/kg K]
t	time [s]
T	temperature [°C or K]
u, v, w	x, y and z components of velocity [m/s]
U	blade speed [m/s]
V	velocity [m/s]
x	direction/distance lateral surface [mm], axial direction
Y	total pressure loss coefficient
y	direction/distance normal to surface [mm], pitch direction [mm], circumferential direction
y/P	pitch-wise measurement location normalised by blade pitch

Greek

α	thermal Diffusivity $= \frac{k}{\rho C_p}$ [m^2/s]
β	Probe calibration flow (yaw) angle [degrees]
γ	ratio of specific heats
Δ	difference
δ	uncertainty
ζ	kinetic energy loss coefficient
η	efficiency, film cooling effectiveness
Θ	temperature ratio
μ	dynamic viscosity [kg/m s]
ν	kinematic viscosity [m^2/s]
ρ	density [kg/m^3]
τ	sampling rate/interval [s], time constant [s]

Subscripts

0	initial condition, stagnation
ad	adiabatic
avg	average of A and C (three-hole probe channels)
ax	axial
A	three-hole probe angled channel
B	three-hole probe centre channel
c	coolant, cooled
cor	corrected
C	three-hole probe angled channel
$exit$	exit conditions
g	gas
i	initial conditions, spatial step
in	inlet conditions, input
$inlet$	inlet conditions
$isen$	isentropic
M	probe calibration Mach number
m	mainstream flow
s	static
T	probe calibration total pressure
t	total, stagnation
uc	uncooled
w	wall
β	Probe calibration yaw angle
∞	Mainstream conditions, infinity

Superscripts

n	time step
$\dot{}$	time derivative

Abbreviations

1-D	one-dimensional
2-D	two-dimensional
3-D	three-dimensional
CAD	computer-aided design
CCTV	closed-circuit television
CFD	computational fluid dynamics
DC	Direct Current
EFE	Environmentally Friendly Engine
HSLC	High-Speed Linear Cascade
HP	high pressure
HPT	high pressure turbine
IR	infrared
LE	leading edge
NGV	nozzle guide vane
OTL	over-tip leakage
PID	Proportional Band-Integral-Derivative (feedback control)
PIV	Particle Image Velocimetry
PR	pressure ratio
PS	pressure side
RMS	root-mean squared
SEE	standard error of estimate
SS	suction surface
TE	trailing edge
TET	turbine entry temperature
TFG	thin-film gauge
TLC	thermochromic liquid crystals
ZnSe	Zinc-Selenide, window for IR test

Other nomenclature

gutter	Groove extending from leading edge to trailing edge of winglet along the camber line
std	standard deviation
SI40	epoxy stereolithography resin produced Rolls-Royce

Chapter 1

Introduction

This thesis presents an experimental and theoretical study of unshrouded turbine tips with different tip geometries, with and without cooling injection and for different tip gaps. The goal of the winglet tip design is to reduce over-tip leakage flow. This thesis assesses the winglet's effectiveness in reducing loss and its capability to cool the blades under engine-realistic aerodynamic flow conditions.

This chapter provides a background to the research presented in this thesis. Section 1.1 gives a brief historical background for the gas turbine engine. Section 1.2 addresses the current trends in the high-pressure turbine (HPT), including the issues driving research into the blade tip gap, such as heat transfer. Section 1.3 then details the challenges that exist as a result of these current trends. Section 1.4 provides the motivation specific to the present study, addressing such issues as unshrouded blade tips, high-speed tip flow and tip film cooling. Section 1.5 then details the aims and objectives of the present work. Section 1.6 provides a summary of the various publications and presentations related to this work. Finally, Section 1.7 details the breakdown of this thesis by chapter.

1.1 Background

The gas turbine engine is arguably one of the most important inventions of the 20th century. It has had a major impact not only in air transportation, but also ground-based power generation. Though there is a trend away from fossil fuels or other

non-renewable energy sources, the use of gas turbine energy is still an essential form of energy production and will be so for years to come. For it to be a viable form of energy production, it must not only improve its power output, but it must do so cleanly and with more efficiency.

The invention of the jet engine is closely tied to the invention of the flying vehicle. The "father of aerodynamics", Sir George Cayley was the first person to design a plane that used a fixed wing for lift and a separate mechanism for propulsion, though his designs did not allow for enough power to sustain flight (Anderson, 1989). Fifty years after Sir George's flight tests using "flappers", on 17 December 1903, at Kill Devil Hill, Kitty Hawk, North Carolina, the Wright brothers were the first to control, power and sustain a heavier-than-air aircraft, using a twelve horsepower internal combustion engine. In the initial years following this first flight, internal combustion engines were used as they were fairly well understood.

In the years following the Wright brothers' first flight, work on air-breathing jet propulsion was taking place. It wasn't until the late 1930s when the turbojet engine (air-breathing jet propulsion system using turbomachinery) was first tested in flight. Dr Hans von Ohain's He.S-3B was successfully flown aboard the Heinkel He-178 in August 1939. Less than two years later, a second turbojet engine, based on the design of Sir Frank Whittle from the early 1930s, was tested in flight. Sir Frank's W.1 engine was flown in May 1941 on the Gloster E28/29.

Over the past 70+ years, advances in technology have brought new challenges, which in turn require new advances in technology to overcome. Perhaps one of the most significant challenges today, as it was over 70+ years ago, is how to increase the power and general efficiency of the turbine within the limitations of current technology. Typically at the top of the list are considerations such as increasing the rotational speed of the turbomachinery (increases pressure ratio and therefore efficiency), improved component efficiency and increasing the turbine entry temperature (TET) (increases specific power), which must be balanced with thermal-mechanical issues, such as stress on the blade disk; as well as material limitations, such as blade melting temperature (Bunker, 2001).

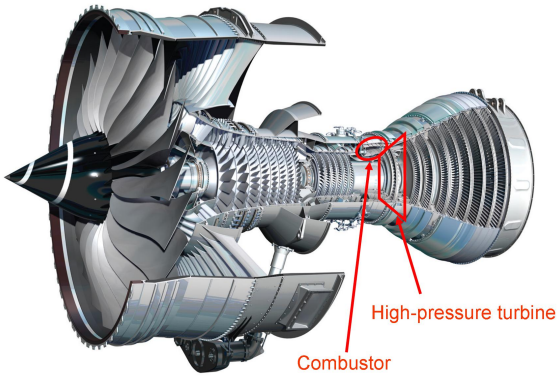

Figure 1.1: Engine cutaway of the Rolls-Royce XWB high-bypass turbofan with shrouded high-pressure turbine highlighted (courtesy Rolls-Royce website)

These considerations are true for any gas turbine cycle. Whether designing turbojets with no bypass, low-bypass turbofans or high-bypass turbofans, performance and efficiency must be optimised based on the mission constraints. With the modern rise in fuel costs, commercial engine manufacturers focus on fuel efficiency, though engine performance cannot be neglected.

1.2 High-Pressure Turbine

Of the list of considerations for improving engine performance and efficiency listed above, perhaps the primary engine component that is capable of making the most impact is the high-pressure turbine (HPT). The HPT, highlighted in Figure 1.1, is responsible for providing power to the high-pressure compressors and is the first component downstream of the combustion system.

Some of the general trends in modern high-pressure turbines include

- increase turbine rotating speed
- minimise losses
- increase TET

Increasing turbine rotating speed provides more power to the high-pressure compressor, but is currently limited by the stress on the blade disk. Besides complex

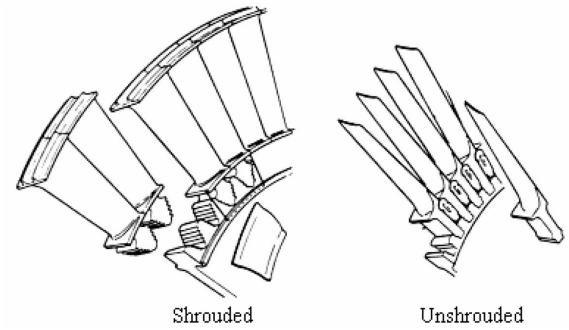

Figure 1.2: Shrouded and unshrouded turbine blades (Rolls-Royce, 1973)

aero-mechanical challenges that turbines suffer from such as flutter, vibrations, fatigue and local stresses, the disk experiences large amounts of stress caused by the centrifugal forces from rotating large, dense metal at high rotating speeds. Many turbines have shrouded blades, where tips of each blade have a large piece of metal that, when placed beside a neighbour blade, limits leakage flow in the radial direction. Eliminating this heavy shroud will reduce the centrifugal stress and allow the turbine to rotate faster, but will also result in leakage flow caused by the pressure difference between the blade pressure side and suction side. Figure 1.2 displays both unshrouded and shrouded blades from Rolls-Royce (1973).

The second general trend for the HPT is to minimise losses. All mechanical devices have inefficiencies, or losses. Though they will never be eliminated, a good design will minimise these inefficiencies. The turbine has many sources of loss, but focusing on the blade and blade tip, these losses are traditionally categorised into three components: "profile loss", "endwall loss" and "leakage loss", though it is recognised that there is some interdependence between them. "Profile loss" is the loss associated with the blade boundary layers away from the endwalls. Using advanced computational techniques, enhanced blade profiles can help reduce the profile loss. "Endwall loss" is the loss associated with the hub and tip endwalls. Only the tip region is considered in the present thesis and the interaction between the tip endwall flow and the tip leakage flow is not distinguished as it is very difficult to separate the two. "Leakage loss" in turbine blades, a major component of this thesis, is the loss associated with the

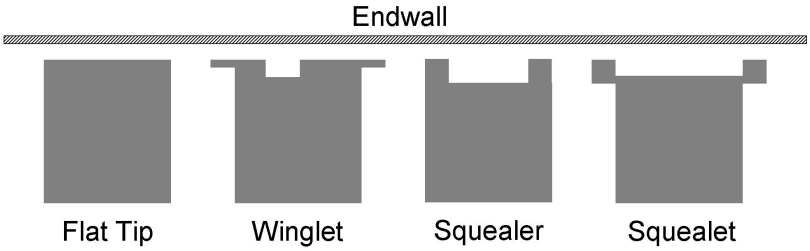

Figure 1.3: Typical blade tip sealing mechanisms including the winglet, squealer and squealet (figure not drawn to scale)

leakage of flow over the blade tips. Even a shrouded blade will have leakage loss, but it is less than the loss of an unshrouded blade. According to Denton (1993) each of the three components of loss are comparable in magnitude and the leakage loss can be as high as the profile loss. Reducing these losses will result in increased efficiency. In addition to these three components of loss, nearly all high-pressure turbines require cooling, which has loss associated with the mixing of the coolant and mainstream flows.

Generally, a decrease in the tip clearance between the blade tip and the outer casing endwall reduces the leakage loss. Additional attempts to reduce leakage loss include tip sealing mechanisms. An example of a tip sealing mechanism includes alternate blade tip geometries such as winglets, squealers or a combination of the two, as shown in Figure 1.3. The figure is not drawn to scale and it is not intended to compare different tip clearances, rim thickness and groove heights. More detail on leakage loss is addressed in Section 1.3.

In addition to increased rotation speed and reduced losses, an alternate way to improve the engine is by increasing the turbine entry temperature (TET), which increases the specific thrust (amount of thrust produced per unit of mass flow). Higher specific thrust, though typically a trade-off with specific fuel consumption (the amount of fuel required per pound of thrust produced), cannot be neglected, as the engine must produce enough thrust to meet mission requirements (e.g. take-off and cruise).

The thermal efficiency of the engine cycle and the power produced by the turbine is, among other factors, a function of the overall pressure ratio (PR) of the compres-

sion system (including the fan and compressor) and TET. There are various ways in which the TET can be increased, including increased PR across the compression system and increased fuel injection in the burner, though each method has their own limitations, as discussed in Mattingly (2005). Though there is a trade-off between increased TET for improved power output and lower fuel flow for improved specific fuel consumption, engine designers have chosen to make a high TET an important design variable. Figure 1.4 shows the trend for the TET for Rolls-Royce engines for the past 50+ years as well as the result from changing TET for various overall pressure ratios and fixed fan pressure ratio. Other engine manufacturers have a similar figure as Figure 1.4a. Note that it is possible for an increase in TET to result in reduced specific fuel consumption, as observed in Figure 1.4b.

In modern engines, the TET must be hundreds of degrees hotter than the temperatures at which the turbine blade experiences fatigue, creep or even melting (which is as high as current materials will allow). Friedrichs (2004) estimates the melting temperatures at 1400°C (2552°F) and the turbine inlet temperatures at 1600°C (2912°F). More recently, the Joint Strike Fighter, the most advanced high-performance fighter aircraft, has a TET up to 1982°C (3600°F) (Langston, 2007). The ability to obtain high TET is one of the designers' best secrets. Designers are forced to consider balancing material type and operating temperature with oxidation rate and cooling flow. They must also consider material ductility, fabrication, reparability and cost (Bunker, 2001).

Besides material improvements and blade coating procedures, improvements in blade cooling (e.g. film cooling and internal cooling) allow for designers to sustain these high TETs. However, designers are generally unable to effectively cool every part of the blade. Cooling the turbine has drawbacks. The "cool air" that cools the turbine blades comes from the last stage(s) of the compressor, in which the air temperature is on the order of 650°C (1202°F) (Friedrichs, 2004). Also, the more air that is used for cooling means the less air is available for mixing with fuel, which reduces the turbine output power. In addition, the cooling air also introduces aerodynamic losses.

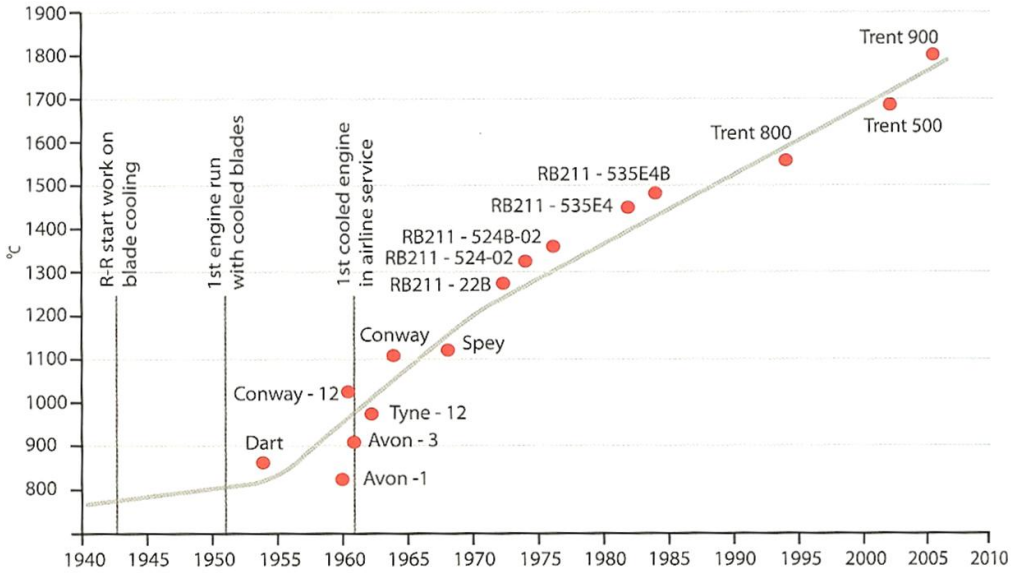

(a) Trend in TET for Rolls-Royce engines

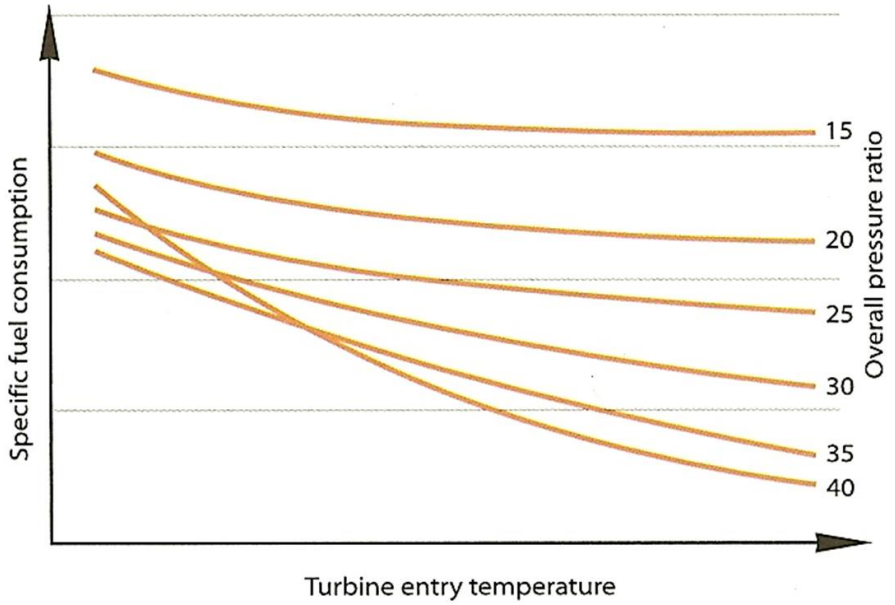

(b) Effect of TET on specific fuel consumption for variable overall pressure ratio and fixed fan pressure ratio

Figure 1.4: Trends in turbine entry temperature (Rolls-Royce, 2005)

As mentioned previously, the trends in turbine design improvements bring about challenges, which require further advances in technology. Modern designs need to be evaluated to determine how effective the unshrouded blades are at reducing tip leakage flow and handling the high TETs. The next section focuses on the tip leakage flow.

1.3 Over-Tip Leakage Flow

Many of the improvements described in Section 1.2 are currently used to improve performance and efficiency of a turbine blade. However, tradeoffs exist that must be considered. The transition to unshrouded blades requires a tip clearance, or tip gap, between the blade tip and the outer casing endwall to prevent rubbings between the metal surfaces as well as allow for mechanical and thermal growth of the turbine disk, blades and stationary outer casing endwall caused by the large number of temperature transients during operation. Typically, a clearance of one percent of blade height is associated with a leakage flow that is approximately two percent of the overall turbine flow. This loss of flow means less mass flow is turning the turbine, resulting in less power produced, leading to a two percent penalty in stage efficiency (Booth et al., 1982), though for engines with more than one stage, these flow and efficiency losses can possibly, though not necessarily, be recouped in later stages.

With a tip gap, the pressure difference between the blade pressure side surface and suction side surface causes over-tip leakage (OTL) flow when the airflow near the tip flows over the blade tip. The losses from the OTL flow are a result of not only the loss in momentum from the over-turning or under-turning of the flow, but also the loss caused by the boundary layer viscous losses in the tip gap as well as subsequent mixing of the OTL flow with the passage flow.

As the OTL flow has high temperature and high velocity, the blade tip experiences high heat transfer. If the tip is not cooled effectively, the blade tip can melt, causing increased tip clearance, or parts of the tip can break off, causing damage to

downstream components and possibly engine failure. This concern also leads to more frequent and costly inspections of the turbine blades.

For this reason, OTL flow must be minimised to reduce not only stagnation pressure loss but also the heat transfer to the tip. Though several approaches have been tried to reduce the OTL flow, the present study focuses on two: changing the tip clearance height and changing the tip geometry. As is addressed in Chapter 2, there are a growing number of studies examining tip clearances and using different geometries for use as tip-sealing mechanisms. Often this research is at low-speed conditions and most of the studies that examine different tip geometries examine squealer tips. Some of these studies employ cooling to understand how cooling impacts the OTL flow and heat transfer. However, there is very little agreement on how these geometries and tip sealing mechanisms perform under low-speed mainstream flow conditions and likewise there is very little understanding on how they perform under high-speed mainstream flow conditions.

Trying to minimise losses by changing tip types tends to make the blades more complicated, and OTL and heat transfer cannot be eliminated. Effective cooling schemes get very complicated (to manufacture) and it is difficult to predict how effective the cooling scheme is at each design point. Low-speed studies are generally easier to conduct and as most previous unshrouded flat tip studies are at low speed conditions, analysis can be easier. However, it is important to understand OTL flow and heat transfer under engine-realistic conditions, as the flow through the tip gap of an HPT is often transonic and cannot be accurately simulated with tests under low-speed conditions.

1.4 Motivation for Current Work

This section provides the motivation for this thesis. Improvements to HPT blades, such as those mentioned in Section 1.2, must be evaluated to determine if they meet the aero-thermal requirements placed on them. The aerodynamics and heat transfer of a design must be understood in order to make any additional improvements. Without

this understanding, it is unknown how effective the blade tip is at reducing OTL flow or how effective the cooling scheme is at reducing heat transfer to the tip. Blade tips that are ineffective at reducing OTL lead to a loss in efficiency. Blade tips that are ineffective at reducing heat transfer can become damaged. A poor understanding of the cooling scheme can lead to a poor estimate of the cooling needed. Finally, underestimating the cooling required leads to overheating of the blade tip, whereas overestimating the cooling required leads to loss in engine performance.

Most of the previous published work on OTL flow has been for low-speed conditions, which is far from being engine-realistic (see Chapter 2). To help design and optimise a blade, investigations should be done at engine realistic conditions (as best as possible) to truly understand the flow physics and heat transfer. Moore et al. (1989); Moore and Elward (1993) used a water table simulation and a hydraulic analogy to examine blade tips under transonic conditions. They observed shock waves over the tip and discussed the possible relationship to tip heat transfer. Their studies, however, seemed to go unnoticed as most tip heat transfer studies are either at very low speed, nearly incompressible, or subsonic compressible flow conditions. The difference between blade tip heat transfer and downstream aerodynamic loss for a blade tip under subsonic and transonic conditions is rarely reported and must be examined.

One of the goals of this work is to help the project sponsor identify and understand the heat transfer, aerodynamic loss and flow physics of a particular blade design that is representative of a high-pressure turbine blade, which must survive a high-temperature and high-speed flow in a rotating environment. Any investigation of uncooled blades must support the understanding of a cooled blade design and the effect of a cooling scheme must be examined under high-speed conditions as well.

Most engine-realistic studies are performed using turbine rotors, which are engine-scaled. The experimental setup of rotors, however, makes it difficult to obtain detailed, spatially resolved, heat transfer maps. For rotors, thin-film gauge are typically used, which are limited in the amount of detail they can provide (Thorpe et al., 2005; Thomas, 2006). Without highly-resolved heat transfer maps, much of the OTL flow-field is difficult to understand. With a detailed heat-transfer flow field, computational

work can be validated and further used to employ relatively moving casing endwall simulations to better understand the tip flow-field.

1.5 Project Aims and Objectives

The overall aims of the present project on aero-thermal performance of a high-speed tip include:

- Assist the development of durable and efficient HP turbine blade tip configurations and tip cooling designs
- Conduct blade tip aero-thermal measurements at engine representative Mach numbers and Reynolds numbers
- In conjunction with CFD investigations, validate Rolls-Royce's numerical code

The goals of this work, which is reported in the present thesis, include:

- Qualify use of High-Speed Linear Cascade (HSLC)
- Qualify the heat transfer technique used under transonic conditions
- Obtain spatially-resolved heat transfer measurements for blade tips with different geometry in an operationally representative transonic linear cascade
- Obtain spatially-resolved aerodynamic loss measurements for blade tips with different geometry in an operationally representative transonic linear cascade
- Determine suitability of cooled winglet (does it work and can it be cooled?)
- Determine a method for correcting heat transfer results near corners

The main purpose of this investigation was to obtain detailed, spatially-resolved heat transfer measurements for blade tips with different geometry in an operationally-representative transonic linear cascade and to provide comments on the physical understanding of these results. The results will provide researchers and designers a physical understanding of the fluid and thermodynamic flow field that, to the best of the author's knowledge, has not been published before.

As the transonic HSLC blow-down wind tunnel is new, it was qualified for use, including determining appropriate inlet and exit conditions. The transient infrared

(IR) thermography heat transfer technique was then qualified. Following the experimental setup, a tip gap study was performed at high transonic speeds and at low, near-incompressible speeds. Lastly various blade tips and near tip regions were investigated, to include flat tips, uncooled winglets and winglets with cooling. This study provides new insights into some of the flow structures that cause the variations in heat transfer and aerodynamic loss. Examples of flow structures include shock waves, shear layers, vortices, flow separation and flow reattachment.

1.6 Accomplishments

This project has been very successful at producing high-quality data that has significance for the gas turbine engine community. The author of this thesis was the lead author and presented three papers at the International Gas Turbine Institute's Turbo Expo (O'Dowd et al., 2010b,a, 2011), two of which are being published in the Journal of Turbomachinery (O'Dowd et al., 2010a, 2011). O'Dowd et al. (2011) details the qualification and use of transient infrared thermography to measure blade tip heat transfer under transonic conditions. To the best of the author's knowledge, spatially-resolved heat transfer results for blade tips under transonic experimental conditions have not been reported in the open literature. This work is detailed in Chapter 4. O'Dowd et al. (2010b) provides aerodynamic loss results downstream of the blade row of a flat tip for different tip clearances, which was presented along side of the blade tip heat transfer work presented by Zhang et al. (2010a). O'Dowd et al. (2010a) presents tip heat transfer results for the winglet tip under transonic conditions, including the effect of relative casing motion. To the best of the author's knowledge, this was the first experimental heat transfer study performed on a high-speed winglet tip.

The present author is also co-author on two other journal articles, to be published in the Journal of Turbomachinery. Zhang et al. (2010b) explores the predicted relationship between high-speed flow structures (such as shock waves, shear stress and turbulence diffusion) and heat transfer, based on the experimental results of the

present author. Zhang et al. (2010a) details the heat transfer results of a tip gap survey using a flat tip.

Much of what is understood about the flow over the tips and presented in these papers is due to the computational effort of Dr Qiang Zhang. As a member of the research group, the present author, jointly analysed these computational results to assess the validity and usefulness of the data to explain the flow physics of the OTL flow. Some of these computational results are presented in this thesis to help provide further understanding of the experimental results. As it is not exclusively the present author's work, the relevant discussion to this thesis is included at the end of each chapter in summary.

The importance of the present experimental work lies in the fact that the CFD study was motivated by the discrepancy between the high-speed results in the HSLC and previously-reported low-speed studies.

1.7 Thesis Outline

Chapter 2 provides a review of the most relevant works in the published literature on the aero-thermodynamics of tips and near-tip regions of an unshrouded turbine blade. Chapter 3 details the high-speed linear cascade, including its qualification, its capabilities and the experimental setup. Chapter 4 describes the heat transfer measurement and analysis technique used in the present thesis and a comparison to other analysis techniques. Chapter 5 presents the heat transfer results on the tip and in the near-tip region for the flat tip for different tip clearances. A comparison between low-speed and high-speed results are compared to emphasise the need for high-speed testing. Chapter 6 provides a tip gap survey for the heat transfer results of an uncooled and cooled winglet blade tip. Chapter 7 presents a tip gap survey of the aerodynamic loss for the flat tip, uncooled winglet and cooled winglet. Chapter 8 details a computational study performed to provide a simple technique to correct heat transfer results near corner edges, for which the semi-infinite, 1-D conduction assumption cannot apply. This chapter corrects heat transfer measurements near the

edges without requiring the use of a complex 3-D computational code. The correction is also applied to experimental results. Finally, Chapter 9 provides a summary of the present work, some of the major conclusions and recommendations for future work.

Chapter 2

Literature Review

2.1 Introduction

The purpose of this chapter is to review literature focused on the study of turbine blade tips. This chapter provides a review of the most relevant works in the published literature on the aero-thermodynamics of tips and the near-tip regions of an unshrouded turbine blade. Section 2.2 addresses the current understanding of aerodynamics in the tip-gap region. Section 2.3 then discusses the different heat transfer studies that are available in the open literature, specifically focusing on low-speed studies, rotor experiments, computational research, methods for tip clearance control, cooling and high-speed experiments. Section 2.4 reviews some of the different approaches that try to correct for corner conduction. Finally, Section 2.5 addresses the different aerodynamic loss studies with the same focus areas of Section 2.3.

2.2 Aerodynamics in the Tip Region

Before examining the heat transfer on an HPT blade tip or the over-tip leakage (OTL) flow downstream of the blade row, it is helpful to understand the flow field aerodynamics over the tip. Metzger and Rued (1989) explained the direct relationship between blade tip heat transfer and tip leakage flow characteristics, concluding that leakage flow through the test section corner gap is associated with large but highly localised increases in local heat transfer rates near the gap. Therefore, to understand

the tip heat transfer and OTL loss, researchers should study the leakage flow over the blade tip, starting with simplified studies.

2.2.1 Simplified ("Idealised") Cases

Study of turbine blade tips begins with a study of the flow field physics, with early work examining flow losses. A strong majority of these studies were under compressible subsonic, if not low-speed incompressible, flow conditions. Allen and Kofskey (1955) examined secondary flows in the blade tip region. Booth et al. (1982); Wadia and Booth (1982) investigated blade losses, both locally and overall, for several configurations of tip geometries using a simplified water tunnel experiment, and related these losses to reduction in stage efficiency. They observed a performance estimate of a two percent loss in turbine efficiency per one percent of tip clearance, which is frequently observed in other experiments.

Yaras et al. (1989) provided detailed velocity and pressure field maps within the tip gap of a simple, front-loaded blade geometry under incompressible conditions and noted separation bubbles on the pressure side corner, which take the form of vortices. Yaras and Sjolander (1992b) observed that the losses inside the gap itself were a relatively small fraction of the total losses as most of the OTL loss was caused by the mixing of the tip leakage and passage flows outside of the gap.

Bindon (1989), however, suggested that a separation bubble could be responsible not only for most of the internal gap shear loss, but also the massive core of loss occurring in the mixing region, which accounts for a large amount of total aerodynamics losses. Bindon observed that the internal gap shear loss had a larger percentage of the total loss and that most of the loss occurs in the aft portion of the blade tip (75–100 percent of axial chord).

Denton (1993) provided great details into the loss mechanisms in turbines. His review paper included both his own analysis as well as studies of other researchers. He described the OTL flow as a generation of entropy within the tip gap, in the blade passage and downstream of the blade row. He presented a schematic detailing the

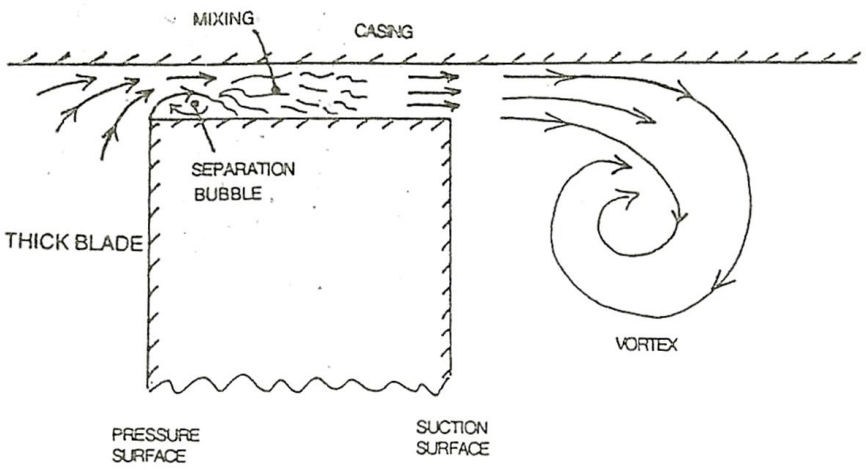

Figure 2.1: Flow over the tip gap for an unshrouded blade (Denton, 1993)

flow over the tip gap, noting a separation bubble occurring on the pressure side tip as well locations of reattachment and mixing, as shown in Figure 2.1.

Denton suggested that entropy creation is primarily associated with the mixing process that takes place between the leakage and mainstream flows and that the OTL flow can contribute up to one third of the total losses.

In a low-speed test, Sjolander and Cao (1995) observed that the OTL loss is closely related to the mass flow through the gap and that there is the presence of a separation bubble on the blade tip, starting at the pressure surface corner.

As the studies cited thus far are carried out at rather idealised conditions, the aerodynamics in the tip gap for engine-realistic conditions must be examined.

2.2.2 Engine-Representative Cases

The studies described in the previous section are considered "idealised", as there are several aspects in which they are not engine-representative. In some of the studies, a simple blade tip is used, but more recent studies use standard blade tip geometries. Though they provided a helpful introduction to flow over a blade tip, the studies previously cited are all under low-speed conditions, with no blade rotation. As an

actual rotor rotates at high speed, there are viscous effects from the relative movement between the casing and the rotor which change the flow physics over the tip.

Yaras and Sjolander (1992a) tested a low-pressure turbine blade in a large-scale linear cascade. Matching an engine-representative flow coefficient, they used a moving belt to simulate blade rotation, but the maximum casing speed only allowed for a very low speed test. They observed that in the first quarter-chord, there was no apparent effect on the separation bubble. At the quarter-chord location, where the blade has its peak blade loading for their setup, the separation bubble enlarged rapidly. They also observed a reduction in both the size of the separation bubble as well as the gap mass flow rate with an increase in relative wall speed. In Part II of a companion paper, Yaras et al. (1992) examined the effect of this rotation on the downstream flow field. Considering this downstream flow field, Yaras and Sjolander (1992a) concluded that the tip gap flow is dominated by pressure rather than shear effects associated with the moving wall. Palafox et al. (2008) also used a moving belt to simulate a moving endwall under low-speed conditions.

The importance of examining a blade tip under rotating conditions is acknowledged, and previous low-speed tests are helpful to understand the effect a moving casing has on the flow physics through the tip. However, there is less understanding of how much of a role a moving endwall has on a tip under transonic conditions. As high-speed, transonic experiments are difficult to perform with a moving endwall, the present author has found no transonic studies that examine the flow phenomena in the tip gap region. Though the present experimental study does not use a relative moving casing, the present study is used to validate CFD, which can then be used to examine the effect of a moving casing.

Another test condition that must be considered to make the test engine representative is the flow speed through the cascade. Very few tests have been performed under high-speed, transonic conditions. Using a water table and the hydraulic analogy, Moore and Elward (1993) translated their results into compressible flow concepts. They studied the formation mechanism of shocks in a sharp-edged rectangular channel. Though their test blade was "ideal", they concluded that after the separation

bubble in a tip gap, the flow reattaches and an oblique shock is subsequently formed. They concluded that the resulting shock-boundary layer interaction may contribute to further enhancement of already high heat transfer to the blade tip in this region.

Though other high-speed tip-leakage studies are in the open literature, few address the flow within the tip gap itself. Key and Arts (2004) examined different tip geometries in a high-speed, non-rotating, linear cascade to determine the effects of exit Reynolds and Mach numbers. A flow visualisation study showed that for the front part of the blade tip, the OTL flow is in the axial direction, as has been observed in low-speed studies. They identified a location, at an estimated 40 percent of axial chord, where the flow changes direction to a stream-wise direction, which is a different finding than that of low-speed studies.

Most recently, Wheeler et al. (2009) computationally investigated high-speed and low-speed flows comparing both aerodynamics and heat transfer over the tip. They presented some experimental findings from the Oxford Rotor Facility, a high-speed turbine rotor test rig. They observed major differences between heat transfer for high-speed and low-speed tests, largely due to the different flow physics over the tip, including separation bubbles, accelerated boundary layers and normal shocks. They concluded that the tip flow structure is significantly different for high-speed testing than it is for low-speed testing. Figure 2.2 shows a computed shock wave structure on the tip of a transonic HP turbine blade. The difference between Figure 2.2b and Figure 2.1 is remarkable and confirms the necessity of transonic over-tip flow studies.

This section concludes with some comments on the review by Denton (1993). Denton stated that Mach number has a significant effect on loss, observing a significant increase in loss coefficient for trailing edge Mach numbers greater than 0.9. He also observed that there are additional sources of loss caused by the interaction between shock waves and the boundary layer. He even commented that a boundary layer separation bubble will usually form at the foot of a weak shock and extra dissipation will occur downstream of the bubble.

Denton's observations, however, are not aimed at the OTL flow, but at the main passage flow. As for the OTL flow, Denton argued that the flow and loss mechanisms

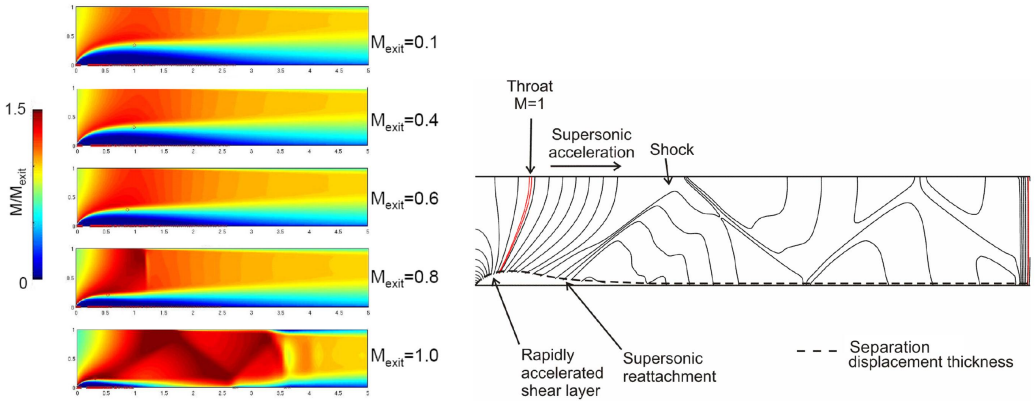

(a) Computed shock structure over the tip of a high-pressure turbine blade

(b) Transonic tip flow Mach contours

Figure 2.2: Predicted low-speed and high-speed flow over blade tip (Wheeler et al., 2009)

are now well understood for unshrouded blades. He concluded that OTL loss is an area that is understood, but cannot be quantified without empirical data. He also concluded that transonic sidewall trailing edges are not well understood and needs further examination. This raises a question: how well understood are transonic blade tips?

Denton suggested that entropy creation in the OTL region is primarily associated with the mixing process between the leakage flow and the mainstream. It appears that there is no consensus as to how extensive the loss from within the gap itself is, and the disagreement is typically in relation to viscous effects. If Moore and Elward (1993) and Wheeler et al. (2009) are correct that the shock structure over the tip governs much of the OTL flow, the loss through shocks in the tip region needs further attention. Denton did discuss the entropy creation through shocks in the passage flow, however, the tip region is much more complex as reflected shocks make the analysis much more complicated. Finally, Denton recognised that endwall losses are a significant source of loss (roughly one-third of the total loss) and that the endwall loss combined with OTL loss makes the problem even more complicated.

The present author argues that flow over the tip is not well understood. Though there may be some consensus for low-speed research, there is little understanding of

the tip leakage flow under engine-representative, high-speed conditions. Though it is expected that many different flow phenomena can be expected on the blade tip, such as separation, reattachment, turbulence diffusion and shock waves, it is unknown how extensive each of these is and how they relate to blade tip heat transfer and aerodynamic loss.

2.3 Tip Heat Transfer Studies

With the trend towards increases in turbine entry temperature (TET), turbine heat transfer is a major problem. Many turbine heat transfer studies examine turbulence effects, radial temperature profiles, endwall heat transfer, sidewall/stagnation point heat transfer and tip heat transfer. Guenette et al. (1989) used a short duration transonic annular cascade to obtain localised sidewall data and compared the results to the data taken at the Oxford Rotor Facility. However, it was Jin and Goldstein (2003); Giel et al. (2004) who were among the first to obtain detailed heat transfer results for rotor blades at the near-tip sidewall surfaces in transonic turbine cascades, but they did not consider the blade tip itself.

Many of the studies cited in Section 2.2 discussed the relationship between the OTL flow and heat transfer over the tip. The OTL flow is both high-pressure and high-temperature. Vortices off the pressure side tend to impinge on the blade tip, causing high amounts of heat transfer and eventual deterioration of the blade tip, making this a very important topic.

2.3.1 Heat Transfer Measurement Techniques

A discussion of the heat transfer results begins with a discussion of the various methods for measuring heat transfer. There are many ways to measure surface temperature or heat flux, but the most common are addressed in this section.

Jin and Goldstein (2003); Srinivasan and Goldstein (2003) used the naphthalene sublimation technique which allows for determination of local mass/heat transfer on a

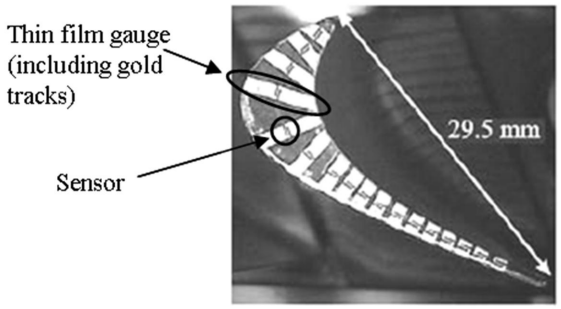

Figure 2.3: Seventeen heat transfer gauges positioned along the mean camber line (Thorpe et al., 2005)

surface using the mass/heat transfer analogy. Though this method is well established, it is certainly not as common as thin-film gauges.

Though thin-film gauges had earlier applications, one of the first studies to use these gauges to determine heat flux was Schultz and Jones (1973), for use in hypersonic wind tunnels. Due to the size of the gauge, including both the sensor as well as the leads, heat flux measurements are only determined at discrete locations. These gauges are particularly suited to environments where there is little to no optical access to the test surface. They can be made to handle robust environments, such as that for a high-speed rotor.

Thorpe et al. (2005) used thin-film gauges on the blade tip of a rotating turbine at the Oxford Rotor Facility. Figure 2.3 shows the heat flux gauge instrumentation on the mean camber line of the blade tip, which demonstrates the limited results that can be obtained (though a better map is obtained with gauges in different tip locations on different blades). The figure shows the large size of the instrument (including the sensor and the gold tracks) relative to the small blade that is used to measure an area-averaged heat transfer coefficient (h). Anthony et al. (1999) used high-density arrays of thin film heat flux gauges to mount more thin-film heat flux gauges in a smaller area, but this greatly increased the number of wire-leads instrumented, which is challenging for rotating rigs.

The thin-film gauges are unable to provide a full picture of the heat transfer on a surface. In order to obtain detailed, spatially-resolved temperature measurements,

alternate measurement techniques must be considered. One such technique is use of thermochromic liquid crystals (TLC). A detailed description of the use of liquid crystals is provided in Ireland and Jones (2000). TLC is capable of providing detailed images of complex surfaces and can be insensitive to reflections. They noted that although this method offers an excellent way of measuring full surface temperatures, there are constraints on their use. The widest colour play range is about 20°C. For blade tips that have temperature differences greater than 20°C, at least two types of crystals are required. Second, with such temperature differences, at high steady heat fluxes, the maximum heat flux is about $2\times10^4\,\mathrm{W/m^2}$. Considering thermal conductivity of the crystals, this heat flux gives a 2°C temperature drop across a $20\,\mu$m layer. This method is very widely used and a small number of examples of TLC studies on the tip and in the near-tip region include Mee et al. (2005); Bunker et al. (2000); Kwak and Han (2003a); Newton et al. (2006). It is important to note that the study by Mee et al. (2005) was conducted under supersonic conditions.

A second measurement technique that is capable of spatially-resolved measurements is infrared (IR) thermography. IR radiation measurement devices have been around since the early 1800s, but one of the first applications of temperature measurement in aeronautics-based research was by Deluca et al. (1995). IR thermography became more popular with turbomachinery in the late 1990s, including a paper by Schulz (2000). Ekkad et al. (2004), who advocated the use of IR thermography, despite the high expense of an IR camera and an IR-spectrum-transmissive window, comments that advantages of the use of IR thermography include the requirement of only a single transient test and the ability to capture the initial temperature distribution (which is very difficult using TLC). The present author acknowledges that some wide-band TLC studies require only one transient test and can capture the initial temperature (Vedula and Metzger, 1991; Licu et al., 2000). Other studies that have used IR thermography include Baldauf et al. (2001); Nasir et al. (2004), but these investigations did not examine blade tips under transonic conditions. Studies that have examined turbomachinery under high-speed, transonic conditions include Ochs

et al. (2006, 2007), who examined coolant injection and shock effects on blade sidewalls under engine-realistic transonic conditions. More recently, Reagle et al. (2010) used transient IR thermography to measure h on vane sidewalls and blade endwalls under transonic conditions.

The present study uses the transient IR technique for several reasons. First, one of the goals for this research was to provide detailed distributions of h to the project sponsor, which usually requires a transient test. Second, the IR thermography technique was chosen for the following reasons.

- The High-Speed Linear Cascade test facility already owned an IR camera and only an IR-observable window was required to be purchased
- IR test has virtually no limitations on temperature band
- Calibrations of liquid crystals are much more complicated

Some of the analysis methods used to determine h will be addressed in Chapter 4.

2.3.2 Idealised Heat Transfer Studies

Having discussed the methods for measuring heat transfer, this section begins to address heat transfer studies in the published literature.

The flow around and through tips has been investigated longer than heat transfer. However, in recent years, more attention has been devoted to the study of heat transfer on the blade tip. A review of high-pressure, high temperature blade tip heat transfer research is presented by Bunker (2001), which highlights some of the research summarised in this section. Most of the initial studies were idealised studies. The first investigation of tip heat transfer was by Mayle and Metzger (1982), who concluded that the effect of a moving wall was negligible on the tip heat transfer. They also concluded that the pressure-driven flow through the tip gap mainly influences the blade tip heat transfer. Chyu et al. (1989) continued the research of Mayle and Metzger (1982) by introducing a moving shroud to study the effects of rotation, affirmed that the relative motion had little effect on the average tip heat transfer, though some local effects were observed. The effect of the tip gap on idealised models

in water tunnels was investigated by Metzger and Rued (1989); Rued and Metzger (1989), concluding that blade tip heat transfer can be so high that thermal-stress-related damage to the tip area will occur unless designed for properly.

While the initial examinations of heat transfer have been useful, it is acknowledged that a more realistic test setup is necessary to properly understand the tip flow. The remainder of this section highlights studies of more realistic blade tips and experimental setup. Note that the effects of unsteady flow (e.g. wakes shed from a relatively moving blade row) and rotating reference frame (e.g. secondary flows created by vortices induced by rotation) will not be considered.

2.3.3 Rotor Heat Transfer Studies

The previous discussion has focused on idealised models. Tests using rotors typically use actual three-dimensional turbine blades with rotation, providing more realism to turbine blade testing. Typical studies use short duration tests as these experiments require less power to run and are generally easier to setup than a full turbine rig test. They can achieve near-operationally representative rotation speeds as well as engine design flow speeds. Using thin-film gauges, Dunn et al. (1984a,b) were among the first to use a real rotor/stator environment to show that large heat transfer rates are measured on the blade tip and the tip casing endwall. Metzger et al. (1991) observed that at higher tip clearances, the heat flux values were higher as a result of higher flow-rate through the tip.

Thorpe et al. (2004a,b); Thomas (2006) observed a relationship between the casing heat transfer and the passing of the rotor blade. Thorpe et al. (2005) investigated blade-tip heat transfer in a transonic rotating turbine at the Oxford Rotor Facility. Results include time-mean heat transfer rate [kW/m^2].

Temperature sensitive paint can be used to determine the metal temperature during engine testing. However, these results are rarely published and the engine designers are generally unable to relate the surface temperatures to the over-tip leakage flow. Brunner et al. (2007) is one of the few exceptions of a rotor test measuring spatially-resolved results. Using a low-pressure turbine stage for a large gas turbine

engine, they used an IR pyrometer to obtain a distribution of h along the mid-span of the blades.

Rotor tests using thin-film gauges are very useful for comparing one test condition to another. However, it is very challenging to obtain detailed results as it is difficult to instrument rotating blade tips with sensors requiring wire leads. The blade rotation is too fast and it is unsafe to place an optical window in a casing wall to measure heat transfer with any type of camera. The results obtained from rotor testing are helpful, but not sufficient to obtain spatially, highly-resolved measurements.

When considering the calibration uncertainty and uncertainty associated with bias and precision errors, and the relationship between the surface heat transfer rate and the derived h, h can have a precision error of up to 25 percent (Yoshino, 2002).

2.3.4 Low-Speed Linear Cascade Heat Transfer Studies

Studies using short duration shock tubes such as the rotor rigs are able to achieve near-engine-representative conditions. However, none have obtained detailed results across the entire blade tip surface. Linear cascades, on the other hand, are typically better for obtaining detailed test results as the blade tips can often be larger in scale (to match the Reynolds number during a low-speed test), which can provide better resolution. Also, optical access is easier as linear cascades do not typically rotate (though some can simulate blade rotation).

Due to their relative simplicity to build and test, a strong majority of the tip heat transfer research is under subsonic conditions, with many of these studies under incompressible or near-incompressible conditions. The general assumption is that the heat transfer does not qualitatively change between low-speed and high-speed and the quantitative values can be scaled as appropriate, such as using Reynolds number scaling. This section provides only a few of the key subsonic cascade heat transfer studies.

Yang and Diller (1995) were among the first to examine tip heat transfer in a linear cascade environment, however their results have limited resolution.

Bunker et al. (2000) were the first to obtain detailed blade tip contours of h using a first-stage blade tip surface for geometry typical of a large power-generation turbine, with an exit Mach number of 0.75. They highlight that the details of the pressure field on the tip are required to fully explain the heat transfer results. They termed the centre portion of the leading edge (at the crown) with the low h as the "*sweet spot*". They also observed high heat transfer at the tip leading edge and on the trailing edge.

Azad et al. (2000a,b) investigated a flat tip and a squealer tip at subsonic, but compressible conditions, with the peak Mach number on the suction side of 0.6. With flow conditions similar to Azad et al. (2000b), Kwak and Han (2003a) obtained contours of h and film cooling effectiveness on a gas turbine blade tip.

Some studies have been done at low subsonic speeds, which requires that larger-scaled blades be used to match the Reynolds number for an actual engine. Teng et al. (2001) obtained detailed h distributions on a turbine blade tip under low speed conditions ($M_{max} = 0.14$) for three different tip gaps. Krishnababu et al. (2007b,a); Newton et al. (2007) jointly examined the effects of tip geometry, tip clearance gap, relative motion and tip cooling. Their results show unusually low h magnitudes compared to the other linear cascade studies previously cited, but the qualitative trends are comparable to Bunker et al. (2000), with an area of low heat transfer in the leading edge and a region of high heat transfer at mid-chord, close to the mean camber line. They also concluded that the effects of relative motion were negligible. Figure 2.4 shows their experimental and computational results for a 3.5 percent (axial chord) tip gap from Krishnababu et al. (2007b). The frontal region of the blade contains a "*sweet spot*" observed by Bunker et al. (2000). It is the aft region of the blade that will be specifically highlighted in Chapters 5 and 6. Additionally, Newton et al. (2006) observed that the highest h for any surface on the blade tip and near tip region are located on the tip, even higher than the stagnation region on the leading edge.

Some linear cascade experiments have been performed to determine the effect of a moving endwall on tip heat transfer. In order to have operationally-representative flow coefficients (ratio of inlet axial velocity to rotor-tip rotation speed), tests are

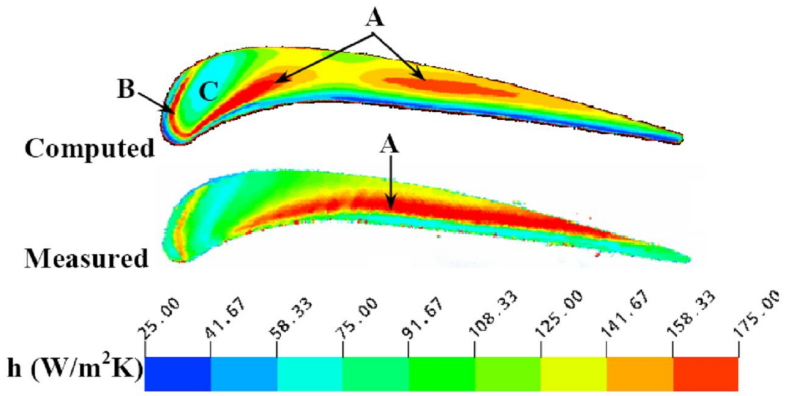

Figure 2.4: Contours of heat transfer coefficient on flat tip with tip gap of 3.5% of axial chord (Krishnababu et al., 2007b)

typically done under low-speed conditions. There appears to be no consensus on the effect of the moving endwall. On one hand, studies such as Srinivasan and Goldstein (2003); Mayle and Metzger (1982); Chyu et al. (1987) argued that there is little effect of endwall rotation on h. On the other hand, others suggest that motion has a significant impact on h. In an experimental study, Palafox et al. (2006) suggested that motion seems to reduce h on the blade tip. In a computational study, Yang et al. (2006) stated that rotation tends to increase the tip leakage flow and heat transfer, though there are local effects where it does not change. Somewhat in the middle, Krishnababu et al. (2007a) argued that motion causes a decrease in the tip leakage mass flow and average heat transfer, though the effect is minor and does not change the ranking of heat transfer for different tip geometries.

As for uncertainty Bunker et al. (2000) reports the experimental uncertainty in local h to be ± 8 percent or better, using the method of Kline and McClintock (1953).

None of the linear cascade studies cited in this section, however, address high-speed, transonic cascade research. Of particular importance is the investigation of flow phenomena and thermal performance in transonic flow, with Mach number distributions which match conditions which are experienced by turbine blades and blade tips in actual engine environments, which is addressed in this thesis.

2.3.5 Computational Heat Transfer Studies

Computational studies have the advantage of testing under engine-realistic, aero-thermal conditions. Examples include realistic temperature inlet profiles, turbulence, transonic conditions and blade tip rotation (including a moving endwall as well as rotation effects). Though it is generally easy to get results, the quantitative and qualitative accuracy of these results are often uncertain. In order to validate the computational domain (for example, mesh and turbulence models), experimental results are used for validation. Rarely will there be a computational study that does not seek to qualify its results with experimental tests. As there appears to be no published study with spatially resolved blade tip experimental heat transfer results under transonic conditions, there are few computational studies on transonic tip heat transfer.

Several subsonic numerical studies have been performed. Ameri et al. (1998) examined the effect of a squealer tip on heat transfer and efficiency of a GE-E3 turbine, which is the same blade profile as Azad et al. (2000a). The computational results obtained by Ameri and Bunker (2000) show good agreement with the experimental results of Bunker et al. (2000). Krishnababu et al. (2007b) is a study with both experimental and computational data. Though the computational results over-predict h, the trends do compare well. Tang et al. (2010) computationally determined the over-tip flow field and the tip heat transfer, comparing results to those of Palafox et al. (2006, 2008)

Few computational high-speed tip heat transfer studies have been performed. Polanka et al. (2003) compared experimental and computational heat transfer results at five discrete tip locations. Computational results include spatially resolved heat flux that has some of the same heat transfer signatures as the results presented in the present work. Though heat transfer trends were slightly different than other spatially-resolved results under low-speed conditions, there was very little discussion provided. Saha et al. (2003) examined a flat tip and a pressure-side winglet tip under high-subsonic (but not transonic) flow conditions. These results were not validated

against experimental results and the tip flow was largely subsonic. More recently, Shyam et al. (2010) provided CFD results of a high-speed, transonic rotor tip showing tip shocks and striping similar to those observed in this thesis.

2.3.6 Heat Transfer Studies with Tip Clearance Control

The transition to unshrouded blade tips allow for increased rotation speed, but at the cost of OTL flow. This high-temperature flow not only causes high amounts of heat transfer to the tip but also leads to total pressure losses. In order to assess this loss, studies employing different tip clearance control methods (tip sealing mechanisms), have been attempted. The focus of this thesis is on geometric tip clearance control methods. The most basic tip is a flat, plain tip. Many of the studies cited above, including the present work, examine flat tips. Many other studies consider how different geometric tip clearance control methods compare to this flat tip.

One geometry is the squealer (see Figure 1.3), which has been studied mostly under subsonic conditions, typically using linear cascades. Most of the investigations show that there are regions of high heat transfer coefficients in the areas which correspond with flow impingement as well as the trailing edge, but the squealer tip has lower h overall, with variations based on cavity depth and rim thickness. Such studies include Newton et al. (2006); Krishnababu et al. (2007b); Kwak and Han (2003b); Azad et al. (2000a). Numerical studies of squealer tips show similar results to experimental ones, as observed in Yang et al. (2006, 2002b); Ameri et al. (1998).

Under engine-representative flow speeds, Mischo et al. (2006) examined squealer tips in a one and a half stage turbine. Both experiments and CFD show that the squealer helped to reduce both suction side and tip heat transfer. Dunn and Haldeman (2000) measured heat transfer using thin-film heat flux gauges on a recessed tip on a transonic turbine blade in a full-stage rotating turbine.

The focus of this thesis is on the winglet geometry (see Figure 1.3). Most research on winglets has been related to aerodynamic loss. Few studies have examined heat transfer. Papa et al. (2003) used the naphthalene sublimation technique to measure mass/heat transfer on the tips of squealer-tipped and squealer-winglet-tipped blades

under subsonic conditions. As for high-speed subsonic conditions, Saha et al. (2003) computationally investigated heat transfer and aerodynamic loss, comparing different forms of winglet on flat tips and squealer tips. They concluded that the double-sided squealer with winglet produces only marginal improvements in heat transfer coefficient.

The author is not aware of any experimental heat transfer examinations on winglet tips under transonic conditions.

2.3.7 Heat Transfer Studies with Cooling

The HPT in an actual engine will likely use various forms of cooling. A search for film cooling in the literature will likely result in studies on the effects of blowing ratio, hole shape, exit angle and hole spacing, frequently on flat plates or on the blade sidewalls or endwalls. Though the casing endwall may employ cooling that can change the flow physics over the tip, the present study only considers blade tip film cooling.

Some of the studies previously cited also tested the effects of coolant injection. The general trend is that film cooling effectiveness increases with decreased tip clearance, but coolant injection generally has little effect on squealer tips. Also, the best film cooling effectiveness for coolant injection is for injection from both the tip and the pressure side sidewall, near the tip. Lastly, pressure side injection provides a "*blockage effect*" such that the flow accelerates over the tip and the heat transfer coefficient decreases on blade tip.

Kim and Metzger (1995) studied an idealised blade tip with pressure side holes under low speed conditions. They measured effectiveness and Nusselt number near the cooling holes, but did not provide spatially resolved results for the entire blade tip. Yang et al. (2004) performed a computational study that examined different arrangements of film holes on flat and squealer tips.

Newton et al. (2007) used a low speed wind tunnel to test an uncooled blade and from the h results, designed a cooled blade's film cooling arrangement. With coolant injection, they observed that the highest heat transfer coefficients were located in the region of attachment just downstream of the pressure-side separation bubble.

By injecting coolant inside the separation bubble, the fluid dynamics of the over tip flow were significantly altered such that the high heat transfer associated with the flow reattachment was nearly eliminated. They observed the "*blockage effect*" of the pressure side injection which reduced tip h levels. Finally, they determined that the cooling design, with a coolant mass flow of 0.5 percent of the mainstream flow, was satisfactory because the integrated average of the net heat flux reduction showed that the net heat flux to the tip at engine-level temperatures would be reduced by 37 percent.

Tip coolant injection studies under high speed conditions are much less common. Due to the experimental complexity, few experimental heat transfer studies in which rotors inject coolant from the blade tip have been performed, which are typically under subsonic conditions (Abhari and Epstein, 1994; Garg and Abhari, 1997). Though coolant injection from tips tested in high-speed, transonic linear cascades is less complex, the present author has found few high-speed rotor heat transfer studies with coolant injection (Haldeman et al., 2006a,b). More specifically, to the best of the author's knowledge, there are no cooled winglet studies in the published literature.

2.3.8 High-Speed Linear Cascade Heat Transfer Studies

Due to the difficulty in obtaining steady flow conditions for longer than a short duration shock tube, there are few high-speed, transonic, linear cascades, where exit Mach numbers are greater than 0.9. Most of the ones capable of transonic flow conditions examine aerodynamics of the main passage flow and/or heat transfer on the blade sidewalls. Few have examined the aerodynamics or heat transfer of the blade tip itself. Key and Arts (2004); Hofer and Arts (2009) investigated the aerodynamic flow field in a transonic linear cascade, but did not consider heat transfer. One of the first studies to consider heat transfer on blade tips under transonic conditions was by Moore et al. (1989), who used a water table to study the flow over an idealised, highly-loaded flat tip, addressing how a shock pattern over the tip affects heat transfer on the tip.

It is acknowledged that under high speed conditions, the pressure field possibly changes enough that the heat transfer results could change as well. Wheeler et al. (2009) computationally showed the difference between high-speed and low-speed heat transfer.

The combined experimental and CFD study of Zhang et al. (2010b), partly summarised in the present thesis, is the first to provide data on the presence of repeated heat transfer variations in the forms of stripes, which are present for the rear portion of a transonic tip surface. According to these investigators, these stripes are linked with a pattern of shock wave initiations and reflections.

To the best of the author's knowledge, there are no published transonic linear cascade studies that provide spatially-resolved experimental heat transfer results.

2.4 Corner Conduction Correction

In the majority of transient heat transfer studies, conduction into the surface is assumed to be semi-infinite 1-D and any lateral conduction is usually assumed to be negligible. As it will be shown in Chapter 8, this is a fairly good assumption far away from any sharp edges. There are cases, however, where this is not the case. Vedula et al. (1988) used a two-dimensional finite element model to assess the accuracy of the one-dimensional assumption used in analysing experimental data. For a rise in h from 400–600 $\mathrm{W/m^2K}$ over a distance of 3 mm, the maximum error is calculated to be 3.5 percent.

The 2-D corner effects on tip heat transfer, however, are rarely addressed, especially in experimental problems. Kingsley-Rowe et al. (2005) derived a correction parameter that can correct the lateral conduction during post-processing of transient narrow-band liquid crystal experiments, avoiding the need to solve the 2-D or 3-D finite-difference equations. This method requires an approximate solution to Fourier's equation in two dimensions as well as an assumption that the experiment has "typical experimental parameters", but the method does not consider heat transfer near corner edges.

Other approaches couple experimental data with 3-D numerical models to determine the surface h (Lin and Wang, 2002; Ling et al., 2002, 2004). Ling et al. (2004) showed that the effect of lateral conduction due to adiabatic wall temperature gradients is more significant than due to h gradients, unlike the conclusion of Vedula et al. (1988). von Wolfersdorf (2007) provides an analytical model to understand lateral conduction, especially close to film cooling holes, for variations in adiabatic wall temperature.

Many of the studies cited in this section indicate that errors in h due to lateral conduction can be as high as 10 percent, if not more, depending on the experimental conditions. Most of the studies correct this lateral conduction through computationally expensive 3-D finite-difference solutions. Those that correct the lateral conduction through more simple correction parameters only correct lateral conduction, away from a corner edge. The present author has not found any studies that address a way to specifically correct experimentally-determined h near corner edges without using a 3-D numerical model. The present study addresses a relatively simple approach to correct the corner conduction effect.

2.5 Aerodynamic Loss Studies

The second major focus of this thesis is on aerodynamic loss. Numerous aerodynamic loss studies have been conducted in many different environments, from compressors to turbines, from rotors to stators and nozzle guide vanes (NGVs), from rotating to linear cascades (with and without simulated moving casing wall), for different tip geometries and tip clearances, for endwall/profile/OTL loss, and for high and low-speed conditions. Aerodynamic loss has been addressed by Denton (1993), who cites the historical aerodynamic loss into three categories: profile loss, endwall loss and leakage loss. Denton also includes boundary layer and shock losses in this study and references several papers on these topics. Mee et al. (1992) studied trailing edge loss in transonic flow. They distinguished between different forms of loss including boundary layer loss, shock loss and mixing loss. Xu and Denton (1988) demonstrated

how changes in Mach number affect the trailing edge loss. Finally, Langston et al. (1977) provided the first detailed endwall loss measurement results.

Tests of NGVs using annular cascades examine engine-realistic geometries as the vanes tested are three-dimensional. In some studies, tests are under engine-realistic flow conditions. Aerodynamic loss measurements downstream of NGVs has been frequently examined by the University of Oxford (Mee et al., 1992; Main et al., 1997; Day et al., 1999; Sargison et al., 2002).

As these studies consider nozzle guide vanes, over-tip leakage is not considered. However, these studies all provide an algorithm for reporting aerodynamic loss in a mixed-out plane, which is used in the present study.

Aerodynamic loss results pertaining to the tip region and OTL flow are a major focus of this thesis. At least one annular cascade examined an unshrouded rotor blade without rotation (Matsunuma, 2006). Most rotor blade studies, however, consider rotation, as it will be addressed in Section 2.5.2.

The relationship between heat transfer and aerodynamics are closely coupled and it is important to examine the effect of transonic flow conditions on aerodynamic loss. If flow over the tip is choked, then the flow field is only affected by upstream total pressure and total temperature, indicating that both aerodynamics and heat transfer for blade tips must be studied together under transonic conditions. It is also useful to conduct a detailed analysis of the aerodynamic loss for the same geometry and under the conditions as those for which heat transfer is determined.

Lakshminarayana (1996) states that a compromise is necessary to optimise thermal gain (increased TET, cycle efficiency, etc.) with aerodynamic losses and decreased efficiency. In addition, Denton (1993) suggests that OTL loss contributes to about one-third of the total loss and reductions in OTL loss lead to increased engine efficiency. The remainder of this section focuses specifically on OTL loss. Studies that examined OTL loss in the tip gap region or immediately downstream of the blade suction side tip was addressed in Section 2.2. While this provides a helpful picture of the OTL flow, determining aerodynamic loss downstream of the blade row provides a

more complete picture, which considers both the momentum and energy of the OTL and passage flows as well as the mixing of the two.

Before addressing these aerodynamic loss studies, however, the measurement and definitions of loss is discussed.

2.5.1 Measurement and Definition of Aerodynamic Loss

The flow field downstream of the blade row is very complex with various vortices in 3-D flow. Pressure probes or velocity measurement devices, such as hot-wire anemometers, must be able to accurately measure these complex flows. To obtain spatially-resolved loss results, many studies use five-hole probes to resolve flow direction in the pitch (blade-span-wise) and yaw (blade-pitch-wise) directions (Treaster and Houtz, 1986; Dominy and Hodson, 1993). Main et al. (1996) noted that these five-hole probes accumulate redundant information as only four holes are needed for four measurements (e.g. total pressure, Mach number and two flow angles). They calibrated and traversed a four-hole pyramid probe in a short-duration transonic turbine cascade tunnel.

In some cases, a four-hole probe may be too large for the calibration facility or the experimental setup. A three-hole probe is described by Povey et al. (2008). With one fewer hole, the probe is unable to resolve one of the flow angles, unless it is rotated.

After determining the pressures downstream of the blade row, the results are typically reported in a form of total pressure loss. Köllen and Koschel (1985) used the following definition for loss (Y) for a turbine blade row

$$Y = \frac{P_{\text{total, inlet}} - P_{\text{total, exit}}}{P_{\text{total, exit}} - P_{\text{static, exit}}} \tag{2.1}$$

where $P_{\text{total, inlet}}$ is the inlet total pressure, $P_{\text{total, exit}}$ is the exit total pressure and $P_{\text{static, exit}}$ is the exit static pressure. In this equation, the local total pressure loss is normalised by the exit dynamic head. As the exit dynamic head can vary significantly, such as is the case with flow with large vortices, care must be taken to determine the exit dynamic head. The exit dynamic head in the present study

is based on the mass-averaged, mid-span value, which has little variation for the different blade tip geometries and tip clearances.

With coolant injection, Equation 2.1 cannot account for the addition of the coolant pressure and temperature. For cooled and uncooled studies, Denton (1993) described the loss (ζ) as a rise in entropy (Δs), which is defined as

$$\zeta_{entropy} = \frac{T_{\text{static, exit}} \Delta s}{h_{\text{total, exit}} - h_{\text{static, exit}}} \tag{2.2}$$

where $T_{\text{static, exit}}$ is the exit static temperature, $h_{\text{total, exit}}$ is the exit total enthalpy and $h_{\text{static, exit}}$ is the exit static enthalpy. The approach of Denton (1993) will account for the coolant pressure. However, for the present study, exit temperatures are not measured and the loss is related to a kinetic energy efficiency, η, as seen in Day et al. (1999), which is defined as

$$\eta = \frac{\text{Actual kinetic energy out}}{\text{Ideal kinetic energy out}} \tag{2.3}$$

Therefore, the loss of efficiency, ζ is

$$\zeta = 1 - \eta = 1 - \frac{h_{\text{total, exit}} - h_{\text{static, exit}}}{h_{\text{total, inlet}} - h_{\text{static, isentropic exit}}} \tag{2.4}$$

where $h_{\text{total, inlet}}$ is the inlet total enthalpy, $h_{\text{total, exit}}$ is the exit total enthalpy, $h_{\text{static, exit}}$ is the exit static enthalpy, and $h_{\text{static, isentropic exit}}$ is the exit static enthalpy assuming isentropic expansion through the blade row.

ζ can be defined in terms of temperatures for a calorically perfect gas or pressures, using compressible flow equations. The denominator is more complicated, as addressed by Young and Horlock (2006), who discusses different ways of defining the ideal kinetic energy out. The present study uses Hartsel's cooled cascade efficiency (Hartsel, 1972), which assumes that the main gas flow and coolant stream expand isentropically without mixing from their supply stagnation conditions to the exit static pressure P_2. Others who have used this definition include Kost and Holmes (1985); Köllen and Koschel (1985); Day (1997).

Since the variation in coolant blowing ratio can affect the aerodynamic loss, Amecke (1970) proposed a method to "*mix out*" the flow for a two-dimensional cascade. Following the study by Amecke (1970), others have applied this to annular cascades (Dzung, 1971; Main et al., 1997) as well as cases for a variation in total temperature between the mainstream and coolant (Oldfield et al., 1981). These methods reduce the exit flow to an "average" state, which is not physically realistic, but it is mathematically consistent (Day, 1997). The mixed-out plane analysis provides a single value of loss for each test condition (e.g. variation in blowing ratios, mainstream Mach number or tip clearance). This makes it difficult to identify the different flow structures downstream of the blade row. Alternatively, many studies will provide contours of exit total pressure normalised by the inlet total pressure or raw pressure difference between inlet and exit for these spatially-resolved contours.

The remainder of this Section 2.5 provides a review of various aerodynamic loss studies.

2.5.2 Rotor Aerodynamic Loss Studies

In addition to the engine-realistic blades, like NGVs, rotor tests usually introduce engine-realistic rotation as well. Rotor tests range from low-speed to engine-realistic high-speed, however, detailed tip loss measurements for the rotor is rarely seen, and often under low-speed conditions.

To properly test under engine-realistic conditions with engine-sized hardware, it is often challenging to instrument the rotor to measure stagnation pressure downstream of the blade row. Some rotors have a stator guide vane for the next stage behind the blade row which limits access and if measurements are made downstream of the stator, the effect of OTL is not known. For those rotor studies that are capable of measuring downstream flow-field, the speed of the rotor makes measurement very challenging. For this reason, most rotor rigs that study aerodynamic loss examine scaled-up blades under subsonic conditions.

Xiao et al. (2001); McCarter et al. (2001) studied the effects of tip clearance flow over the tips of a low-speed large-scale rotor. They considered the growth of the total

pressure loss coefficient at 70, 80, 90 and 110 percent of axial chord (starting at the leading edge). Xiao et al. (2001) concluded that the movement of the casing wall had a significant effect on the flow field with an additional scraping vortex that is created that is not seen in cascade studies, unless tested with a moving wall (Palafox et al., 2008). They also observed a large increase in loss at 90 percent of axial chord due to merging of tip vortex and passage vortex. Finally, they observed that the tip leakage vortex is relatively small compared to the passage vortex, but the OTL vortex's loss coefficient was nearly twice as high. McCarter et al. (2001) observed very little interaction between the OTL and mainstream flows up until 70 percent of axial chord. Beyond 80 percent of axial chord, the leakage flow strengthens and penetrates further into the passage both tangentially and radially. They compared their results to cascade studies and determined that the leakage flow for rotating tips stays closer to the blade. Finally, they observed that losses due to leakage flow were approximately 25 percent higher than losses due to the passage vortex.

Other aerodynamic loss studies using low-speed rotors include Rao et al. (2006) who considered the effects of roughness on loss and Mischo et al. (2007) who computationally examined controlling the OTL through coolant injection from the casing.

Very few high-speed experimental rotor studies have examined aerodynamic loss downstream of an unshrouded blade row. Payne et al. (2003) presented measurements of entropy in the Oxford Rotor Facility using stationary probes. They measured total temperature using an aspirating probe 15 percent of axial chord downstream of the blade trailing edge. Their spatially-resolved results distinguished the OTL vortex, upper passage vortex, lower passage vortex (from the hub) and the wake.

2.5.3 Low-Speed Linear Cascade Aerodynamic Loss Studies

As most rotor studies examine aerodynamic loss using low-speed rotors, most linear cascade studies are also under low-speed or subsonic conditions as they are relatively simple to build and are generally inexpensive to run. Measurement probes for subsonic cascades are also generally simpler to calibrate. Most subsonic linear cascades are

larger and have the ability to run continuously which allows for a probe to traverse with a high spatial resolution.

Yamamoto (1989) examined endwall flow and loss mechanisms in a low-speed linear cascade for three different tip gaps, using a micro 5-hole pressure probe. He concluded that the leakage flow vectors largely depend on the tip gap size, particularly in the front part of the blade. Like Bindon (1989), Yamamoto (1989) also observed that most of the leakage flow that forms the vortex occurs at the rear part of the tip.

Yaras et al. (1992); Yaras and Sjolander (1992a) studied the effects of a moving endwall experimentally using a low-speed linear cascade, concluding that the moving endwall significantly decreased the tip gap flow. They also observed that the location of the vortex with moving wall shifted closer to the blade suction side compared to the stationary wall test, which agrees with the rotor results of McCarter et al. (2001). Sjolander and Cao (1995) observed that the size of the vortex increased as the tip gap increased. This leads to increased losses due to the mixing of the leakage flow vortex and the passage flow on the suction side.

Palafox et al. (2008) used PIV in a very large-scale, low-speed wind tunnel with moving endwall to characterise the OTL loss. They observed that the OTL vortex was significantly affected by endwall-movement, as it distorted the shape of the tip leakage vortex and it shifted the tip leakage vortex back towards the blade suction-side, consistent with observations by McCarter et al. (2001); Yaras et al. (1992). Palafox et al. (2008) also observed that the tip flow had a dramatic influence on the passage vortex and they observed a scraping vortex generated by the leakage jet and opposing moving endwall, also observed by Xiao et al. (2001); McCarter et al. (2001).

Aerodynamic loss measurements of flat tips in low-speed linear cascades are frequently used as baselines for comparison to alternate tip geometries, such as the squealer or winglet designs. These studies are discussed in Section 2.5.5.

2.5.4 Computational Aerodynamic Loss Studies

As pointed out in Section 2.3, many computational studies accompany experimental studies. Generally the trends in aerodynamic loss indicate that an increased tip gap

equates to increased pressure loss as well as a shifting of the OTL vortex further away from the blade suction side. Computational studies provide the ability to examine the effects of a moving casing endwall, something that few experimental linear cascade studies have the capability for. As a majority of experimental aerodynamic loss studies are under low-speed conditions, so too are most computational aerodynamic loss studies, with a few that are high-subsonic (but not transonic).

Tallman and Lakshminarayana (2001b,a) performed a low-speed computational study for different tip clearances and a moving casing wall for a blade in a linear cascade. They concluded that an increased size of the OTL vortex was observed with increased tip clearance and that the OTL vortex size for the moving wall simulation was about one-third the size of the fixed-wall case counterpart.

Some of the heat transfer studies cited in Section 2.3 also considered the OTL flow over the tip and slightly downstream of the blade row. These studies are for high-subsonic exit Mach numbers (but not transonic). Yang et al. (2002b); Acharya et al. (2003); Yang et al. (2006) determined velocity magnitudes and Mach numbers of the OTL flow just downstream of the suction-side exit. Yang et al. (2002a); Saha et al. (2003) obtained velocity magnitudes and Mach numbers, respectively, over the tip as well as $0.2C_{ax}$ downstream of the blade row. Ameri et al. (1998) calculated the integrated efficiency loss downstream of the blade row, but concluded that there was no significant difference between the flat tip and squealer tips.

2.5.5 Aerodynamic Loss Studies with Tip Clearance Control

The major purpose for tip clearance control is to reduce aerodynamic loss. For this reason, most studies that have examined aerodynamic loss have done so with tips that control the tip leakage flow over the tip, especially through alternate tip geometries. Many of the aerodynamic loss studies have considered squealers. Booth et al. (1982), using a water flow rig, showed that the squealer tip was better than the flat tip. Using a low-speed linear cascade, Heyes et al. (1992) measured contours of stagnation pressure loss for the flat, suction-side squealer and pressure-side squealer

tips, concluding the benefit of the squealer tip over the flat tip. Schabowski and Hodson (2007) tested several tips, including the squealer, in a low-speed linear cascade. Few papers have investigated the aerodynamic loss downstream of a squealer tip in a transonic linear cascade environment. Key and Arts (2004) examined squealer tip blades in a high-speed linear cascade, observing a reduction in loss compared to that of flat tip blades. Other high-speed aerodynamic loss investigations of the squealer include Hofer and Arts (2009); Vass and Arts (2009).

A compromise to reducing the mass of the shroud and limiting OTL loss is to use a partial shroud. Porreca et al. (2005, 2009) examined the aero-thermal-mechanical aspects of partial and full shrouds in a subsonic rotor. However, these partial shrouds are not the same as a winglet, as they contain many remnants of the shroud, including fences. The partial shroud does extend circumferentially around the annulus, but has slightly less mass, as the partial shroud does not cover the entire axial area.

Another tip geometry is the winglet. Patel (1980) studied a double-sided winglet design that resulted in a stage efficiency improvement of 1.2 percent. Booth et al. (1982); Wadia and Booth (1982), in addition to flat tip and squealer tip designs, examined different winglet designs. From their experimental and computational study, results showed a superior performance with the winglet configurations (Wadia and Booth, 1982).

Dey and Camci (2001) tested different tip platform extensions (winglets) in a single-stage low-speed rotor to show that pressure-side extensions are highly effective in reducing the OTL. Harvey and Ramsden (2001) used a 3-D CFD code to show that the winglet is a suitable alternative to a full shroud. Their calculations demonstrate that the winglet significantly reduces the OTL flow and loss. Harvey et al. (2006); Willer et al. (2006) later tested a winglet design computationally and experimentally in a high-speed cold flow rotating environment. Results showed that the winglet tested was as good as a shroud with two fins in reducing over tip leakage loss. Figure 2.5 shows the winglet tested by Harvey et al. (2006); Willer et al. (2006), which is similar to the one examined in this thesis. In addition to testing different squealer tips, Schabowski and Hodson (2007) tested different winglet designs and compared

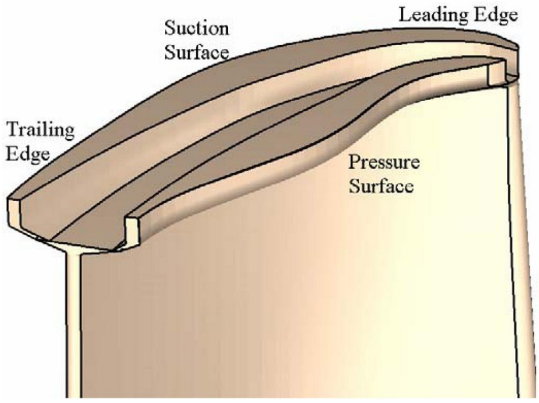

Figure 2.5: Illustration of winglet geometry investigated by Harvey et al. (2006)

them to CFD results and showed that both winglets and squealers have their own advantages and both have reduced aerodynamic loss compared to that of the flat tip. Schabowski et al. (2010) later studied a combined winglet-squealer tip experimentally and computationally in a low-speed linear cascade. Staubach et al. (1996) was one of the few studies that did not see an advantage of a winglet over flat tip geometries, as stage efficiency reduced by 0.35 percent.

Finally, Denton (1993) described many sources of entropy production in turbomachines. One source is a part-span shroud. Fans often have these to reduce vibration, while HPTs generally do not, as the span of an HPT is relatively short. However, the extra surface area of the winglet tested in this study, both on the tip itself as well as the streamlines that follow the blade curvature, would generate additional losses, in a similar way as the part-span shroud.

2.5.6 Aerodynamic Loss Studies with Cooling

In general, there is a consistent agreement that, in addition to other forms of losses such as tip leakage, endwall and profile losses, coolant injection leads to increased mixing loss (Oates, 1985; Denton, 1993; Lakshminarayana, 1996). Much of this mixing loss is attributed to the large temperature differences between the mainstream and coolant flows as well as the velocity gradient in the shear between the coolant and the mainstream boundary layer. Denton (1993) argued that in cooled turbines, the

large temperature difference between the mainstream and coolant flows is a major source of entropy production due to heat transfer. As a result, the mainstream flow will do less work than if it were expanded adiabatically from its supply pressure and temperature. In addition, there is also an additional loss of mass flow to provide for cooling that would otherwise be used to produce more work by the turbine, which, Denton (1993) argued, can have a large effect on overall cycle efficiency.

In order to optimise the cooling scheme on the blade tip with the need to reduce tip clearance loss, it is important to understand which studies have examined aerodynamic loss in conjunction with coolant injection.

One of the possible exceptions to the principal that coolant injection increases aerodynamic loss is in the area of trailing edge injection. Trailing edge injection has been known to reduce loss as the cooling flow can increase the base pressure (Deckers, 1996). Kost and Holmes (1985) showed that there are benefits for trailing edge injection, especially for blades with thick trailing edges, helping to prevent separation on the blade suction side.

In a film-cooled transonic NGV endwall experiment, Kost and Nicklas (2001) showed that endwall cross flow, and consequently the passage vortex, is reduced by coolant injection. They also showed that the net secondary losses increase with coolant injection, if thermodynamic energy losses are compared. Results showed that if the temperature difference was not taken into consideration, the coolant injection can reduce loss. This highlights the importance of using an equation that accounts for temperature differences, which is even more important in an actual engine.

Aerodynamic loss with coolant injection from the blade sidewalls has also been examined. Some of the early studies used low-speed linear cascades (Ito et al., 1980). Yamamoto et al. (1991) studied coolant injection from various locations on the blade surface, showing that secondary air interacted with the cascade passage vortices and changed the loss distribution. The overall loss decreased when air is injected along the mainstream, but increased when air was injected against the mainstream. They attributed the decrease in loss to additional momentum from the coolant.

Some coolant injection studies from blade or vane sidewalls were performed under high-speed conditions. Köllen and Koschel (1985) used an annular cascade from low-speed to transonic conditions to study film cooling on aerofoil surfaces. They concluded that when accounting for the energy of the coolant, injection in the trailing edge region could be beneficial while ejection in the leading edge region was generally harmful. In a high-speed linear cascade, Kiock et al. (1985) observed that the injection of coolant can have a significant influence on the boundary layer, especially its effect on transition, but their conclusions depended on the definition of loss chosen. In a 2-D transonic cascade, Haller and Camus (1984) showed that coolant injection always increases loss. Other studies that considered coolant injection on a transonic NGV include Day et al. (1999, 2000).

As for the tip region, there are fewer studies on the effect of coolant injection on aerodynamic loss. Wadia and Booth (1982) used a water tunnel to show that coolant injection from a flat tip reduced the leakage flow within the tip gap. Examining a squealer tip in a low-speed linear cascade, Krishnababu et al. (2008) observed that coolant flow partially blocked the tip gap, reducing the area available for the OTL flow. Rao and Camci (2004) provided oil paint flow visualisations of coolant injection from a tip trench in a low-speed rotor rig. They were able to identify the pressure-side separation, OTL reattachment and pressure-side edge recirculation features commonly seen on axial turbine blades. They concluded that with coolant injection, the recirculation was completely eliminated in the last 40 percent of axial chord, which likely reduced gap mixing losses as well as heat transfer in this region. Lastly, the tip separation was eliminated in the last 1/3rd of the blade with coolant injection.

In one of the few transonic tip studies, different squealer geometries were tested in a high-speed linear cascade by Hofer and Arts (2009), who showed that for high Reynolds numbers and high Mach numbers for a partial suction-side squealer tip geometry, loss decreased with coolant, but was within the uncertainty of the measurements. They only provided spatially-resolved results for low Reynolds number cases.

In addition to tip coolant injection, coolant injection from the casing wall, used as an active flow control mechanism, has been tested in a subsonic one and one-half stage rotor. Behr et al. (2008) experimentally showed that with casing endwall coolant injection, the size and turbulence intensity reduced for both the tip leakage and tip passage vortices. With an appropriate combination of injection mass flow rate and axial injection position, the isentropic efficiency of the stage was improved by 0.55 percentage points. These results were compared to a study by Mischo et al. (2007) who observed that flow injection from the casing delays the formation of the OTL vortex through re-direction and partly obstructing the tip leakage flow. The computational results, however, did not seem to agree well with the experimental results.

Despite earlier statements that coolant injection tends to increase losses, there seems to be a lack of consensus as to the effect of coolant injection. Many factors seem to influence this effect, from the location, size and exit angle of a cooling hole to whether the temperature of the coolant is considered. The injection of coolant can also change the base pressure, resulting in a reduction in loss. Coolant injection can also help with boundary layer transition.

There appears to be no experimentally-obtained, spatially-resolved aerodynamic loss results for winglet blades under transonic conditions. In addition, there appears to be no studies with tip coolant injection from a winglet design, especially under engine-representative transonic conditions.

2.5.7 High-Speed Linear Cascade Aerodynamic Loss Studies

Most of the previously-cited unshrouded aerodynamic loss experiments have been under low-speed conditions. Measuring aerodynamic loss in high-speed linear cascades is very challenging. If the facility uses a light piston compression tube (Key and Arts, 2004; Hofer and Arts, 2009), steady flow conditions are possible, but run times can be limited to fractions of a second. To obtain a map of the exit flow conditions, a probe must be traversed at high speed. If the facility uses a blow-down facility, such as is used in the present study, flow conditions are typically less steady, but run times can

extend beyond 90 seconds, depending on the facility. This time allows for a probe to be traversed at small spatial steps as well as allow for any unsteady effects, induced by the movement of the probe, to dissipate before taking measurements.

Xu and Denton (1988) examined the trailing edge losses of transonic turbine blades for different blade trailing edge thicknesses, including the effects of blade boundary layers on the subsequent mixing downstream of the blade. Other 2-D transonic linear cascade loss studies include Kiock et al. (1985); Haller and Camus (1984); Zhang et al. (2004, 2005).

Few studies have considered aerodynamic loss downstream of a high-speed linear cascade blade row. Key and Arts (2004) provided span-wise loss coefficients in the blade tip region. Due to the short duration of their test, they were unable to obtain a detailed downstream pressure distribution. They traversed a three-hole probe at a speed of 500 mm/s, and the centre hole provided the local total pressure. The probe was traversed at eight span-wise positions for the flat tip, up to just over 90 percent of span, and ten span-wise positions for the squealer tip, up to about 97 percent of span. The exit static pressure used for the aerodynamic loss was determined from the casing pressure taps downstream. The reason for using the centre channel of the three-hole probe for total pressure measurements is not stated. The flow angle over the tip is likely large enough to affect the actual total pressure.

Using the same facility, Hofer and Arts (2009) examined two different squealer tips with and without coolant injection. They used the three-hole probe for both total and static pressure measurements, unlike Key and Arts (2004), which allowed for both span-wise and pitch-wise total pressure loss coefficients. Figure 2.6 shows a contour of total pressure loss coefficient for a full squealer with $M_{exit} = 0.9$, which shows the OTL vortex, wake flow and passage vortex. The passage vortex was not observed for the $M_{exit} = 1.1$ condition (Hofer and Arts, 2009). They used a form of Equation 2.4, accounting for different temperatures of coolant and mainstream, though they assumed that the specific heat was the same for both.

Finally, if there is a shock structure over the tip as suggested by Moore and Elward (1993); Wheeler et al. (2009); Zhang et al. (2010b); Shyam et al. (2010), then

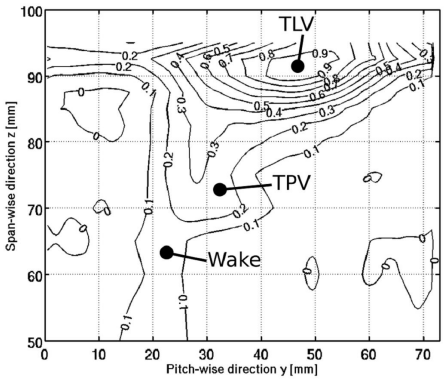

Figure 2.6: Aerodynamic loss coefficient for full squealer under high-speed conditions (Hofer and Arts, 2009)

the choked tip will affect the OTL flow, likely resulting in a change in the aerodynamic loss. Can the low-speed studies help to describe aerodynamic loss for operationally-representative high-speed conditions? Wheeler et al. (2009) argued that low-speed heat transfer results cannot be scaled up to engine-realistic conditions. Similarly, the low-speed aerodynamic loss results should not be expected to scale up to engine-realistic conditions.

In addition, if the winglet tip potentially reduces aerodynamic loss, aerodynamic loss for a winglet with coolant injection must be considered. Coolant tests are generally easier in a linear cascade, however the present author has found no cooled winglet experimental studies. Therefore, the winglet should be tested in a linear cascade both with and without tip cooling injection, which has not previously been reported.

2.6 Summary

In summary, a review of the published literature shows that there is a lack of understanding of the effect that high-speed, transonic flow conditions has on tip heat transfer and aerodynamic loss. Generally speaking, most studies that provide engine-realistic, transonic flow conditions, such as rotors, do not provide detailed, spatially-resolved results. They typically only measure heat transfer at a few discrete locations on the tip, which makes it difficult to observe any variations in tip flow conditions,

such as shock waves. Transonic rotors use engine-sized hardware, which makes detailed aerodynamic loss measurements very difficult.

Those experiments that do provide spatially-resolved results are usually under low speed incompressible or subsonic flow conditions. Low-speed rotors match exit Reynolds numbers by increasing the size of the blade. This allows for the ability to measure aerodynamic loss. However, low-speed rotors, like transonic rotors, are only able to measure heat transfer at few locations. Linear cascades, on the other hand, generally allow for optical access for spatially-resolved tip heat transfer measurements. They can also allow for an easy traverse to obtain pressure measurements downstream of the blade row. Some linear cascades are even used to measure the effect of a moving casing endwall. Most of these studies, however, are performed under low-speed conditions, which cannot capture the various flow phenomena that occur over blade tips under transonic conditions.

There are a few linear cascade investigations that have been used to examine blade tips under high-speed, transonic conditions. However, these studies only consider aerodynamics.

To consider a HPT blade design to be effective, it is argued that research must consider both the heat transfer and either the aerodynamic loss or efficiency. Few have experimentally done this and most studies are under subsonic conditions (Krishnababu et al., 2007b,a). Others that have considered both the aerodynamics and thermodynamics have done so computationally and under high-subsonic but not transonic conditions (Saha et al., 2003; Yang et al., 2002a,b; Acharya et al., 2003; Yang et al., 2006). If any part of the blade tip is choked, which is generally only true with a high-speed blade load, then the mass flow through the choked region can only be changed with changes in the gap inlet's total pressure and total temperature, which highlights the need for examining the aerodynamics and thermodynamics of high-speed tip flows.

It is presently argued that there is a need for highly-resolved data at high-speed conditions. With a validated CFD code, the effects of engine-realistic flow conditions

can be examined, such as the effects of rotation, turbulence intensity and non-uniform inlet temperature distribution.

To the best of the author's knowledge, there is no published research for detailed, spatially-resolved heat transfer over blade tips under transonic conditions. In addition, the present study is the first time that heat transfer on either an uncooled or cooled winglet has been experimentally investigated for transonic flow conditions. Finally, the present author has found no studies in which spatially-resolved aerodynamic loss experimental results have been determined for a cooled winglet. The remainder of this thesis addresses these issues.

Chapter 3

High-Speed Linear Cascade Facility

3.1 Introduction

This chapter provides an introduction to the High Speed Linear Cascade (HSLC) facility. It provides overviews of the HSLC facility and the experimental setup. This chapter also details the HSLC qualification and aerodynamic loss measurement setup.

The facility was designed and installed by Dr Qiang Zhang, Post-Doctoral Research Assistant with the help of other research assistants and laboratory technicians, prior to the present author's arrival. This initial work included the installation of the inlet and exit piping, inlet and exit plenum and all valves. In addition, the test section geometry was designed by Rolls-Royce, and Dr Zhang modified this design for construction by an external company. The present author was responsible for all of the instrumentation setup, the commissioning of the facility and obtaining all aero-thermal experimental results.

It should be noted that unless otherwise stated, all of the CAD drawings were produced by Dr Zhang and modified by the present author. In addition, all CFD work was executed by Dr Zhang. As a member of the HSLC Research Group, the present author was responsible for analysing and understanding the CFD results in conjunction with the author's experimental data.

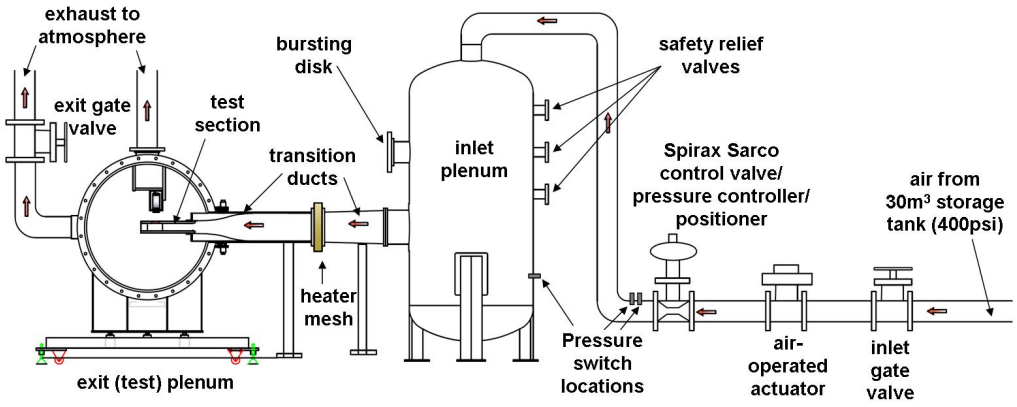

Figure 3.1: The schematic of the Oxford High Speed Linear Cascade facility (drawing not to scale, based on Zhang (2007a))

3.2 Facility Overview

The experiments were conducted in the Oxford HSLC facility shown in Figure 3.1. The HSLC consists of a blowdown wind tunnel and a linear turbine cascade.

Up to 2750 kPa (400 psi) air is compressed with two compressors, dried by three consecutive driers and stored in two 30 m^3 storage tanks.

A 203 mm (8 in) mechanical gate valve, a 203 mm (8 in) Worcester ball valve with pneumatic actuator and spring return, and a Spirax-Sarco control valve (including actuator and positioner) are located downstream of the air storage tank, as shown in Figure 3.2a. The mechanical gate valve is in place for long-term safety. The ball valve, Norbro Series 40R, is controlled by the researcher and opens and closes within 11 seconds. This valve is in place for near-term safety. Finally, the Spirax-Sarco control valve with SP200 electro-pneumatic smart-positioner is used in conjunction with a proportional-integral-derivative (PID) process controller to open and close the valve to maintain a set pressure. The PID process controller will be discussed in Section 3.4.1.

A 40 bar pressure transducer is installed between the mechanical gate valve and the ball valve to record and display real-time supply pressure readings. Three pressure switches, Omega PSW-800 Series, are installed downstream of the control valve and are used for safety. Two pressure switches provide a signal to trigger the closing

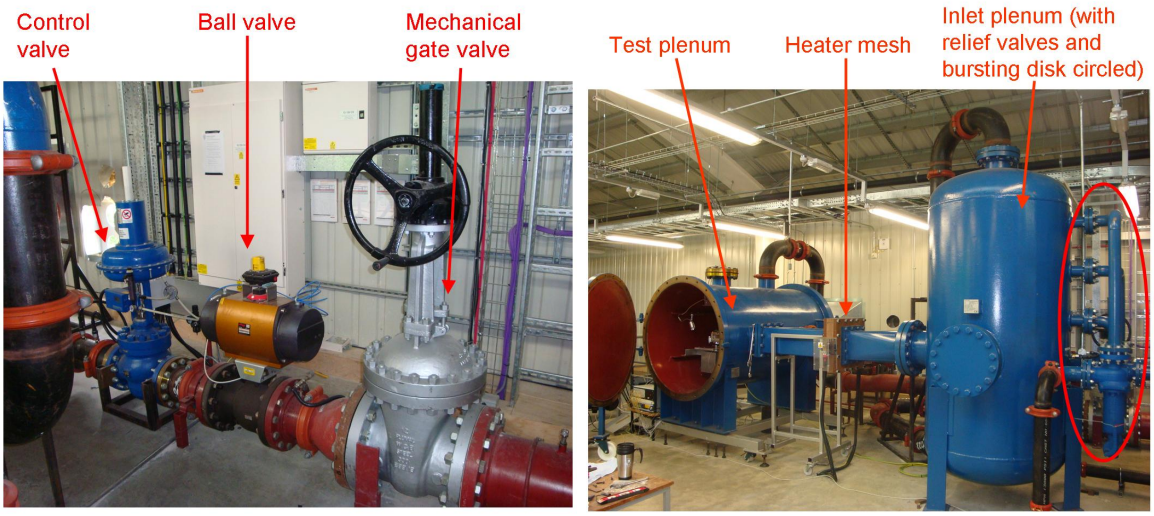

(a) HSLC piping and valves upstream of the inlet plenum

(b) HSLC inlet plenum, piping and heater mesh

Figure 3.2: Pictures of The HSLC facility

of both the ball valve and the control valve if a maximum set pressure is exceeded. A third pressure switch is only enabled when a minimum pressure is reached, to ensure that there is enough airflow in the system to prevent the heating mesh element from overheating. Additional safety features include three safety relief valves (for $P > 310\,\text{kPa}$ or $45\,\text{psi}$) and one bursting disk (for $P > 414\,\text{kPa}$ or $60\,\text{psi}$), located on the inlet plenum.

Figure 3.2b shows the inlet and test plenum as well as the connecting pipes. These ducts allow for a proper transition from the circular pipes located on the inlet plenum to the rectangular test section located in the test plenum.

The square transition duct allows for the installation of a heater mesh element which is used to provide a step increase in mainstream flow temperature. The heater mesh is described in Gillespie et al. (1995). The heater mesh employed in the HSLC is rated at of over 140 kW, though is typically operated at just under 120 kW (80 V and 1450 A), and can raise the mainstream temperature by 22–24°C. Figure 3.3 shows the heater mesh used in the present study. It is important to inspect the heating

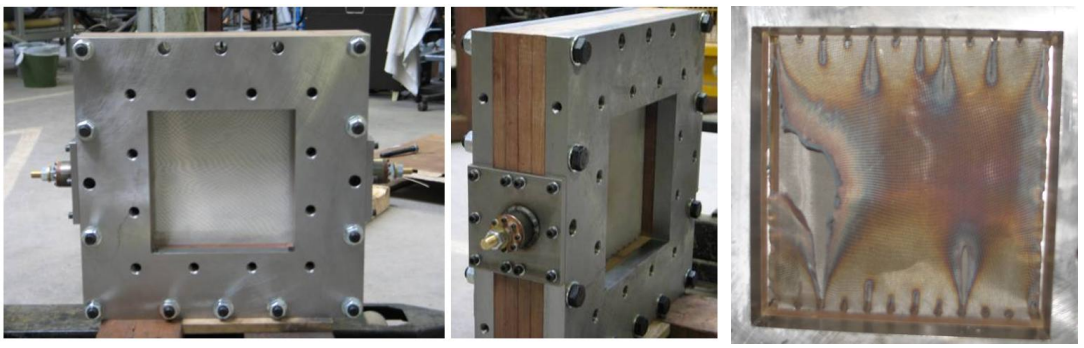

(a) Heater mesh used for step change in temperature

(b) Heater mesh indicating both tearing and burning

Figure 3.3: Pictures of heater mesh element used in present study

element frequently for burn patterns. If neglected, uneven temperature profiles can occur. Failure of the heating element can also occur, as shown in Figure 3.3b.

There are three exhaust ducts downstream of the test plenum, each of 203 mm (8 in) diameter, which exhaust to the atmosphere, as seen in Figure 3.4a. The fourth pipe in this figure is the bursting disk exhaust pipe. A 203 mm (8 in) mechanical gate valve is installed downstream of the test plenum to allow for an increase in the back pressure, when necessary for reaching a set pressure ratio during testing, and is shown in Figure 3.4b.

Figure 3.5 shows a picture of the test plenum and the internal arrangement. The test section is mounted inside the pressurised test plenum, which provides an environment in which the Mach number and Reynolds number can be varied independently.

Thermocouple wires and pressure tubing are supplied through a protective pipe, and are connected to the data acquisition system outside the exit plenum. A closed-circuit television camera is also placed inside the plenum to monitor the test section and the plenum environment during each blowdown test.

An infrared (IR) camera (see Figure 3.6) is mounted in a protective housing unit and is free to traverse as required to obtain a perpendicular view of the blade surface. The camera can also be secured in locations that allow for observation of the pressure-

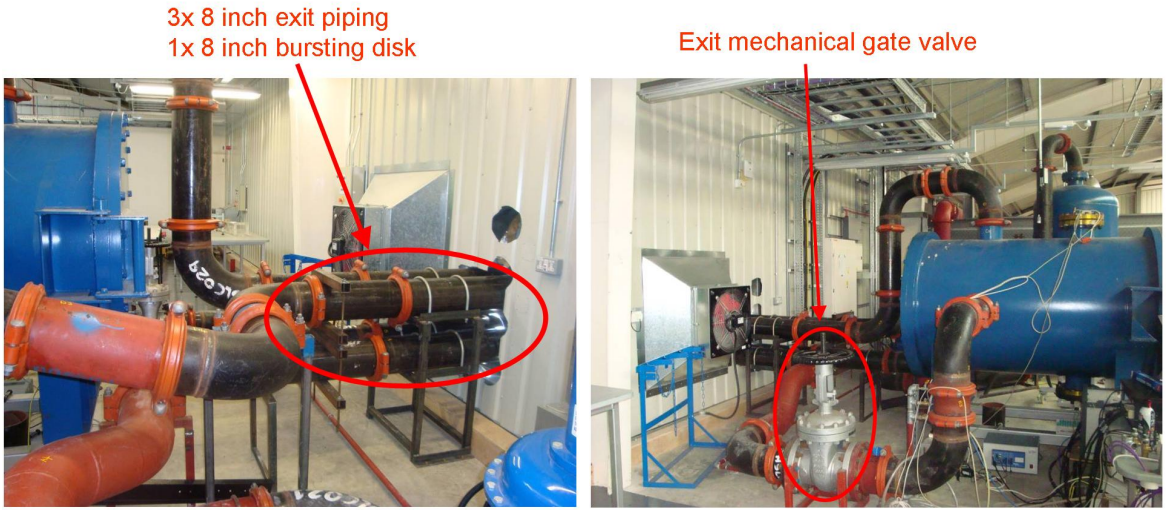

(a) HSLC exit piping out of building to atmosphere, using three 203 mm (8 in) pipes

(b) HSLC exit piping and 203 mm (8 in) mechanical valve used to change back pressure as necessary

Figure 3.4: Pictures of exit piping and exit gate valve used in present study

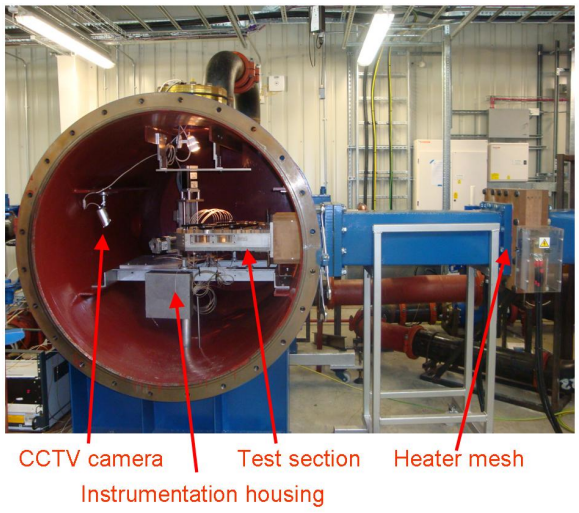

Figure 3.5: Picture of the HSLC test plenum, including heater mesh, test section and instrumentation housing

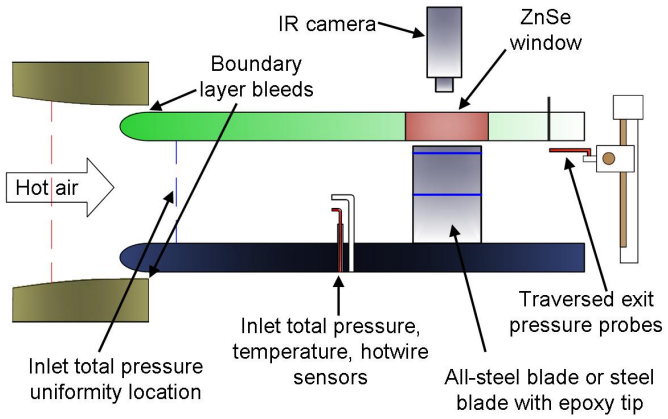

Figure 3.6: Side view schematic of HSLC test section instrumentation (drawing not to scale, based on Zhang (2007a))

side surface, suction-side surface, and the suction-side crown region of the leading edge. More details about the IR camera is addressed in Section 4.2.2.

3.3 Experimental Setup Overview

This section provides details of the experimental setup for the present study, including instrumentation as well as the test section and blade tip examined. The coolant feed system is also described in this section.

3.3.1 Instrumentation

The HSLC test section is instrumented to measure pressures and temperatures, as shown in Figure 3.6. An inlet rake is used to check total pressure uniformity in the inlet plane. The inlet pitot-static probes and inlet thermocouple are located about one axial-chord distance upstream of the blade row. A Dantec hot-wire probe is interchanged with the pitot-static probe for turbulence and boundary layer studies. There are static pressure ports on the top and bottom casing walls, one axial chord downstream of the blade row. A traversing system containing a three-hole pressure probe is used to determine periodicity and to measure exit flow conditions (see Section 3.5).

A 32-channel pressure measurement unit with very low noise levels was developed by the present author and is shown in Figure 3.7. It consists of SDX-series sensors

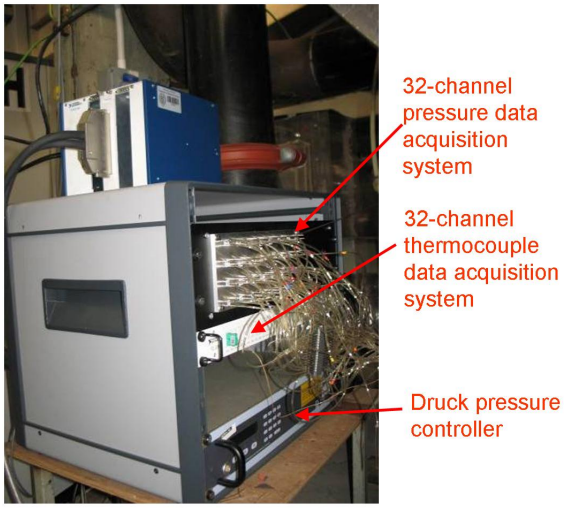

Figure 3.7: Instrumentation rack showing, from top to bottom, 32-channel pressure transducer unit, 32-channel thermocouple unit and Druck DPI520 pressure controller

manufactured by SensorTechnics with ranges of 34.5 kPa (5 psi), 103.4 kPa (15 psi) and 206.8 kPa (30 psi). The transducers have combined non-linearity and hysteresis of ±0.2 percent and repeatability of ±0.2 percent. The pressure measurement unit also uses precision instrumentation amplifiers (AD524) and National Instruments SCB-68 connector blocks. The whole system is calibrated with a GE Druck DPI520 pressure controller, with a combined non-linearity, hysteresis and repeatability of ±0.05 percent. A Druck PMP4070 absolute pressure transducer (±0.04 percent accuracy) is used to measure the inlet total pressure, which is used as a reference pressure for other pressure measurement locations. The response time of the SDX sensor is 100 μs. In addition, the time delay due to the total length of the tubing (in and out of the plenum) is measured. The maximum time delay for 3 m length tubing with 1.6 mm diameter is 23 ms.

A National Instruments 32-channel temperature measurement unit with built-in cold junction compensation is also employed with a K-type 0.0254 mm (0.001 in) diameter thermocouple installed at the inlet of the test section to measure the mainstream gas temperature.

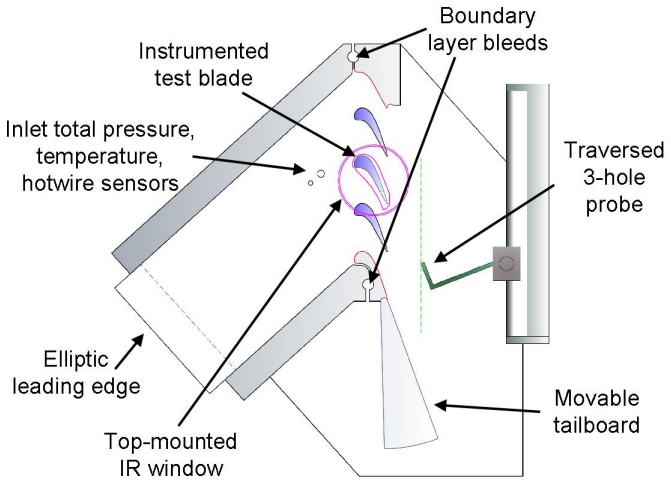

Figure 3.8: Top view schematic of HSLC test section instrumentation (drawing not to scale, based on Zhang (2007a))

All the pressure and temperature data are logged into a PC workstation through several National Instruments M-series cards. LabVIEW 8.6 is employed for pressure, temperature and video data acquisition programming.

3.3.2 Test Section

Figure 3.8 presents a schematic diagram of the test section with 4 blade-passages and 5 blades, including 2 sidewalls representing a suction side and a pressure side. The side and bottom walls of the test section are made of stainless steel, and the top wall is made up of Perspex. Due to the length of the transition ducts and inlet, a boundary layer naturally builds on all four inlet duct walls. An actual engine does not likely have as much boundary layer growth, so the HSLC bleeds off some of this boundary layer at two locations in the inlet. The top and bottom surface boundary layers are bled off at the entrance to the test section, as labelled in Figure 3.6. The top and bottom walls have an elliptic leading edge to help ensure a smooth transition following the boundary layer bleed. The side surface boundary layers are bled off immediately upstream of the outside blades, as labelled in Figure 3.8. These boundary layer bleeds have been installed to maintain appropriate cascade flow conditions.

As shown in Figures 3.6 and 3.8, A Zinc Selenide (ZnSe) window is placed on the top casing wall so that the central test blade tip surface is optically accessible to an IR camera. The test section is modified to measure side-wall heat transfer. A ZnSe window is employed for optical access of the blade pressure side and suction side, which is addressed in Section 4.2.2.

One movable tailboard is attached to the suction-side sidewall (the lower blade in Figure 3.8). The tailboard on the pressure side (the top blade in the figure) was originally installed but removed later due to issues related to the periodicity and the reflection of shock waves. Though the use of porous tailboards can help reduce the strength of a reflected shock (Schreiber et al., 1993), and have been used by others (Langston et al., 1977), their use adds complexity and experimental effort (Hodson and Dominy, 1993). In addition, the periodicity results presented in Section 3.4.2.4 indicate that a porous tailboard is not needed.

3.3.3 EFE Blade

The blade profile used in the current study is based on the 90 percent span cross-section of Rolls-Royce's Environmentally Friendly Engine (EFE) transonic first-stage high-pressure turbine blade and is scaled at 1.9 times larger than the operational blade. Two types of blade tips are used for this investigation. The first is an all-stainless-steel blade, with circumferentially-placed pressure taps at mid-span and 90 percent span of the HSLC blade. The second is a blade with a stainless-steel base section and a separate tip section which can be replaced with different tip geometries. The low thermal conductivity tip material for the second blade tip is made of an epoxy resin known as SI40, manufactured using the stereolithography technique by Rolls-Royce. Pictures of the flat tip as well as uncooled and cooled winglet tips are presented in Figure 3.9.

It is likely that the surface roughness between the two blades are different. The all-stainless steel blade is used for rig qualification tests as well as flat tip aerodynamic loss tests. The blades with the epoxy tips are painted with a flat black paint and are used for all heat transfer tests and by the winglets for the aerodynamic loss tests. All

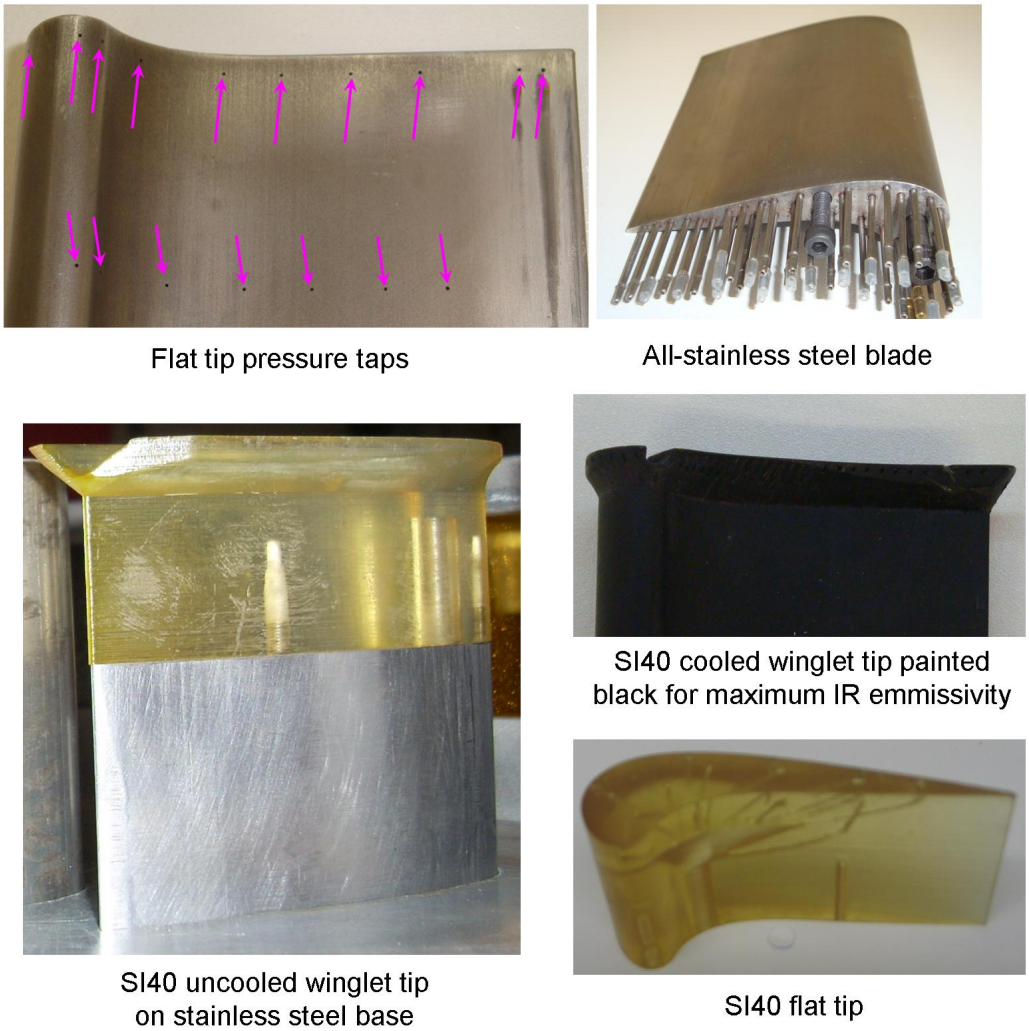

Figure 3.9: Blade tips used for aero-thermal measurements, including all-metal for blade loading measurements and SI40-tip blade for heat transfer measurements

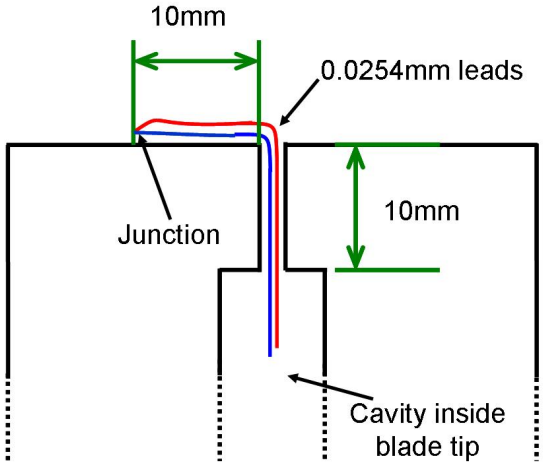

Figure 3.10: Schematic of thermocouple placement on blade tip to help understand conduction losses.

comparisons of blade geometry are made with equivalent blade material except for aerodynamic loss.

The thermal product ($\sqrt{\rho C_p k}$) was experimentally determined by Zhang (2007b). The thermal product of SI40 was calculated to be $\sqrt{\rho C_p k} = 627 \pm 33\,\mathrm{W}\cdot\sqrt{\mathrm{sec}}/\mathrm{m}^2\cdot\mathrm{K}$. This uncertainty in the thermal product is used to determine the uncertainty in heat transfer described in Section 4.7.

Thermocouples with 0.0254 mm (0.001 in) wire diameter are placed on the tip and sidewall surfaces to provide in situ data for calibration of the IR camera images. These fast-response thermocouples enable measurements of time-resolved surface temperatures. The conduction losses through the thermocouple leads were not examined, though these losses are not likely to affect the heat transfer results. The heat transfer analysis technique is based on temperature differences and not on the absolute value of the temperature. Thermocouple placement dimensions are shown in Figure 3.10.

The blade tip clearance is adjustable. For the present study, the tip clearance is approximately 0.4, 0.9 and 1.3 percent of the actual EFE blade span, or approximately 1, 2 and 3 percent of axial chord.

The EFE blade and test section dimensions are provided in Table 3.1.

Table 3.1: EFE blade and test section dimensions

Inlet angle	42°
Exit angle	68°
Scaling factor	1.9
Axial chord	47.72 mm
Axial chord to blade height ratio	1.5
Axial chord to pitch ratio	1.4
True chord	78.53 mm
Pitch per blade	68.40 mm
Test section duct height	71.84 mm
Test section duct width	203.31 mm
Engine-equivalent blade span	106.78 mm

In addition to the flat tip, the uncooled and cooled winglets are also examined, shown in Figure 3.11. Note that the uncooled winglet geometry is very similar to the design presented by Harvey et al. (2006) (see Figure 2.5). Both tip surfaces are made of SI40. The uncooled winglet has no cooling holes. The figure shows key features including the gutter entrance, recess, pressure-side (PS) lip overhang, suction-side (SS) lip overhang and gutter exit.

The design motivation for the uncooled winglet is based on work by Harvey and Ramsden (2001) who proposed an alternate means of controlling the OTL loss by modifying the local surface velocities at the rotor tip, particularly by increasing the velocity at the pressure-side overhang. According to Harvey and Ramsden, the pressure-side overhang is intended to increase blockage and thus lower the local static pressure driving the OTL flow. In addition, the gutter allows for chordwise leakage flow from the leading edge. The follow-up work by Harvey et al. (2006); Willer et al. (2006) further modified the winglet, but did not consider cavities (or recesses), and recommended further optimisation to include cavities in order to reduce loss and heat transfer. Also, cavities decrease the amount of material that can contact the casing wall and will also lessen the weight of the blade. Though not stated by Harvey et al. (2006), the present author believes that one of the purposes for the suction-side over-

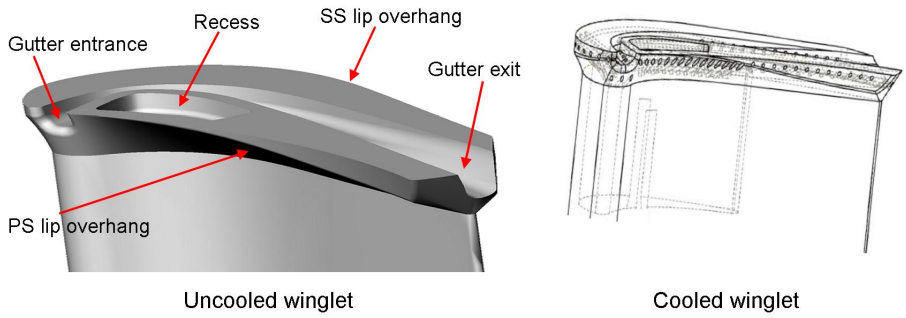

Figure 3.11: The schematics of the winglet tips tested in the HSLC for the uncooled and cooled winglets (modified from drawings by Rolls-Royce)

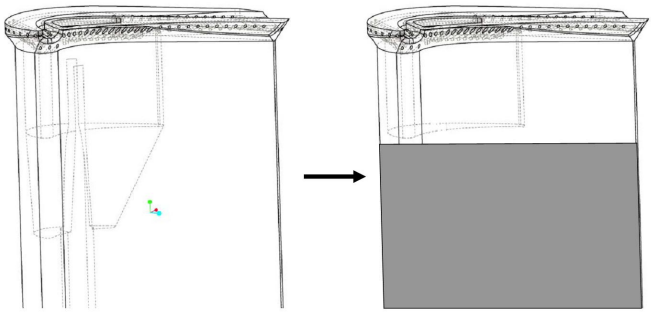

Figure 3.12: The schematics of the old and new cooled winglet tips (modified from drawings by Rolls-Royce)

hang is to reduce pressure at the gap exit in order to reduce pressure difference with the pressure side of the adjacent blade, reducing secondary flows.

The cooled winglet has cooling holes on the pressure-side lip overhang and on the suction-side inward surface of the gutter. The original cooled winglets were designed to be made entirely of SI40 (see Figure 3.12). This allowed for a relatively large reservoir inside the blade to help still the flow. Initial aerodynamic loss results for the all-SI40 cooled winglet showed a significant difference compared to the uncooled winglet, which has a 30 mm epoxy tip attached to a stainless-steel base, as seen in Figure 3.9. Due to these erroneous results, the cooled winglet was altered to be attached to a stainless steel base, like the uncooled winglet. Further details will be addressed in Section 7.4.

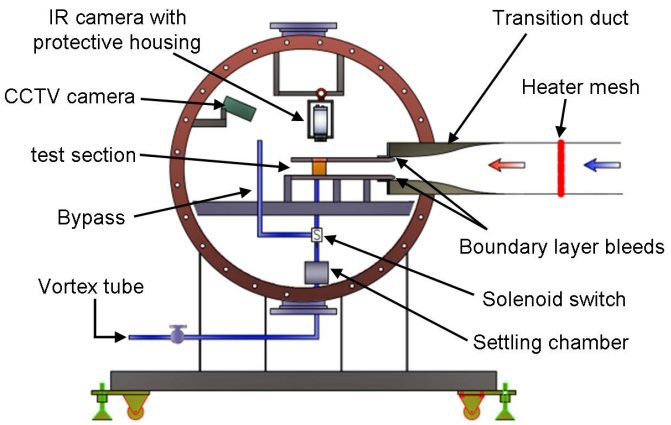

Figure 3.13: Schematic of the test plenum, including heater mesh, settling chamber, solenoid switch and bypass line (drawing not to scale, based on Zhang (2007a))

3.3.4 Coolant Feed System

The HSLC facility is capable of providing coolant to the test section. The current study only considers tip film cooling injection. During testing, pressure and temperature measurements are obtained in a reservoir inside the test blade. During a test, the total pressure ratio between the coolant and mainstream flows is 1.08. The maximum pressure ratio is a structural limitation of the cooled winglet tip.

A sonic orifice plate is used to determine the coolant mass flow rate for a tip clearance of 1.3 percent of engine-equivalent span, based on the set coolant to mainstream total pressure ratio of 1.08. The coolant mass flow rate is approximately 1.19 percent of the HSLC mainstream mass flow rate, or 0.80 percent of the engine-equivalent mass flow rate, based on blade span and pitch. Variations of mass flow rate are addressed later in this section.

The cooling flow enters a settling chamber inside the test plenum, as shown in Figure 3.13, where total pressure and total temperature measurements are taken. The coolant then flows to the cooled winglet in the test section. As it will be explained in Section 3.4.2.4, the settling chamber is capable of distributing cooling flow to the three central test blades.

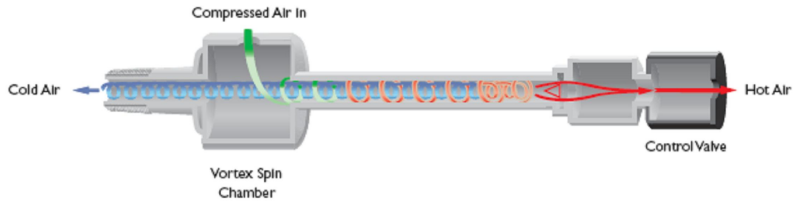

Figure 3.14: The schematic of the vortex tube (Meech Static Eliminators Limited, 2010)

The original coolant plan was to use room-temperature air. However, as shown in Chapters 4–6, adiabatic wall temperatures lower than the ambient temperature are calculated near the trailing edge region, where the mainstream flow cools the cooling flow. Therefore, the coolant temperature must be lower than the lowest adiabatic wall temperature determined on the blade tip.

Cooling flow with temperatures lower than the ambient temperature is achieved by using vortex tubes. Room-temperature air at 689 kPa (100 psi) pressure is supplied to three linked vortex tubes, which can be adjusted to provide a 0–50°C temperature drop, depending on the required flow rate and pressure. A schematic of a single vortex tube is shown in Figure 3.14.

As illustrated in Figure 3.14, compressed air tangentially enters the vortex tube into a vortex spin chamber, also known as the vortex generator. High-energy air advects toward the outer radius of the tube while the low-energy air advects toward the inner radius of the tube. Due to a conical nozzle at the "hot air" tube end with the control valve, only the flow at the outer radius is able to exhaust. The flow at the inner radius is forced to return out the other end of the tube through the "cold air" port. A control valve is used to adjust the pressure and temperature of the "cold air". To meet the pressure requirement for the cooling design and to obtain a reasonable temperature ratio, one vortex tube is not enough. Therefore, three vortex tubes are employed with a manifold to supply high-pressure, low-temperature air to the blade.

To prevent the coolant from absorbing ambient thermal energy, the coolant pipes downstream of the vortex tubes are insulated. Despite the use of insulation, the coolant must be operating for at least 30 minutes to ensure that the coolant feed

and piping temperatures are stable. However, as this would pre-cool the winglet and significantly affect heat transfer measurements, a solenoid switch is added so that the cooling flow is bypassed until the temperature inside the settling chamber is stable (see Figure 3.13). During a blowdown test, the solenoid valve is engaged to direct cooling flow to the blade when the heater mesh is engaged, as described in Chapter 6.

The temperature ratio between the mainstream and coolant flows for the heat transfer study is approximately 1.1. It is acknowledged that the temperature ratio at the tip for the operational engine exceeds 1.5, though this value depends on relative or absolute reference as well as which temperature is used for the coolant (e.g. wall or internal supply). Obtaining an engine-realistic temperature ratio is challenging for transient heat transfer experiments using epoxy blade tips. One option is to raise the mainstream temperature. First, the power required to raise the temperature of a high-volumetric flow rate using a heating element would require purchasing a new, more powerful and highly expensive power supply. Second, the thermal-structural limits of the epoxy blade tip prohibit raising the temperature much greater than used in the present study. The other option is to lower the coolant temperature. Under near-perfect experimental conditions, the maximum temperature ratio that can be achieved in the HSLC, considering the heating and cooling issues, is estimated to be a maximum of 1.3 in the relative frame.

When changing tip clearances, the coolant to mainstream total pressure ratio is kept constant. The static pressure distribution near the cooling holes is expected to vary with changes in tip clearance. However, for a constant coolant pressure ratio, the variation in coolant mass flow rate is expected to be minor. Also, the impact of this variation on the heat transfer and aerodynamic loss is expected to be minimal.

3.4 Rig Qualification

This section discusses the qualification of the HSLC. First, the proportional-integral-derivative (PID) control system setup is described. Next, the flow conditions are

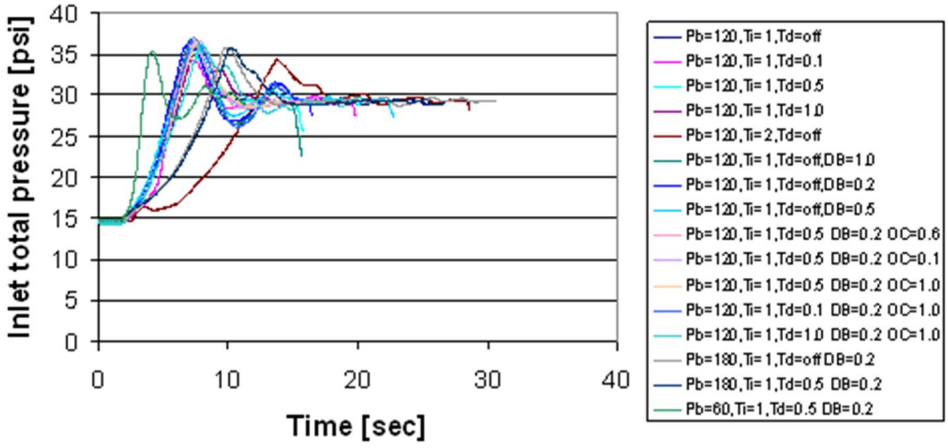

Figure 3.15: Example of various experimental runs to determine optimal PID settings, including proportional band, integral time, derivative time, error dead band and overshoot cycle control

provided, concluding with the impact of the rig relocation from the old lab to the new one during the project period.

3.4.1 PID Setup

A Spirax-Sarco SX76 process controller regulates the pressure in the test section as the storage tank discharges. The PID feedback control system enables a steady flow at the inlet of the test section during every blowdown test. A relatively constant total pressure of 200 kPa absolute (29.1 psia) is maintained for about 90 seconds. Figure 3.15 shows an example of the inlet total pressure by varying the proportional band, integral time, derivative time, error dead band and overshoot cycle control. This figure is not meant to identify the chosen settings, but rather highlight the different settings and the impact on the ability to control the inlet pressure. The figure shows that these settings can change the time in which steady state flow conditions is achieved as well as the amount of overshoot that exists. Initial commissioning required dozens of runs to optimise the responding pressure signal to ensure that a steady pressure can be achieved in a short amount of time. The optimisation is based on a subjective consideration of amount of overshoot and the time constant.

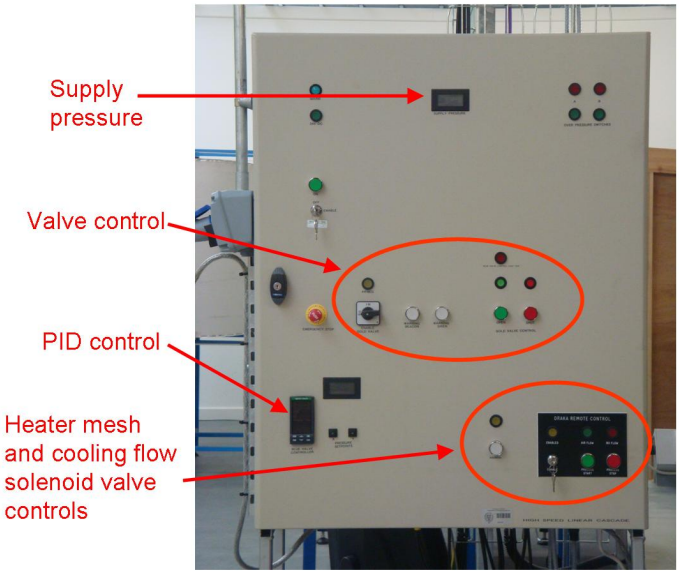

Figure 3.16: Picture of the control box, including SX76 PID controller, heater mesh switches, solenoid valve switch for coolant feed and supply pressure reading

The PID settings employed during the initial commissioning of the HSLC included a proportional band of 180 percent, an integral time of 1.0 sec, no derivative time, 0.2 percent error dead band and no overshoot cycle control. The flow conditions for this setting are provided in Section 3.4.2.

The move of the HSLC from the old lab to the new lab required improvements to the control system. A control box shown in Figure 3.16 was made to provide enhanced safety and better organisation of the internal circuitry. The control box integrates the PID controller, air-actuated ball valve, control valve and pressure switches for safe operation. The use of the new control box required new PID settings, which is discussed in Section 3.4.3.

3.4.2 HSLC Flow Conditions

This section provides the flow conditions of the HSLC, to include the steady state inlet and exit conditions, inlet uniformity, inlet hot-wire survey, exit periodicity and the blade loading. The section concludes with a discussion of the impact of the move of the HSLC to the new lab.

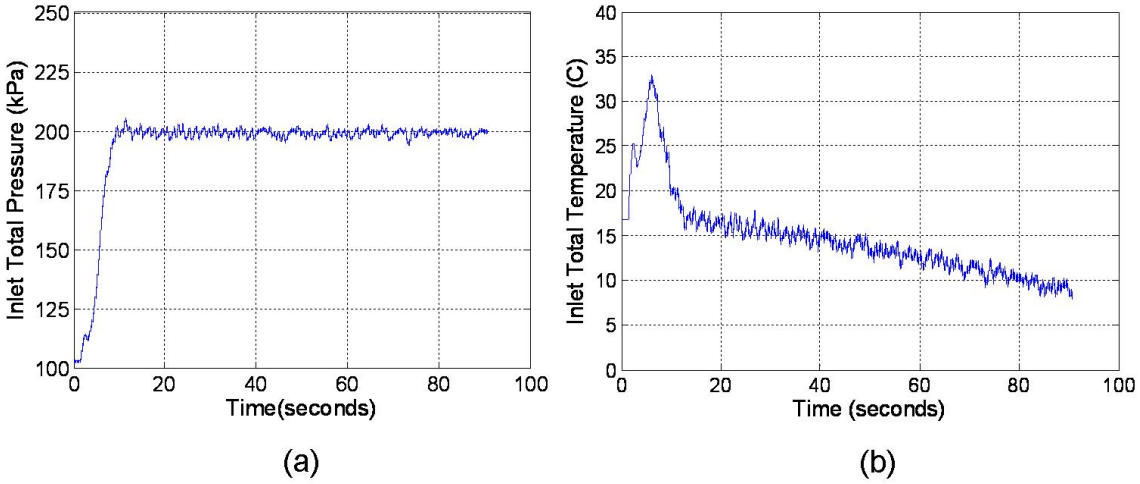

Figure 3.17: HSLC inlet conditions for 90 second run. Steady conditions achieved after 12 seconds for (a) inlet total pressure and (b) inlet total temperature

3.4.2.1 Steady State Flow Conditions

As mentioned in Section 3.4.1, the HSLC control system has the ability to maintain a relatively constant total pressure of 200 kPa (29.1 psia) for about 90 seconds. The inlet measurements are taken at one axial-chord distance upstream of the centre blade. Figure 3.17a shows that steady-state total pressure is achieved in about 10 seconds and that the pressure is relatively constant (within 2 percent). The inlet temperature is measured and shown in Figure 3.17b, indicating that a slowly and steadily decreasing temperature is achieved after about 12 seconds, which is expected with the near-isentropic decrease in pressure within the air storage tank.

It is interesting to point out that Figure 3.17b also shows the compression heating that moves through the test section when the control valve is initially opened. This shock is caused by the pressure difference between the test section and the pressure upstream of the control valve at the beginning of the experiment. The effect that this has on heat transfer measurements is addressed in Chapter 4.

Table 3.2 summaries the flow conditions of the test rig. The inlet Reynolds number is just over 0.6×10^6, representative of an actual turbine rotor inlet. The exit Reynolds number is 1.27×10^6 and exit Mach number is 1.02.

Table 3.2: Transonic flow conditions of the test rig (all pressures are absolute)

Inlet total pressure	200 kPa (29.1 psi)
Inlet static pressure	190 kPa (27.5 psi)
Inlet Mach number	0.28
Inlet velocity	95.1 m/s
Inlet Reynolds number (based on C_{ax})	0.60×10^6
Mass flow rate	3.23 kg/s
Exit static pressure	103 kPa (14.9 psi)
Exit Mach number (isentropic)	1.02
Exit velocity	322.9 m/s
Exit Reynolds number (based on C_{ax})	1.27×10^6

During a 90 second blowdown test, the air storage tank pressure drops from 2650 kPa (385 psi) to 1550 kPa (225 psi). A typical aerodynamic loss test lasts 75 seconds and a typical heat transfer test lasts 25 seconds.

3.4.2.2 Inlet Uniformity

The uniformity of the inlet flow is measured with an inlet total pressure rake as shown in Figure 3.18a. The distance of the rake upstream of the blade row is approximately $5\times C_{ax}$. It should be pointed out that the instrumentation of the rake is limited to three horizontal locations. Due to its size, the rake is not capable of measuring total pressure at the top casing wall. An inlet boundary layer study for this top casing wall is addressed in the next section. Two experimental tests were run for each vertical rake location, as shown with the red and blue circles in Figure 3.18b.

The inlet total pressure coefficient is determined based on the inlet total pressure relative to the inlet dynamic head, as shown in Equation 3.1, where P_t is the local rake total pressure, $\bar{P}_t$ is the average rake total pressure for all locations, and $\frac{1}{2}\rho_\infty V_\infty^2$ is the area-averaged inlet dynamic head.

$$\text{Total Pressure Coefficient} = \frac{P_t - \bar{P}_t}{\frac{1}{2}\rho_\infty V_\infty^2} \tag{3.1}$$

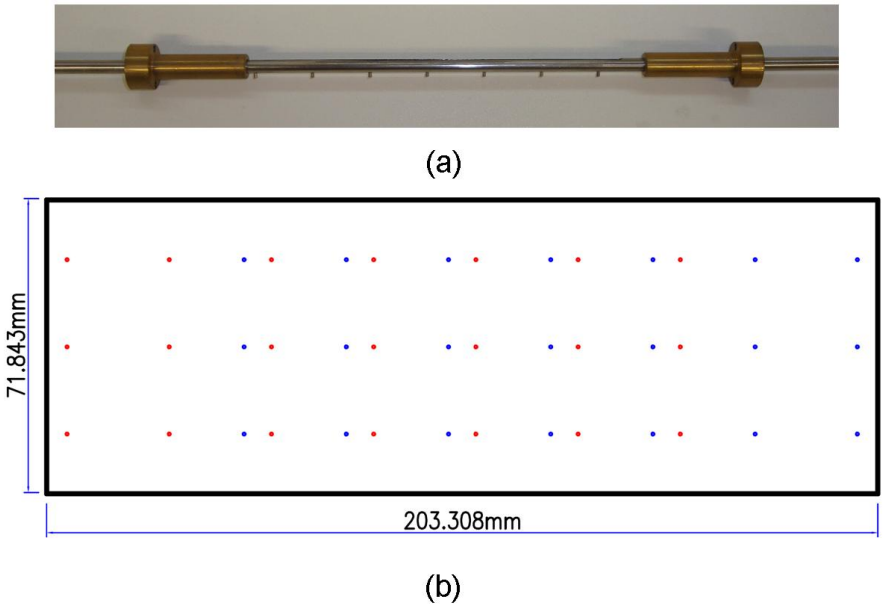

Figure 3.18: Inlet uniformity measurements examined using (a) total pressure rake, at (b) inlet uniformity measurement locations

Figure 3.19 shows the contours of the inlet total pressure coefficient. Though there are differences in the contour colours, the magnitudes are quite small. Results show that the inlet total pressure coefficient distribution varies within 0.5 percent of the mainstream average total pressure. The total pressure measurements have a statistical variance of 9.7 Pa (0.0014 psi), where the average mainstream total pressure is 200 kPa (29.1 psi). The average total pressure coefficient is zero, by definition. Figure 3.19 shows that the left and right sidewalls have less total pressure than the centre due to the sidewall boundary layers.

3.4.2.3 Inlet Hot-wire Survey

Though a real engine will have a certain level of turbulence intensity at the inlet to a rotor blade row, and some studies try to determine the effect of this turbulence intensity on heat transfer and aerodynamic loss, the present study has low turbulence intensity. The turbulence intensity is measured using a Dantec hot-wire anemometer located one axial-chord distance upstream of the blade row, near the centre of the cross section. The probe is calibrated in the HSLC by exchanging the pitot-static

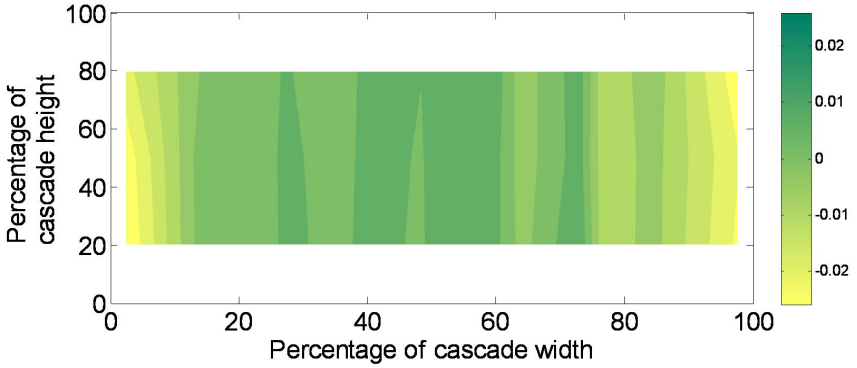

Figure 3.19: Inlet total pressure coefficient distribution $(P_t - \bar{P}_t)/\frac{1}{2}\rho_\infty V_\infty^2$ (dimensionless units) at the inlet

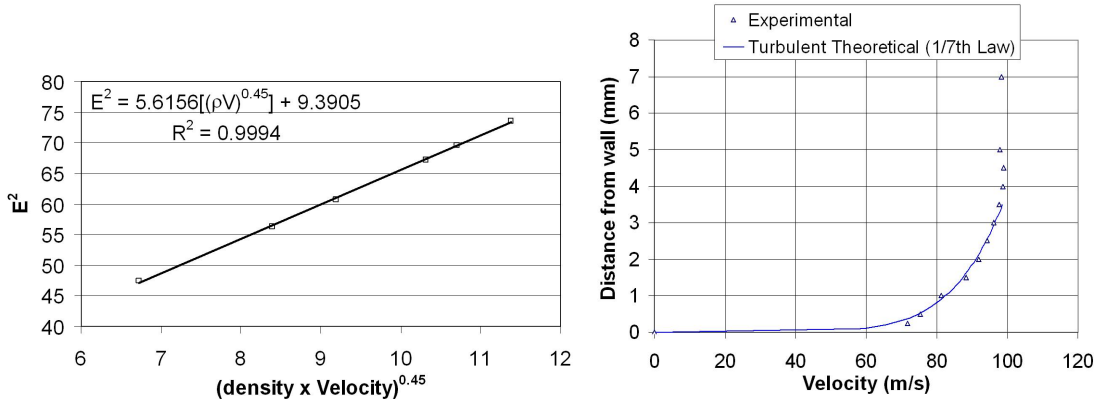

(a) Hot-wire anemometer calibration curve

(b) Inlet boundary layer velocity profile

Figure 3.20: Inlet hot-wire survey

probe and the hot-wire anemometer at mid-span height with different runs with the same set pressure. An initial calibration using King's Law, $E^2 \propto V^{0.45}$ (Lekakis, 1996) showed a non-linear relationship for compressible flow and results yielded a very low turbulence intensity value. By accounting for density, the King's Law relationship, $E^2 \propto (\rho V)^{0.45}$, is linear, and the calibration is shown in Figure 3.20a.

The turbulence intensity is calculated to be 1.1 percent. Since the flow is accelerated to transonic velocities over the parts of the tip, the upstream turbulence may not have much of an effect on the over tip flow.

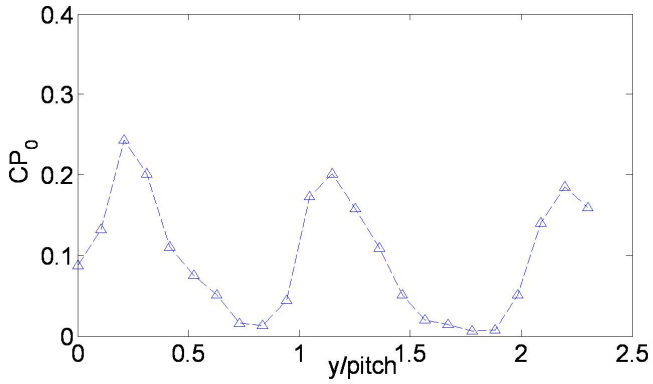

Figure 3.21: Exit total pressure loss relative to inlet total pressure shows near-periodic flow conditions

The hot-wire anemometer is also used to measure the boundary layer thickness. Figure 3.20b shows the boundary layer velocity profile and a boundary layer thickness of approximately 4 mm (8.4 percent of axial chord and 3.7 percent of EFE span). The experimental results are consistent with the theoretical 1/7th law for a turbulent boundary layer, also shown in the figure.

This profile was employed as the inlet casing wall boundary condition of the CFD study performed by Zhang (2010).

3.4.2.4 Periodicity

The exit flow conditions are also an important part of this study. Periodicity is important to show that each blade observes the same flow conditions and this can be demonstrated from the wake loss profile.

An examination of the exit flow conditions shows that the cascade is close to periodic within the limitations of a four-passage transonic linear cascade, as shown in Figure 3.21. The figure plots Cp_0 as the stagnation pressure loss normalised by the exit mid-span mass-averaged dynamic head (see Chapter 7). "y/pitch" is the pitch-wise location normalised by the blade pitch.

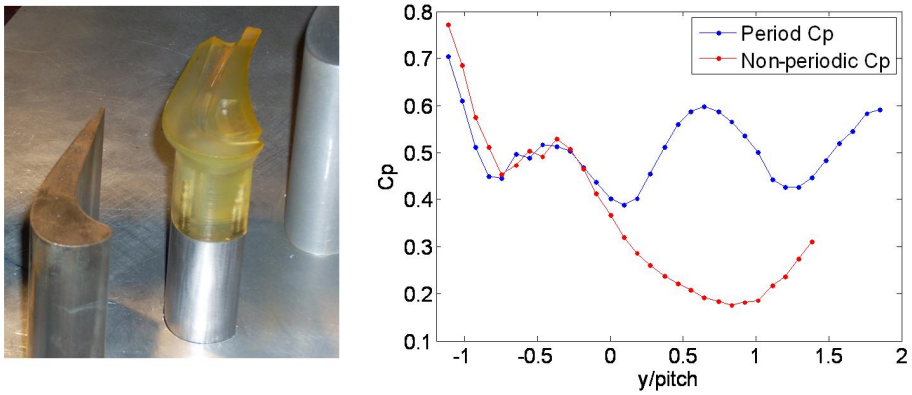

Figure 3.22: Exit total pressure loss coefficient for test with only one winglet ("Non-periodic Cp") and with three winglets ("Period Cp")

These measurements are taken just over one axial-chord distance downstream of the blade row using a traversing three-hole probe. The experimental setup for the exit wake flow measurements is discussed in Section 3.5, with results in Chapter 7.

When examining the periodicity for alternate tip geometries, such as the uncooled and cooled winglets, an additional examination of the test section periodicity showed the requirement to use the same blade geometry for all three blades during a single test. Figure 3.22 compares the mid-span total pressure loss coefficient, Cp_0, of a test in which only the centre blade is the winglet ("non-periodic Cp") and a test in which the three centre blades are winglets ("Period Cp").

Results clearly show the importance of using the same blade geometry for as many blades as possible.

In addition, for aerodynamic loss measurements, all three centre blades inject coolant at approximately the same mainstream to coolant total pressure ratio in order to obtain periodicity. For heat transfer, on the other hand, obtaining a temperature ratio that allows for a sensible value of film cooling effectiveness means that only the centre blade can inject coolant with the limited pressure supply. Therefore it is acknowledged that the cooled winglet tip heat transfer experiments are not as periodic as the aerodynamic loss conditions. However, the heat transfer is not expected to vary much under less-periodic conditions.

3.4.2.5 Blade Loading

Finally, to achieve operationally-representative Mach numbers for a transonic linear cascade, the inlet total pressure is set to achieve the blade loading consistent with the blade tip design. Static pressure measurements obtained at circumferential locations on the mid-span and 90 percent span of the blade surface are used to calculate the local coefficient of pressure and isentropic Mach number. The coefficient of pressure is defined by Equation 3.2.

$$C_p = \frac{P - P_{t_\infty}}{\frac{1}{2}\rho_\infty V_\infty^2} \tag{3.2}$$

where P is the local static pressure on the blade and P_{t_∞}, ρ_∞ and V_∞ are the mainstream total pressure, density and velocity, respectively, measured at the test section inlet. The local isentropic Mach number is determined from Equation 3.3.

$$\frac{P_{t_\infty}}{P} = \left(1 + \frac{\gamma - 1}{2} M_{isen}^2\right)^{\frac{\gamma}{\gamma - 1}} \tag{3.3}$$

where P is the local static pressure on the blade, P_{t_∞} is the mainstream total pressure, γ is the ratio of specific heats and M_{isen} is the local isentropic Mach number.

Figure 3.23 presents the pressure coefficient and isentropic Mach number distributions along the test blade at mid-span and 90 percent span. The 2-D FLUENT predictions shown in the figures are provided by Dr Zhang.

The overall aft-loaded shape of the distribution is consistent for the blade profile. The peak Mach number on the suction surface is approximately 1.2, consistent with the blade design. The mid-span Mach number data match the 2-D FLUENT time-steady predictions well, except at the near-trailing edge area on the suction surface. This is reasonable due to the unsteady nature of shock waves (and possibly due to poor resolution of the CFD near the trailing edge). The near tip Mach number distribution shows some higher peaks and abrupt variations near the suction-side surface. The tip leakage flow likely has a dramatic effect on the pressure distribution near the measurement locations.

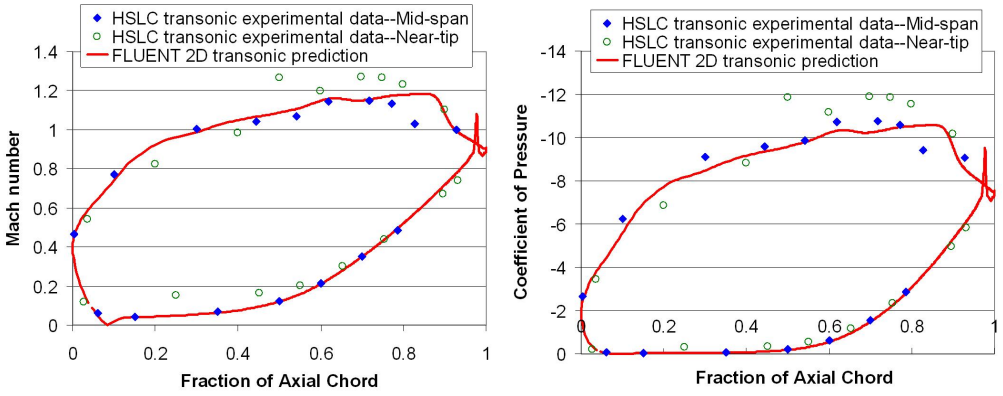

Figure 3.23: Isentropic Mach number and Coefficient of Pressure distributions around the blade (CFD courtesy of Dr Zhang (Zhang, 2010))

3.4.3 Rig Relocation

Following the move of the HSLC from the old lab to the new lab in summer 2010, the excess length of the exit pipes was removed before venting to the atmosphere outside of the building. This change in duct length affected the back pressure inside the test plenum. With a shorter length of pipe than before, there was less loss and therefore the back pressure decreased, which slightly raised the peak Mach number on the blade suction side. A partial closing of the mechanical gate valve shown in Figure 3.4b was used to raise the back pressure to be consistent with testing prior to the move. After a series of tests, closing the valve half-way provided this consistent back pressure and Mach number profile. Figure 3.24 provides the Mach number profile for both before and after the move as well as the FLUENT 2-D prediction provided by Dr Zhang.

As mentioned previously in Section 3.4.1, the control box shown in Figure 3.16 was created for better organisation and enhanced safety. With the power requirement for this new control box, there was a small tolerance between the power that the SX76 process controller provided (using a 4–20 mA signal) and the power that the control valve required. In addition, the high-power traversing motor used for aerodynamic loss testing created electrical noise and interfered with the control box. The problem was enhanced during longer runs, as the supply pressure was reduced and as the valve opening increased. To increase the valve opening, the current provided by the SX76

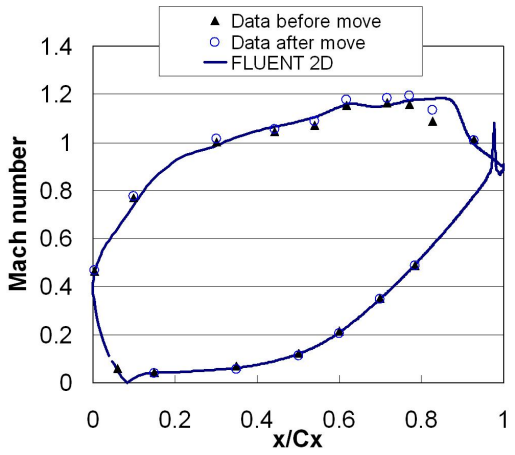

Figure 3.24: Isentropic Mach number distributions around the blade at mid-span before and after relocation (CFD courtesy of Dr Zhang (Zhang, 2010))

increased, which in turn limited the power to open and close the valve. The control valve frequently lagged behind the PID controller, creating large oscillations in inlet pressure.

The solution to this problem was to run aerodynamic loss tests with different PID settings than those used for heat transfer tests. For long tests, such as aerodynamic loss traverse measurement tests, all PID settings were used (proportional band of 90 percent, integral time of 0.1 sec and derivative time of 0.5 sec), which resulted in a ± 2 percent variation in inlet total pressure, as described in Section 3.4. The chosen PID settings minimised the fluctuations, though fluctuations still occurred. The exit conditions were referenced relative to the inlet pressure, so the exit conditions did not show as much of a fluctuation as the inlet. The statistical variance of the inlet total pressure for the aerodynamic loss tests was calculated to be 1 kPa (0.15 psi, or approximately 1 percent of exit dynamic head).

For heat transfer testing, inlet conditions with less fluctuation are desired as heat transfer coefficient is only constant for constant aerodynamic flow conditions. Since the traversing gear was not required, this eliminated the electrical noise caused by the stepper motor. Using a large proportional band (180 percent), a small integral time (0.5 sec) and no derivative time, the valve did not need to adjust frequently,

however an offset between the inlet pressure and set pressure occurred. This was resolved by increasing the set pressure. Changes in the 2750 kPa (400 psi) supply pressure would change the amount of offset needed, therefore all tests were run with the maximum supply pressure and for as short time as possible, which conforms with the requirements for the heat transfer techniques. The statistical variance of the inlet total pressure for the heat transfer tests was calculated to be 700 Pa (0.1 psi).

3.5 Aerodynamic Loss Measurement Setup

As the aerodynamic loss is an integral part of the project, this section discusses the key components of the aerodynamic loss experimental setup: the traversing system and the pressure probes. Both the traversing system and three-hole probe are shown in Figures 3.6 and 3.8. The calibration of the three-hole probe is also addressed and the section concludes with a discussion of the uncertainty analysis of the three-hole probe.

3.5.1 Traversing System

A two-dimensional downstream traverse system driven by two stepper-motors was employed to obtain total pressure surveys one axial chord downstream of the blade row, as seen in Figure 3.8.

LabVIEW 8.6 is used to control the traversing system. A National Instruments PCI-7352 two-axis stepper motion controller is connected to a National Instruments P70530 stepper drive via a National Instruments UMI-7772 universal motion interface. Two different motors are used. A smaller motor, Pacific Scientific model N31HRLG, drives the probe in the pitch-wise direction while a larger motor, Pacific Scientific model N33HRLG, drives the entire pitch-wise traversing system in the span-wise direction, as pictured in Figure 3.25.

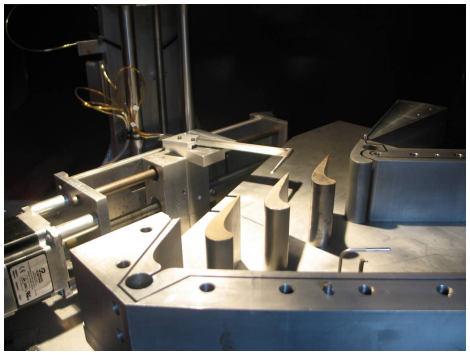

Figure 3.25: Traversing system including three-hole probe

3.5.2 Aerodynamic Loss Probes

Two probes were used to obtain pressure measurements one axial chord downstream of the blade row, a three-hole probe and a single-hole probe as shown in Figure 3.26.

The three-hole probe tip is constructed from three stainless steel tubes of 0.7 mm outer diameter and 0.4 mm inner diameter, giving an overall tip width of 0.7 mm in the span-wise traverse direction. The difference between the calibration facility and experimental test facility required that the probe be insensitive to Reynolds number (Main et al., 1996). Therefore the steel tubes have all been machined to have sharp edges. The two outer tubes have a 60° face angle. A knife-edge stem was used to minimise the disturbance to the downstream flow. A sting with 7 mm diameter is used to support the probe in the transonic flow field. Figure 3.26 also shows the three-hole probe, the characteristic dimension, as well as the sting and stem that support the probe.

To resolve the near tip region pressure field, a smaller probe capable of high-resolution measurements is required. Due to the size of the three-hole probe, it is not possible to measure within 4 mm of the tip endwall. A smaller, single-hole probe with a 0.7 mm diameter was employed so that total pressures can be measured to within 0.5 mm of the casing wall. The probe was mechanically rotated at 3 different angles to obtain the maximum total pressure and approximate flow angle. The flow in the near-casing region can be mostly resolved by this approach. Figure 3.27 shows a total pressure loss coefficient profile one axial chord downstream of the blade row, which

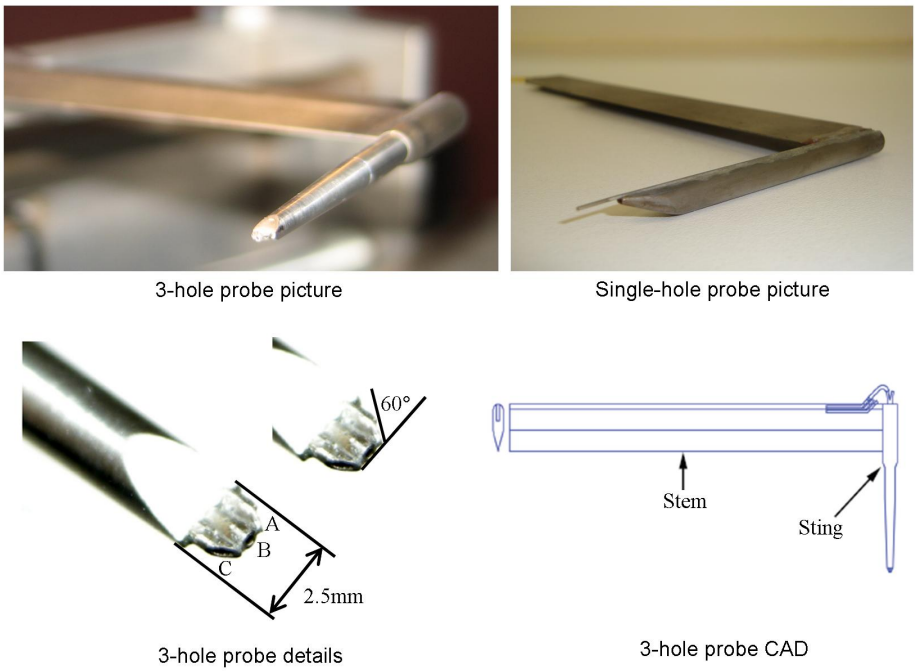

Figure 3.26: Probes employed to measure aerodynamic loss

is measured 4 mm from the casing endwall (the total pressure loss coefficient was introduced in Chapter 2 and addressed in Chapter 7). The data in these figures were obtained both with the single-hole probe and three-hole probe at the same span-wise location. In the figure, y/P is an arbitrary location normalised by the blade pitch P.

For all tests, the three-hole probe sting and the single-hole probe sting (with no rotation) were lined up parallel to the metal exit angle. In addition, both entrances to

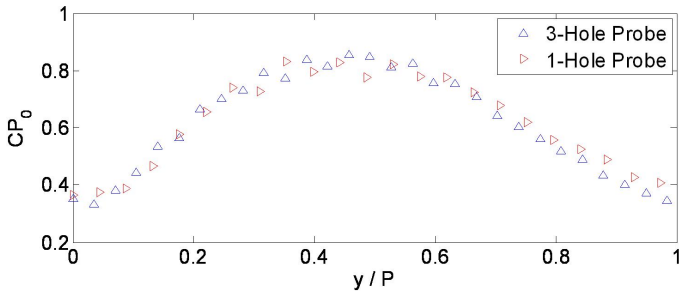

Figure 3.27: Total pressure loss coefficient profile measured across the blade pitch with the single-hole probe and three-hole probe at same span

the three-hole probe centre tube and the single-hole probe (with and without rotation) were located at the same pitch-wise location (y/P) at the start of each experiment.

Pressure measurements were taken at eleven span-wise locations (from 75–100 percent of the engine-equivalent blade span), and twenty-four pitch-wise locations. After each step-wise traverse, data collection was delayed for one second in order to ensure the flow around the probe, sting and stem was stable. One-second of data was then recorded at each step-wise location to ensure enough response time for the transducer to obtain the appropriate reading.

3.5.3 Three-Hole Probe Calibration and Uncertainty

The three-hole probe was calibrated in a 9 in $\times$3 in transonic tunnel at the University of Oxford, over the range -20° $\leqslant \beta \leqslant$ 20° and 0.6$\leqslant M \leqslant$ 1.3. The probe design and calibration are based on work by Povey et al. (2008).

The yaw (β), total pressure and Mach coefficients (C_β, C_T and C_M, respectively) are defined as follows, where probe ports are shown in Figure 3.26.

$$C_\beta = \frac{P_A - P_C}{P_B - P_{avg}} \tag{3.4}$$

$$C_T = \frac{P_t - P_B}{P_B - P_{avg}} \tag{3.5}$$

$$C_M = \sqrt{\frac{2}{\gamma - 1}\left[\left(\frac{P_{avg}}{P_B}\right)^{\frac{1-\gamma}{\gamma}} - 1\right]} \tag{3.6}$$

$$P_{avg} = \frac{P_A + P_C}{2} \tag{3.7}$$

Figure 3.28 presents the total pressure calibration matrix $C_T(M, \beta)$ and application matrix $C_T(C_\beta, C_M)$. The calibration map is smooth and largely symmetric. Other calibration maps for C_M and C_β also indicate a good performance of the probe. Flow angle, total pressure, and Mach number are obtained by linear interpolation using the application matrix as a lookup table. The computation technique used in the present study follows the technique described by Main et al. (1996).

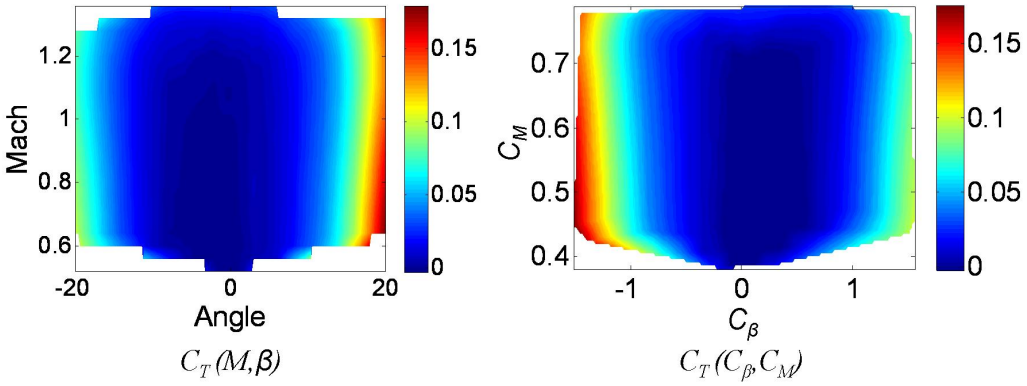

Figure 3.28: Three-hole pressure probe C_T calibration and application matrix

Table 3.3: Three-hole probe uncertainty

Total Pressure P_t	Yaw β	Mach M
0.1354 (0.96%)	2.2°	0.081

The uncertainty of the three-hole probe was determined by substituting the calibration data back into the application matrix and computing P_t, β and M at each point. The uncertainty magnitudes of probe measurements were then calculated. The uncertainties of P_t, M, and P_s are based on the RMS differences between the data over the whole field, but do not include bias or precision errors of the transducers, and are given in Table 3.3.

During calibration, a problem with the 4° flow angle was observed. The Mach number and total pressure did not appear to be affected. The test was repeated for 4° yaw with consistent results. A yaw angle of 3° was also examined and had similar, though not as significant, results to the 4° calibration.

It was concluded that the manufactured probe had a flaw which prevented the probe from measuring the flow angle accurately at the 3° and 4° angles. These 4° flow angle results are not included in the yaw uncertainty in Table 3.3. The high degree of uncertainty of the yaw angle reported in Table 3.3 is mostly due to the 3°

yaw angle as well as angles measured at the lowest Mach number of approximately 0.6.

An additional source of uncertainty is the inability of the three-hole probe to measure pitch flow angles. A three-hole probe was used because a transonic wind tunnel was unavailable to calibrate a four-hole probe. The option to rotate the probe by 90° was not used because no time was available to modify the facility to accept a rotated probe.

The lack of a four-hole (or five-hole) probe leads to additional uncertainty by not accounting for the pitch (span-wise) flow direction. However, it is possible to estimate this uncertainty. The pitch (span-wise) angle is not expected to be greater than the yaw angle deviation from the metal exit angle. Within the over-tip leakage vortex, the centre-hole channel measurements at 20° yaw angle differ from the true total pressure by 2.8 percent. This gives an indication of the maximum error of the total pressure.

3.6 Summary

This chapter introduced the High-Speed Linear Cascade facility, including the instrumentation, test section, blades and the coolant feed system.

The PID controller was optimised to obtain steady inlet pressures under high-speed flow conditions. The test section has transonic exit flow conditions. The exit Mach number is approximately 1.0 and the exit Reynolds number is approximately 1.2×10^6. An inlet uniformity study was performed and showed that the inlet total pressure distribution varied within 0.5 percent. An inlet hot-wire survey was used to measure a turbulence intensity of 1.0 percent and a boundary layer of 4 mm thickness on the tip casing wall. Pressure measurements downstream of the blade row showed periodic flow conditions for the test section, specifically when the same tip geometry is used for the three centre blades. Finally, the blade loading experimental results compared well to FLUENT predictions and the blade loading of the operating engine.

The aerodynamic loss experimental setup was described. A two-dimensional traversing system traverses a three-hole probe and a single-hole probe to obtain

spatially-resolved exit pressure maps one axial chord downstream of the blade row. The calibration of the three-hole probe was described along with uncertainty calculations.

Chapter 4

Heat Transfer Measurement Setup and Qualifications

4.1 Introduction

This chapter introduces the heat transfer measurement setup used in the present study, including infrared (IR) theory, the equipment used for IR thermography tests, the calibration of the IR camera and the effect of distance and angle on the IR testing.

A penetration depth analysis is then performed to determine if the blade material is suitable for a semi-infinite 1-D conduction assumption.

The chapter then considers several heat transfer measurement and analysis techniques to determine spatially-resolved surface heat transfer coefficients and adiabatic wall temperatures on a flat blade tip. All the techniques used in the present study use IR thermography and the analysis methodology for all the techniques is discussed. A comparison of the different methods and techniques is performed to determine which of the different methods is the most suited experimental heat transfer technique based on repeatability, accuracy and computational efficiency.

An additional heat transfer measurement approach was attempted. Thin-film heat flux gauges were used to obtain discrete heat transfer coefficients for four locations on the blade tip. During testing, one gauge failed to give a reading. Post-test analysis revealed that the sensor leads had broken. The other three gauges provided fair results. It is now known that the calibration of the thin-film gauge was not done

properly and it is unknown if any of the results can be trusted. For this reason, these results are not included in the thesis.

4.2 Heat Transfer Measurement Setup

Having described the aerodynamic qualification of the HSLC in Chapter 3, the thermal investigation requires a qualification of the heat transfer measurement and analysis technique. This section describes the experimental setup for all of the heat transfer techniques examined in this study, though some techniques do not use all of the equipment discussed. Further details of the qualification of the heat transfer measurement and analysis technique employed in the present study are addressed in Section 4.3.

Aside from the use of the thin foil heater, all other measurement and analysis techniques require the use of the heater mesh described in Section 3.2. The purpose of the heater mesh is to provide a step increase in mainstream flow temperature. Heat transfer is then determined from the blade tip response to this step-change.

The use of surface-mounted thermocouples for an in situ calibration of the IR camera was addressed in Section 3.3.3. The remainder of this section addresses the use of an IR camera as well as its experimental setup. Figure 4.1 presents the experimental setup for use of the IR camera to measure the blade tip heat transfer. The SI40 tip and metal blade base were discussed in Section 3.3.3. The IR camera and the ZnSe window is addressed in Section 4.2.2.

4.2.1 Summary of Infrared Theory

Every surface which has a temperature greater than absolute zero radiates energy. Planck's law states that this radiant emittance of an object is related to the temperature of the surface for a given wavelength. By integrating Planck's formula for all wavelengths (between 0–∞), the result is the total radiant emittance, which is proportional to the fourth power of an object's absolute temperature (Stefan-Boltzmann's formula).

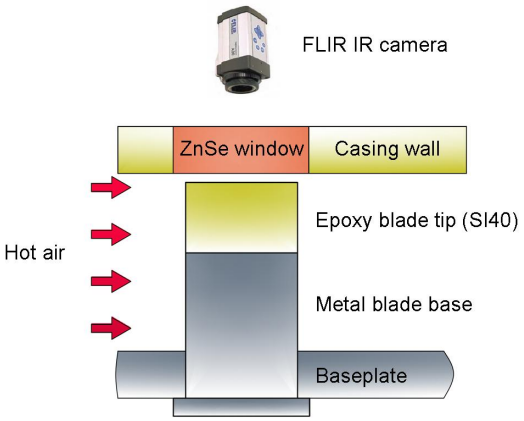

Figure 4.1: Transient thermal measurement experimental setup (drawing not to scale, based on Zhang (2007a))

When considering the electromagnetic spectrum, infrared radiation lies at the boundary to visible light, with wavelengths just longer (or frequencies just shorter) than the colour red. An infrared camera contains a sensor that detects the infrared radiant energy for a given frequency band.

Of course, an IR camera senses radiant energy absorbed by the sensor from all sources, not just the object being considered. The sensor measures an energy signal and along with the manufacturer's calibration and some IR characteristics of the materials and gases in the optical path, the emittance is determined. These IR characteristics are discussed in the next section.

Depending on the temperature settings of the camera, the camera assigns a "greyscale" value for the relative linearised signal between this temperature range. For a 16-bit camera, this greyscale value is between 0–65535 (2^{16} values). As an example, if the temperature settings are between -20°C and 120°C, then the greyscale value for -20°C is 0 and the greyscale value for 120°C is 65535 (or vice versa). For an 8-bit camera, the range of greyscale values has less resolution, with values between 0–255 (2^8 values).

If the IR characteristics change, then the output signal changes. However, as it is discussed in the next section, it is very difficult to know these IR characteristics.

4.2.2 IR Camera and ZnSe Window

Two IR cameras are used in this study for spatially-resolved surface temperature history measurements. Both cameras are capable of operating in the far infrared wavelength band between 7.5–13 μm. Using Wien's displacement law and the range of HSLC operating temperatures, the range of maximum wavelengths observed by the camera is between 9–10.2 μm. Also, the object being measured is considered a greybody, in which the object emits a fraction of the radiant power of a black body with equal temperature and wavelength. The blade is painted using a flat black oil-based paint (see Figure 3.9), which has an estimated emissivity of 0.94 (FLIR Systems, Inc., 2008).

The FLIR A20M was used in the heat transfer qualification testing and for the comparison between high-speed and low-speed testing. The A20M is equipped with a FireWire 400 connection that supplies an 8-bit greyscale output for a 160x120 infrared detection sensor at a data acquisition rate of 30 frames per second. The linear-output temperature scale is customisable and a temperature range of 0–50°C was used. For an 8-bit camera, this equates to approximately 0.2°C per greyscale value.

Following the heat transfer qualification and flow-speed comparison testing, a new camera, the FLIR A325 Researcher, was used. The A325 is equipped with an RJ-45 Gigabit Ethernet connection that supplies a 16-bit greyscale output for a 320x240 infrared detection sensor at a data acquisition rate of 60 frames per second. The linear-output temperature scale is not customisable, but the -20 to 120°C pre-set temperature scale in conjunction with a 16-bit greyscale output provides a better temperature to grey-scale resolution, approximately 0.002°C per greyscale value, which is likely less than the noise floor, but it is certainly better than an 8-bit camera.

As the A325 is slightly larger than the A20M, and the new camera required additional mechanical support, a new camera housing unit was developed, as seen in Figure 4.2a. Silicone O-rings are used to prevent the camera from vibrating.

The outside of the housing was attached to mechanical supports within the facility, which allowed for the camera to be placed above the test section to measure tip heat

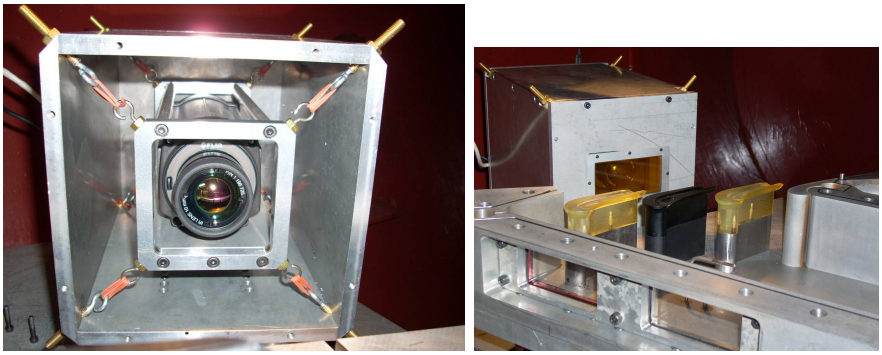

(a) Anti-vibration housing

(b) Measurement of suction-side heat transfer

Figure 4.2: Photographs of the IR camera anti-vibration housing and sidewall measurement location

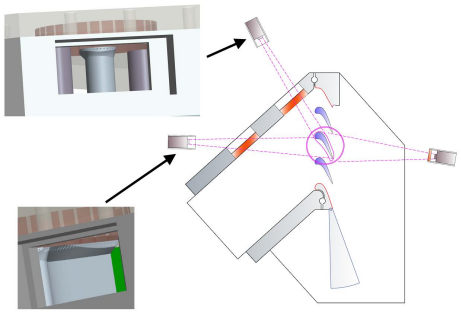

Figure 4.3: Sidewall heat transfer measurements (drawing not to scale, based on Zhang (2007a))

transfer or next to the test section to measure sidewall heat transfer. Figure 4.2b shows a picture of the IR camera inside the housing placed next to the test section to measure heat transfer on the blade's suction-side surface. Figure 4.3 displays the camera locations where sidewall heat transfer is measured, including the orange-coloured ZnSe windows.

As shown in Figures 4.1 and 4.3, ZnSe windows are placed on the top casing wall above the centre blade and on the test section sidewall, both to prevent flow leakage and so that the IR camera can observe the IR wavelengths emitted by the blade surface. The ZnSe window has a spectral transmissivity with wavelengths observable to the IR camera. The temperature of the window varies between 10–45°C (considering both sides of the window) and using Wien's displacement law, the

transmissivity of the window is approximately 99.5 percent for the entire temperature range.

4.2.3 IR calibration

As mentioned in Section 4.2.1, an IR camera measures the radiant energy of an object *and* its surroundings, and based on the temperature range selected, converts this energy into a greyscale value. If the object's surroundings and atmospheric conditions are known, the temperature can be determined, which is very challenging.

At the relatively low temperatures tested, 10–45°C, stray radiation from intense radiation sources is not likely. Also the temperature of the surroundings inside of the test section varies by location and attempting to quantify this affect is very challenging.

Knowledge of the object's surroundings requires knowledge of the following IR characteristics:

- Emissivity of the object
- Relative humidity
- Temperatures of IR lens and ZnSe window
- Temperature of the atmosphere (between the camera and the object)
- "Effective" temperature of the object's surroundings
- Transmissivities of extra IR lens and ZnSe window

Some of these values can be found in a table or graph, but using these values will add to the uncertainty. Other values will vary throughout a test for different parts of an object. For example, the temperature of air over the tip gap is variable over time and space.

Rather than try to evaluate the IR characteristics, the procedure used in the present study involved an in situ calibration of the camera using surface-mounted thermocouples. The camera settings still require values for some of the different variables such as humidity, emissivity of the object and temperature of the ZnSe

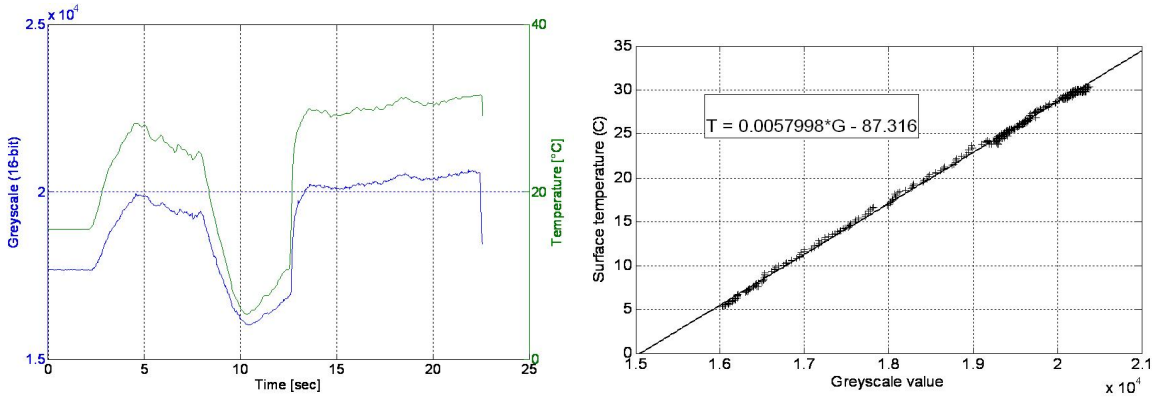

(a) IR greyscale and thermocouple temperature time histories

(b) IR calibration curve

Figure 4.4: IR in situ calibration results for a single test

window. Estimates for these values were used and kept constant for all heat transfer experiments.

MATLAB was employed to import the IR video file and to interpret 65,536 levels of grey. This greyscale value was compared to the known thermocouple reading to obtain a calibration curve. Figure 4.4 shows a sample in situ calibration. Figure 4.4a shows the time histories of the IR camera's greyscale output as well as the surface thermocouple's temperature. The calibration curve is determined by plotting the IR camera greyscale against the surface-mounted thermocouple, as in Figure 4.4b.

The calibration curve shows a linear relationship between the greyscale values and the temperature readings. At this point, it is assumed that the different IR characteristics previously mentioned are all rigorously accommodated for in the in situ infrared camera calibration process. It should be highlighted that one single run is used both for the in-situ calibration and the heat transfer calculations.

4.2.4 Distance and Angle Effects

One of the variables that affect the output of the IR camera is the distance to the object. This effect is accounted for during the tip tests. However when examining the blade sidewalls, not only is the camera further away from the blade than it was during tip experiments, but part of the blade surface is not normal to the camera due to the

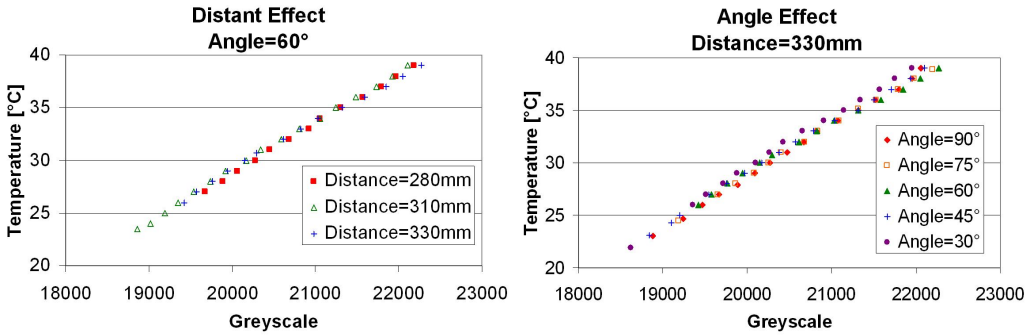

Figure 4.5: Effect of distance and angle on the IR calibration curve

curvature of the blade. As the energy received by the sensor detector is a function of the distance and angle, an examination into the effect of distance and angle was performed using a flat plate made of SI40 with a surface mounted thermocouple. Figure 4.5 shows two sets of calibration curves. One set holds the distance constant while varying the angle between 30–90°, where 90° is when the camera is pointed normal to the object surface.

From Figure 4.5, it appears that the effect of distance is minor. The three distances examined are representative of the range of distances from the camera to the blade for the three sidewall locations. The differences that do exist are within the uncertainty of the camera's calibration. The effect of angle, on the other hand, shows larger variations between the different angles. The 90° angle is the angle at which most of the IR energy is detected by the camera's sensor. The variation for angles of 45–90° is fairly consistent, especially at the lower temperatures. For the higher temperatures, the differences are greater. The 30° angle, which has the least amount of IR energy being detected by the camera's sensor, has a higher slope and y-intercept. For the actual blades tested, however, most of the angles are greater than 60°. There are a few regions where the angle is less and these locations have greater uncertainty.

It should be noted that the heat transfer measurement technique discussed in Section 4.3 is based on temperature differences over time. With the maximum and minimum calibration curves shown in Figure 4.5, the temperature difference is only a function of the difference in slope. This temperature difference is within the uncer-

Table 4.1: Heat transfer measurement techniques used to qualify HSLC heat transfer experiments

Measurement technique	Analysis type
Idealised process	Transient IR thermography assuming idealised initial conditions
Finite-difference	Transient IR thermography with heat flux reconstruction using finite-difference approach
Impulse	Transient IR thermography with heat flux reconstruction using Impulse approach
Thin-foil heater	Quasi-steady IR thermography
Quasi-adiabatic	Quasi-steady IR thermography

tainty of the camera's calibration. Further details of the heat transfer measurements and uncertainty analysis are provided in Section 4.3. Heat transfer results are provided in Chapters 5 and 6.

4.3 Heat Transfer Qualification Overview

Having discussed the heat transfer measurement setup, this section introduces the heat transfer qualification methods. It also defines that heat transfer descriptors that are compared between the different methods. Lastly, the approach used to determine these descriptors is described.

Five analysis methods are used to obtain detailed, spatially-resolved heat transfer results across the blade tip. These five techniques are divided into two types: transient techniques and steady-state techniques. The transient technique requires a step change in temperature of the mainstream flow. The heat transfer measurements are based on the response of the blade tip to this step change, which makes it a function of time. The steady-state technique assumes that the blade is in a quasi-steady state when heat transfer measurements are collected. A brief summary of these techniques and the analysis type is provided in Table 4.1. Discussion of the heat transfer results for all methods is provided in Section 4.6.

The descriptors compared between the different heat transfer techniques are the convective heat transfer coefficient h and the adiabatic wall temperature T_{ad}. h is determined experimentally using Equation 4.1

$$\dot{q} = h(T_{ad} - T_w) \tag{4.1}$$

where $\dot{q}$ is the heat flux, T_w is the wall temperature and T_{ad} is the adiabatic wall temperature.

The use of the adiabatic wall (recovery) temperature is important to this present work as the local recovery temperature varies greatly over the blade tip and use of the inlet flow temperature is insufficient. This is particularly true for high speed flow where the adiabatic wall temperature is less than the inlet total temperature.

4.4 Penetration Depth Analysis

The experimental setup used to determine these heat transfer descriptors was discussed in Section 4.2. This section address a key assumption made for the different techniques as well as its suitability for the present study.

Because of the very low conductivity of the tip material, heat transfer on the blade tip surface is modelled using a semi-infinite solid conduction analysis procedure. A penetration depth analysis is performed to justify the use of the different heat transfer techniques. Penetration depth is a measure of the thickness of thermal energy propagating into the surface through conduction, usually the depth at which the temperature changes by a fixed but arbitrary percentage. Fourier's law of heat conduction for a one-dimensional, unsteady solid is given in Equation 4.2.

$$k\frac{\partial^2 T}{\partial y^2} = \rho C_p \frac{\partial T}{\partial t} \tag{4.2}$$

where k is the thermal conductivity, T is the temperature, y is the depth into the solid normal to the surface, ρ is the density of the solid, C_p is the specific heat of the solid and t is the time. Equation 4.2 has been solved using the following initial and boundary conditions:

$$T(y, t = 0) = T_i \tag{4.3}$$

$$T(y = \infty, t) = T_i \tag{4.4}$$

$$-k\frac{\partial T}{\partial y}\bigg|_{y=0} = h(T_{ad} - T_w) \tag{4.5}$$

Equation 4.3 is the initial condition, Equation 4.4 is the "semi-infinite" boundary condition and Equation 4.5 is a convective boundary condition and is imposed by sudden transient heating.

If the temperature at the maximum depth changes throughout the test, energy is less likely to conduct into the blade tip, thus affecting the convective heat transfer. The solution to Equation 4.2 with the given initial and boundary conditions is shown in Equation 4.6.

$$\frac{T_w(y,t) - T_i}{T_t - T_i} = 1 - \mathrm{erf}\Big(\frac{y}{2\sqrt{\alpha t}}\Big) - \Big[\exp\Big(\frac{hy}{k} + \frac{h^2\alpha t}{k^2}\Big)\Big]\Big[1 - \mathrm{erf}\Big(\frac{y}{2\sqrt{\alpha t}} + \frac{h\sqrt{\alpha t}}{k}\Big)\Big] \tag{4.6}$$

This solution has been demonstrated in Schneider (1955). This equation is a function of the initial temperature T_i, the solid temperature $T_w(y,t)$ (which is also a function time), the mainstream total temperature T_t, the thermal characteristics of the solid ($\alpha = k/\rho Cp$ and k), the depth of the solid y, the time t and the heat transfer coefficient, h. This equation also requires a step change in T_t after $t = 0$. The only unknown in this equation is h. Calculations of the spatially-resolved h (as presented in Chapter 5) are used to estimate h in Equation 4.6. For the penetration depth study, an overestimated h of 2000 $\mathrm{W/m^2K}$ is assumed.

Figure 4.6 shows how the temperature changes in the leading edge area of the blade over time. The assumed maximum depth of 10 mm is less than the actual depth of the epoxy blade tip, 30 mm. Note that the two lines in Figure 4.6 represent different times during the test. The test runs actually take less than 10 seconds under the heater mesh thermal load. Therefore, from Figure 4.6, at 10 seconds, the

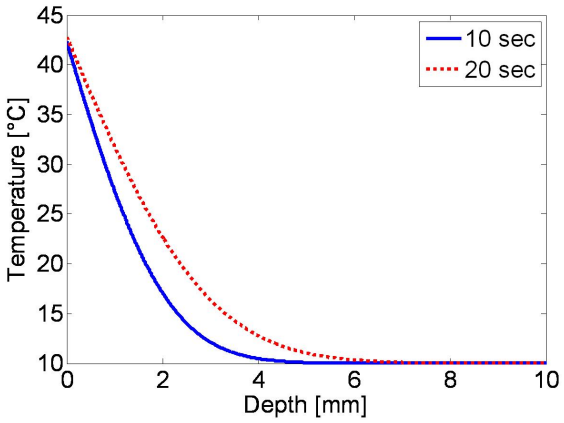

Figure 4.6: Penetration depth analysis at leading edge for heat transfer coefficient of 2000 W/m^2K, at 10 and 20 seconds into test

temperature at 6 mm (20 percent of the maximum depth) has changed 0.09 percent (on relative scale) and the temperature at 10 mm is unchanged. Therefore, based on this penetration depth analysis, the semi-infinite assumption is a good assumption for the material used and for the length of the test. Note that this penetration depth analysis cannot be used for the trailing edge or parts of the winglet geometry, where three-dimensional conduction effects dominate.

4.5 Heat Transfer Measurement and Analysis Techniques

The experimental setup used to determine the heat transfer coefficients and adiabatic wall temperatures was discussed in Section 4.2. As mentioned in that section, the heat transfer to the blade tip surface is considered to be to a semi-infinite solid domain, since the tip material has low conductivity and the thermal penetration depth is small during a tunnel run.

This section addresses how the heat transfer coefficients and adiabatic wall temperature are determined, including an explanation of the technique and the underlying assumptions. All methods use infrared thermography. The first three methods are transient methods and the last two are quasi-steady state methods, as listed in Table 4.1.

Any discussion of the results is reserved for a later section, Section 4.6.

4.5.1 Idealised Transient Infrared Thermography Technique

The first method used to determine the tip heat transfer is the classic solution to the 1-D heat equation, or idealised process technique. This method uses a heater mesh to provide a near-instantaneous step-change in mainstream temperature (with a time constant of 0.03 sec) and an IR camera to measure surface temperature. During a blow down test, roughly 12 seconds is needed for the mainstream to reach the desired operating condition. Pre-heating of the blade tip occurs due to the initial isentropic compression process caused by the opening of the air supply valve, as highlighted in Section 3.4.2.

The idealised process technique neglects the preheating that occurs within the first 10 seconds. This technique uses the classical solution to Fourier's law of heat conduction for a one-dimensional, unsteady, semi-infinite solid, with convective boundary conditions (see Equation 4.7).

$$\frac{T_w(t) - T_i}{T_{ad} - T_i} = 1 - \exp\Big(\frac{h^2 t}{\rho C_p k}\Big)\mathrm{erfc}\Big(\frac{h\sqrt{t}}{\sqrt{\rho C_p k}}\Big) \tag{4.7}$$

In this equation, $T_w(t)$, T_i and T_{ad} are the local wall temperature, initial temperature and adiabatic wall temperature, respectively. Also, h, $\sqrt{\rho C_p k}$, and t are the heat transfer coefficient, thermal product (a property of the material used in the experiment) and time, respectively. The equation is simplified with the following relationship, erfc(y)=1-erf(y). When using the definition of the adiabatic heat transfer coefficient, the total temperature T_t becomes the adiabatic wall temperature T_{ad}. Also, as $\alpha = k/(\rho C_p)$, $\sqrt{\alpha}/k = 1/\sqrt{\rho C_p k}$, where $\sqrt{\rho C_p k}$, the thermal product of the test material, is experimentally determined and briefly discussed in Section 3.3.3.

Note that this is the same as Equation 4.6 for $y = 0$ on the blade tip surface. There are two unknowns in Equation 4.7, h and T_{ad}. Since it is difficult to perfectly repeat each experiment (e.g. start with the same T_i), two different times during the

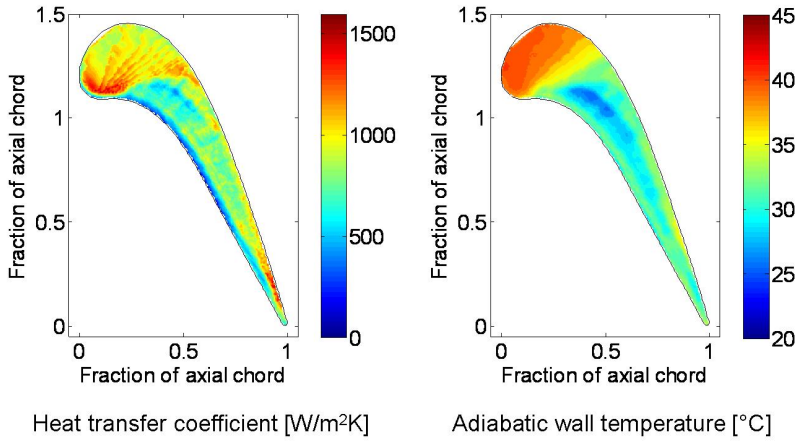

Figure 4.7: Contours of (a) heat transfer coefficient [W/m^{2}K] and (b) adiabatic wall temperature [°C] using idealised process technique

same test run are used with regression analysis to determine the unknowns h, T_{ad} and t.

The initial temperature T_i is the temperature immediately before powering the heater mesh (the time step immediately before the step change). To solve for h, T_{ad} and t, Equation 4.7 is solved for $T_w(h, T_{ad}, t)_{\text{calc}}$ using an array of h from 0–3000 W/m^{2}K, T_{ad} from 0–50°C and t from 0–10 s. The minimum of the the difference between $T_w(h, T_{ad}, t)_{\text{calc}}$ and $T_{w,\text{meas}}$ is used to determine h and T_{ad}.

This analysis technique is called the idealised process technique because it is a step-change isothermal approximation and assumes that before the heater mesh is enabled, the test section and blade tip are in equilibrium, $T_t = T_w = T_i$. However, as it has already been mentioned, preheating of the blade tip occurs within the first 10 seconds of the test, before the heater mesh is enabled. Though the blade tip surface temperature does decrease after the compression shock, a certain amount of conduction has taken place, which could affect the heat transfer results.

Figure 4.7 presents contours of heat transfer coefficient and adiabatic wall temperature distributions using the idealised process technique.

The algorithm used to determine heat transfer coefficient was computationally expensive, both in time and computer memory. This method takes about 15–20

hours to calculate the spatially-resolved h, but a better processing algorithm would likely solve this problem in less than an hour.

4.5.2 Transient Infrared Thermography Technique using Heat Flux Reconstruction with Finite-Difference Approach

In order to properly account for the preheating effect, as well as determine a more computationally efficient solution technique, an alternative method is used.

As mentioned in Section 4.5.1, during the blow down test, roughly 12 seconds is needed for the mainstream to reach the desired operating condition. Pre-heating of the blade tip occurs due to the initial isentropic compression process caused by the opening of the air supply valve. To account for the effect of preheating, a complete heat flux history for each blade tip location is reconstructed from temperature traces provided by the IR camera. The first heat flux reconstruction method uses a finite difference approach and uses the same experimental approach and transient test data as the idealised process technique. Equation 4.8, which is derived in Oldfield et al. (1978), relates the time history of the temperature and the heat flux. In this equation, τ is the sampling rate of the temperature history, t is the time, m is the number of measurements taken and n is the integration variable.

$$\dot{q}(t) = \dot{q}(m\tau) = \left(\frac{2\sqrt{\rho C_p k}}{\sqrt{\pi\tau}}\right) \sum_{n=0}^{m} \left[\Big(T_{n+1} - 2T_n + T_{n-1}\Big)\Big(m-n\Big)^{\frac{1}{2}} \right] \tag{4.8}$$

This heat flux reconstruction technique is a numerical finite-difference approximation. After reconstruction of the heat flux from temperature traces, the heat flux is then plotted against temperature for the time period after the heater mesh is turned on. In order to accommodate for small fluctuations in the mainstream flow caused by the opening and closing of the control valve, a non-dimensional approach is used, which also reduces uncertainty and leads to more repeatable results. The wall temperature is normalised by the inlet temperature and the heat flux is normalised by multiplying it by $C_{ax}/(k_{air}T)$ (a form of Nusselt number for a constant-heat-flux case).

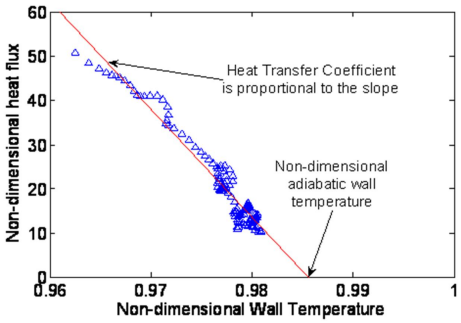

Figure 4.8: An example of heat flux versus temperature history after the heater mesh is turned on

A linear relationship between the heat flux and wall temperature is expected and observed when using the linear convective heat transfer equation (see Equation 4.1). The slope and x-intercept are determined using the transient temperature data and the calculated heat flux. MATLAB's "*mldivide*" function is used, which divides the non-dimensional temperature time trace by the non-dimensional heat flux time trace. How well the slope matches the data was not calculated, though the slope, as shown in Figure 4.8, shows a good fit, consistent with other tip data.

Therefore, the slope in Figure 4.8 is proportional to the local heat transfer coefficient, and adiabatic wall temperature can be extrapolated for zero heat flux. This reconstruction method is then used for all the tip surface locations.

Not only does this method properly account for the preheating effect at the start of a test run, it greatly improves the computational processing time by a factor of 60 compared to the idealised process technique.

Figure 4.9 presents contours of heat transfer coefficient and adiabatic wall temperature for the blade tip using this approach.

4.5.3 Transient Infrared Thermography Technique using Heat Flux Reconstruction with Impulse Approach

The previous method uses finite differences to generate a heat flux history from the temperature time history. This worked well for the 1970s-era computers and works today for low sampling rates and for small number of data locations. High sampling

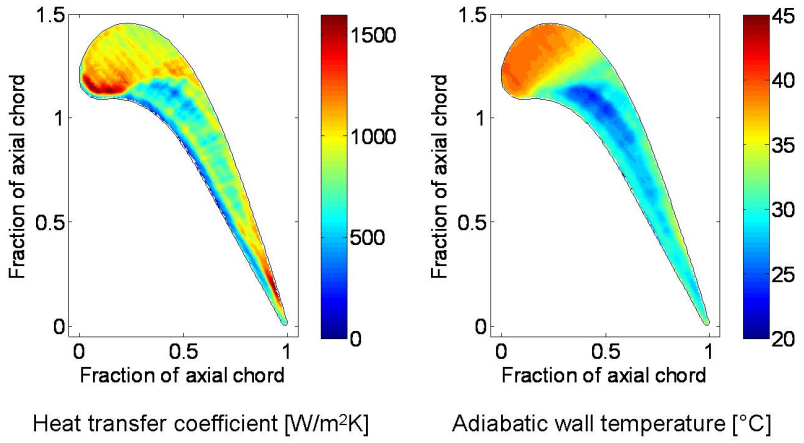

Figure 4.9: Contours of (a) heat transfer coefficient [W/m^{2}K] and (b) adiabatic wall temperature [°C] using finite difference heat flux reconstruction method

rate of thin film gauges requires a new, more sophisticated approach. By using the frequency domain, the Impulse method of Oldfield (2008) has a 60-fold increase in computational speed over the finite-difference heat flux reconstruction method.

This method is identical to the finite-difference reconstruction method with the exception of the technique used to derive the heat flux from the temperature trace. Like the finite difference equation (Equation 4.8), the Impulse method uses discrete deconvolution and known pairs of exact solutions to the convective heat transfer equation to derive a digital filter impulse response, which is used in conjunction with a Fast Fourier Transform to reconstruct the heat flux from temperature traces. A MATLAB program written by Professor Martin Oldfield is used to derive this response function, $h(t)$ (not to be confused with the heat transfer coefficient). The filter design is accurate to the order of 10^{-12}, taking advantage of MATLAB's ability to store numbers to 15 decimal places.

As with the finite-difference approach, a non-dimensionalised plot of the heat flux versus wall temperature leads to heat transfer coefficients and adiabatic wall temperatures at each blade tip pixel location. Figure 4.10 presents contours of heat transfer coefficient and adiabatic wall temperature for the blade tip using this approach.

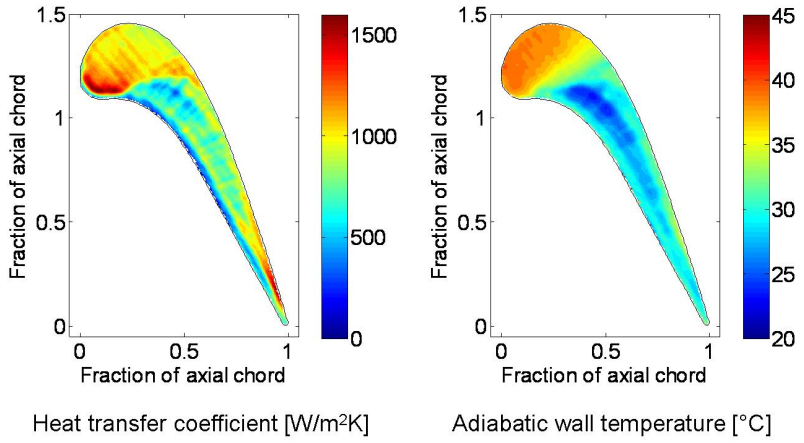

Figure 4.10: Contours of (a) heat transfer coefficient [W/m^{2}K] and (b) adiabatic wall temperature [°C] using impulse heat flux reconstruction method

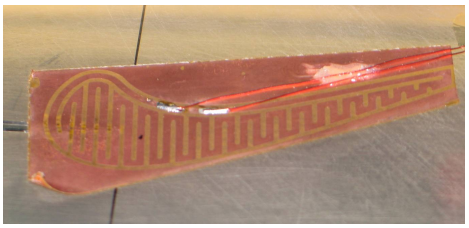

Figure 4.11: Thin foil heater employed in the present study

This method was intended for high frequency data. However, though the temperature history is sampled at relatively low frequency, the large number of pixels requires a computationally efficient technique, which is found in the Impulse method.

4.5.4 Thin-Foil Heater

The first three methods previously described are all transient tests, as all three require a step change in inlet total temperature.

This section shifts from the transient techniques to the first steady-state technique, the thin-foil heater. Figure 4.11 presents the thin-foil heater specially designed and employed. For this test, the exit plenum has the capability to run power lines to the test section to provide power to the thin-foil heater.

The heater is placed on the blade tip aimed to obtain a constant/uniform heat flux. This technique assumes that the power supplied to the heater is the total heat flux

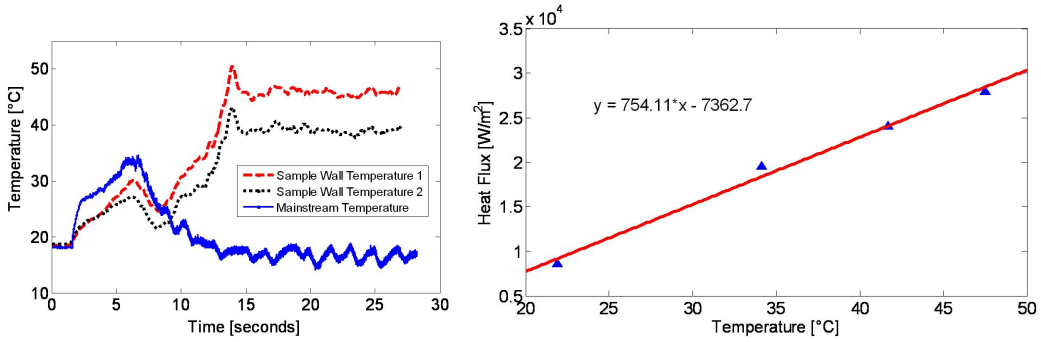

(a) Temperature history of mainstream and blade tip where thin-foil heater is powered after 10 seconds

(b) Heat flux versus temperature for 4 sets of experimental data using thin-foil heater

Figure 4.12: Temperature time trace and $\dot{q}$-T plot for thin-foil heater approach

across the blade tip, and since the blade tip has low conductivity, the power supplied to the heater is assumed to be the convective heat flux, neglecting any conduction within the test model. Also, the power is assumed to be constant across the blade tip, equal to the square of current supplied multiplied by the resistance across the foil heater.

For a given run, the heat flux, $\dot{q}$, and blade tip surface temperature, T_w, are known, leaving two unknowns, the heat transfer coefficient, h, and the adiabatic wall temperature, T_{ad}. At least two separate runs at different heater power settings are required to solve the convective heat transfer equation (Equation 4.1). Note that the surface temperature distribution is measured using infrared thermography.

A steady state is assumed to be achieved after 20 seconds of heating the blade tip, as shown in Figure 4.12a, where the mainstream temperature and two sample IR wall temperatures are displayed.

For each location on the blade tip, four sets of heat flux and temperature data are obtained and a multiple regression analysis is used to solve for h and T_{ad}. The heat transfer coefficient and adiabatic wall temperature can then be extrapolated, as shown in Figure 4.12b.

Figure 4.13 presents contours of heat transfer coefficients and adiabatic wall temperatures using the thin-foil heater. Note that these distributions are seemingly very

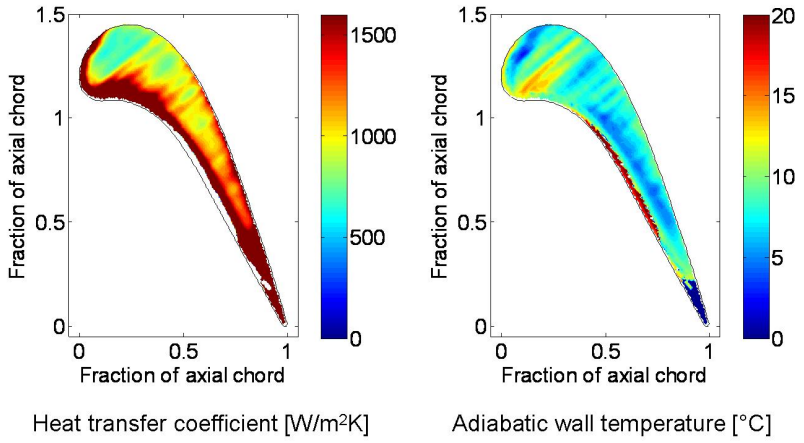

Figure 4.13: Contours of (a) heat transfer coefficient [W/m^{2}K] and (b) adiabatic wall temperature [°C] using thin-foil heater

different relative to the distributions in Figures 4.7, 4.9 and 4.10 because of spatially-varying conduction into the test model, and spatially-varying surface heat flux along the surface of the model. Both are neglected in this method.

4.5.5 Quasi-Adiabatic Technique

The other steady-state approach is the quasi-adiabatic technique. To compare these results to the other methods, the mainstream temperature during these tests must be the same as the mainstream temperature measured during the other transient methods, in order to have near-equivalent driving temperatures. The heater mesh is used to raise the mainstream temperature and the IR camera is used to determine the surface temperature.

This method assumes that after a certain period of time with a thermal load, the tip will absorb less and less heat transfer energy as the temperature difference between the blade tip surface and the mainstream flow becomes smaller. This approach assumes that 20 seconds after the heater mesh is enabled, the blade tip will reach steady state. Unlike the other techniques, the quasi-adiabatic technique only determines the adiabatic wall temperature. Figure 4.14 shows the tip temperature distribution after the heater mesh is turned on for 20 seconds. This temperature distribution then approximates that which would exist on an adiabatic test surface.

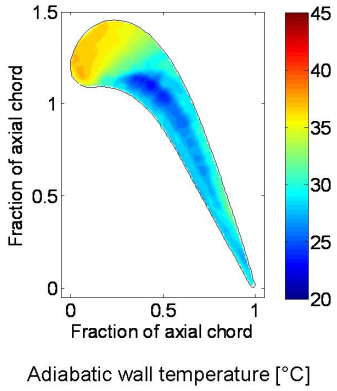

Figure 4.14: Contour of the adiabatic wall temperature [°C] using quasi-adiabatic assumption. The very last snapshot of tip temperature distribution after the heater mesh is turned on for 20 seconds

4.6 Comparison and Qualification

For reasons that are addressed in this section, the heat flux reconstruction technique using the Impulse method is chosen to be the primary method for obtaining spatially-resolved heat transfer results. The results of this method are compared to the other heat transfer measurement methods for qualification. First, the three transient analysis methods are compared to each other. All three techniques are experimentally equivalent. The only difference is the post-processing.

Results of the heat transfer coefficient between the two heat flux reconstruction methods are within seven percent (maximum percent difference between the two comparing pixel to pixel, with reference to the Impulse method), where most of the blade tip is within three percent. When comparing the Impulse method to the idealised process technique, the percent difference in heat transfer coefficient between the two, comparing pixel to pixel, is within 15 percent. Figure 4.15 shows the circumferentially-averaged heat transfer coefficients and adiabatic wall temperatures. The averages are taken at axial chord-wise locations. The plot uses lines for the discrete data points to make it easier to see the data.

As the quasi-adiabatic approach does not resolve a heat transfer coefficient, only the adiabatic wall temperature can be compared.

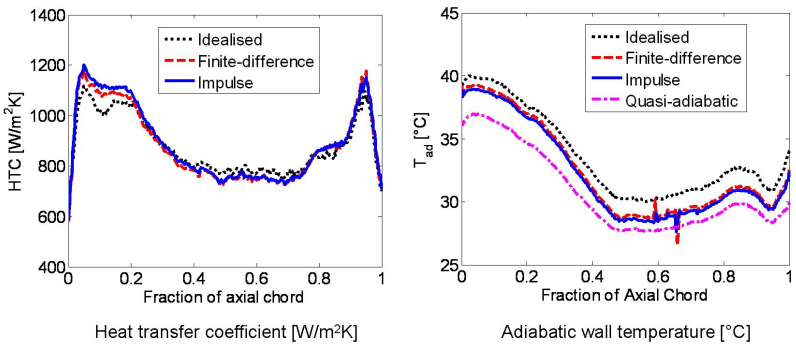

Figure 4.15: Circumferentially-averaged transient thermal measurement calculations on tip (axial-chordwise averages) for heat transfer coefficient and adiabatic wall temperature

Table 4.2: Average transient thermal measurement calculations across the blade tip

Measurement technique	Heat transfer coefficient [W/m^{2}K]	Adiabatic wall temperature [°C]
Idealised process	970.0	33.4
Finite-difference	814.2	33.0
Impulse	859.6	32.8
Quasi-adiabatic	N/A	30.6

Table 4.2 shows the blade-wise average heat transfer coefficients and adiabatic wall temperatures for the three transient IR methods and the quasi-adiabatic method.

The rest of this section compares the different techniques to the transient IR method with heat flux reconstruction using the Impulse method, first looking at heat transfer coefficient and then the adiabatic wall temperature.

4.6.1 Heat Transfer Coefficient and Nusselt Number

When providing heat transfer coefficient results, it is often best to present them in non-dimensional form, such as the Nusselt number. The surface Nusselt numbers can be determined from the heat transfer coefficient using Equation 4.9. The conductivity of air, $k_{\text{air, local}}$, used in this equation is based on the local adiabatic wall temperature at each pixel location. The heat transfer coefficient is based on the local adiabatic wall temperature and the wall temperature.

$$Nu = \frac{hC_{ax}}{k_{\text{air, local}}} \tag{4.9}$$

However, as the results in this chapter are only being compared to each other, results are reported as the dimensional heat transfer coefficient with units W/m^2K. Future chapters will provide Nusselt number results for comparison to other studies.

At first glance, Figure 4.10 from the Impulse method and Figure 4.13 from the thin-foil heater method look nothing alike. The heat transfer coefficients from the thin-foil heater method around the edges are greater than those using the Impulse method. Also the heat transfer coefficients in the central portion of the blade from the thin-foil heater method are less than those using the Impulse method. However, when considering the assumptions that are made when employing the thin-foil heater method, the different results between the two analyses can possibly be explained. The major assumptions behind the thin-foil heater are:

1. Very low conductive material and no 3-D effects on the edges
2. Constant/uniform heat flux applied throughout the blade tip

When testing the thin-foil heater, some of the energy is conducting into the material, as to be expected. However, due to the complexity of the solution, there are 3-D conduction effects that are not considered when analysing the data. The trailing edge in Figure 4.13 shows very high heat transfer coefficient results, indicating that there is a large amount of energy that is not transferred via convection. This indicates that more energy is being conducted over the edges and laterally than originally assumed with the thin-foil heater method.

The heat flux provided by the power supply is also assumed to be uniform over the blade tip. This assumption requires that each part of the blade tip has an equivalent amount of resistance. It is impossible to perfectly design a foil heater that provides equal amounts of resistance at each discrete point on the blade tip. As evident from Figure 4.11, obviously no current is conducted through the gold-coloured non-conducting lines, and so there will not be any heat flux over these areas.

Even more importantly, as seen in Figure 4.11, the width of the copper conducting lines around the border are greater than the width of the conducting lines in the centre portion of the tip. The greater width of the copper means a greater resistance, indicating that the power provided to the edges is overestimated. Therefore the heat transfer coefficient around the edges is overestimated. It is just the opposite with the centre portion of the blade. The copper lines are less wide, which means that the resistance is lower than estimated, indicating that the power provided to the central portion of the tip is underestimated. Therefore the heat transfer coefficient provided to the central portion of the blade tip is underestimated. Based on these results, the h results using the thin-foil heater is invalid.

As these results do not compare well qualitatively or quantitatively, and since the assumptions proved to be invalid, the thin-foil heater results were removed from consideration for the heat transfer qualification study.

4.6.2 Adiabatic Wall Temperature

Based on the thin-foil heater results, as the h results are invalid, so are the T_{ad} results.

When comparing the Impulse method to the quasi-adiabatic method, Figures 4.10 and 4.14 look very similar. The temperature difference is, on average, only 2 K different. This is also observed in Figure 4.15. The only difference is the amount of time it takes to achieve the steady state. If the experiment is carried out longer, it is likely that the difference would be smaller.

4.7 Uncertainty Analysis

A measurement uncertainty analysis was performed for the different methods tested and for a few blade tip locations. The experimental uncertainty can have many sources including, but not limited to, material properties, measured wall temperature and mainstream temperature. The uncertainty in measured wall temperature is a function of the uncertainty in thermocouple location relative to the IR pixels and the

calibration of the IR camera. It is determined using the method of partial derivatives described by Kline and McClintock (1953) (see Equation 4.10)

$$\delta_{T_w} = \sqrt{\left(\frac{\partial T}{\partial G}\delta G\right)^2 + \left(\frac{\partial T}{\partial G}\frac{\partial G}{\partial L}\delta L\right)^2 + \Big(\text{SEE}\Big)^2 + \Big(\text{std}(T_w)\Big)^2} \tag{4.10}$$

where δ_{T_w} is the uncertainty in wall temperature, T is the thermocouple temperature, G is the greyscale value and L is the location. The uncertainty in T_w with respect to the greyscale relates to the calibration coefficients. "SEE" is the standard error of estimate which is used to calculate the error from performing a regression analysis and is defined by Coleman and Steele (1989) as

$$\text{SEE} = \left\{\frac{\sum_{i=1}^{N}[Y_i - (aX_i + b)]^2}{N-2}\right\}^{\frac{1}{2}} \tag{4.11}$$

In Equation 4.11, Y corresponds to the thermocouple reading, X corresponds to the Greyscale reading, and a and b are the calibration coefficients.

A jitter analysis described by Moffat (1988) is performed to determine the uncertainty in h by estimating the partial derivatives using finite difference approximations. First, baseline h and T_{ad} are determined for a set of data and for a particular method. Then the contribution of the uncertainty in material properties (i.e. thermal product) to the uncertainty in h and T_{ad} is calculated by determining h and T_{ad} assuming the maximum value of the thermal product. For example, as the thermal product is $\sqrt{\rho C_p k} = 627 \pm 33\,\text{W}\cdot\sqrt{\text{sec}}/\text{m}^2\cdot\text{K}$, then $\sqrt{\rho C_p k} = 627\,\text{W}\cdot\sqrt{\text{sec}}/\text{m}^2\cdot\text{K}$ is used for the baseline and $\sqrt{\rho C_p k} = 660\,\text{W}\cdot\sqrt{\text{sec}}/\text{m}^2\cdot\text{K}$ was used for the maximum value of uncertainty. The change in h with respect to this change in $\sqrt{\rho C_p k}$ approximates the partial derivative $\partial h/\partial\sqrt{\rho C_p k}$. This approach is then used for the other sources of uncertainty and the overall uncertainty was calculated using the method of partial derivatives.

For all methods used, the uncertainty in the material properties (thermal product) and the measured wall temperature are the highest contributors to the uncertainty in heat transfer coefficient. The uncertainty in measured wall temperature is the highest contributor to the uncertainty in the adiabatic wall temperature. Table 4.3 provides

Table 4.3: Measurement uncertainty for 4 different heat transfer measurement techniques (0* means that the value is negligible)

Method → / Measurement ↓	Idealised process	Finite-difference	Impulse method	Quasi-adibatic
Heat transfer coefficient				
Material property	6.4%	6.4%	6.4%	N/A
Measured wall temperature	11.9%	10.0%	7.1%	N/A
Mainstream temperature	N/A	0*	0*	N/A
Overall uncertainty	13.5%	11.8%	9.5%	N/A
Adiabatic wall temperature				
Material property	0*	0*	0*	N/A
Measured wall temperature	1.0 K	1.4 K	1.2 K	1.0 K
Mainstream temperature	N/A	0*	0*	N/A
Overall uncertainty	1.0 K	1.4 K	1.2 K	1.0 K

the maximum measurement uncertainty for heat transfer coefficients and adiabatic wall temperatures for a few blade tip locations. The quasi-adiabatic approach shows uncertainty only in adiabatic wall temperature. Since it is a quasi-steady approach, the true value of the adiabatic wall temperature is likely 2–3 K higher than the reported value for the quasi-adiabatic approach. This difference is not a measurement uncertainty and is not reflected in Table 4.3. Note that the uncertainty in time t and initial temperature T_i are not included in the table, which would increase the uncertainty of the idealised process.

The preceding discussion focuses on measurement uncertainty. However, there are other sources of uncertainty that are possibly more significant than the measurement uncertainties. One source is the effects of two-dimensionality on the blade tip. Section 2.4 includes a discussion of the studies that have considered the uncertainty from neglecting lateral conduction. For their experimental setup, Vedula et al. (1988) measured a maximum error in h of 3.5 percent. Lin and Wang (2002) computationally showed that lateral conduction could result in errors in h of 12 percent. As will be addressed in Chapter 8, the effect of the corner conduction, close to the blade tip edges, can be even more significant. Also, though the flow is largely constant, the

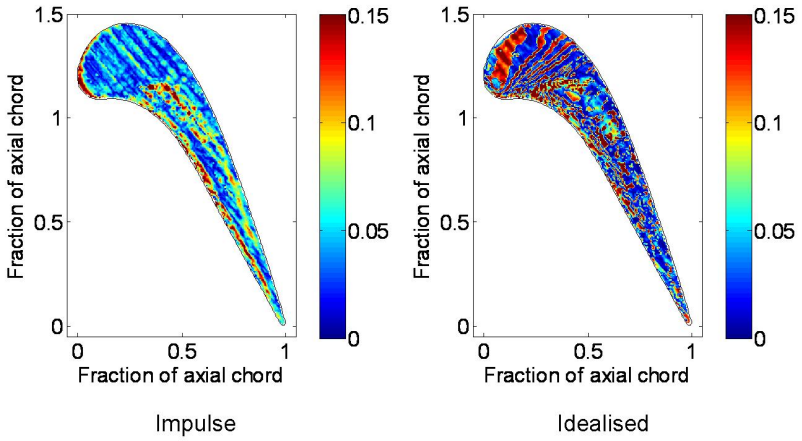

Figure 4.16: Heat transfer technique repeatability indicating fraction difference between heat transfer coefficient for 3 experimental runs (local variation divided by area-weighted mean value) for impulse method and idealised process

highest uncertainty is likely due to the small changes in experimental flow conditions during a test run (with the opening and closing of the air supply valve) and from run to run.

Another way to compare the different methods is to determine the consistency (or repeatability) of the heat transfer results. First, the Impulse method is very consistent. Figure 4.16 shows a contour of the local deviation of the heat transfer coefficient normalised by the area-averaged heat transfer coefficient for three different test runs using the Impulse method.

Note that the variation is determined using MATLAB's standard deviation function "*std*", and is not meant to provide a statistical value, only to relate three different runs. The figure shows very little variation between test runs for a majority of the blade. There are locations where the variation is higher, as would be expected for the edges and the trailing edge. Most of the local variations are within 6 percent of the blade mean heat transfer coefficient, though local variations of 15 percent occur on the edges and at the trailing edge. The area-weighted average of the normalised variation is less than 6 percent.

As both heat flux reconstruction methods use similar numerical approximations for the heat flux reconstruction, both have similar variation trends. However, the

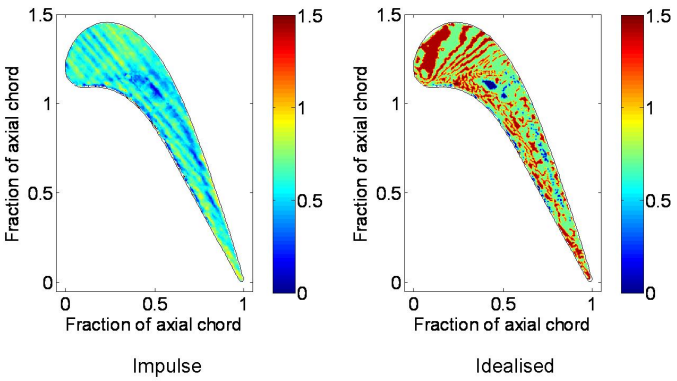

Figure 4.17: Heat transfer technique repeatability indicating variation of adiabatic wall temperature [K] for 3 experimental runs for impulse method and idealised process

idealised process method shows less repeatability, as demonstrated in Figure 4.16. The leading edge observes local variations within 15 percent of the area-weighted mean, whereas the trailing edges and other tip edges are within 10 percent. The area-weighted average normalised variation is less than 9 percent.

Also, the variation of the adiabatic wall temperature for the three test runs is less than 1 K for the Impulse method as observed in Figure 4.17. The variation of the adiabatic wall temperature for the Idealised process method is less than 1.5 K, as seen in Figure 4.17. Some parts of the blade have less of a variation, but the unevenness across the tip is much greater than for the Impulse method. For the three transient methods, the Impulse method observes a consistent repeatability for a fraction of the computational cost.

Finally, an attempt was made to reduce the uncertainty by applying the superposition principle to remove the heat flux caused by the initial compression preheating of the blade. A separate run in which the heater mesh was not employed was initially used to determine the unheated heat flux. This separate run, however, has its own run-to-run uncertainty. When using the same run and subtracting the unheated heat flux, there was less uncertainty compared to using a second run. However, it did not change the uncertainty in the heat transfer coefficient results. When considering the convective heat transfer equation, a change in a constant heat flux over time does

not change the slope (h), rather only the adiabatic wall temperature changes. This change is on the order of 0.25–0.5°C, depending on the location on the blade tip. This approach was later abandoned as it did not qualitatively change the results (and only slightly changed the quantitative results).

4.8 Summary

In this chapter, the heat transfer experimental setup was described. The present study uses the transient infrared thermography technique to obtain spatially-resolved heat transfer measurements on the tip and sidewalls. The IR camera and ZnSe window were described and the IR calibration showed a linear relationship between the IR greyscale value and surface-mounted thermocouples. The camera's distance to the object and relative angle to the object was considered and the effect on heat transfer results is negligible.

The present study then compared several different techniques for measurement of spatially-resolved distributions of surface heat transfer coefficient and adiabatic surface temperature under engine-realistic aerodynamic flow conditions.

Overall, the results indicate that transient IR thermography method is well suited to obtain detailed, spatially-resolved surface heat transfer coefficients and adiabatic wall temperatures for blade tips under transonic conditions in a linear cascade environment, particularly when the Impulse method is employed to reconstruct variations of heat flux with surface temperature. Qualitative results are similar among the different techniques, within variations in heat transfer coefficient of about 15 percent between them. However, the heat flux reconstruction methods are most consistent and have the least uncertainty, with pixel-to-pixel differences of less than 10 percent. The heat flux reconstruction approach using the Impulse method has the lowest measurement uncertainty, is the most consistent and is the most computationally efficient. Finally, all tests which employ infrared thermography use this technique for measurements on flat surfaces, which are effectively bounded by a semi-infinite solid. As such, infrared thermography is a most suitable choice for such thermal measurements.

Chapter 5

Flat Tip Heat Transfer

5.1 Introduction

This chapter provides heat transfer results for a flat tip blade. This blade is the linearised blading profile taken from 90 percent span of the Environmentally Friendly Engine (EFE) blade design. The flat tip blade serves as a baseline for winglet testing. As the flat tip has no grooves or recesses, it is an ideal blade tip for heat transfer qualification testing (see Chapter 4). Both uncooled and cooled EFE winglet heat transfer results are presented in Chapter 6.

In the present chapter, the effects of tip gap clearance are experimentally investigated at the operating condition of the normal design of the EFE blade (see operating conditions in Table 3.2). Five different tip gap clearances are considered, 0.4, 0.9, 1.3, 1.8 and 2.2 percent of the EFE engine-equivalent blade span (1.0, 2.0, 3.0, 4.0 and 5.0 percent of the axial chord). Table 5.1 shows the relationship between the tip gap (g), axial chord (C_{ax}), true chord (C_{true}), and blade span (both the height of the HSLC test section and the actual EFE engine-equivalent blade span). The axial chord of the blade tip under investigation is 47.72 mm and is scaled at 1.9 times the axial chord of the actual EFE blade tip. The engine-equivalent blade span is 106.78 mm. The other blade measurements are listed in Table 3.1. Throughout the rest of this thesis, tip gaps are referred to by their relationship to the EFE engine-equivalent blade span. Note that the tip gap percentages of 0.4, 0.9 and 1.3 percent are rounded up to 0.5, 1.0 and 1.5 percent in the present author's other publications.

Table 5.1: Relationship between tip gap and blade geometry

	Gap (g) [mm]	g/C_{ax} %	g/C_{true} %	g/HSLC span %	g/EFE span %
Gap #1	0.475	1.00	0.69	0.66	0.44
Gap #2	0.950	2.00	1.39	1.32	0.89
Gap #3	1.425	3.00	2.08	1.98	1.33
Gap #4	1.900	3.98	2.42	2.64	1.78
Gap #5	2.375	4.98	3.02	3.31	2.22

Detailed, spatially-resolved Nusselt numbers on the blade tip and near-tip region are experimentally determined. Experimental results are limited to blades in a stationary linear cascade. Results and a discussion of results are presented for different tip gaps under engine-representative experimental conditions. First, however, heat transfer results are compared for high-speed and low-speed (near-incompressible) flows.

5.2 Low-Speed Versus High-Speed Conditions

Tests were originally conducted on the flat tip under transonic conditions using the FLIR A20M IR camera. The results did not appear to agree with results in the open literature (for example, see Figure 2.4). This section begins by addressing the aerodynamic flow conditions for the low-speed tests. It then concludes by comparing the high-speed and low-speed results.

5.2.1 Low-Speed Aerodynamic Conditions

A tip gap study was performed running the wind tunnel at a low-speed condition, with the blade tip under near-incompressible flow conditions. Table 5.2 lists the inlet and exit flow conditions for the low-speed test.

Figure 5.1 presents the Mach number and pressure coefficient distributions, respectively, as a fraction of the axial chord. The definition of pressure coefficient is the same as that which was used for the experimental setup in Chapter 3 (see Equation 3.2). The peak Mach number on the blade tip suction side during this test is

Table 5.2: Low-speed inlet and exit flow conditions (all pressures are absolute)

Inlet total pressure	106 kPa (15.3 psi)
Inlet static pressure	105 kPa (15.2 psi)
Inlet Mach number	0.13
Inlet velocity	43.3 m/s
Inlet Reynolds number	0.15×10^6
Mass flow rate	0.79 kg/s
Exit static pressure	101 kPa (14.6 psi)
Exit Mach number	0.27
Exit velocity	92.0 m/s
Exit Reynolds number	0.35×10^6

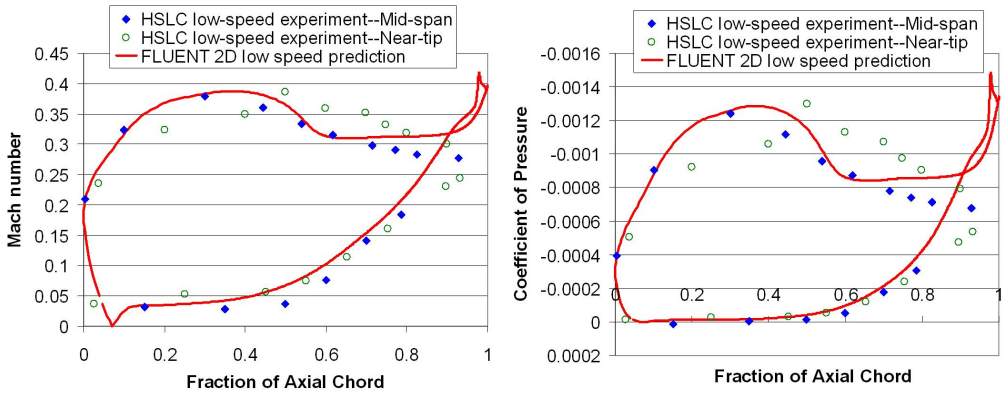

Figure 5.1: Mach number and Coefficient of Pressure distributions around the blade (CFD courtesy of Dr Zhang (Zhang, 2010))

under 0.4. The Mach number and pressure coefficient distributions demonstrate that this blade is not designed for low-speed conditions. The blade loading under nominal conditions was presented in Figure 3.23. The blade is not properly loaded on the suction surface as evidenced by an adverse pressure gradient at 50 percent of axial chord.

5.2.2 High-Speed Versus Low-Speed Heat Transfer

A tip gap survey under high-speed and low-speed conditions was investigated. Tip gaps of 0.9, 1.3, 1.8 and 2.2 percent of blade span were considered. The trends were consistent for all tip gaps, but only the 1.3 percent tip gap results are compared

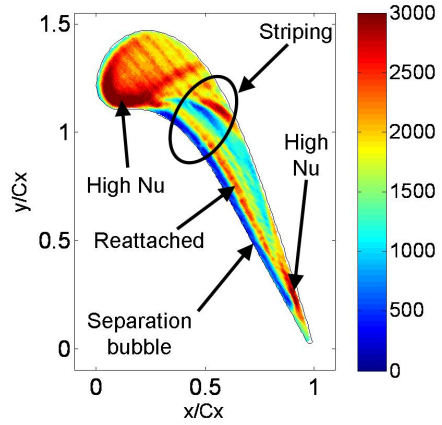

Figure 5.2: Nusselt number distributions on the blade tip for 2.2% tip gap under transonic conditions

in this section. Surface wall temperature measurements were taken using the FLIR A20M IR camera and heat transfer coefficients and adiabatic wall temperatures were determined using the Impulse method described in Chapter 4. Nusselt number results were determined using Equation 4.9, where h is the heat transfer coefficient, C_{ax} is the EFE blade axial chord and k_{air} is the conductivity of air based on the local surface adiabatic wall temperature.

Though the 2.2 percent tip gap is not engine-representative for the EFE design, the characteristics of the heat transfer results are most clearly observed for the 2.2 percent tip gap, shown in Figure 5.2. In this figure, higher heat transfer is seen at the leading edge and the frontal part of the blade (first 30 percent of axial chord) than compared to the aft part of the blade (40–90 percent of axial chord). There is also a high heat transfer region on the pressure-side edge near the trailing edge. This high heat transfer region is also very difficult to cool in an engine-environment. There is a region of low Nusselt number along the pressure-side edge due to the presence of a separation bubble. Just after the separation bubble, there is a region of high Nusselt number where the over-tip leakage (OTL) flow reattaches. Finally, there is a striped region of repeating high and low heat transfer at the 40–90 percent axial chord location, but the 50 percent location is most clearly observed.

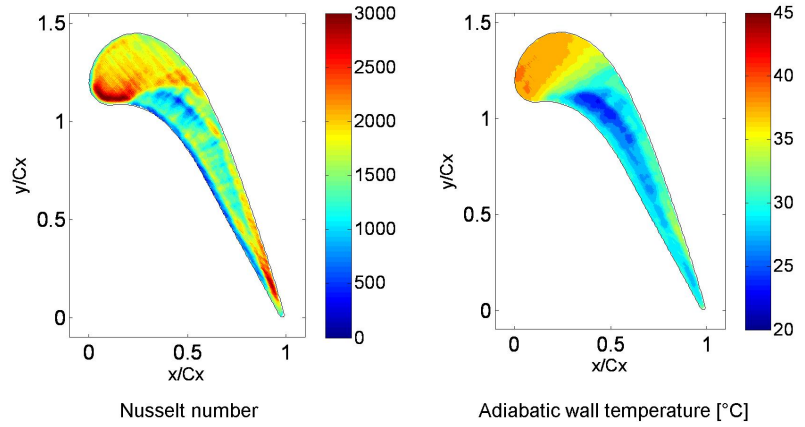

Figure 5.3: Nusselt number and adiabatic wall temperature distributions on the blade tip for 1.3% tip gap under transonic conditions

The 1.3 percent tip gap shows similar results. Figure 5.3 presents the contours of the tip Nusselt number and adiabatic wall temperature for high-speed, transonic flow conditions. The high and low heat transfer regions as well as the striping are all consistent with the 2.2 percent tip gap.

When compared to low-speed studies, the high-speed results are very different. For high-subsonic (though not transonic) flow conditions, Bunker et al. (2000) reported a "*sweet spot*" of low heat transfer over the thickest part of the blade tip and relatively high heat transfer toward the trailing edge, just the opposite of what is observed under transonic conditions. Under low-speed, near-incompressible conditions, Newton et al. (2006) and Krishnababu et al. (2007b) both observed that there is low heat transfer toward the front part of the blade and that the highest heat transfer on the tip is at the flow reattachment region, which is close to and runs parallel to the suction-side edge.

Results similar to those of Krishnababu et al. (2007b) (see Figure 2.4) were observed when testing the HSLC under low-speed conditions. Figure 5.4 presents the unscaled contours of the tip Nusselt number and adiabatic wall temperature for low-speed, near-incompressible flow conditions..

The opposite trend between high-speed and low-speed testing is also seen when comparing the circumferentially-averaged Nusselt numbers, as shown in Figure 5.5.

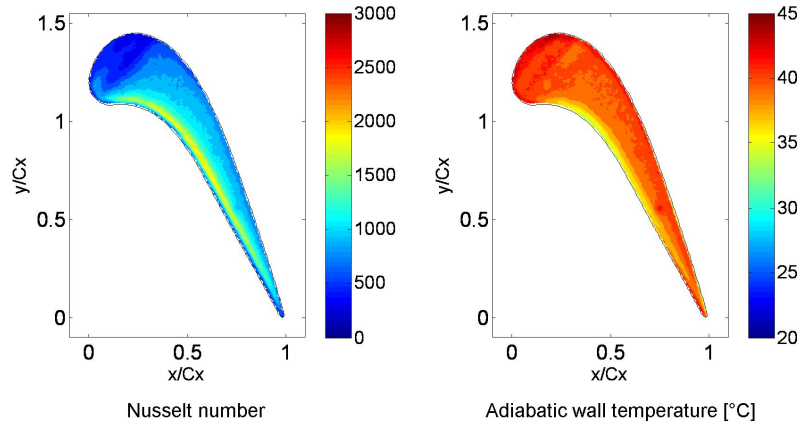

Figure 5.4: Nusselt number and adiabatic wall temperature distributions on the blade tip for 1.3% tip gap under low-speed conditions

Note that the Reynolds number measured during transonic testing (see Table 3.2 in Section 3.4.2) is nearly four times greater than the Reynolds number measuring during low-speed testing (see Table 5.2). The low-speed heat transfer results have been scaled-up by using Reynolds scaling for comparison purposes. For this comparison, the Reynolds scaling for a flat plate with a laminar boundary layer is used as given in Equation 5.1 ((Lakshminarayana, 1996). The laminar boundary layer scaling produced Nusselt numbers closer in magnitude to the high-speed Nusselt numbers. However, the tip is likely more turbulent than laminar, but vortices over the tip make the calculation even more difficult. Therefore, it is emphasised that the purpose of scaling the results is not to determine the right magnitudes, but the trends.

$$Nu(x) = 0.332(Re_x)^{1/2} PR^{1/3} \tag{5.1}$$

In Figure 5.5, the high-speed results show the highest heat transfer in the first 20 percent of axial chord as well as the final 10 percent of axial chord. From 20–80 percent of axial chord, the Nusselt number continually decreases. The low-speed results, on the other hand, shows low heat transfer at the leading edge, with continually increasing Nusselt numbers until 90 percent of axial chord, when the Nusselt number sharply decreases.

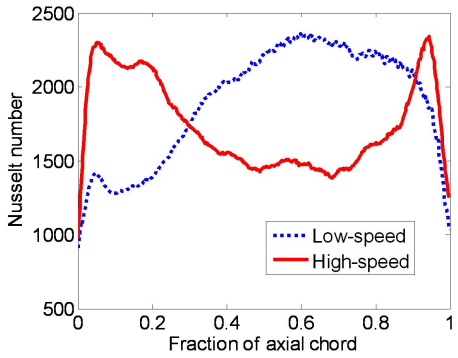

Figure 5.5: Circumferentially-averaged Nusselt number distributions on the blade tip for 1.3% tip gap

The only similarity between the high-speed and low-speed results in the present study are the fact that Nusselt number increases at the leading edge (but only for the first 5 percent of axial chord for the low-speed case) and decreases at the trailing edge (for the final 10 percent of axial chord).

These trends are consistent with the results for the 0.9, 1.8 and 2.2 percent tip gaps. From these results, it is concluded that low-speed testing cannot simply be scaled up. Even with Reynolds number scaling, the heat transfer trends are completely opposite to each other. Although the load (pressure distributions) are not matched, the loading distribution is not expected to make a qualitative difference.

5.3 High-Speed Results

Having compared the high-speed and low-speed results for an unaltered blade profile (using the same test setup with the exception of the inlet and exit flow conditions), a new IR camera was acquired and used for all other experimental heat transfer results, to include flat tip heat transfer in the present chapter and winglet heat transfer in Chapter 6.

It is acknowledged that the results in the present section are slightly different quantitatively (though not qualitatively) than the high-speed results reported in the previous section. There are likely two possibilities for this difference. Either the camera is able to better capture the surface temperatures with its improved sensor

resolution and Bit count, or the flow over the tip is slightly different due to a slightly different blade tip geometry (slightly different shape, roughness and painting).

The remainder of this chapter examines flat tip heat transfer for blade tips under the transonic conditions addressed in Section 3.4.2 using the new FLIR A325 IR camera. First, spatially-resolved heat transfer results are obtained on the tip. Second, spatially-resolved heat transfer results are presented for the sidewalls at the near-tip region.

5.3.1 Tip Gap Survey for Tip Heat Transfer

This section provides a tip gap survey of the tip heat transfer for the flat tip. Tip surface Nusselt number distributions are obtained from experiments for three different tip gaps of 0.4, 0.9 and 1.3 percent of span. Figure 5.6 displays the tip Nusselt number for the 1.3 percent tip gap. Like Figure 5.2, Figure 5.6 shows some of the same major characteristics. The one difference is the region affected by the fast-response thermocouple, circled in the figure. In the lower right part of the circle is a low heat transfer region where the thermocouple penetrates the tip surface, surrounded by glue. The top left part of the circle is where the thermocouple junction is placed on the tip surface. Besides the region affected by the thermocouple, the major characteristics are the same, such as the higher heat transfer at the leading edge, the frontal part of the blade and on the suction-side trailing edge. The region of low Nusselt number along the pressure-side edge due to the presence of a separation bubble is still present. Just after the separation bubble, the region of high Nusselt number where the OTL flow reattaches is still observed. Finally, the striped region of repeating high and low heat transfer at the 40–90 percent axial chord location continues to be present.

Presented in Figure 5.7 are the tip surface Nusselt number distributions obtained from experiments for the three different tip gaps of 0.4, 0.9 and 1.3 percent of span. For all three tip clearances, the Nusselt number decreases as the tip gap is reduced for most of the blade tip surface. For all tip gaps investigated, the Nusselt number is higher near the leading edge region of the tip surface and relatively low on the middle and rear parts of the blade tip. A small "*hot spot*" is present which is located very

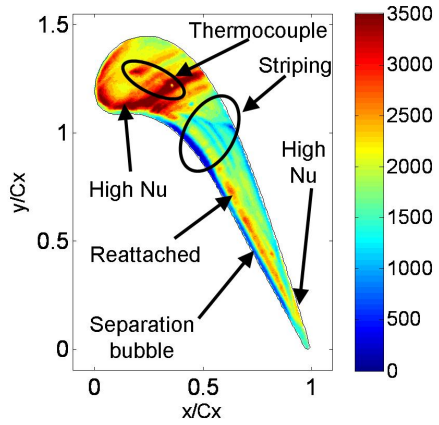

Figure 5.6: Nusselt number distributions on the blade tip for 1.3% tip gap under transonic conditions

near the trailing edge portion of the tip. Note that a linear interpolation is used to rotate the blade tip figure from the camera viewing angle. An over-interpolation is likely the cause of the camberline-wise strips, which are highlighted in the figure.

Circumferentially-averaged Nusselt number variations along the axial chord are presented in Figure 5.8. In general, as the tip gap increases, the tip Nusselt number increases, especially for the first 75 percent of chord. It is likely that the high heat transfer on the pressure side region of the tip is caused by flow reattachment. As the tip gap increases, the location of the high heat transfer appears to move further from the pressure side edge. All tip gaps also show a low heat transfer region in crown region and the trailing edge.

5.3.2 Tip Mach Number Estimation

An analytic study of the adiabatic wall (recovery) temperature has been performed to determine the tip Mach number distribution. The definition of recovery factor (see Equation 5.2) is used along with the compressible flow equation relating total to static temperature (see Equation 5.3) to calculate the local tip Mach number.

$$r = \frac{T_{ad} - T_\infty}{T_t - T_\infty} \tag{5.2}$$

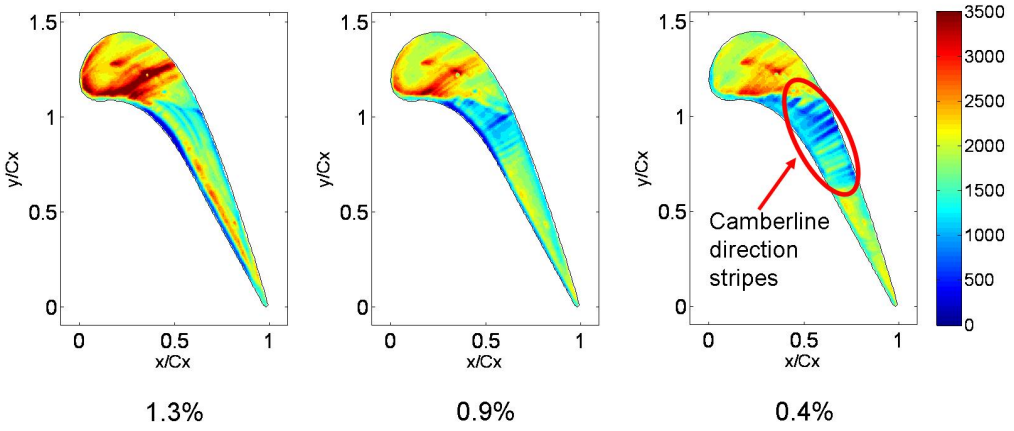

Figure 5.7: Tip Nusselt number distributions on the blade tip for 0.4, 0.9 and 1.3% tip clearances (note the camberline stripes that are likely caused by over-interpolation)

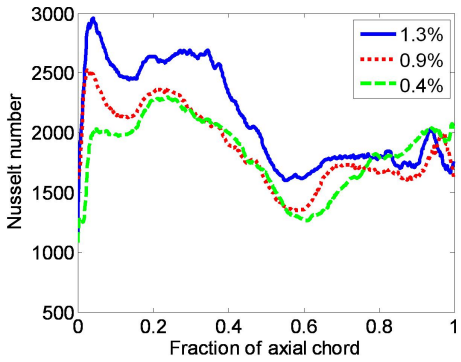

Figure 5.8: Circumferentially-averaged Nusselt number distributions on the blade tip for the three tip gaps investigated

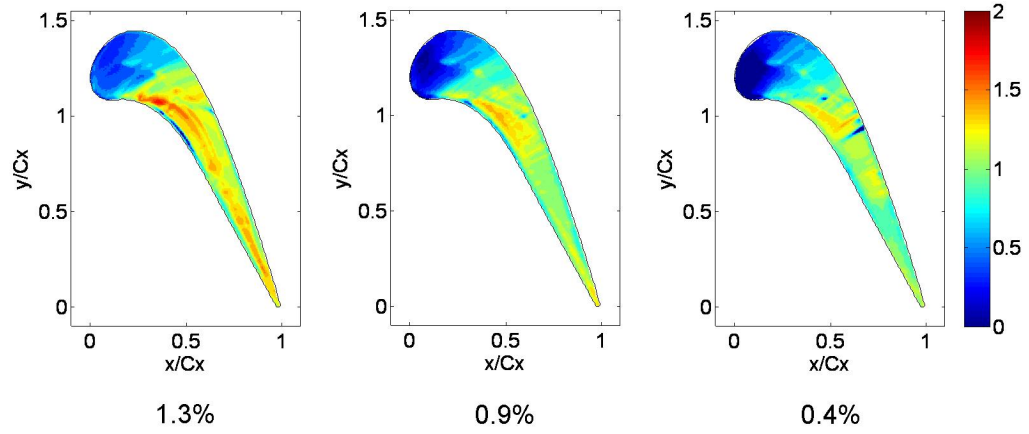

Figure 5.9: Recovery temperature-derived Mach number distributions on the blade tip for 0.4, 0.9 and 1.3% tip clearances (recovery factor=0.86)

In Equation 5.2, r is the recovery factor, T_t is the inlet total temperature, T_∞ is the mainstream static temperature and T_{ad} is the adiabatic wall temperature.

$$\frac{T_t}{T_\infty} = 1 + \frac{\gamma - 1}{2} M^2 \tag{5.3}$$

According to Holman (2002), an estimate for the recovery factor is related to the Prandtl number (Pr), where $r = Pr^{1/2}$ for laminar flow and $r = Pr^{1/3}$ for turbulent flow. Since air is used, the recovery factor is approximately 0.83 to 0.89, depending on the flow turbulence. Of course, the recovery factor will certainly vary over the tip with changing Mach number and separated flow and may not be limited to the range of 0.83–0.89. However, for the value for the recovery factor is used, the flow over the tip trailing edge is supersonic (see Section 5.4 for computationally-determined tip Mach number). Mach number contours shown in Figure 5.9 assume a recovery factor of 0.86.

It is evident from Figure 5.9 that the flow over the leading edge and crown region is subsonic and therefore not choked. The Nusselt number in this region is generally lower, except at the leading edge. As for the trailing edge region, the flow is supersonic and therefore choked.

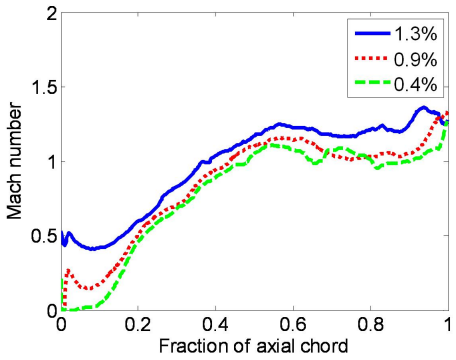

Figure 5.10: Circumferentially-averaged recovery temperature-derived tip Mach numbers on the blade tip for 0.4, 0.9 and 1.3% tip clearances (recovery factor=0.86)

Figure 5.10 shows the circumferentially-averaged Mach number. The tip is choked for 50–100 percent of chord. Since the mass flow through this region is choked for each tip gap, the trailing edge Nusselt number does not appear to vary as much. The Mach number does show increases for larger tip gaps.

As for the frontal region, what could be considered a "*sweet spot*" of low heat transfer observed by Bunker et al. (2000) appears to be observed at the leading edge closer to the suction side, though the magnitude is still high.

5.3.3 Tip Gap Survey for Sidewall Heat Transfer

Following the results from the blade tip, the tip sidewalls at the near-tip region are now addressed. Presented in this section are near-tip blade surface Nusselt number and Mach number distributions obtained from experiments for the same tip clearances of 0.4, 0.9 and 1.3 percent of span. Contours of Nusselt number and Mach number are presented for both the suction-side and pressure-side sidewalls.

5.3.3.1 Suction-Side Heat Transfer

Spatially-resolved Nusselt numbers on the suction side near the tip region are presented in Figure 5.11. Based on the camera viewing angle, the suction side is observable for 35–100 percent of axial chord (see Figure 4.3). These experimentally-measured data generally show that Nusselt number values decrease as tip gap in-

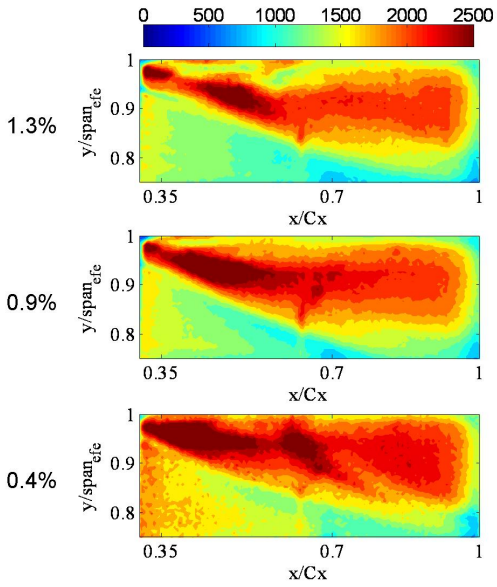

Figure 5.11: Nusselt number distributions for 0.4, 0.9 and 1.3% tip clearances (Suction Side)

creases. As the tip gap decreases, the heat transfer on the suction side increases both in magnitude as well as the amount of the surface that is affected by the over-tip leakage flow.

The increase in suction side Nusselt number with a decrease in tip clearance is also seen in the circumferentially-averaged Nusselt numbers shown in Figure 5.12. Except from 95–100 percent of chord, the averaged Nusselt number consistently increases with a decrease in tip gap.

An examination of the analytically-determined Mach number distribution is shown in Figure 5.13. It is reasonably assumed that part of the suction side is laminar and part is turbulent. However, since the location of the transition region is unknown, the same recovery factor assumed for the tip is used in the present analysis. The Mach number magnitude on the suction side close to the tip decreases with the decrease in tip clearance.

For all tip clearances, the suction-side Mach number is supersonic, which is also evident from the circumferentially-averaged Mach numbers as shown in Figure 5.14. For the 1.3 percent tip gap, the Mach number is lower near 35–50 percent of chord

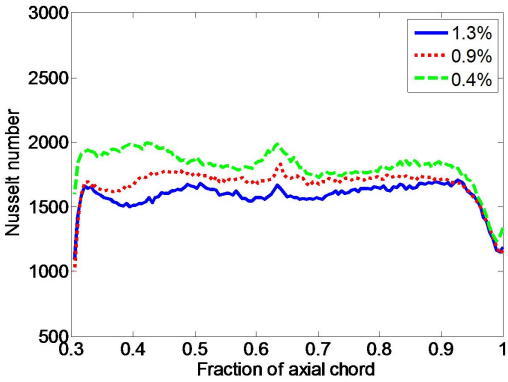

Figure 5.12: Circumferentially-averaged Nusselt number for 0.4, 0.9 and 1.3% tip clearances (Suction Side)

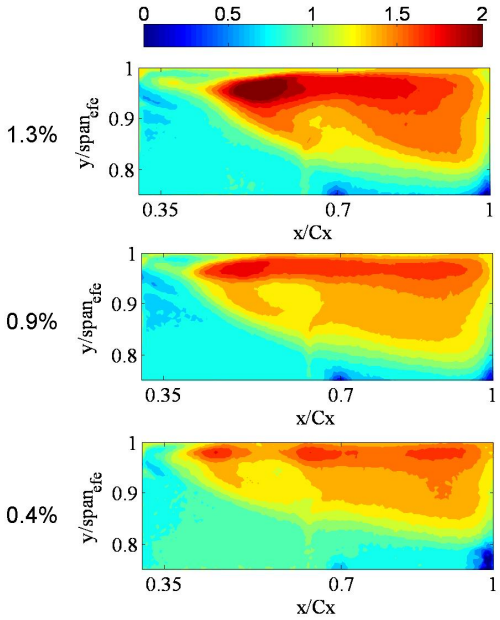

Figure 5.13: Recovery temperature-derived Mach number distributions for 0.4, 0.9 and 1.3% tip clearances (recovery factor=0.86) (Suction Side)

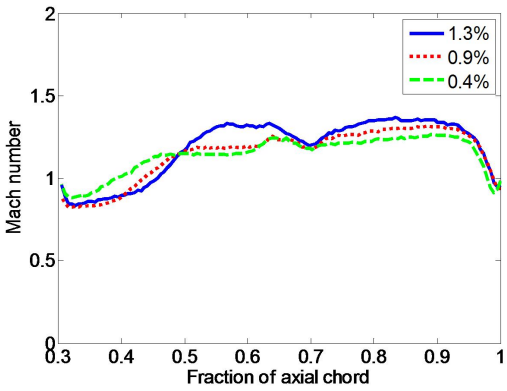

Figure 5.14: Circumferentially-averaged recovery temperature-derived Mach number for 0.4, 0.9 and 1.3% tip clearances (recovery factor=0.86) (Suction Side)

compared to the smaller tip clearances. This may indicate where the over-tip leakage flow initially emerges over the tip. For the remainder of the suction side, the 1.3 percent tip gap has a higher average Mach number. As tip gap decreases, the average Mach number increases from 30–50 percent of chord, but decreases from 50–100 percent of chord.

5.3.3.2 Pressure-Side Heat Transfer

Spatially-resolved Nusselt numbers on the pressure side near the tip region are presented in Figure 5.15. Part of the crown region on the suction side is observed by the camera (for $x/C_{ax} < 0$). There is also a region where the camera cannot see the pressure side (for x/C_{ax} =0). This is clearly seen in sharp axial-chord-wise gradient running along the blade span (as indicated in the figure). Also, the relative view of the blade appears as if the tip radius decreases towards the trailing edge. This is because the camera viewing angle is about 30° from normal to the blade surface. In this section, all data is captured as a rectangle. It is emphasised that there are two regions of results that are not surfaces. The first is the tip edge for x/C_{ax} between 0.25 and 1. A sharp gradient is observed between the tip edge and the tip gap. The second region is the trailing edge, where the camera is unable to resolve the precise location of the trailing edge (indicated on figure). It is unlikely that the surface Nus-

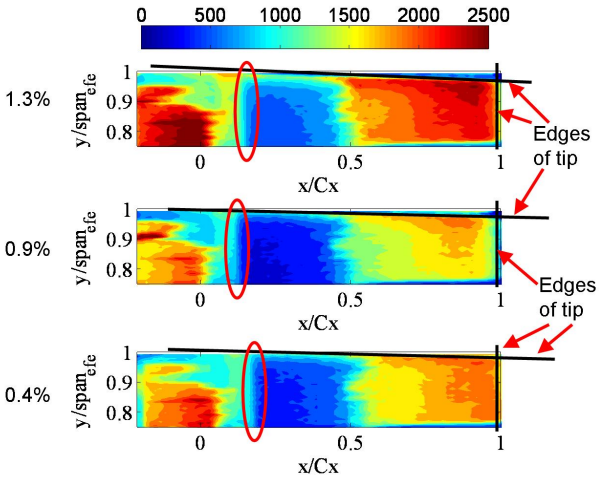

Figure 5.15: Nusselt number distributions for 0.4, 0.9 and 1.3% tip clearances (Pressure Side)

selt number continues to increase with x/C_{ax} then suddenly decreases at the trailing edge.

Overall, the Nusselt numbers increase with x/C_{ax} as the flow advects in the axial direction. Values also increase as the radial location increases toward the trailing edge. The peak Nusselt numbers are present near the tip trailing edge downstream corner. This is important because, in actual applications, this is normally a region of the blade that is most susceptible to high thermal loading and excessive surface material temperatures, even when significant amounts of cooling are employed.

The pressure side Nusselt number is higher for the 1.3 percent case than the smaller tip clearances. As for the two smaller tip clearances, the Nusselt number appears to be higher for the smallest tip clearance, which does not agree with the trend between the two largest tip clearances. It is unknown why this trend occurs, however, the trend towards increasing Nusselt number with an increase in x/C_{ax} and with an increase in radial location is consistent for all tip clearances. This trend is also seen in the circumferentially-averaged Nusselt numbers, as shown in Figure 5.16. The averaged Nusselt number consistently increases for $0.2 < C_{ax} < 0.95$.

An examination of the analytically-determined Mach number distribution is shown in Figure 5.17. The same recovery factor assumed for the tip is used on the pressure

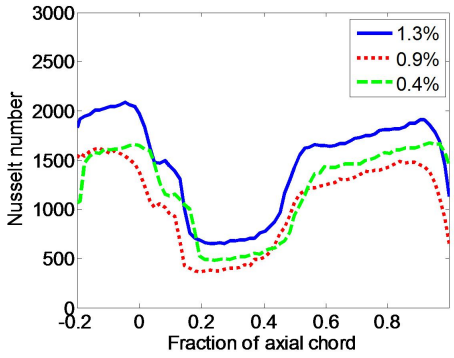

Figure 5.16: Circumferentially-averaged Nusselt number for 0.4, 0.9 and 1.3% tip clearances (Pressure Side)

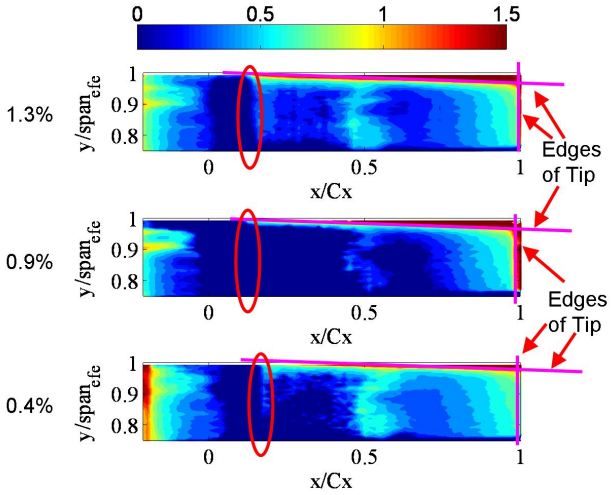

Figure 5.17: Recovery temperature-derived Mach number distributions for 0.4, 0.9 and 1.3% tip clearances (recovery factor=0.86) (Pressure Side)

side as well, though it is believed that the boundary layer may be laminar. Like the Nusselt number distribution, the Mach number increases for both increasing x/C_{ax} as well as blade radius. A surface mounted thermocouple may be the reason for the increase then decrease in Mach number at approximately $x/C_{ax} = 0.5$.

For all tip clearances, the pressure side Mach number is subsonic, which is also evident from the circumferentially-averaged Mach numbers as shown in Figure 5.18. The large increase at the trailing edge is not a result of the surface Mach number but the inability for the camera to resolve those locations. The sharp increase and

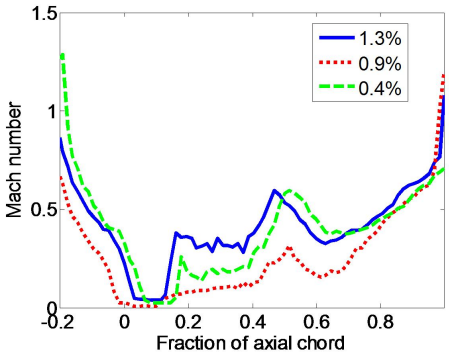

Figure 5.18: Circumferentially-averaged recovery temperature-derived Mach number for 0.4, 0.9 and 1.3% tip clearances (recovery factor=0.86) (Pressure Side)

decrease in Nusselt number for x/C_{ax} from 0.4 to 0.6 is a result of a surface-mounted thermocouple.

5.4 Flat Tip Heat Transfer Computational Results

This section provides work of the HSLC research group. The computational study was performed by Dr Zhang while all members of the research group jointly analysed and discussed the results. These results were presented in Zhang et al. (2010a) and are provided here to not only show agreement with the experimental results, but also to help understand some of the flow phenomena.

A comparison between experimental and computational flat tip heat transfer results provided in Figure 5.19 shows very good agreement. The agreement not only includes the overall variations but the detailed local variations as well. These results were used to validate the CFD modelling effort.

The predicted local Mach number for the 0.9 percent tip gap (calculated halfway between the tip and casing wall surfaces) is shown in Figure 5.20. This figure shows that the tip is largely supersonic. These results agree well qualitatively and are very close quantitatively with the analytical Mach number results in Figure 5.9.

Zhang et al. (2010b) described the relationship between the heat transfer and the shock structure that exists over the tip. Figure 5.21 shows a flat tip with 0.9 percent

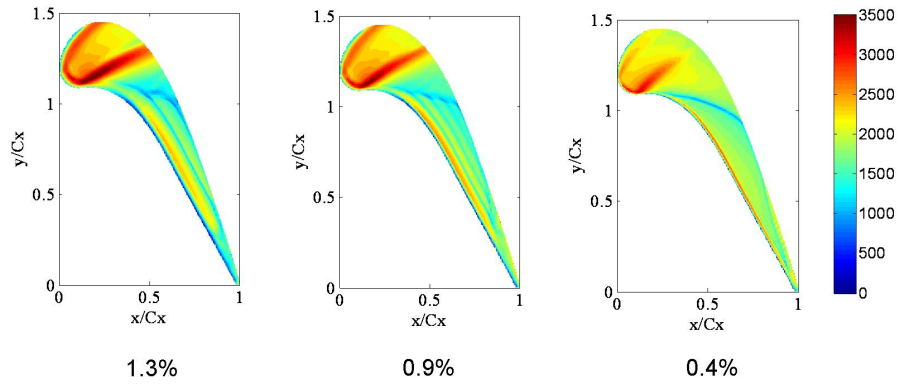

Figure 5.19: Computationally-determined Nusselt number distributions on the tip for 1.3, 0.9 and 0.4% tip clearances

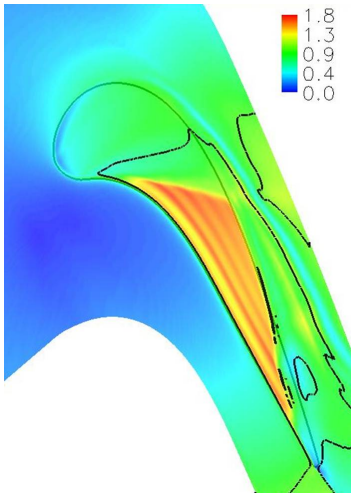

Figure 5.20: Computationally-determined Mach number distributions on the tip for 0.9% tip clearance

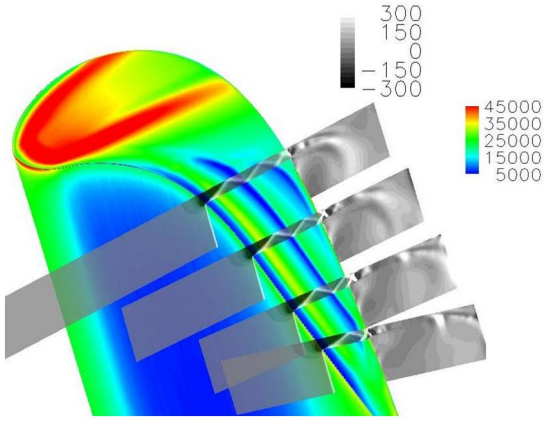

Figure 5.21: Predicted tip surface heat flux [W/m^2] and X-components of density gradient [kg/m^2] distributions on four cut planes

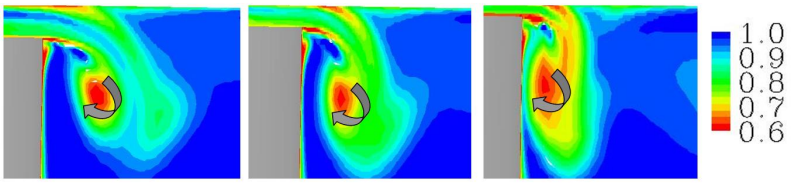

Figure 5.22: Predicted total pressure ratio contour $P_{t,\,\mathrm{local}}/P_{t,\,\mathrm{inlet}}$ along a stream-wise cut plane for three tip gaps

tip clearance. The coloured contours are the heat flux and the gray contours are the density gradients, which highlights the oblique shock system.

The computational sidewall results help to provide insight into the over-tip leakage flow. Figure 5.22 shows the locations of the OTL flow for the different tip clearances. The figure plots the ratio of the local total pressure to the inlet mainstream total pressure. With the larger tip clearance, the OTL flow has more momentum when mixing with the mainstream flow and the vortex appears to form further away from the blade suction side. For the smaller tip clearance, the OTL flow has less momentum and mixes closer to the blade suction side, attaching itself more to the suction-side surface. The attachment of the vortex to the suction side would explain why the smaller tip gap has enhanced heat transfer, as shown in Figure 5.11.

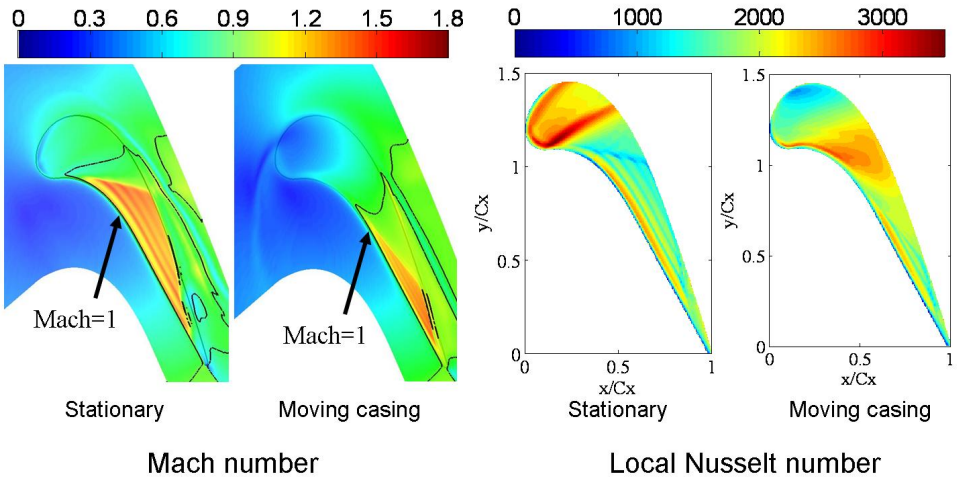

Figure 5.23: Predicted local tip Mach number and Nusselt number distributions for 0.9% tip gap with and without moving casing

Finally, as an operational blade has rotation, the computational study considers the effects of a moving casing wall. Figure 5.23 shows the effect of the moving casing on the local Mach number (left two figures) and the local Nusselt number (right two figures). With a moving casing, the area of the supersonic region becomes smaller, but a large portion of the blade is still choked. The subsonic region toward the frontal part of the blade is greatly affected by the moving casing, as seen in large reductions of the local Mach number and the Nusselt number. The supersonic region toward the trailing edge is not affected as much by the moving casing. The magnitude of the peak Mach number and the size of the sonic region all decrease a little bit, but the Nusselt number does not change as much.

5.5 Further Discussion of Results

This chapter has compared high-speed and low-speed heat transfer results. First of all, the blade loading is much different. There is a large adverse pressure gradient on the suction side. Also, the blade tested under low speed conditions is front-loaded whereas the blade tested under transonic conditions is more aft-loaded.

For a proper low-speed test, the blade camber must be increased to better match the blade loading. However, the pressure distribution between the passages will change, which must be considered. This highlights the importance of high-speed testing.

In addition to the aerodynamic differences between high-speed and low-speed testing, the heat transfer is both quantitatively and qualitatively different. The low-speed testing in the present study had a low Reynolds number (due to a smaller blade and low velocity). Other studies that consider low-speed testing typically use larger blades to match the Reynolds number. After Reynolds scaling the heat transfer results, the results are closer quantitatively, but are still qualitatively different. The major high and low heat transfer regions identified in low-speed studies are characteristically different than those in the present study. The plot of the circumferentially-averaged Nusselt number shows the qualitative difference best as the blade under transonic conditions starts high and decreases with x/C_{ax} whereas the blade under low-speed conditions starts out low and increases with x/C_{ax}. These results show the importance of engine-realistic high-speed testing.

Not only is this new data that has not been previously presented, it provides insight into the different flow phenomena that occurs of the tip and that cannot be replicated with low-speed testing. Some have tested at high subsonic conditions, but merely providing for a compressible environment is not enough. The blade must be tested in the same aerodynamic environment as the operational engine.

It is recognised that the present study is not completely engine-realistic for many reasons, such as the lack of a moving casing wall and the lack of a three-dimensional blade. However, this study, in conjunction with computational work can provide much more insight into the aero-thermodynamics of high-pressure turbine blades without the cost and loss of spatial detail of a rotor test.

Following the high-speed and low-speed comparison, a tip gap survey has been conducted for the tip as well as the sidewalls close to the tip. First, tip heat transfer results show high heat transfer at the trailing edge next to the suction side surface. This region is problematic for blade tip designers as this region is difficult to cool.

Perhaps one of the most significant features is the stripes of heat transfer that correspond to a shock structure, a feature that has not previously been identified and which cannot be observed with subsonic studies.

Increases in tip clearance show a general increase in heat transfer, especially from 0–75 percent of chord. This is due to the increase in high-temperature mass flow over the tip. An analytical study showed that there is a region of supersonic flow from 50–100 percent of axial chord. This was confirmed by computational results. As tip gap increases, the Mach number over the tip not only increases, but so does the mass flow, which leads to higher heat transfer, especially in the leading edge and frontal part of the blade.

The suction-side surface reveals the relationship between the surface Nusselt number and the over-tip leakage flow in terms of total pressure lost. The increase in tip clearance leads to a larger OTL vortex core. This flow has higher momentum which advects further away from the suction-side sidewall before mixing with the mainstream flow. With this detachment of the vortex, the peak heat transfer position is moved further away from the tip edge. The smallest tip gap shows a generally smaller OTL vortex core that remains attached to the suction-side sidewall at a larger radial position, which helps enhance surface heat transfer.

An examination of the near-tip sidewalls shows how the flow of the over-tip leakage flow progresses over the tip. The high heat transfer towards the pressure side trailing edge shows the region where high-heat transfer is taking place. This is possibly due to the high-temperature mass flow that is prevented from travelling over the choked trailing edge region.

5.6 Summary

Thermal performance of a flat blade tip at different tip gaps is experimentally investigated in the present chapter. Spatially-resolved heat transfer data are obtained by transient thermal measurement using Oxford High Speed Linear Cascade research facility for both transonic and low-speed aerodynamic conditions. Calculations of

Nusselt number and local Mach number are determined from the experimental data for each tip clearance. Finally, numerical results produced by Dr Zhang are used to help explain some of the flow phenomena.

The main conclusions of this chapter are:

1. High-speed and low-speed heat transfer characteristics are qualitatively different from 50–100 percent axial chord for a stationary blade. Even if the Reynolds number is matched, the regions of high and low heat transfer are different for high-speed and low-speed testing.
2. The frontal region of the blade tip Nusselt number decreases as tip gaps get smaller (from 1.3 to 0.4 percent). The tip Nusselt number towards the aft region of the blade is less straightforward. For all tip gaps, the Nusselt number is high towards the frontal region and decreases towards the trailing edge. Also, although the recovery temperature-derived Mach number results suggest a decrease in Mach number for the tip flow as the tip gap decreases, a large portion of the blade tip is still supersonic for all three tip gaps investigated.
3. Heat transfer distributions for the near-tip blade surface are also investigated. On the suction side, as tip gap increases, the Nusselt number decreases and the peak value position is moved away from the tip edge due to the tip leakage vortex detachment. On the pressure side, the peak heat transfer occurs around the near tip trailing edge corner.
4. Overall experimental heat transfer data for all three tip gaps are in good agreement with CFD predictions. This allows for further understanding of the flow physics over the tip. The local heat transfer distribution on the blade tip is noticeably affected by the relative casing motion. There is a fundamental change in the flow regime from transonic to subsonic in the mid-chord region when the moving end wall is modelled. A moving casing results in a smaller supersonic region over the tip and slightly higher heat transfer near the tip trailing edge. A significant portion of the tip leakage flow however still remains supersonic with easily identifiable shock wave structures. The frontal part of the blade is the most affected by the moving casing.

Chapter 6

Winglet Heat Transfer

6.1 Introduction

In the present chapter, results of detailed, spatially-resolved Nusselt numbers on the blade tip and near-tip region are presented for a modern winglet blade tip under transonic conditions. Experimental results are limited to blades in a stationary linear cascade. As with Chapter 5, both the tip and near-tip sidewalls are examined for the uncooled winglet. Additionally, the cooled winglet tip heat transfer is investigated. Finally, computational results prepared by Dr Qiang Zhang and analysed by the High-Speed Linear Cascade research team are briefly discussed, especially with respect to relative casing movement.

6.2 Uncooled Winglet Tip

This section examines the uncooled winglet. The uncooled winglet uses the same epoxy material as the flat tip. The major features of the winglet tip are presented in Figure 3.11 in Section 3.3.3. A tip gap survey of tip and sidewall heat transfer is investigated for tip clearances of 0.9 and 1.3 percent of span. As is shown in Chapter 7, the 0.4 percent tip gap did not show periodic aerodynamic loss results and therefore the heat transfer for the 0.4 percent tip gap was not examined.

First, with the move to Axis Point, an investigation of the repeatability of the uncooled winglet heat transfer data was performed. Several runs were performed and all showed results consistent with those presented in this chapter.

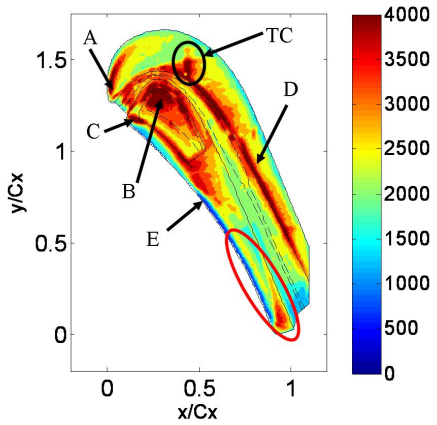

Figure 6.1: Nusselt number distributions on the uncooled winglet tip for 1.3% tip gap, indicating major heat transfer features

6.2.1 Tip Gap Survey for Tip Heat Transfer

A tip gap survey was performed for the uncooled winglet for 0.9 and 1.3 percent of span. Figure 6.1 presents a contour plot of the experimentally-determined Nusselt number for the winglet blade tip with a tip clearance of 1.3 percent. The major heat transfer characteristics are shown in the figure. High heat transfer is observed in several locations on the winglet (as noted by arrows), including

1. Leading edge corner (marked A)
2. Pressure side recess corner (marked B)
3. Leading-edge part of the winglet gutter (marked C)
4. Edge between the gutter and suction side tip (marked D)

In addition, a striped region of low Nusselt number is observed on the pressure side edge, corresponding to a separation bubble (marked E). Also, stripes of high and low heat transfer are observed near the trailing edge (circled in red in Figure 6.1), consistent with other tip gaps as well as the flat tip heat transfer results. The location of the high-response thermocouple is also included, marked "TC".

Results of the tip gap survey are presented in Figure 6.2. Results from both tip clearances are consistent with the major heat transfer characteristics introduced above. The figure indicates that there is higher Nusselt number associated with the

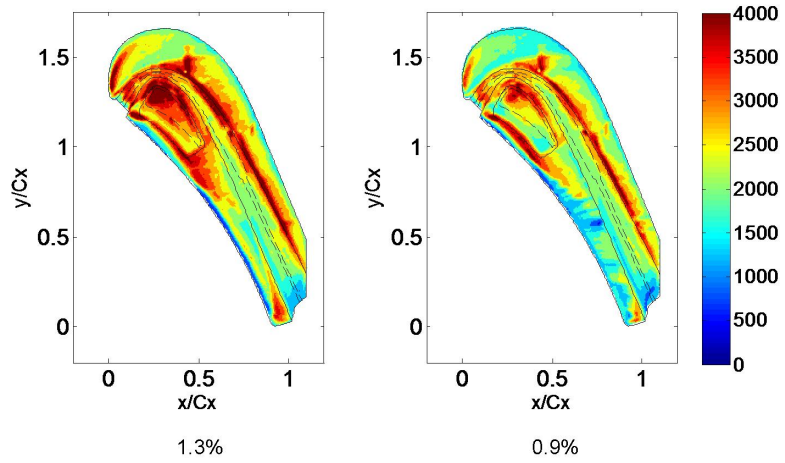

Figure 6.2: Nusselt number distributions on the uncooled winglet tip for 1.3 and 0.9% tip gaps

larger tip clearance. For the 0.9 percent tip gap, the heat transfer caused by the flow reattachment is less pronounced.

An analytic study of the recovery temperature-derived Mach number, as shown in Figure 6.3, reveals tip isentropic Mach numbers in excess of 1.3, which is less than the peak Mach number on the flat tip. However, care must be taken when interpreting these experimentally-based results. The analytic study assumes a recovery factor of 0.86, which is an average of the estimate recovery factors for laminar and turbulent boundary layers. The actual recovery factor is unknown. The study also assumes that the flow is isentropic through the tip gap. Results from the frontal part of the blade tip is likely near-isentropic through the gap. Losses are present, however, towards the trailing edge where shock waves are present, making the flow non-isentropic and the analytical results less realistic. More specifically, the Mach numbers downstream of the gutter are perhaps the least realistic considering the number of shock waves the flow has observed. Nevertheless, though the Mach number values are not necessarily realistic, the results can help to explain where the high-speed and low-speed flow occurs.

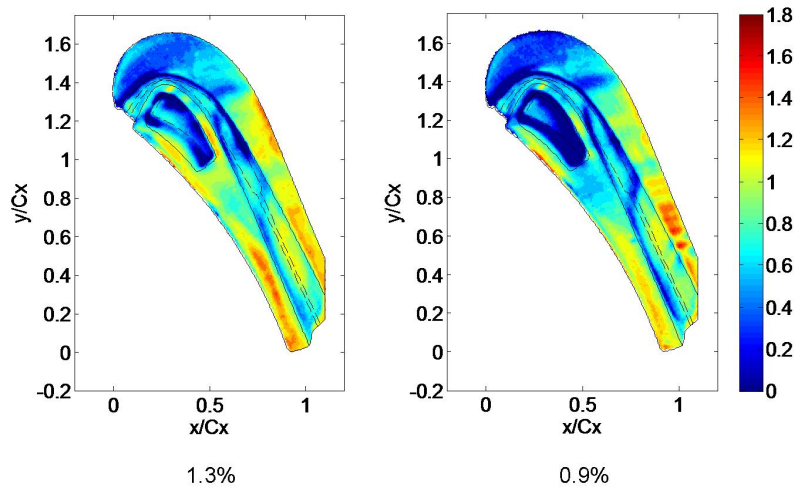

Figure 6.3: Recovery temperature-derived Mach number distributions on the uncooled winglet tip for 1.3 and 0.9% tip gaps (recovery factor=0.86)

Both tip clearances appear to have supersonic flow over the final 50 percent of axial chord, especially near the pressure side. The figure also shows that for an increase in tip clearance, the Mach number generally increases over the tip.

Further analysis of the uncooled winglet tip results, including average evaluations, is addressed in Section 6.3 alongside the cooled winglet results.

6.2.2 Tip Gap Survey for Sidewall Heat Transfer

Sidewall heat transfer measurements are only investigated for the uncooled winglet. Figure 6.4 presents the experimentally-determined Nusselt number results for the uncooled winglet suction-side surface in the near-tip region. Based on the camera viewing angle, the suction side is observable for 35–100 percent of axial chord based on the mid-span profile (see Figure 4.3). For both tip clearances, as the x/C_{ax} increases, the size of the over-tip leakage (OTL) vortex increases and is associated with enhanced heat transfer on the suction-side sidewall. Unlike the flat tip, the winglet suction-side heat transfer results show that the Nusselt number generally increases as the tip as the tip gap increases, especially close to the suction-side lip overhang. This could be due to stronger tip leakage vortex as gap increases, which is different compared to the flat tip.

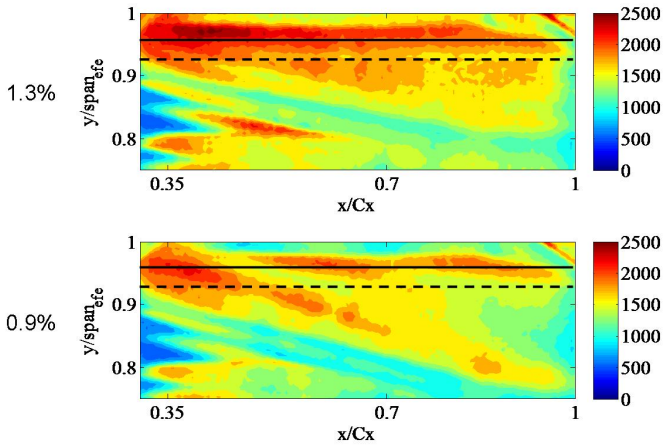

Figure 6.4: Nusselt number distributions on the uncooled winglet tip for 1.3 and 0.9% tip gaps (Suction Side)

For the pressure-side surface, based on the camera viewing angle, there are two regions that are not actual surfaces (indicated by the black and pink lines in Figure 6.5). The first is tip edge for x/C_{ax} between 0.25 and 1. A sharp gradient is observed between the tip edge and the tip gap. The second region is the trailing edge, where the camera is unable to resolve the precise location of the trailing edge. It is unlikely that the surface Nusselt number continues to increase with x/C_{ax} then suddenly decreases at the trailing edge. Because of the camera viewing angle, the winglet pressure-side lip overhang extends past the trailing edge of the mid-span profile. Figure 6.5 presents the experimentally-determined Nusselt number results for the uncooled winglet pressure-side surface in the near-tip region. Like the flat tip pressure-side surface, the Nusselt numbers increase with x/C_{ax} as the flow advects in the axial direction. Nusselt number values also increase with radius, especially toward the trailing edge. Like the flat tip, the tip region at the trailing edge has high Nusselt number, where this region is susceptible to high thermal loading, even when significant amounts of cooling are employed. Though there are some local differences, both tip clearances in Figure 6.5 look very similar.

Span-wise averaged Nusselt numbers for the suction side and pressure side of the uncooled winglet tip are presented in Figure 6.6, showing that tip clearance clearly has

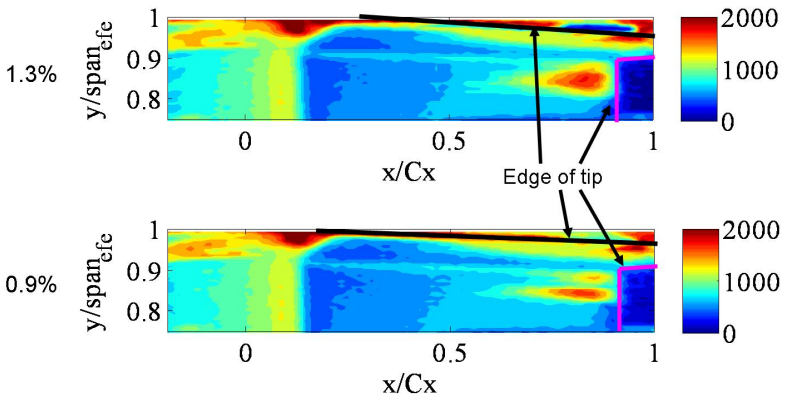

Figure 6.5: Nusselt number distributions on the uncooled winglet tip for 1.3 and 0.9% tip gaps (Pressure Side)

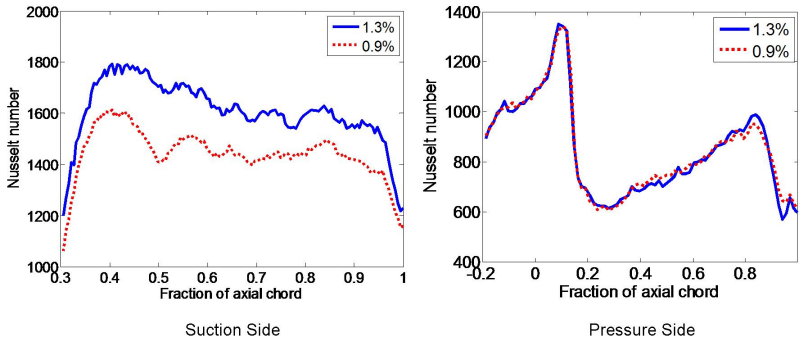

Figure 6.6: Circumferentially-averaged Nusselt numbers on the sidewalls of the uncooled winglet tip for 1.3 and 0.9% tip gaps

an effect on the suction-side surface, whereas the pressure-side surface heat transfer differences are negligible.

A comparison of the span-wise averaged Nusselt numbers for the suction side and pressure side of the flat tip and the uncooled winglet are provided in Figure 6.7. The suction side results show opposite trends. The larger tip clearance for the winglet results in higher Nusselt number. Also, the flat tip average Nusselt number generally stays the same for increased x/C_{ax}, though with some increases and decreases. The winglet tip, on the other hand, starts out high and decreases with increased x/C_{ax}. When comparing the winglet and flat tip for common tip gaps (see Figure 6.7), the winglet has a higher circumferentially-averaged Nusselt number for the 0.9 percent

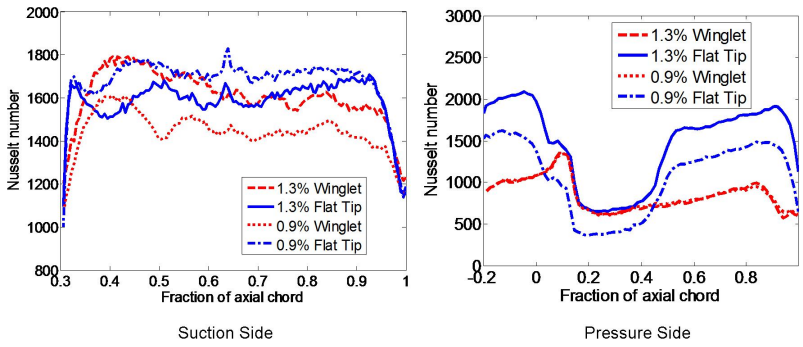

Figure 6.7: Circumferentially-averaged Nusselt numbers on the sidewalls of the flat tip and the uncooled winglet tips for 1.3 and 0.9% tip gaps

tip clearance for most of the suction side, but for the 1.3 percent tip clearance, the winglet has higher Nusselt number toward the leading edge but then decreases to below the average Nusselt number for the flat tip (from about 75 to 95 percent of axial chord).

The uncooled winglet pressure side results reveal that tip clearance has negligible effects on Nusselt number, unlike the enhanced heat transfer observed on the flat tip. Flat tip results also reveal larger variation in average Nusselt number with increasing x/C_{ax}. The flat tip has a higher average Nusselt number than the winglet tip for 45–100 percent of axial chord.

An examination of the recovery factor-derived Mach number distributions on the suction-side and pressure-side sidewalls is shown in Figures 6.8 and 6.9, respectively. For simplicity of analysis, the same recovery factor is also used for the pressure side even though the boundary layer could be laminar. Also, the flow over the tip rolls up into a vortex and is attached to the suction-side sidewall. The recovery factor for this flow mechanism is therefore unknown. In addition, shock waves are likely present on the suction side, making the Mach number results less realistic as the flow is non-isentropic. Therefore the values of the Mach number are not necessarily realistic, but they provide a visualisation of the locations of high and low speed flows. Also, the results show that the Mach number magnitudes on the suction side close to the tip appear to decrease with an increase in tip clearance.

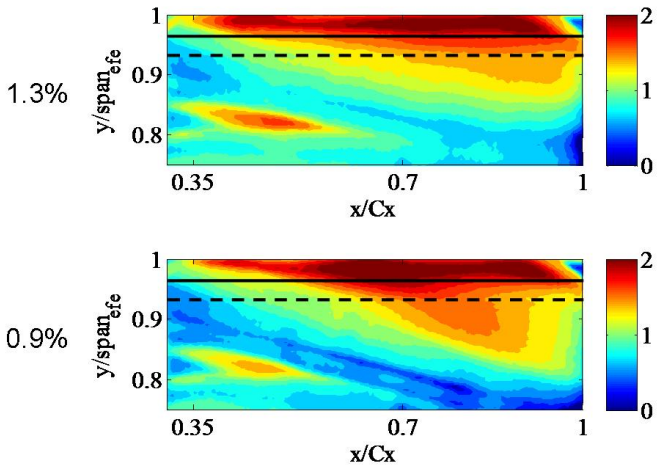

Figure 6.8: Recovery temperature-derived Mach number distributions on the uncooled winglet tip for 1.3 and 0.9% tip gaps (Suction Side) (recovery factor = 0.86)

The pressure side Mach number is very low for most of the pressure side, up to about 60 percent of chord, as shown in Figure 6.9. Both tip clearances show similar results. Like the pressure side Nusselt number reports, areas of the figure are not actual surfaces (indicated by pink lines in the figure).

Span-wise average Mach numbers for both the pressure side and suction side uncooled winglet are presented in Figure 6.10. The figure shows that the average suction side Mach number increases with increased tip gap for 30–70 percent of axial chord. The results appear to be negligible for 70–100 percent of chord. The pressure side Mach number results show minor differences with changes in tip gap.

A comparison of the span-wise averaged Mach numbers for the suction side and pressure side of the flat tip and the uncooled winglet are provided in Figure 6.11.

For both tip clearances and both geometries, the suction-side Mach number is transonic. The average suction side Mach number is higher for the flat tip than the winglet tip. Both the flat tip and winglet tip show little difference in average suction side Mach number, where the biggest difference occurs between 40–70 percent of axial chord, which may suggest that the winglet is unloading. As with heat transfer, the uncooled winglet pressure side average Mach number shows little effect of tip

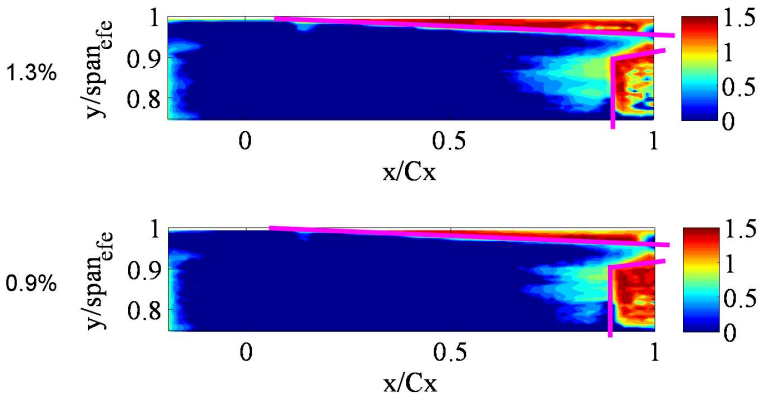

Figure 6.9: Recovery temperature-derived Mach number distributions on the uncooled winglet tip for 1.3 and 0.9% tip gaps (Pressure Side) (recovery factor = 0.86)

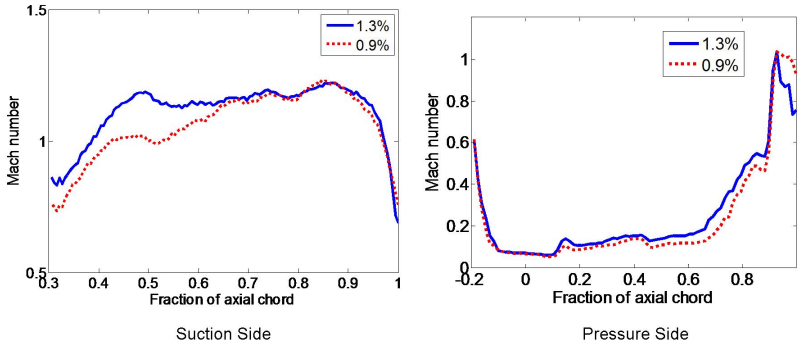

Figure 6.10: Circumferentially-averaged recovery temperature-derived Mach numbers on the sidewalls of the uncooled winglet tip for 1.3 and 0.9% tip gaps (recovery factor = 0.86)

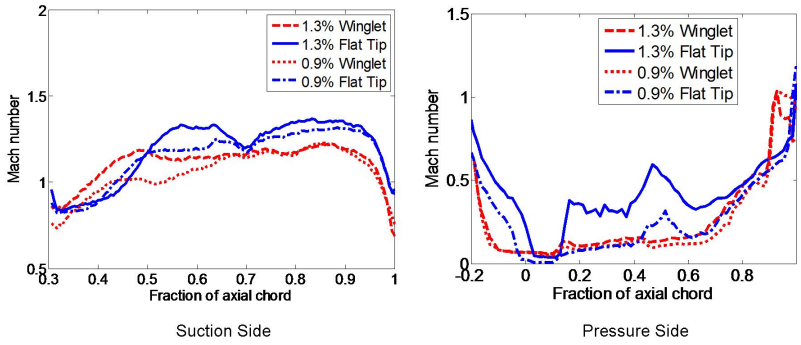

Figure 6.11: Circumferentially-averaged recovery temperature-derived Mach numbers on the sidewalls of the flat tip and the uncooled winglet tip for 1.3 and 0.9% tip gaps (recovery factor = 0.86)

gap. Mach number results for the flat tip show more significant differences that are unexpected, especially for 20–70 percent of chord. For all tip geometries and tip clearances, the pressure side Mach number is subsonic, as expected.

6.3 Cooled Winglet Tip Heat Transfer Tip Gap Survey

The setup of the coolant system is addressed in Chapter 3. Initially, air at room temperature was used for the coolant. The focus was on the effectiveness of the film. However, with the low adiabatic wall temperatures resulting from high Mach numbers, the coolant was actually heating certain parts of the blade tip. In order to be able to measure reasonable non-negative values of film cooling effectiveness, vortex tubes are used to provide coolant with temperatures less than the lowest measured adiabatic wall temperature. Under the current configuration, there was not enough volume of air to provide the pressure necessary to cool all three blades. There was only enough pressure to provide the three centre blades with uncooled air or one blade with cooled air. Because of the importance of measuring non-negative film cooling effectiveness, the heat transfer test injected cold coolant into the centre blade while two other blades employed the uncooled winglet. Future testing might address this issue.

As mentioned in Chapter 3, the cooling supply system takes at least 30 minutes to achieve a steady state temperature. In order to prevent pre-cooling the blade tip, the cooling air bypasses the blade tip until a steady state temperature and pressure is achieved for both the cooling flow and the HSLC inlet flow. A solenoid valve (indicated with an "S" in Figure 3.13) is used to direct the cooling flow toward the blade tip nearly one second before the heater mesh is engaged. This is due to a sudden and slight increase and decrease of the coolant temperature caused by the opening of the solenoid valve. When heat transfer measurements are taken, both the mainstream and coolant temperatures are steady.

The addition of cooling flow turns a two-temperature problem into a three temperature problem: mainstream temperature, wall temperature and coolant temperature. The single-experiment test procedures developed in Chapter 4 continued to be used during the cooled winglet testing. The use of one or two experimental tests was addressed in Chapter 2. During cooled winglet testing, the surface temperature is experimentally-measured and from the temperature trace, the heat flux is calculated. The plot of the heat flux versus temperature leads to the heat transfer coefficient and adiabatic wall temperature. This adiabatic wall temperature is then used to calculate the film cooling effectiveness, η, defined in Equation 6.1.

$$\eta = \frac{T_{rec} - T_{ad}}{T_{rec} - T_c} \tag{6.1}$$

In this equation, T_c is the coolant temperature, T_{ad} is the adiabatic wall temperature of the cooled winglet and T_{rec} is the recovery temperature. The recovery temperature is the adiabatic wall temperature when no cooling is present. T_{rec} is the calculated adiabatic wall temperature using the uncooled winglet while T_{ad} is the adiabatic wall temperature using the cooled winglet.

A decision was made to test a separate uncooled winglet blade (with no cooling holes). To determine the film cooling effectiveness, the flow conditions must be consistent for each test. The variation in atmospheric pressure and temperature in a given day meant that the uncooled and cooled winglets had to be changed frequently, which appeared to rule out plugging the holes of the cooled winglet.

In the open literature, there are different definitions of film cooling effectiveness. Some studies use the mainstream temperature in place of T_{rec} in both the numerator and denominator of Equation 6.1. This is a fair assumption for low-speed tests in which the adiabatic wall temperature does not vary much from the mainstream temperature (see the near-uniformity of the adiabatic wall temperature in Figure 5.4). For transonic tests, adiabatic wall temperatures are significantly different from the mainstream temperature. Some studies use mainstream temperature in place of T_{rec} only in the numerator. While the adiabatic wall temperature is accounted for, use of this form of the equation assumes that one part of the blade can be less effective simply because it has a higher Mach number.

Unlike with previous sections, the recovery-temperature-derived Mach number results are not presented, as the uncertainty in M increased with the increased uncertainty of the recovery factor with coolant injection.

Lastly, though the coolant temperature is not a local value, it is experimentally very difficult to measure this value at the exit to each cooling hole. Therefore, a single value of the coolant temperature must be assumed.

6.3.1 Tip Heat Transfer

A tip gap survey is performed for a cooled winglet with 1.3 and 0.9 percent tip clearances. Figure 6.12 presents contours of the tip Nusselt number for the two tip clearances. In general, the figure shows a large increase in Nusselt number with coolant injection. Decreases in Nusselt number are noted in regions where coolant holes are located, though there is an increase in Nusselt number in regions of close proximity to the films. The results show that Nusselt number increases with increased tip clearance. Also, it appears that there is a region of high Nusselt number on the pressure side lip overhang (circled in the figure), which is adjacent to regions of very low Nusselt number. This is most pronounced in the 1.3 percent tip gap results. The reason for this increased Nusselt number is addressed in Section 6.3.2.

The Nu difference between the cooled winglet and the uncooled winglet, for each tip gap, is presented in Figure 6.13. Note that most of the values are positive,

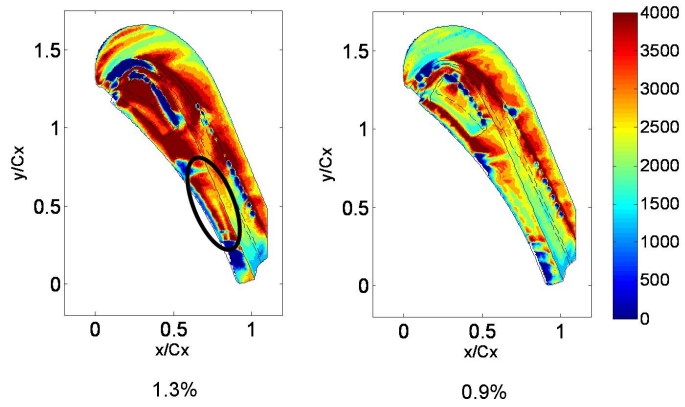

Figure 6.12: Nusselt number distributions on the cooled winglet tip for 1.3 and 0.9% tip gaps

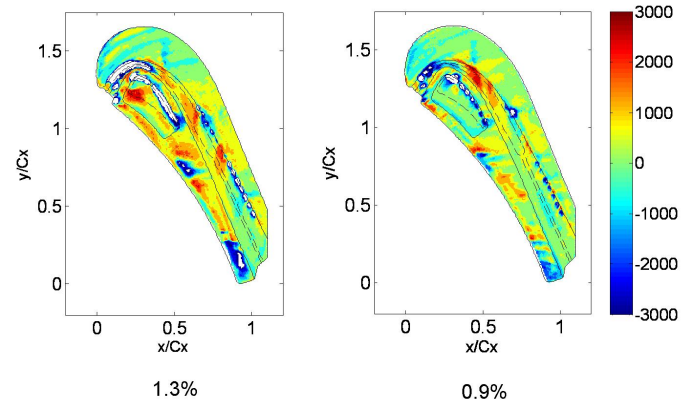

Figure 6.13: Nusselt number differences between cooled and uncooled winglets for 1.3 and 0.9% tip gaps

indicating the enhanced Nu for the cooled winglet. The negative values which indicate the decreased Nu with cooling are very close to cooling holes, which have increased uncertainty.

The circumferentially-averaged Nusselt numbers for both the cooled and uncooled winglets for both the 1.3 and 0.9 percent tip gaps are shown in Figure 6.14. The increased tip gap clearly results in increased Nusselt number for both the uncooled and cooled winglets. In addition, for both tip gaps, the cooled winglet Nusselt number is generally greater than the uncooled winglet, except at approximately 8–12 percent

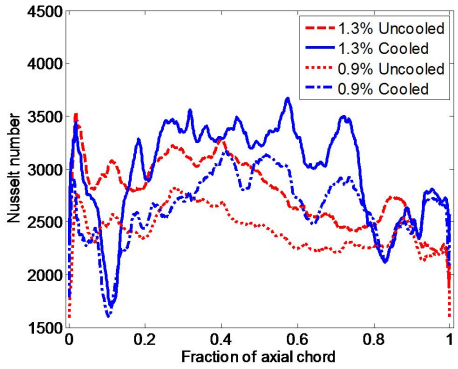

Figure 6.14: Circumferentially-averaged Nusselt numbers on the uncooled and cooled winglet tips for 1.3 and 0.9% tip gaps

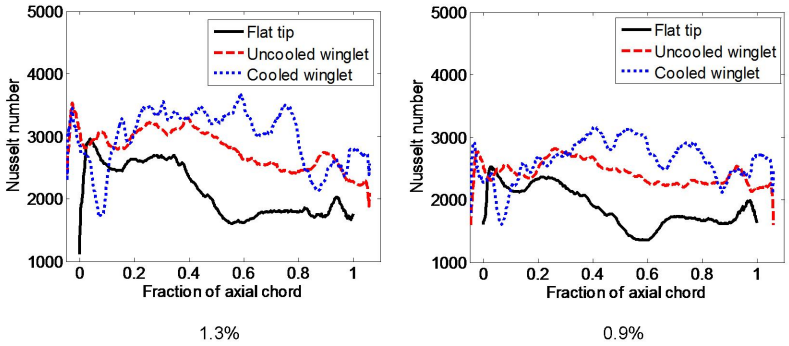

Figure 6.15: Circumferentially-averaged Nusselt numbers on the flat tip and the uncooled and cooled winglet tips for 1.3 and 0.9% tip gaps

(in a region with a large number of cooling holes) and 80–85 percent of chord, where the cooled winglet shows a large decrease in Nusselt number.

The circumferentially-averaged Nusselt numbers for the three tip configurations (flat tip, uncooled winglet and cooled winglet) are presented in Figure 6.15. In general, for both tip gaps, the cooled winglet has the highest Nusselt number, followed by the uncooled winglet, with the flat tip having the lowest Nusselt number, with the exception of 8–12 and 80–85 percent of axial chord, where there is a large decrease in average Nusselt number for the cooled winglet.

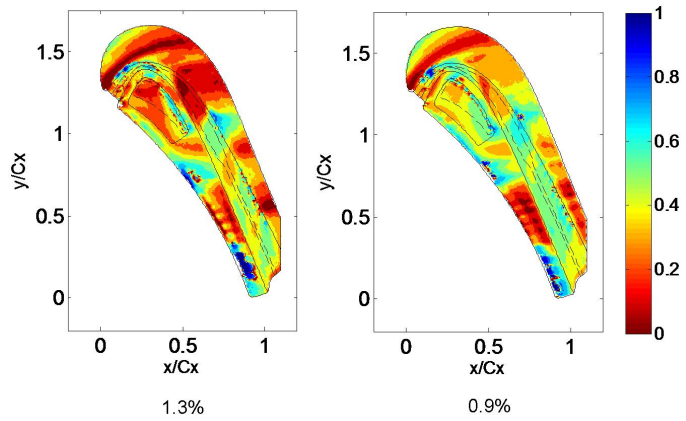

Figure 6.16: Film cooling effectiveness distributions on the winglet tip for 1.3 and 0.9% tip gaps

6.3.2 Tip Film Cooling Effectiveness

Contours of tip film cooling effectiveness are shown in Figure 6.16. Note that the colour scale is inverted, where higher film cooling effectiveness is blue and lower film cooling effectiveness is red. Results show that film cooling effectiveness increases with smaller tip clearances. In addition to low effectiveness in the crown region, there is a region of low film cooling effectiveness on the pressure side lip overhang in the same location circled in Figure 6.12. When injecting coolant without mainstream air, the velocity of the coolant exiting the holes in this region is clearly weaker than the adjacent holes. An inspection of the blade design shows that the cooling holes in question are fed by the gallery feed via angles greater than 90°. The adjacent cooling holes all have angles less than 90°. It is not clear if these angles are intended by design.

The circumferentially-averaged film cooling effectiveness is presented in Figure 6.17. From this figure, it appears that the average film cooling effectiveness for the small gap is greater at all axial-chordwise locations, with the exception of only a few parts of the trailing edge. Also, for both tip gaps, the film cooling effectiveness increases with increasing x/C_{ax}.

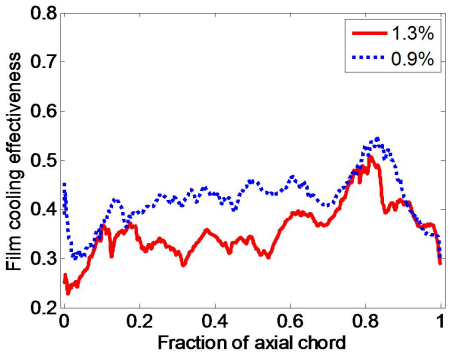

Figure 6.17: Circumferentially-averaged film cooling effectiveness on the winglet tip for 1.3 and 0.9% tip gaps

Compared to the flat tip, the uncooled winglet has over a 35 percent higher area-averaged heat transfer coefficient. Compared to the flat tip, the cooled winglet has a 41 percent higher area-averaged heat transfer coefficient. In addition, the winglet has nearly 2.4 times the surface area of the flat tip. Therefore, the average heat load for the uncooled winglet is nearly 3.2 times greater than the flat tip while the average heat load for the cooled winglet is nearly 3.4 times greater than the flat tip.

6.3.3 Tip Net Heat Flux Reduction

To understand the effect of the coolant in an actual engine environment, a net heat flux reduction (NHFR) was defined by Sen et al. (1996), which considers the combined effect of heat transfer coefficient (h) and film cooling effectiveness (η). The objective of film cooling is to increase η while reducing the h. The NHFR is defined as:

$$\text{NHFR} = \frac{\dot{q}_{uc} - \dot{q}_c}{\dot{q}_{uc}} = 1 - \frac{h_c}{h_{uc}}(1 - \eta\Theta_E) \tag{6.2}$$

where the subscripts used are for uncooled (uc), cooled (c) and Engine environment (E). Also, the engine-scaled temperature ratio Θ_E is defined as

$$\Theta_E = \frac{T_{t_m} - T_{t_c}}{T_r - T_w} \tag{6.3}$$

Newton et al. (2006) performed a calculation of NHFR using the following engine conditions:

- Mainstream total temperature $T_{t_m} = 1900\,\mathrm{K}$
- Coolant total temperature $T_{t_c} = 880\,\mathrm{K}$
- Wall temperature $T_w = 1200\,\mathrm{K}$

As their study was low speed, they used a recovery temperature nearly equivalent to the mainstream total pressure. As presented in Section 6.2.1, the tip Mach number distribution was calculated using the recovery temperature and a recovery factor of 0.86. Using the following equation from Sargison et al. (2002), the recovery temperature distribution is determined from the following equation

$$T_r = T_{t_m} \frac{1 + r\frac{\gamma-1}{2}M^2}{1 + \frac{\gamma-1}{2}M^2} \tag{6.4}$$

Using the local engine-scaled recovery temperature from Equation 6.4, the engine-scaled temperature ratio was determined and NHFR was calculated using the h and η determined experimentally.

Contours of tip NHFR are shown in Figure 6.18 for both tip clearances. Note that the colour scale is inverted, where higher NHFR is blue and lower NHFR is red. Results show that, in general, NHFR increases with smaller tip clearances (as with η. In addition to low NHFR in the crown region, there is a region of low NHFR on the pressure side lip overhang in the same location as the low η previously presented.

The circumferentially-averaged NHFR presented in Figure 6.19. The results are similar to the circumferentially-averaged η. NHFR for the smaller tip gap is greater for the smaller tip clearance for x/C_{ax} from 0.2–0.9.

The area-averaged NHFR is 0.49 for the 1.3 percent tip gap and 0.59 for the 0.9 percent tip gap. The area-averaged NHFR result may be misleading as the flow varies significantly over a supersonic tip.

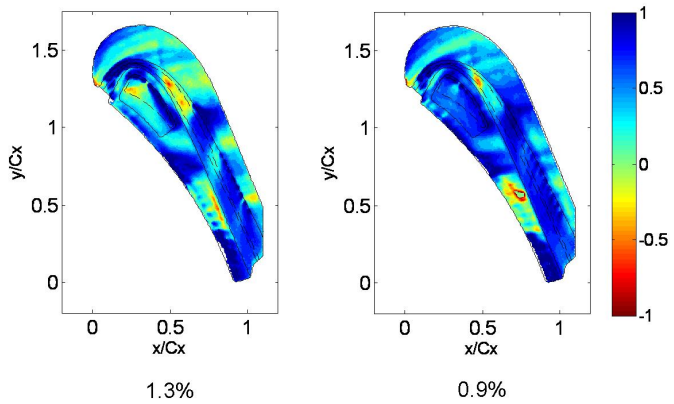

Figure 6.18: Net Heat Flux Reduction distributions on the winglet tip for 1.3 and 0.9% tip gaps

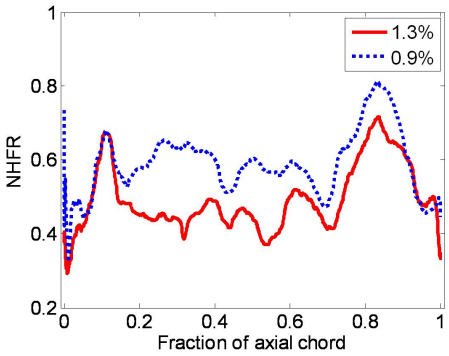

Figure 6.19: Circumferentially-averaged Net Heat Flux Reduction on the winglet tip for 1.3 and 0.9% tip gaps

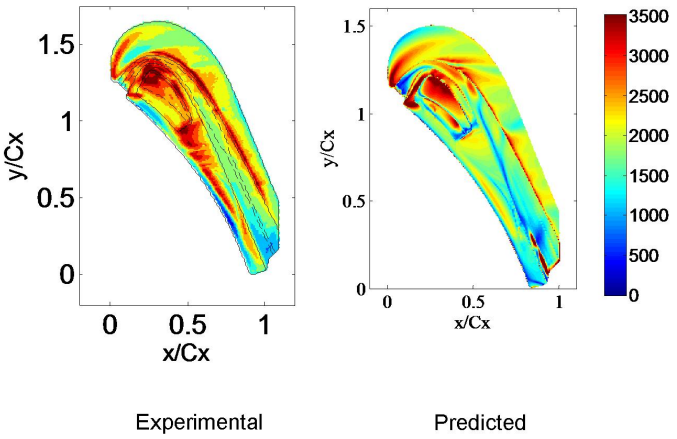

Figure 6.20: Experimental and predicted Nusselt number distributions on the tip for 1.3% tip clearance

6.4 Winglet Heat Transfer Computational Results

This section provides computational work of the HSLC research group. The computational study was performed by Dr Zhang while all members of the research group jointly analysed and discussed the results. Some of these results were presented in O'Dowd et al. (2010b), while others have been included in another conference paper submission. Results are provided here to not only show agreement with the experimental results, but also to help understand some of the flow phenomena over the tip. A computational analysis of the cooled winglet has yet to be performed.

A comparison of experimental and computational uncooled winglet heat transfer results presented in Figure 6.20 shows fairly good agreement. Though the Nusselt number is under-predicted, the major heat transfer characteristics discussed in Figure 6.1 are also evident in the computational results. These results are actually good for such complex flow over complicated geometry.

The predicted local Mach number for the 1.3 percent tip gap (calculated halfway between the blade tip and casing wall surfaces) is shown in Figure 6.21. The calculated isentropic Mach number results are based on the local static and the local total pressure. This figure shows that the tip is largely supersonic. These results agree fairly well qualitatively with the analytical Mach number results in Figure 6.3. Care

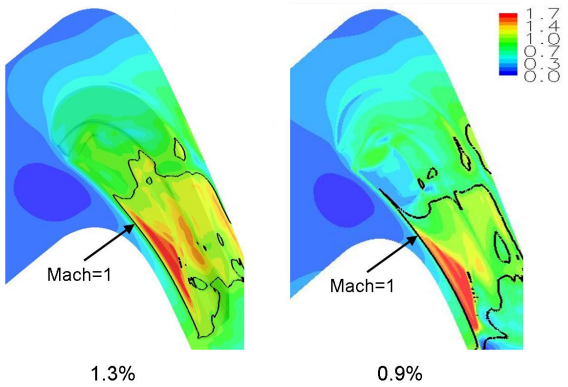

Figure 6.21: Predicted local Mach number distributions on the winglet tip for 1.3 and 0.9% tip clearances

should be taken, however, when comparing the experimentally-based results to the predicted results, as only the computational results are isentropic values. Even in regions where the flow is expected to be near-isentropic (such as the frontal part of the blade), the experimental and computational Mach number magnitudes do not agree, perhaps partly due to the estimated recover factor. Despite the differences in Mach number magnitudes, both the experimental and predicted results show that the size of the supersonic region is reduced for the winglet (see Figures 6.21 and 6.3) compared to the flat tip (see Figure 5.9).

The relationship between the heat transfer and the shock structure that exists over the flat tip (Zhang et al., 2010b) also occurs on the winglet tip. Figure 6.22 shows an uncooled winglet with a 1.3 percent tip clearance, where the coloured contours are the heat flux and the gray contours are the density gradients, which highlights the oblique shock system.

In Figure 6.4, the dashed line indicates the radial transition of the mid-span blade profile to the winglet and the solid line indicates the region of constant tip area at the tip. Most of the high heat transfer region is on this lip overhang. The predicted sidewall results help to provide insight into the relationship between the OTL flow and the heat transfer. Plots of the local total pressure to inlet mainstream total

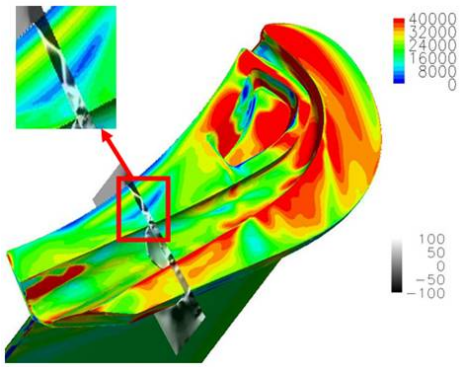

Figure 6.22: Predicted tip surface heat flux [W/m^2] (in colour) and X-components of density gradient [kg/m^2] (in greyscale) distributions on a cut plane

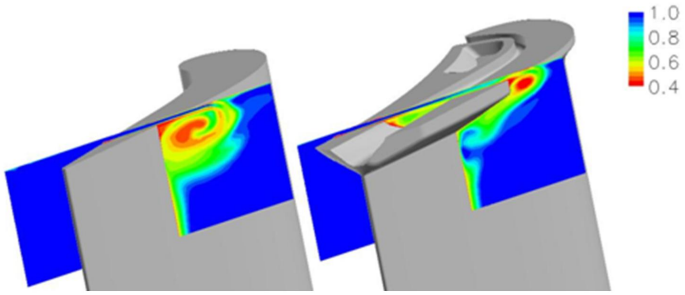

Figure 6.23: Predicted total pressure ratio contour $P_{t,\,\text{local}}/P_{t,\,\text{inlet}}$ along a stream-wise cut plane for both the flat tip and the uncooled winglet for a 1.3% tip gap

pressure ratio, as presented in Figure 6.23, show the locations of the OTL vortices for the flat tip and the uncooled winglet.

The results in Figure 6.23 show that the tip leakage vortex on the winglet suction side is mostly attached to the lip, which is also where the highest Nusselt numbers are on the suction side, while the tip leakage vortex on the flat tip suction side is attached further down in the span-wise direction, away from the tip.

Finally, the computational winglet study considers the effects of a moving casing wall. Figure 6.24 shows the effect of the moving casing on the local isentropic Mach number (left two figures, based on the local static and total pressures) and the local Nusselt number (right two figures). With a moving casing, the area of the supersonic region becomes smaller, but a large portion of the blade is still choked. The subsonic

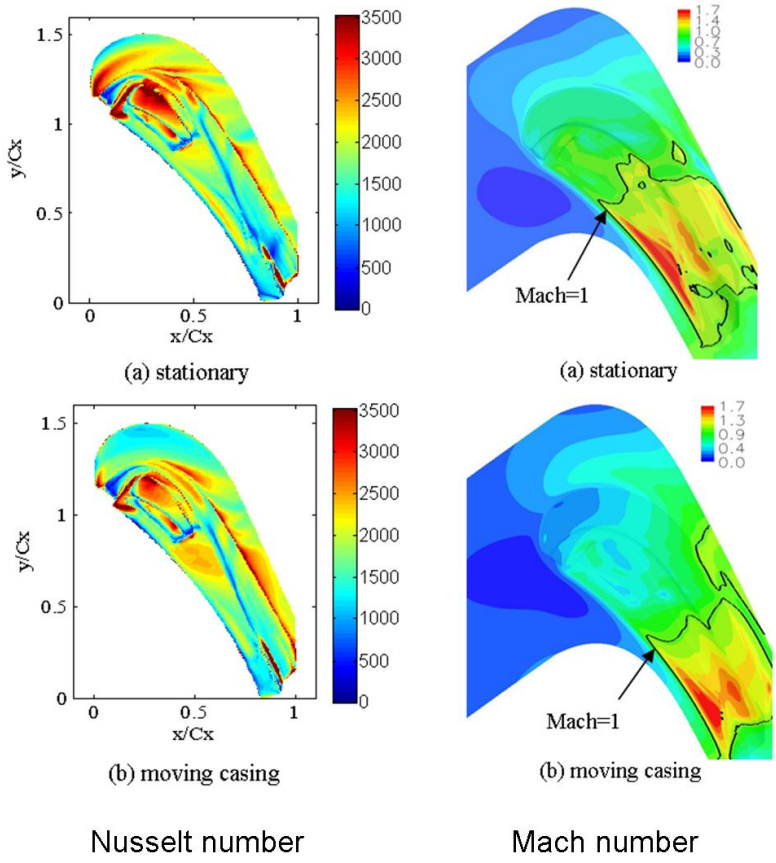

Figure 6.24: Predicted local tip Nusselt number and local Mach number distributions for 1.3% tip gap with and without moving casing

region toward the frontal part of the blade is greatly affected by the moving casing, as seen in large reductions of the local Mach number and the Nusselt number. Though there are differences, the supersonic region toward the trailing edge does not appear to be affected as much by the moving casing.

6.5 Further Discussion of Results

This chapter has considered the effects of tip gap, geometry and coolant injection on tip and sidewall heat transfer and Mach number. It is difficult to provide much detailed analysis of the flow physics over the tip without computational analysis. A description of just some of the flow phenomena over the tip is included in the present

chapter as well as the published papers produced by the HSLC research group. This chapter includes experimental and predicted heat transfer and Mach number results for the uncooled winglet, which does not appear to have been previously investigated. This chapter also includes coolant injection effects.

The effect of tip gap on the winglet tip heat transfer is consistent with the flat tip, where the increase in tip gap results in increased Nusselt number over the tip. This is true both with and without coolant injection. Results from this study have shown that the tip clearance has little effect on the winglet pressure side heat transfer. Perhaps the pressure-side lip overhang helps to keep the stream-lines advecting axially, leading to similar results for different tip gap. The suction side heat transfer on the other hand, is greatly affected by tip clearance. The higher tip clearance has higher Nu on the suction-side lip overhang.

The winglet was designed to minimise the aerodynamic loss caused by OTL flow and the initial plan for this research was to consider the effect on heat transfer. The results show that the winglet heat transfer is greater than for the flat tip. With the additional area of the winglet tip, more cooling flow is required to keep the winglet cool.

A computational study can help explain the reason for higher heat transfer on the uncooled winglet compared to the flat tip, but the source of this enhanced heat transfer is not fully understood. The skin friction and turbulence diffusion over the tip and its relationship to heat transfer is not well understood, especially under a transonic environment. On average, the uncooled winglet Nusselt number is over 35 percent greater than the flat tip Nusselt number, indicating a need for an increased coolant flow rate. In addition, the cooled winglet Nusselt number is over 41 percent greater than the flat tip Nusselt number.

An analysis of the Mach number over the tip shows that like the flat tip, much of the tip is transonic. Like the flat tip, the over-tip shock system for the winglet leads to striping of high and low Nusselt number regions.

The suction side heat transfer results show that the OTL vortex remains attached to the suction-side lip overhang, while the OTL vortex over the flat tip is attached to

the suction side at a lower radial position. This could indicate a loss of momentum caused by the winglet tip.

This chapter also addressed coolant injection. When introducing coolant, the tip Nusselt number is increased. The film cooling effectiveness, however, shows the regions of poor film cooling. Much of this region is the subsonic region at the crown of the winglet. However, part is at trailing edge, on the pressure-side lip overhang. This transonic region needs to be carefully considered. Film cooling effectiveness is improved with a smaller tip clearance. When considering net heat flux reduction, the smaller tip appears to be more effective.

6.6 Summary

In summary, the focus of this chapter is on heat transfer of the tip and near-tip region of an uncooled and cooled winglet. Spatially-resolved heat transfer data are obtained using the transient infrared thermography using the Oxford High Speed Linear Cascade facility. The experimental results introduce the underlying complex transonic flow structures, and the associated over-tip heat transfer characteristics, where further CFD studies help to explain these complex flow structures in further detail. It should be noted that these structures would not have been seen in previous low-speed experiments.

The major conclusions for this chapter are:

1. A large portion of the winglet tip experiences supersonic flow, from approximately 40–100 percent axial chord. Approximately 50 percent of the tip surface area is transonic. This is consistently shown by both experimental and CFD results. The peak Mach number is about 1.8 from the HYDRA prediction.
2. The high and low heat transfer stripes around the aft region of the winglet tip surface appear to be directly linked to transonic flow.
3. On the suction surface near-tip region, the winglet has a region of high Nusselt number close to the tip, whereas the flat tip has a region of high Nusselt number at a lower span-wise position than the winglet.

4. The tip Nusselt number increases with coolant injection, consistent for both tip clearances.
5. The tip Nusselt number increases with increased tip clearance as more mass flow passes over the tip. However, the trailing edge (90–100% C_{ax}) shows small variation in Nusselt number.
6. The tip film cooling effectiveness is generally higher for the 0.9% tip gap, especially from 30–80% C_{ax}. This may be due to cooling films that have been weakened or diluted by the increased over-tip leakage flow for the larger tip clearance.
7. The local heat transfer distribution on the blade tip is noticeably affected by the relative casing motion. With the relative moving casing travelling in the opposite direction to the flow, the Mach number is reduced at each node location. Inclusion of a moving casing leads to a smaller supersonic region over the tip. However, a significant portion of the tip leakage flow remains transonic with identifiable choked regions and shock wave structures.

Chapter 7

Aerodynamic Loss

7.1 Introduction

In this chapter, aerodynamic loss results for the flat tip, uncooled winglet and cooled winglet are provided. Detailed, spatially-resolved measurements of total pressure, yaw angle and Mach number are measured one-axial chord downstream of the blade row and total pressure loss coefficients are calculated and presented. Span-wise and mixed-out plane calculations are also given.

Section 3.5 introduces the traversing system and pressure probes used as well as the calibration and uncertainty analysis of the three-hole probe. The present chapter presents the aerodynamic loss results.

The traversed three-hole and single-hole probes obtain pressure measurements at 24 individual pitch-wise locations at eleven span-wise locations (from 75–100 percent of the engine equivalent blade span). Loss coefficient results for the flat tip with a 0.9 percent tip gap (see Section 7.2) are repeated in Figure 7.1, showing the resolution of the aerodynamic loss measurement points (indicated by "+").

This figure shows evenly-spaced grid points in the pitch-wise direction. To better resolve the local boundary layer characteristics at the near-tip region, the span-wise grid spacing has finer resolution close to the endwall. Also, the over-tip leakage (OTL) vortex swirl angle is represented in the figure, as indicated by the arrow. Note that the contour plots provided in this chapter indicate measurements taken downstream of the blade row looking upstream (see the "SS" and "PS" annotations in Figure 7.2).

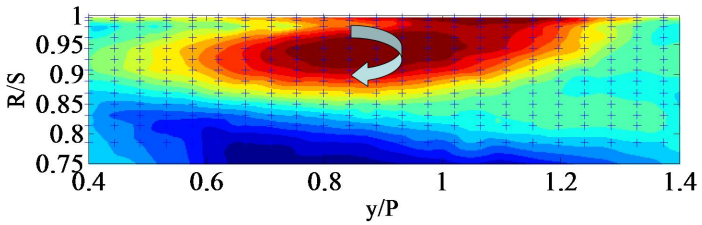

Figure 7.1: Total pressure loss coefficient Cp_0 contour indicating spatial resolution of data (note that the trailing edge is $y/P = 1$, the suction-side is $1 < y/P < 1.4$ and the pressure-side is $0.4 < y/P < 1$)

The results presented help to give insight into the OTL vortex. To help visualise the results, most contour plots in this chapter are presented for two pitch widths, though measurements were only taken through one pitch width.

7.2 Flat Tip Tip-Gap Survey

This section presents the aerodynamic loss results of a detailed tip gap survey of a flat blade tip. Total pressure loss coefficient, exit flow angle and Mach number contours are provided.

7.2.1 Total Pressure Loss Coefficient

Most definitions of total pressure loss coefficient (Cp_0) consider the pressure difference between the mainstream inlet total pressure and the local exit total pressure, normalised by the dynamic head. For low speed studies, $P_{t,\text{ exit}} - P_{s,\text{ exit}}$ is frequently used for the dynamic head. For compressible flow, however, Equation 7.1 is used. The dynamic head is determined by mass-averaging local dynamic pressure magnitudes along the mid-span of the cascade exit flow one axial chord length downstream from the blade trailing edge. The static pressures are determined using the isentropic relationship between the experimentally-obtained Mach numbers and total pressures.

$$Cp_0 = \frac{P_{t\infty,\text{ inlet}} - P_{t,\text{ exit local}}}{\frac{1}{2}\bar{\rho}_{\text{mid-span}}\bar{V}^2_{\text{mid-span}}} = \frac{P_{t\infty,\text{ inlet}} - P_{t,\text{ exit local}}}{\frac{1}{2}\gamma\bar{P}_{s,\text{ mid-span}}\bar{M}^2_{\text{mid-span}}} \tag{7.1}$$

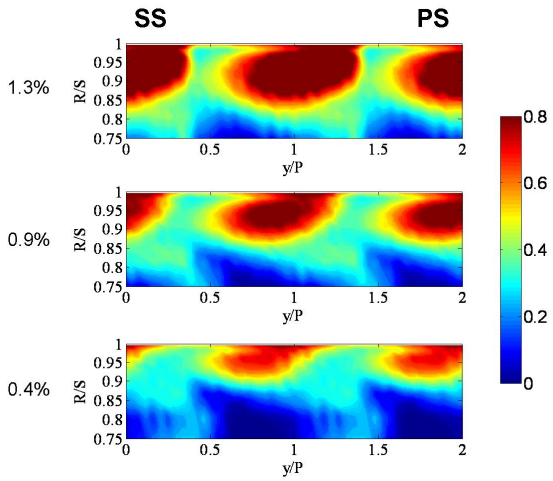

Figure 7.2: Total pressure loss coefficient Cp_0 contours of flat tip for 1.3, 0.9 and 0.4% tip gaps

Detailed loss coefficient results for tip clearances of 1.3, 0.9 and 0.4 percent are presented in Figure 7.2. Results show that the size of the loss core increases with an increase in tip clearance, as expected with additional OTL flow. In addition the centre of the loss core shifts to increased y/P values (further from the blade suction side) for increased tip gap.

7.2.2 Exit Flow Angle and Mach Number Distributions

The intensity of the secondary flows and the extent of the OTL vortices are further illustrated by the results which are given within Figure 7.3. Here, distributions of the exit yaw flow angle are relative to the metal exit angle (68°) and are given for all three tip gaps which are considered.

The results in Figure 7.3 show that magnitudes of the yaw flow angle increase within the OTL vortices, as these vortices become stronger and the tip leakage flow increases. This is illustrated by the arrows which are presented for the 1.3 percent tip gap, which also shows the spatial extent of one tip-leakage vortex. The positive flow angle indicates under-turning relative to the metal exit angle and the negative angle indicates over-turning relative to the metal exit angle.

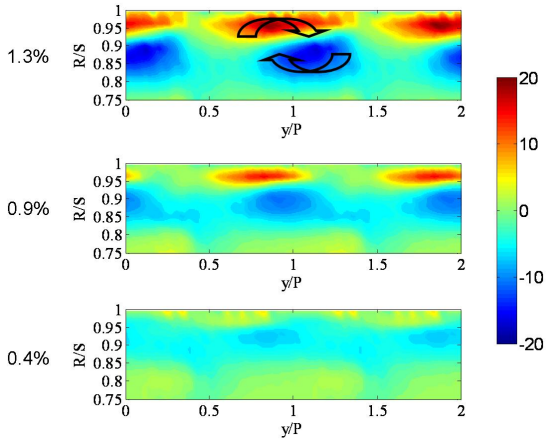

Figure 7.3: Yaw flow angle contours of flat tip for 1.3, 0.9 and 0.4% tip gaps

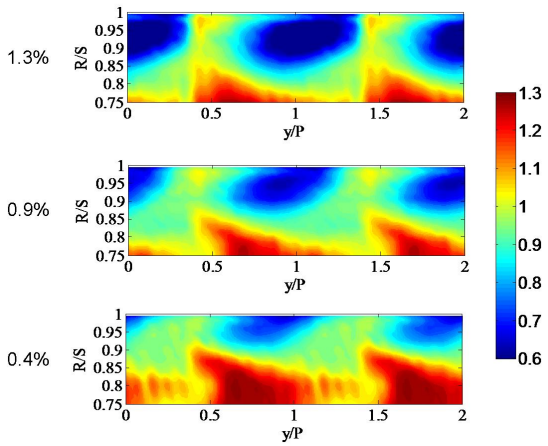

Figure 7.4: Exit Mach number contours of flat tip for 1.3, 0.9 and 0.4% tip gaps

Figure 7.4 presents the relative local Mach number distribution at the exit plane. Results show a decrease in Mach number where the OTL vortices are located. The passage flow has high relative Mach number where there is minimal amount of aerodynamic loss.

7.2.3 Mass-Averaged Overall Total Pressure Loss Coefficients

As a way of understanding the aerodynamic loss, pitch-wise mass-averaged total pressure loss coefficient contours for the 1.3, 0.9 and 0.4 percent tip gaps are presented in Figure 7.5. At $R/S = 0.75$, all three tip clearances have the same pitch-wise

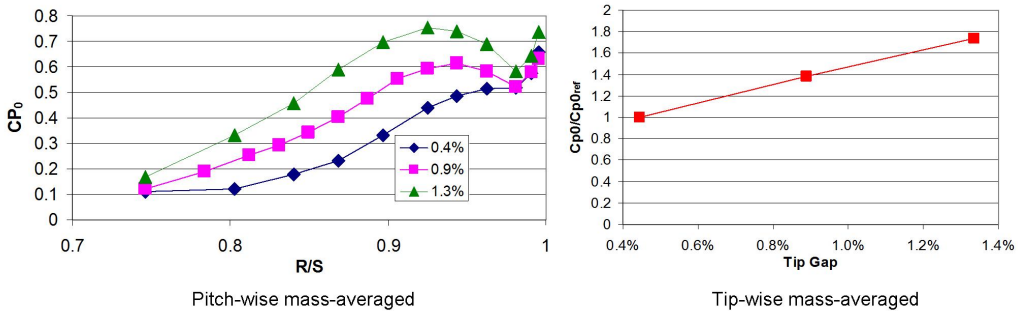

Figure 7.5: Pitch-wise mass-averaged and exit-plane mass-averaged total pressure loss coefficient contours of flat tip for 1.3, 0.9 and 0.4% tip gaps

mass-averaged Cp_0. Towards the tip, the larger tip clearances have noticeably higher values of Cp_0 until approximately $R/S = 0.96$, inside the assumed boundary layer.

The exit-plane mass-averaged total pressure loss coefficient variations with tip gap magnitude are also given in Figure 7.5. These data are normalised by the loss coefficient for the 0.4 percent tip gap. The loss results show the same general trend, with values increasing as the tip gap magnitude increases. For each 0.4 percent span increase, the mass-averaged loss coefficient increases by approximately 40 percent compared to the 0.4 percent tip gap.

A computational analysis has been conducted for the flat tip and results are provided in Section 7.6.

7.3 Uncooled Winglet Tip-Gap Survey

The section transitions to the aerodynamic loss investigation of the uncooled winglet. The results presented include contours of aerodynamic loss, exit flow angle and Mach number.

7.3.1 Kinetic Energy Loss Coefficient

The study of a flat tip helped to develop the experimental and analytical processing tools used for further investigations. General conclusions from the flat tip examination

are consistent with other aerodynamic loss studies. However, the main focus of this thesis is on the winglet blade design.

In transitioning to the winglet results and subsequently the cooled winglet results, the experimental definition of aerodynamic loss had to be reconsidered. Use of Equation 7.1 neglects any contribution of the coolant pressure and temperature. As an alternative, the loss in efficiency (in the form of kinetic energy) can be used to characterise the aerodynamic loss, derived in Haller and Camus (1984) and used by Mee (1992); Day et al. (1999) (see Equation 2.3). The ideal kinetic energy can be defined in several ways (Young and Horlock, 2006), and the present study assumes that the mainstream and coolant expand isentropically without mixing from their supply stagnation conditions to the exit static pressure. This definition for loss coefficient ζ, has been used by Day (1997) and is shown in Equation 7.2. When using ambient-temperature air as the coolant, the mainstream to coolant total temperature ratio is one, and therefore the temperatures and specific heats of the mainstream and coolant flow cancel.

$$\zeta = 1 - \frac{[\dot{m}_c C_{p_c} T_{t_c} + \dot{m}_m C_{p_m} T_{t_m}] \left[1 - \left(\frac{P_{s,\text{ local exit}}}{P_{t,\text{ local exit}}}\right)^{\left(\frac{\gamma-1}{\gamma}\right)_{\text{mean}}}\right]}{\dot{m}_m C_{p_m} T_{t_m} \left[1 - \left(\frac{P_{s,\text{ mid-span}}}{P_{t,\text{ inlet}}}\right)^{\left(\frac{\gamma-1}{\gamma}\right)_{\text{m}}}\right] + \dot{m}_c C_{p_c} T_{t_m} \left[1 - \left(\frac{P_{s,\text{ mid-span}}}{P_{t,\text{ coolant}}}\right)^{\left(\frac{\gamma-1}{\gamma}\right)_{\text{c}}}\right]} \tag{7.2}$$

In this equation, the numerator uses the local values of the static ($P_{\text{s, local exit}}$) and total pressure ($P_{\text{t, local exit}}$). The denominator is somewhat arbitarily based on the mid-span, mass-averaged exit static pressure ($P_{\text{s, mid-span}}$) and the average mainstream and coolant total pressures ($P_{\text{t, inlet}}$ and $P_{\text{t, coolant}}$ respectively) for a given tip geometry and tip clearance. It was desired to use the same ideal values in the denominator for all traversing locations. The experimental results for kinetic energy loss coefficient are presented in Figure 7.6 for both the 1.3 and 0.9 percent tip gaps. Like the flat tip, increases in tip gap result in a larger loss core as well as a shifting of the OTL vortex further away from the suction surface.

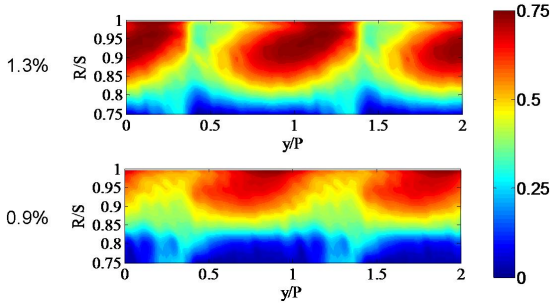

Figure 7.6: Kinetic energy loss coefficient ζ contours of uncooled winglet tip for 1.3 and 0.9% tip gaps

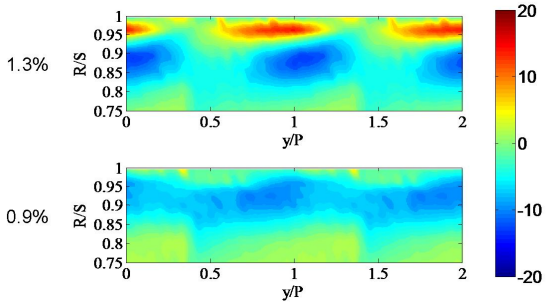

Figure 7.7: Yaw flow angle contours of uncooled winglet tip for 1.3 and 0.9% tip gaps

7.3.2 Exit Flow Angle and Mach Number Distributions

Contours of yaw flow angle are presented in Figure 7.7. Despite observing a large loss core, the magnitudes of the yaw flow angle are reduced compared to the flat tip results. In fact, the flow angle appears to correspond to similar results of the flat tip for a 0.4 percent smaller tip gap. In other words, the uncooled winglet flow angle contours for the 1.3 percent tip gap are similar to the flat tip flow angle contours for the 0.9 percent tip gap. The uncooled winglet appears to have less over-turning and under-turning than the flat tip.

Contours of exit Mach number are presented in Figure 7.8. Like the flat tip, the region of low Mach number is associated with the loss core.

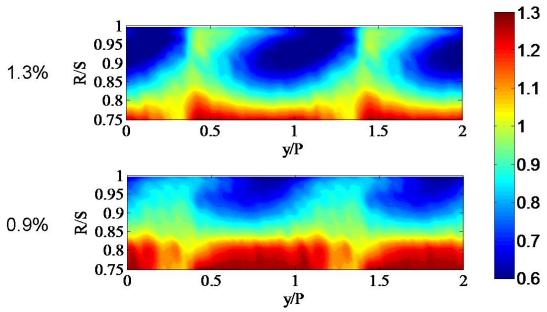

Figure 7.8: Exit Mach number contours of uncooled winglet tip for 1.3 and 0.9% tip gaps

7.3.3 Mass-Averaged Overall Kinetic Energy Loss Coefficients

Pitch-wise mass-averaged kinetic energy loss coefficient as well as kinetic energy loss at a mixed-out plane were calculated and will be addressed in Section 7.5 in order to compare uncooled winglet results to those with coolant injection.

7.4 Initial Cooled Winglet Data (All-SI40 Model)

Just prior to the rig relocation, an aerodynamic loss examination of a cooled winglet was carried out. This section briefly discusses the blade used in the initial study and the results of both the initial as well as the follow-up investigations.

The cooled winglet blade is described in Section 3.3.3. The original cooled winglet blade was made entirely of SI40. This allowed for a relatively large plenum inside the blade to help still the flow (see Figure 3.12).

Results from this initial testing is shown in Figure 7.9 for a 0.9 percent tip gap and one pitch width. There was virtually no loss associated with the cooled winglet and the cooled winglet results do not appear periodic, even at $R/S = 0.75$.

Based upon a more thorough look at data as well as an examination of the blade, a hypothesis was developed that suggested that the cooled winglet deformed and twisted under load. Figure 7.10 shows an exaggerated schematic with the potential cause of the low aerodynamic loss as the deformation effectively decreases the tip gap, reducing aerodynamic loss.

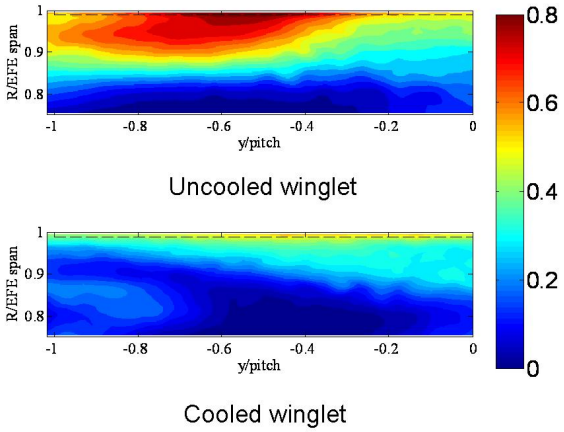

Figure 7.9: Initial kinetic energy loss coefficient ζ contours of cooled winglet tip with a 0.9% tip gap (all-SI40)

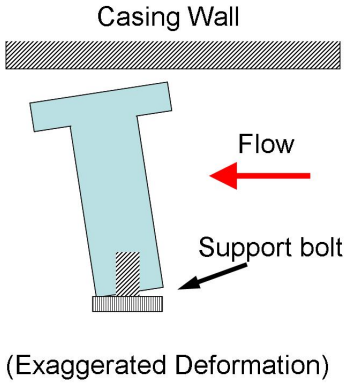

Figure 7.10: Schematic of suspected deformation using an all-SI40 winglet blade tip, reducing effective tip clearance

To test this hypothesis, a number of tests were performed at the new lab. Results from these tests revealed that even deformation of an all-SI40 uncooled winglet blade tip caused a significant decrease in loss. Therefore, it is concluded that the all-SI40 blade cannot be used with the HSLC. A new cooled winglet design was manufactured using a 30 mm SI40 tip mounted on the stainless steel base blade, as previously used for uncooled winglet testing (see Figure 3.12).

The coolant reservoir inside the blade tip is considerably smaller. The pressure readings are not necessarily measured in stagnation regions, however the measurement of pressure and temperature inside the reservoir are assumed to be stagnation. Nevertheless, this design was not only more realistic, it was required to accommodate the necessarily added metal base.

7.5 Cooled Winglet Tip Gap Survey Using Ambient Air as Coolant

With a new cooled winglet test blade in hand, an investigation of the effect of coolant injection and tip clearance on aerodynamic loss is considered. This section addresses the effects of temperature ratio, followed by a tip gap survey of the cooled winglet using ambient-temperature air as the coolant.

7.5.1 Use of "Colder Coolant"

As addressed in Chapter 6, for cooled winglet heat transfer testing, it was important to have a temperature ratio high enough to obtain reasonable non-negative film cooling effectiveness values. Use of the vortex tubes required a trade off between coolant pressure and temperature. In order to obtain a higher temperature ratio, there was not enough volume of air in the current configuration of the rig to feed three blades, so coolant was fed to one blade only.

To maintain periodicity, however, aerodynamic loss measurements were done with injections of uncooled air for all three blades.

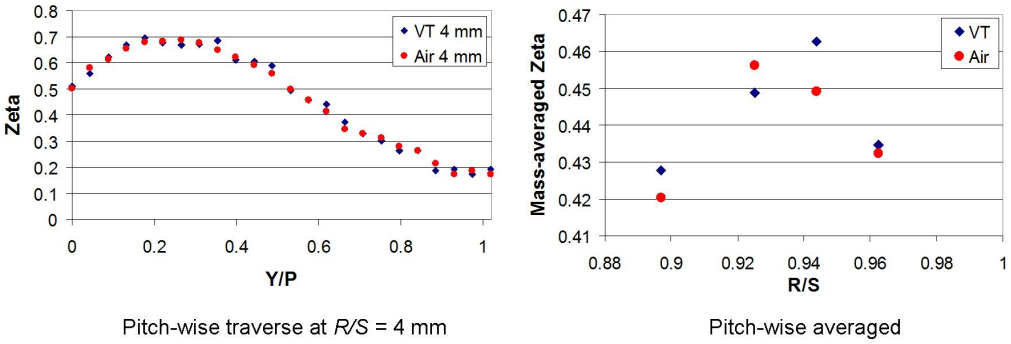

Figure 7.11: Kinetic energy loss coefficients ζ of cooled winglet tip with "cold" coolant for 0.9% tip gap

Nevertheless, a study was performed to determine the effect of coolant temperature ratio on aerodynamic loss. Use of the vortex tube allowed for a coolant to mainstream total pressure ratio of 1.01 (to prevent ingestion of mainstream flow) and a coolant to mainstream total temperature ratio of 1.06. Results in Figure 7.11 show that for the temperature and pressure ratios tested, temperature ratio has a negligible effect on aerodynamic loss. Plots of pitch-wise mass-averaged loss coefficient for R/S of 6, 8 and 11 mm show consistent results to those of $R/S = 4$ mm.

Cooled winglet testing under these colder-coolant conditions has additional problems. It is unknown if any of the cooling holes in a given cooled winglet are choked or if some of the cooling holes are not injecting coolant. Since the pressure and temperature ratios tested had a negligible effect on aerodynamic loss, testing with operationally-representative pressure ratios with a low temperature ratio is conducted.

7.5.2 Kinetic Energy Loss Coefficient

Using air at ambient temperature for the coolant, a tip gap survey is conducted on the winglet tip for tip clearances of 1.3 and 0.9 percent. The experimental results are presented in Figure 7.12 for both the 1.3 and 0.9 percent tip gaps with coolant injection using ambient-temperature air. Like the flat tip and the uncooled winglet, increasing the tip gap results in a larger loss core.

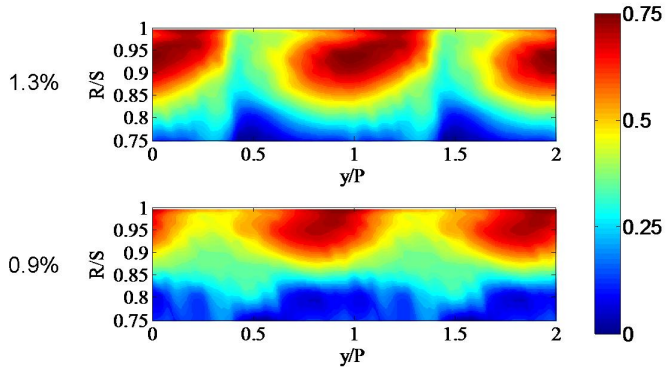

Figure 7.12: Kinetic energy loss coefficient ζ contours of cooled winglet tip for 1.3 and 0.9% tip gaps

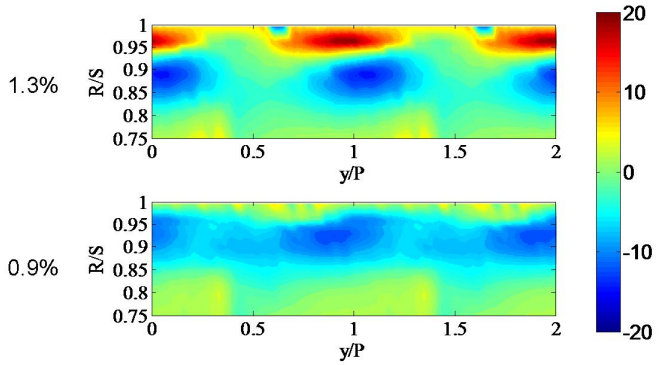

Figure 7.13: Yaw flow angle contours of cooled winglet tip for 1.3 and 0.9% tip gaps

Compared to the uncooled winglet results in Figure 7.6, the cooled winglet results in Figure 7.12 appears to slightly reduce the size of the OTL loss core. Section 7.5.4 provides further comparison between the uncooled and cooled winglets.

7.5.3 Exit Flow Angle and Mach Number Distributions

Contours of yaw flow angle are presented in Figure 7.13. Though coolant injection seems to slightly reduce the size of the loss core, coolant injection appears to increase the yaw flow angle, but only slightly. The cooled winglet flow angle is still less than that of the flat tip for the same tip gap.

Contours of exit Mach number are presented in Figure 7.14. Like the flat tip and the uncooled winglet, the region of low Mach number is associated with the loss core.

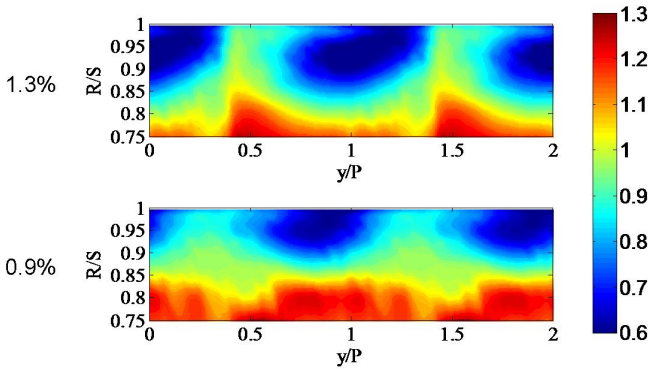

Figure 7.14: Exit Mach number contours of cooled winglet tip for 1.3 and 0.9% tip gaps

There does not appear to be much of a difference between the uncooled and cooled winglets with respect to exit Mach number.

7.5.4 Pitch-Wise Mass-Averaged Overall Kinetic Energy Loss Coefficients

Another way to compare the winglet with and without cooling injection is by examining the pitch-wise averaged kinetic energy loss as well as the loss at a mixed-out plane.

Figure 7.15 shows the pitch-wise mass-averaged kinetic energy loss coefficient for both the uncooled and cooled winglets for 1.3 and 0.9 percent tip clearances. In general, an increase in tip clearance results in higher loss coefficient for both the uncooled and cooled winglets, like the flat tip (see Figure 7.5). The difference is more pronounced for the uncooled winglet. For radii greater than 95 percent, the smaller tip clearance actually has a higher average loss coefficient.

When considering the pitch-wise mass-averaged aerodynamic loss for both tip gaps, the coolant consistently decreases the loss coefficient from 80-95% of engine-equivalent span, as shown in Figure 7.16. For the larger tip gap, the difference in loss coefficients for the uncooled and cooled winglets is greater.

Based on earlier work by Dzung (1971), Day (1997) provided a motivation and framework for determining aerodynamic conditions at a mixed-out plane. This method

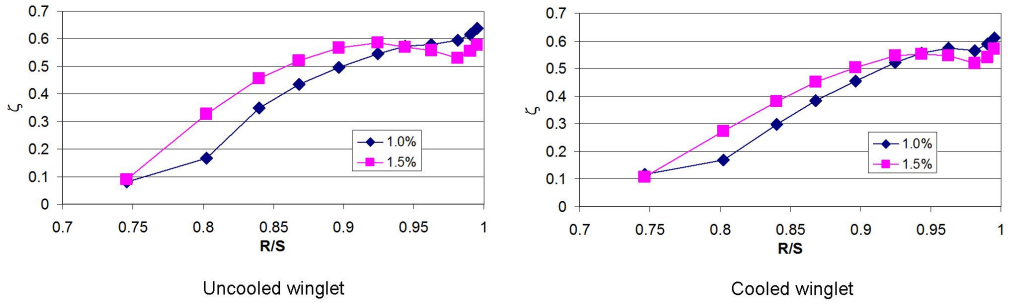

Figure 7.15: Tip gap comparison of pitch-wise mass-averaged kinetic energy loss coefficient ζ contours of uncooled and cooled winglet

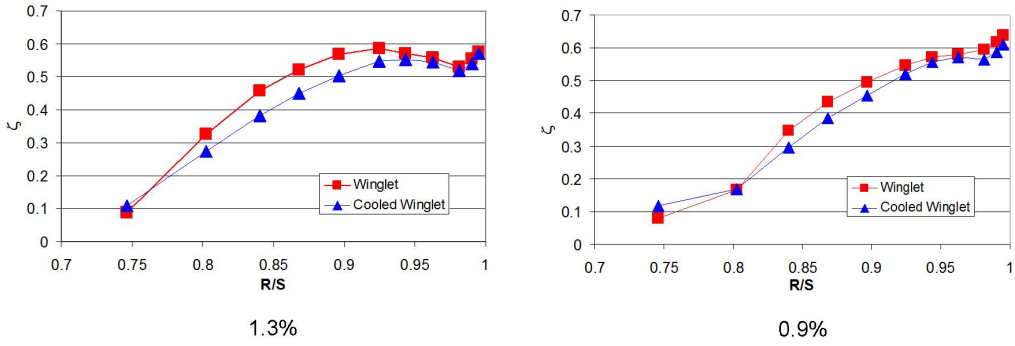

Figure 7.16: Coolant injection comparison of pitch-wise mass-averaged kinetic energy loss coefficient ζ contours of for 1.3 and 0.9% tip gaps

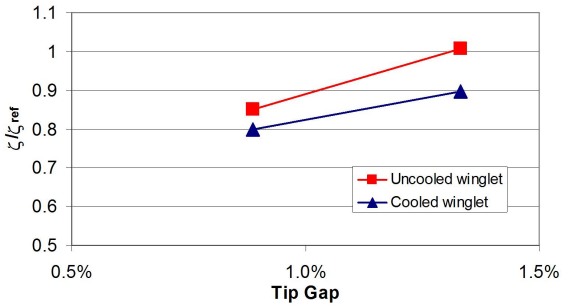

Figure 7.17: Kinetic energy loss coefficient ζ values at mixed-out plane for 1.3 and 0.9% tip gaps

was used in the present study to calculate the kinetic energy loss coefficient at a mixed-out plane.

The local static and total pressures in the numerator of Equation 7.2 are replaced with the static and total pressure at the mixed-out plane. These results are shown in Figure 7.17. The results are normalised by the loss coefficient of the uncooled winglet with 1.3 percent tip gap. The results show that the cooled winglet results in a lower aerodynamic loss than the uncooled winglet, which may be indicative of an aerodynamic sealing effect created by the films, which is thought to have reduced over-tip leakage, as also observed by Krishnababu et al. (2008).

7.6 Aerodynamic Loss Computational Results

This section provides computational work of the HSLC research group. The computational study was performed by Dr Zhang while all members of the research group jointly analysed and discussed the results. These results were presented in O'Dowd et al. (2010a). Results are provided here to not only show agreement with the experimental results (which were used to validate the CFD model), but also to help understand some of the flow phenomena of the OTL flow. This section will conclude with a discussion on the effects of a moving casing wall.

A computational analysis of the cooled winglet has yet to be performed and the uncooled winglet will not be discussed in this section. Only the predicted flat tip results are presented.

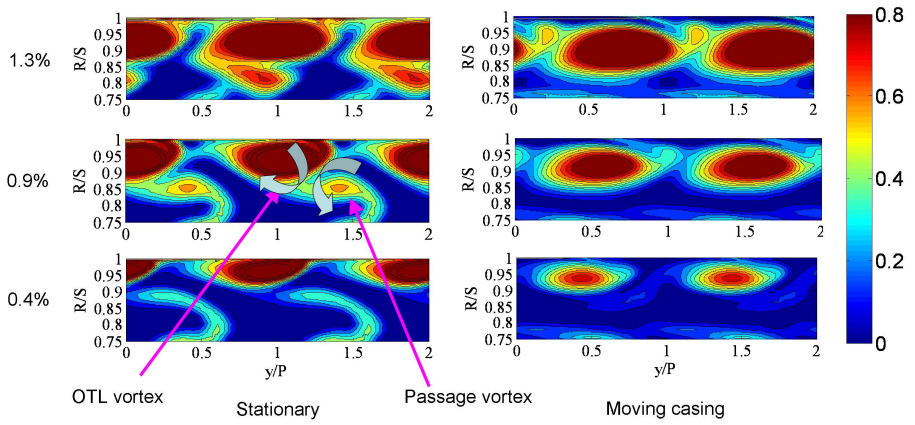

Figure 7.18: Predicted total pressure loss coefficient Cp_0 of flat tip for 1.3 and 0.9% tip gaps (stationary and moving casing)

Predicted total pressure loss coefficient Cp_0 is presented in Figure 7.18 and shows overall good agreement to the experimental results in Figure 7.2, especially in regard to the presence of total pressure losses which are advected with the tip leakage vortex. Like the experimental results, the OTL vortex advects away from the upstream blade's suction side for the 0.4 and 0.9 percent tip gaps. Similar trends are described by Yamamoto (1989) and Tallman and Lakshminarayana (2001b). The extent of the vortex core also increases with tip gap height, with the largest total pressure signature evident for the 1.3 percent tip gap.

The most important difference between experimental and numerical results is in relation to the passage vortex signatures. In the experimental results given in Figure 7.2, total pressure variations from the passage vortices are barely noticeable since their presence is overshadowed by strong tip leakage vortices. In addition, the traversing resolution may not be detailed enough to resolve the passage vortex signature. Cp_0 variations from the passages vortices, however, are much more apparent for all three tip gaps presented in Figure 7.18, where the passage vortices are rotating anticlockwise as indicated in the figure for the 0.9 tip gap. For the 1.3 percent tip gap, the passage vortex signature is positioned around $y/P = 0.90$ and $R/S = 0.82$, while for the 0.9 percent tip gap, the passage vortex signature is positioned around $y/P = 1.4$ and $R/S = 0.87$. As the tip clearance increases, the loss coefficients associated with

the passage vortex not only increases in magnitudes, its location changes relative to the OTL vortex.

A study of the effect of casing motion on total pressure loss coefficients is also performed and is also presented in Figure 7.18. The casing speed is representative of a high-pressure turbine designs. Like results from Yaras and Sjolander (1992a); Palafox et al. (2008); McCarter et al. (2001), the moving casing seems to cause the OTL vortex to shift toward the blade suction surface. The relative casing motion also causes the OTL vortices to detach such that they are positioned some distance from the casing surface. Overall, the relative casing movement appears to have a minor impact on the size of the OTL vortex, but this impact increases as the tip clearance decreases.

Mass-averaged total pressure loss coefficient variations with tip gap magnitude, both with and without casing motion, are given in Figure 7.19. These results are normalised by the loss coefficient for the 0.9 percent tip clearance. The experimentally and computationally determined aerodynamic loss results show the same general trend, with values increasing as the tip gap magnitude increases. With no casing surface motion, experimental and HYDRA prediction results are also in fairly good agreement, especially for larger OTL flow magnitudes. With the moving casing surface, total pressure loss coefficients are consistently lower than stationary casing values at each tip gap.

7.7 Further Discussion of Results

This chapter has considered the effects of tip gap, geometry and coolant injection on aerodynamic loss. This chapter includes experimental and predicted aerodynamic loss, exit flow angle and exit Mach number results for the flat tip, uncooled winglet and cooled winglet. To the best of the author's knowledge, this is the first time that cooled winglet results have been presented under transonic, engine-realistic conditions.

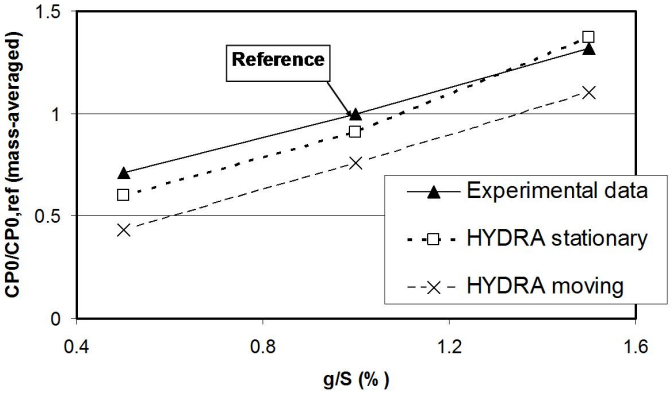

Figure 7.19: Nomalised mass-averaged total pressure loss coefficient Cp_0 variations with tip gap magnitude, both with and without casing motion for three different tip gaps of 1.3, 0.9 and 0.4%

While Chapter 6 sought to answer the question of how to be able to cool the winglet, this chapter seeks to answer the fundamental question: will the winglet blade tip reduce aerodynamic loss when tested under high-speed engine-realistic conditions?

There has been no surprise as to the effect that changing the tip gap has on aerodynamic loss. With the increased tip clearance, more mass flow advects over the tip, which mixes with the passage flow resulting in increased loss. In addition, with the larger tip gap, the OTL flow has higher momentum, which extends the mixing to further away from the blade suction side.

There have been two major observations made during this work. The first is the size of the loss core associated with the winglet tips. The design philosophy for the winglet is to reduce OTL flow by effectively changing the pressure at the gap exit. However, as it has been shown in Chapters 5 and 6, the flow over most of the blade tip is choked and therefore not driven by the pressure difference across the tip from the pressure to the suction side. Changing the back pressure will not change the mass flow across the tip (for pressure ratios less than the critical pressure ratio). Therefore, the capability of the winglet to reduce aerodynamic loss under high-speed conditions is unknown. Experimental work in the present chapter, however, is confined to a linear cascade with no moving endwall.

The leading edge and crown region of the winglet is subsonic and not choked. Therefore the winglet may be effective at reducing mass flow over this region. Moreover, with a moving casing, the size of the supersonic region over the tip is reduced. The moving casing has been shown to reduce the leakage flow over a winglet tip (Wadia and Booth, 1982). Therefore, actual winglet results in an engine-realistic environment may be better than what has been presented here. However, it is not sufficient to suggest that because it works well in a low speed environment, a moving casing in a high-speed environment will make up the difference.

What has not been shown experimentally, but has been observed computationally is how the loss core is formed with the winglet. Predicted results on the uncooled winglet by Dr Zhang (Zhang, 2010) and analysis by the HSLC research group has shown that for a flat tip, the OTL flow mixes with the passage flow and the shear layer between the two helps to creating a vortex that advects downstream (O'Dowd et al., 2010a). Analysis for the uncooled winglet tip, on the other hand, shows that due to the effect that the crown region has on reducing loss, OTL loss appears to be reduced. However, the blunt pressure side lip overhang at the trailing edge of the uncooled winglet leads to additional losses. The OTL vortex and the loss from the pressure side lip overhang mix and form a large vortex core downstream of the blade row.

The second major observation has been the effect that cooling injection has on aerodynamic loss. Some studies have shown that coolant injection can reduce leakage flow in the gap (Wadia and Booth, 1982), possibly because the coolant creates a blockage (Krishnababu et al., 2008). Such results have been not previously been observed for a cooled winglet tip under transonic conditions.

7.8 Summary

Blade tip aerodynamic loss results from experimental and numerical investigations are presented for engine representative conditions with an exit Mach number of 1.0, and an engine representative Reynolds number of 1.27×10^6. These results are presented

for three different tip gaps of the flat tip and two different tip gaps of the uncooled and cooled winglets. As such, the present results are complementary to the heat transfer results which are presented in Chapters 5 and 6. Included in this chapter are detailed distributions of stagnation pressure losses and kinetic energy losses as well as yaw flow angle and exit Mach number, which are measured in the transonic flow-field downstream of the blade row. These measurements are obtained using an extensively calibrated three-hole probe and a single-hole probe.

The following detailed conclusions pertain to the results.

1. Local total pressure data and mass-averaged total pressure loss coefficients show that the size of the loss core decreases as the tip gap decreases as commonly expected. This expected trend serves to confirm the validity of the data. Greater loss magnitudes are then associated with larger leakage vortices, with the centre of the vortex located further away from the blade suction side as the tip gap flow increases.
2. Magnitudes of the yaw flow angle increase within over-tip leakage vortices, as these vortices become stronger and the tip leakage flow increases. With the smallest tip gaps tested (0.4 percent for the flat tip and 0.9 percent for the winglets), though there is still noticeable pressure loss, non-uniformity in the yaw flow angle is reduced compared to distributions present for higher tip gap magnitudes.
3. The cooled winglet aerodynamic loss coefficient results show a decrease in aerodynamic loss compared to the uncooled winglet. This is possibly due to an aerodynamic sealing effect created by the films.
4. Aero-loss data seem to suggest that the size of the loss core associated with the over-tip leakage vortex is slightly reduced when the coolant injection is introduced. The same observation applies to both tip gaps.
5. CFD results are consistently in good agreement with the measured experimental results, which validates CFD modelling and predictive capabilities for prediction of blade tip aerodynamic losses at the present conditions.

6. Inclusion of the relative casing movement has a relatively small impact on the size of the over-tip leakage vortex for the 0.9 and 1.3 percent tip gaps of the flat blade tip, with more noticeable impact for the 0.4 percent tip gap. The moving casing wall also appears to cause the tip leakage vortex to be detached from the casing endwall. Finally, the inclusion of relative casing movement consistently reduces the mass-averaged total pressure loss coefficient consistently for all tip clearances, which is expected because the friction force reduces the OTL in general.

Chapter 8

2-D Correction on Corner Conduction Effect

8.1 Introduction

This chapter addresses a problem with most experimental heat transfer studies, that of accounting for the corner conduction effect. A brief introduction to the corner conduction effect is included in Section 2.4 and is summarised here. Details of the transient heat transfer measurement and analysis process are provided in Chapter 4.

When two adjoining surfaces (see Figure 8.1), experience a step change in surface temperature, conduction not only takes place into the solid from one surface, but also from the adjacent surface.

The 2-D corner effect is rarely addressed, especially in experimental examinations. As there is no closed-form analytical solution to the 2-D non-steady conduction equation, studies often assume that the solid is semi-infinite and 1-D, even near a corner, especially if the material has low thermal conductivity. However, as will be shown in the next section, this is a poor assumption for regions close to a corner.

Most examinations of corner conduction are computational. If experiments are involved, a complicated and computationally-expensive 3-D conjugate heat transfer analysis is sometimes used to correct for the corner conduction effect (Lin and Wang, 2002).

Though He and Oldfield (2011) provided the original motivation and insight into the present study, it is acknowledged that the work of Kingsley-Rowe et al. (2005) is

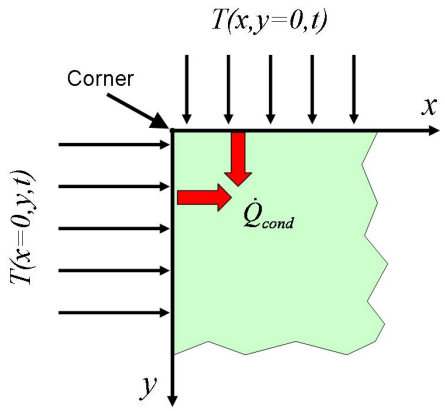

Figure 8.1: Schematic of corner and effect of 2-D conduction

similar to the work in the present study, as it requires a computationally-determined correction factor, but their approach only considers lateral conduction away from corners. They approximated a solution to the 2-D non-steady conduction equation (see Equation 8.2 in Section 8.4) using a correction factor that depended on the solution to the 1-D non-steady conduction equation (see Equation 4.7 in Section 4.5.1). As demonstrated in Chapter 4, using the analytical solution to the 1-D non-steady conduction equation in the present work had more uncertainty and more computational expense than the Impulse method and therefore was not used for the heat transfer analysis technique in the present study. For this reason, the approach by Kingsley-Rowe et al. (2005) was not used in to correct for the corner effect.

Though some computational work is necessary, the present study aims to serve as a good compromise between the uncertainty of a one-dimensional experimental analysis and the computational expense of a full 3-D computational model coupled to experimental data.

The remainder of this chapter begins by providing details of the computational setup, including a mesh-independence study. The computational program is then used to obtain surface temperature traces for a set of initial and boundary conditions in order to determine the effect of the semi-infinite 1-D conduction assumption. A correction approach is then described and verified for use on experimental data. At

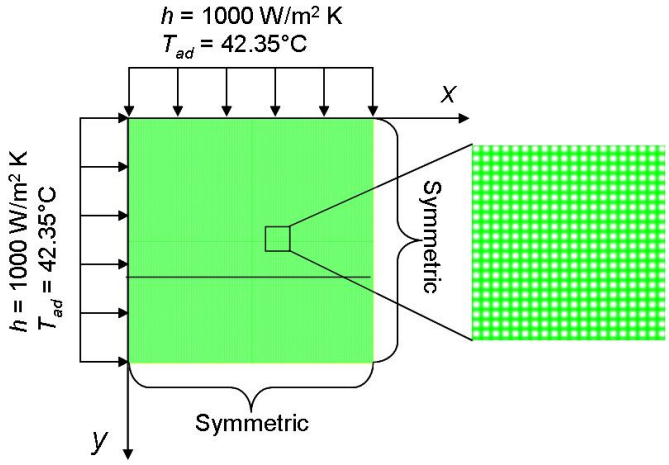

Figure 8.2: Computational domain and boundary conditions

the end of the chapter, results are presented for the correction approach that is applied to experimental data.

8.2 Computational Setup and Details

The 2-D corner correction study begins with understanding what effect the corner has on heat transfer results when the semi-infinite 1-D assumption is used. It is important to have access to a baseline solution as a consistent reference point. As there is no known analytical solution to the 2-D non-steady conduction equation, a 2-D finite volume numerical conduction solution is pursued to serve as a reference solution. GAMBIT version 2.3.16 software is used for geometry and mesh generation. Figure 8.2 presents the computational domain and mesh employed for the present study. The computational domain consists of a 2-D square, 10 mm by 10 mm. FLUENT version 12.0.16 of the ANSYS 12.0 package is employed to solve the energy equation with constant material properties within the domain.

There are two different regions of boundary conditions employed, as shown in Figure 8.2. The two sides adjacent to the solid corner include prescribed heat transfer coefficients ($h = 1000\,\mathrm{W/m^2K}$) and film (or driver) temperature ($T_{ad} = 42.35°\mathrm{C}$). The heat transfer coefficient is a nominal value for the flat tip leading edge experimental

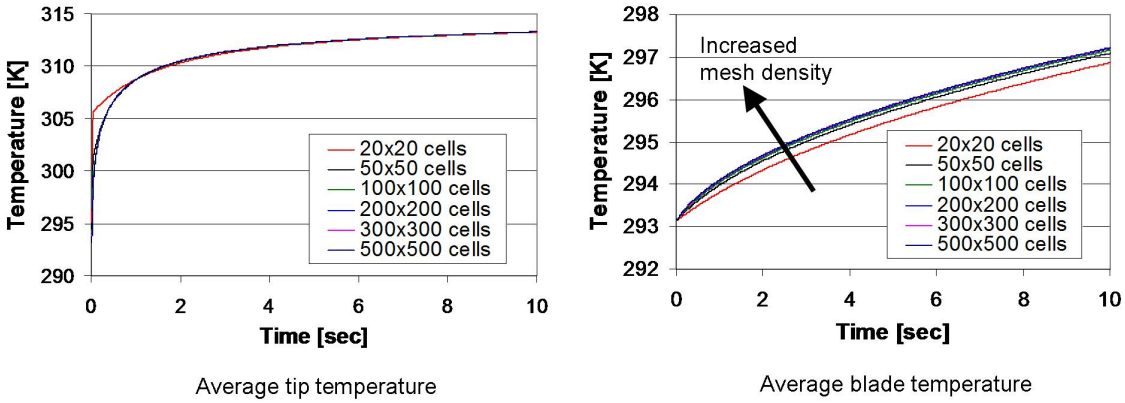

Figure 8.3: Mesh independence achieved for at least 100 cells for both top-averaged and solid-averaged temperatures

results. The film temperature is a transient boundary condition and is a typical near-step change for an experimental run (20–42.35°C). The driver temperature gradually increases for 0.042 s before becoming constant (42 time steps with $\Delta t = 0.001$ s), consistent with experimental data. The other two sides of the solid use symmetric boundary conditions.

In order to ensure a stable solution, the time step chosen must meet the Fourier number requirement for a solid domain, as described by He and Oldfield (2011) and shown in Equation 8.1.

$$\alpha \frac{\Delta t}{\Delta x^2} < 0.5 \tag{8.1}$$

where $\alpha = \frac{k}{\rho C_p} = 1 \times 10^{-7}$.

The mesh has a total grid size of 40,000 cells (200x200). All solutions presented are grid-independent, which is verified by negligible changes to predicted surface temperature quantities as the grid density is increased. Results presented in Figure 8.3 clearly show that a mesh width of 20 cells is not enough. Negligible changes are observed for grid widths between 100 and 500 cells. A grid width of 200 cells is chosen for this study.

Following the computations, additional analysis and visualisation of the solutions are accomplished using MATLAB and Excel.

8.3 Uncertainty of Heat Transfer Coefficient Near Corner

Since the geometry, mesh and thermal loading are symmetric, only the top surface is examined. During the transient test, the prescribed heat transfer coefficient is held constant and the time-history of the top surface temperature is recorded as a transient film temperature is applied.

Note that, when specified, location percentages refer to the percent of the solid width (10 mm) where 0 percent is at the corner and 100 percent at the maximum depth ($x = 10$ mm for this study, see Figure 8.1). The penetration depth will be shown to be smaller than this width dimension.

A computational run of just under 60 seconds (real-time) shows that time traces of the temperatures throughout the top surface slowly (due to low conductivity) converge towards the film temperature.

As it is done during the experimental analysis, only five seconds of the temperature trace following the temperature step change is examined. Though the length of the penetration depth is generally not an issue for the points away from the corner, penetration depth has a larger effect close to the corner.

Figure 8.4 presents the temperature time histories at discrete locations on the top surface, which shows the effect of the corner. As the distance from the corner increases, it takes longer for the temperature to approach the driver temperature. In fact, the rate of temperature change is decreasing.

In addition, from 2–10 mm (20–100 percent) away from the corner, very small changes in the temperature trace are observed, especially for less than 5 seconds (the time that is used for analysis).

The heat transfer coefficients at each node location are calculated using the heat transfer measurement and analysis techniques discussed in Chapter 4. These results are shown in Figure 8.5. The red dashed line is the exact solution (the prescribed boundary condition) and the blue solid line is the heat transfer coefficient obtained following the existing procedure assuming semi-infinite 1-D conduction.

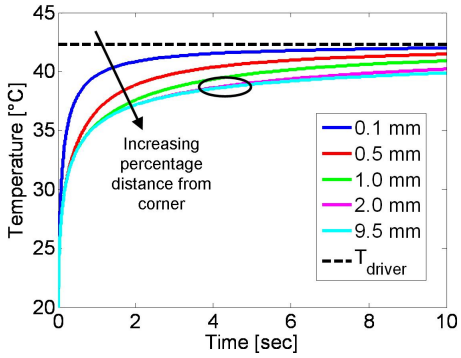

Figure 8.4: Temperature time history at discrete distances from the corner

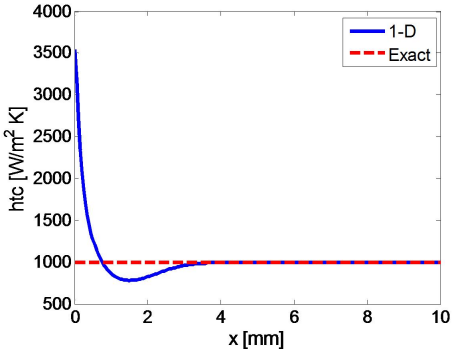

Figure 8.5: Results if semi-infinite 1-D conduction is assumed at the corner

The solution shows an overestimated error in h of nearly 300 percent at the top corner (27.5 percent at $x = 0.5\,\text{mm}$). The heat transfer coefficient then decreases, approaches the prescribed h until a transition occurs (at $x = 0.75\,\text{mm}$ in Figure 8.5), where h is underestimated by up to 20 percent. After a low point in predicted h (at $x = 1.5\,\text{mm}$), the heat transfer coefficient finally approaches the prescribed h at about $x = 4\,\text{mm}$. Note that if 10 seconds of data is used for the analysis, the non-1-D region extends to just over $x = 4\,\text{mm}$.

This overestimation is significantly larger than the lateral coefficient error that has been reported of up to 20 percent (Yan and Owen, 2002). Aside from the transition from overestimate to underestimate, h does not settle down until nearly 4 mm, showing the importance of the issue.

This transition can be understood by examining the temperature and the 1-D calculated heat flux at several distinctive surface locations, as shown in Figure 8.6. Here three locations are considered: 5, 20 and 95 percent of the width. What makes this figure interesting is the sensitivity of temperature changes. The 5 percent location (over-estimated h) is clearly different from the other two locations for all three plots, especially in the $Q - T$ plot. The difference between the 20 percent location (largest under-estimation) and the 95 percent location (near-exact) appear to be minor. In the $Q - T$ plot, the lines diverge, but the time that this begins to happen is between 1–5 seconds after the step-change in film temperature. This small divergence is enough to create a 20 percent difference in h.

The figure highlights a trade-off that takes place when determining the time used to analyse the data. If a shorter time is used, there is less divergence between the temperature and heat flux traces. However, this means that there is a smaller change in temperature from the initial temperature, which increases uncertainty in obtaining h. If a longer time is used, there is a larger change in temperature from the initial temperature, which improves the regression analysis to obtain h, however penetration depth becomes more of a problem which increases uncertainty in obtaining h. The 5 seconds chosen is determined to be a good compromise between the two constraints.

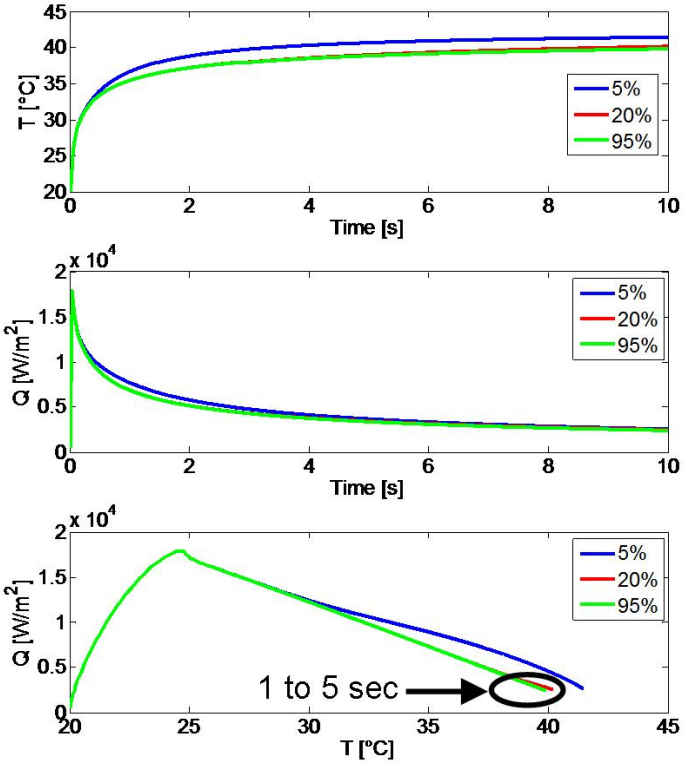

Figure 8.6: Time histories of temperature (top) and calculated 1-D heat flux (middle) as well as plot of temperature versus heat flux (bottom) for different surface locations

It is clear, then, that the semi-infinite 1-D conduction is a poor assumption near a corner and the next section discusses how these results can be corrected.

8.4 2-D Corner Correction Approach

Different attempts were made to correct for the corner conduction effect. The first idea was to correct the top wall based on knowledge of the sidewall heat transfer, but this approach failed to satisfactorily correct h. A new methodology was then considered with a focus on the lateral locations on the same surface, as opposed to the adjacent sidewall. Studies that examine lateral conduction typically consider locations away from edges (which tend to observe smaller gradients). The present study examines lateral conduction close to the corner, but where this lateral conduction effect diminishes further away from the corner, as the region becomes more 1-D.

The first approach using this methodology attempted to split the contributions from two surfaces along the two surfaces. The 2-D non-steady heat equation is provided in Equation 8.2. Equation 8.3 shows the contribution of T_x in the x direction. Likewise, Equation 8.4 shows the contribution of T_y in the y direction. In these equations, $\alpha = k/\rho C_p$ (thermal diffusivity). Note that y is the direction normal to the surface and x is the lateral direction (see Figure 8.1). The linear nature of the equation means that the contributions should be able to be superimposed.

$$\frac{\partial T}{\partial t} = \alpha\Big(\frac{\partial^2 T}{\partial x^2} + \frac{\partial^2 T}{\partial y^2}\Big) \tag{8.2}$$

$$\frac{\partial T_x}{\partial t} = \alpha\frac{\partial^2 T_x}{\partial x^2} \tag{8.3}$$

$$\frac{\partial T_y}{\partial t} = \alpha\frac{\partial^2 T_y}{\partial y^2} \tag{8.4}$$

The x- and y-components can only be analytically split if the relationship in Equation 8.3 is valid. If it is valid, then the time-derivative of temperature obtained from experiments can be subtracted from Equation 8.2, which leaves the equation exclusively in terms of y. This would also make this problem entirely analytical.

When attempting to correct the data, it was determined that the x- and y-components were *largely* coupled with time and therefore could not be analytically split without introducing new errors.

Elements of this approach, however, showed merit (specifically considering Equation 8.3), and were used in developing the final approach, which is described in the next section.

8.4.1 Lateral Gradient Construction and Correction Method

This section introduces the method and provides details on its implementation.

8.4.1.1 Method Introduction

The goal for the development of the new lateral corner correction algorithm is to reconstruct the temperature trace at each location to a temperature trace that is 1-D-equivalent. For example, when considering Figure 8.4, the temperature trace for the 1 percent location will be reconstructed using a correction variable in order to match the temperature trace for the 95 percent location (which is near-exact). This approach requires a computational solution of experimental data using finite difference equations.

The notations used in this approach distinguish between two regions. One region is considered 1-D, where the lateral effect of heat transfer is negligible (e.g. 95 percent). The second region is considered 2-D, where lateral heat transfer has an effect (e.g. 1 percent). Subscripts "1-D" and "2-D" will be used to distinguish the two regions and "*cor*" in the subscript signifies a corrected value. n in the superscript is a particular time step and i is a spatial node in the x direction. The general reconstruction is shown in Equation 8.5

$$T^{n+1}_{1-D,cor} = T^{n}_{1-D,cor} + \Delta T^{n}_{2-D} \tag{8.5}$$

where

$$\Delta T^{n}_{2-D} = T^{n+1}_{2-D} - T^{n}_{2-D} \tag{8.6}$$

The equations above are rather straightforward, where at each time step, the temperature difference is being added to the previous value. When using these equations, the original temperature traces are reconstructed (as shown in Figure 8.4).

Equation 8.5 is then modified in order to construct a 1-D equivalent surface temperature from a measured 2-D temperature at the same point and at adjacent points. Those 2-D temperatures at the adjacent points at the given time instant are to be used to construct the spatial gradient for that instant, which is used to form the correction term, which is seen in Equation 8.7 and defined in Equation 8.8.

$$T^{n+1}_{1-D,cor} = T^{n}_{1-D,cor} + \Delta T^{n}_{2-D} - \Delta T^{n}_{cor,lateral} \tag{8.7}$$

where ΔT^{n}_{2-D} is the same as Equation 8.6 and

$$\Delta T^{n}_{cor,lateral} \approx \alpha \frac{T^{n}_{i-1} - 2T^{n}_{i} + T^{n}_{i+1}}{(\Delta x)^2} \tag{8.8}$$

In Equation 8.8, i is a spatial node and α is the thermal diffusivity. This equation assumes that the x-component's contribution to the conduction equation is the correction variable that must be subtracted to reconstruct a 1-D equivalent temperature trace. It also assumes that split of the conduction equation (Equation 8.3) is valid. If this is valid, then the correction can be determined experimentally for any h boundary conditions.

Results from using this correction, however, overcompensate the temperature reconstruction. In other words, $\Delta T^{n}_{cor,lateral}$ was too large. It is concluded that the spatial-temporal coupled nature of the temperature prevents this correction from being applied as it is.

As Equation 8.7 cannot be exclusively used to correct of the corner effect, a computational analysis beyond the use of experimental data is required. To correct for this over-compensation, a temporal correction is applied as shown in Equations 8.9 and 8.10. This new correction is the temporal difference in temperature at each node location minus the temporal difference in temperature at the "end" of the solid ($y = 10\,\text{mm}$).

$$T^{n+1}_{1-D,cor} = T^{n}_{1-D,cor} + \Delta T^{n}_{2-D} - \Delta T^{n}_{cor,lateral} + \Delta T^{n}_{cor,time} \tag{8.9}$$

where

$$\begin{aligned} \Delta T^{n}_{cor,time} &= \Delta T^{n}_{2-D} - \Delta T^{n}_{1-D} \\ &= (T^{n+1}_{2-D} - T^{n}_{2-D}) - (T^{n+1}_{1-D} - T^{n}_{1-D}) \end{aligned} \tag{8.10}$$

If in Equation 8.10, the node location is at the "end", where the solid is effectively 1-D, then the temporal difference in Equation 8.10 and the lateral difference in Equation 8.9 will both approach zero.

During experiments, the lateral correction $\Delta T^{n}_{cor,lateral}$ can be obtained, but as h will likely vary across the blade tip, $\Delta T^{n}_{cor,time}$ cannot be determined. The temporal correction in Equation 8.10 must be obtained numerically.

When using the computational analysis, h must be uniformly distributed across the surface, as the temperature trace of T_{1-D} must be known. Any variations in T_{1-D} will cause variations in h. However, this method must be modified to be able to apply it to a non-uniform h test condition.

It is presupposed that the relationship between the temporal and lateral corrections is constant, as suggested in Equation 8.11. It will be shown that when accounting for this relationship under a constant h boundary condition, the true heat transfer coefficient is calculated. This relationship is termed the lateral corner correction coefficient $C_{lateral}$, which is a function of time and space and is expressed as:

$$C_{lateral} = \frac{\Delta T^{n}_{cor,time}}{\Delta T^{n}_{cor,lateral}} \Longrightarrow \Delta T^{n}_{cor,time} = C_{lateral} \Delta T^{n}_{cor,lateral} \tag{8.11}$$

Having applied this approach to the computational study, Figure 8.7 shows that this approach corrects the entire top surface. The values for $C_{lateral}(y,t)$ are saved and can be used for future analysis.

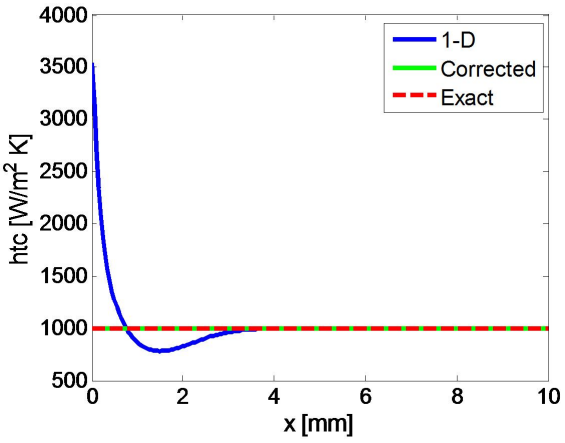

Figure 8.7: Results for semi-infinite 1-D conduction approach and corrected approach

8.4.1.2 Method Implementation

This section provides the general equations used within MATLAB to obtain the correction coefficient. For a known set of computationally-determined $T(x, y = 0, t)$, the temperature difference in time at a location i is shown in Equation 8.12.

$$\Delta T_i^n = T_i^{n+1} - T_i^n \tag{8.12}$$

Equation 8.12 is used to reconstruct the temperature into its original time trace. Next, Equation 8.13 calculates the lateral correction.

$$\Delta T_{i,cor,lateral}^n = \alpha \frac{T_{i-1}^n - 2T_i^n + T_{i+1}^n}{(\Delta x)^2} \tag{8.13}$$

Use of Equation 8.13, however, overcompensates the temperature reconstruction. To correct this, the temporal correction is applied as shown in Equation 8.14. The temporal difference in temperature at the "end" of the solid ($y_{max} = 10\,\text{mm}$) is subtracted from the temporal difference in temperature at each other node location.

$$\Delta T_{i,cor,time}^n = \Delta T_i^n - \Delta T_{y_{max}}^n \tag{8.14}$$

The overall correction is the difference between the lateral and temporal corrections, shown in Equation 8.15.

$$\Delta T^n_{i,cor,overall} = \Delta T^n_{i,cor,lateral} - \Delta T^n_{i,cor,time} \tag{8.15}$$

The lateral corner correction coefficient is then calculated using Equation 8.16

$$C^n_{i,lateral} = \frac{\Delta T^n_{i,cor,overall}}{\Delta T^n_{i,cor,lateral}} \tag{8.16}$$

With a known matrix of $C_{lateral}$, the final reconstruction equation is presented in Equation 8.17.

$$T^{n+1}_i = T^n_i + \Delta T^n_i - \Delta T^n_{i,cor,lateral} + C^n_{i,lateral}\Delta T^n_{i,cor,lateral} \tag{8.17}$$

If $C_{lateral}$ is constant and if it is determined from constant h conditions obtained from the present computational study, then it can be applied to an experiments with varying h, where only the experimentally-determined $\Delta T^n_{cor,lateral}$ is needed to correct the temperature history. The next section shows how well this lateral corner correction coefficient works for a non-uniform h boundary condition.

8.4.2 Use of Lateral Corner Correction Coefficient with Non-Uniform Heat Transfer Coefficient

As mentioned in the previous section, the lateral corner correction coefficient developed in the previous section was determined for a uniform h condition. The correlation between the computationally-determined temporal correction and the experimentally-determined spatial correction would allow for this method to be applied to a test in which h varies. This section aims to show that the coefficient can be used with non-uniform h.

This section discusses a series of computational tests using different non-uniform h boundary conditions that were investigated. By imposing the same initial and transient condition, but using different h boundary conditions, the surface temperature histories were recorded and analysed to determine the h using the *uncorrected* semi-infinite, 1-D conduction assumptions as well as the *corrected* h using the lateral corner correction algorithm described in the previous section.

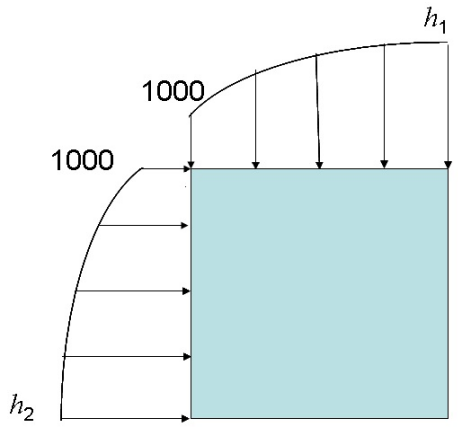

Figure 8.8: Example of boundary conditions for non-uniform heat transfer coefficient study

As symmetric boundary conditions are employed in this study, the thermal boundary conditions should approach smoothly towards the edge with the symmetric boundary conditions. Figure 8.8 shows an example of varying boundary conditions employed, where h_1 and h_2 can be different heat transfer coefficients.

Several different boundary conditions were examined and four are presented in this section. The first test condition gradually raised the h by 20 percent (h=1000 W/m^{2}K at the corner and h=1200 at maximum depth). Results show that this technique significantly reduced the error from the results that assumed semi-infinite 1-D conduction, as shown in Figure 8.9. The correction caused the h to be underestimated by 20 percent close to the corner, but quickly approaches the exact h within 0.5 mm.

For a larger change in h of 100 percent (h = 1000 W/m^{2}K at the corner and h = 2000 W/m^{2}K at maximum depth), error still exists close to the corner, but the error continues to be significantly reduced. The correction underestimates h by 45 percent, but this is small compared to the 250 percent without correction, and the h for the corrected case quickly approaches the exact h within 0.5 mm. When h decreases by 50 percent from the corner (h = 1500 W/m^{2}K at the corner and h = 1000 W/m^{2}K at maximum depth), the calculated h at the corner is overestimated by 45 percent and approaches the exact value within 0.5 mm. Finally, a test case is considered in which h increases for half of the depth, then decreases (h = 1000 W/m^{2}Kt the corner to

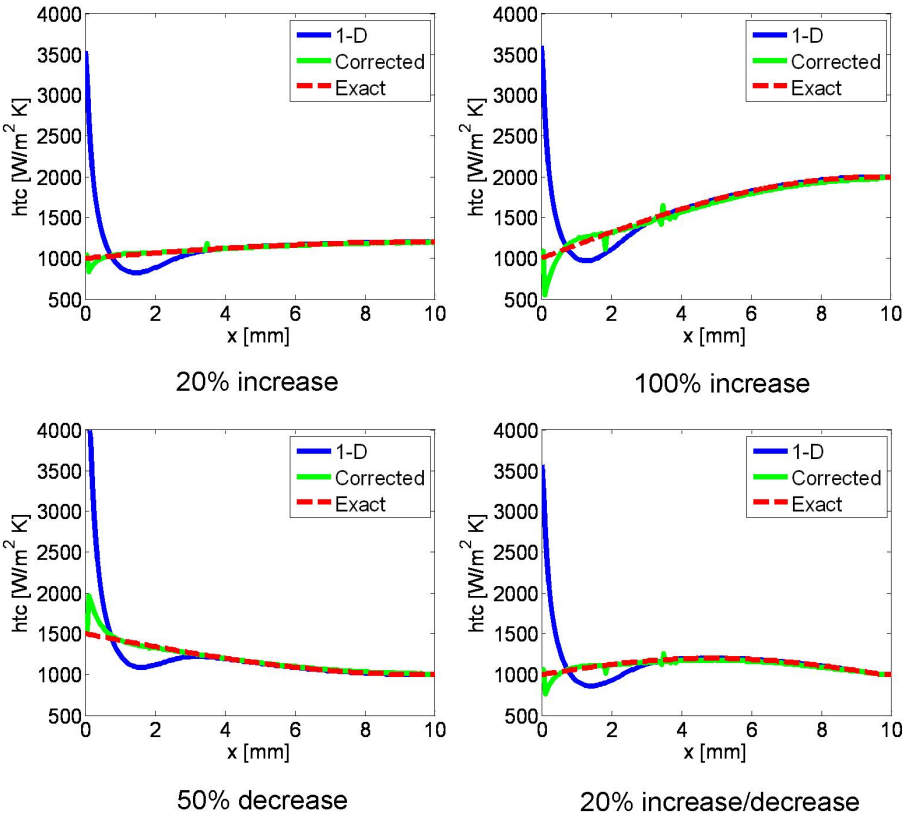

Figure 8.9: Examples of corrected heat transfer coefficient results for non-uniform heat transfer coefficient study

$h = 1200\,\mathrm{W/m^2K}$ at 5 mm and then decreases back to $h = 1000\,\mathrm{W/m^2K}$ at 10 mm). These results were consistent with the tests in which h increases from the corner.

8.5 Lateral Corner Correction Algorithm Application to Flat Tip Experimental Data

In this final section, the lateral corner correction coefficient $C_{lateral}$ previously developed and validated for use with a non-uniform boundary condition, is tested against experimental data. Note that during the development of the coefficient, the coefficient diminished further away from the corner. Therefore, only the first 3.5 mm of data is affected by the lateral corner correction coefficient.

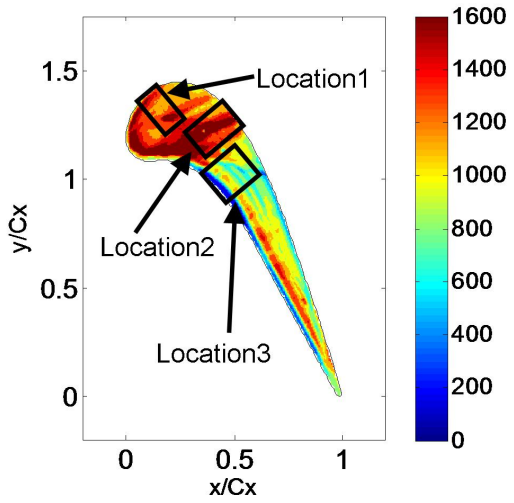

Figure 8.10: Contour of flat tip heat transfer coefficient identifying regions for corrected heat transfer coefficient study

The correction coefficient is applied to experimental data in three different regions of the flat blade tip with 1.3 percent tip gap. The regions are indicated by the boxes in Figure 8.10.

The results of this application are shown in Figure 8.11. It is observed that for locations 1 and 2, the corrected h shows signs of localised increasing and decreasing of h compared to the uncorrected case. These differences are between ± 30 percent. Location 3 shows larger changes in h. Region 3 is a transonic region where heat transfer striping occurs. The initial low h region is the separation region. The correction appeared to significantly increase this region, effectively reducing the size of the low h region. Note that in the figures, the corner is the y-axis in each figure. The difference between the corrected h and and the uncorrected h are also shown in the Figure. Locations 1 and 2 both show regions of increased and decreased h. Location 3, on the other hand, shows a thin region of decreased h next to the corner, followed by an increase, followed by another decrease.

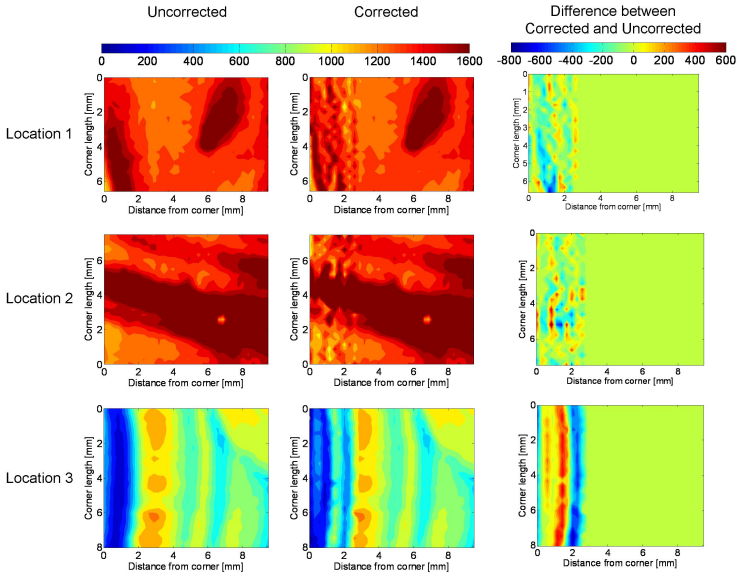

Figure 8.11: Results of corrected heat transfer coefficient for corner conduction effect (left-hand column are uncorrected contours, centre column are corrected contours and the right-hand column are the differences)

8.6 Summary

Though the 2-D lateral corner correction approach has not been applied to the experimental results of the *entire* blade tip, the method has the capability of correcting for the corner conduction effect on all blade corners, especially if access to higher resolution data.

The major conclusions for this chapter are:

1. The length of time used to calculate the heat transfer coefficient close to a corner must be carefully considered. The length of time must be long enough time to have a large enough $T_w - T_i$ temperature difference to obtain a suitable h. The length of time must not be too long to avoid penetration depth issues, which is problematic for corner conduction. Though the top surface is deep enough such that the semi-infinite assumption is valid, the proximity to corners appears to be more important.
2. The corner conduction effect leads to high errors in calculating the heat transfer coefficient when using the semi-infinite 1-D conduction assumption (27.5%

errors in h at location of 5% of blade thickness and higher closer to the corner). The issues have been rarely addressed previously. Studies that correct for the corner conduction effect often use very complex and expensive computational correction approaches.

3. A computationally efficient and simple approach has been developed to correct the corner conduction using a lateral corner correction coefficient. Though this coefficient was determined for a baseline case with a constant heat transfer coefficient, results show its applicability to non-uniform h boundary conditions.

Chapter 9

Summary, Conclusions and Recommendations

9.1 Introduction

This Chapter concludes the thesis with a summary of the work performed by the present author and presented in this thesis. The conclusions will also be presented followed by recommendations for future work.

9.2 Summary

A review of the open literature has shown that there is a lack of understanding of the flow over unshrouded high-pressure turbine tips under transonic flow conditions. The detailed, spatially-resolved measurement of tip heat transfer and aerodynamic loss is very challenging, especially under transonic conditions. Though rotors can be tested with 3-D rotating blades under high-speed conditions, it is challenging for experimenters to measure and calculate spatially-resolved heat transfer and aerodynamic loss results. Though they can generate spatially-resolved heat transfer and aerodynamic loss results, most linear cascades are generally run under subsonic exit conditions ($M < 0.9$). Without transonic flow conditions, many of engine-realistic flow physics will not occur over the tip; and without highly-resolved results, it is difficult to understand the flow physics. Commonly adopted wisdom and considerations in tip design have been largely based on low-speed data and results.

Few studies have examined tip heat transfer and aerodynamic loss together. This thesis has shown that the heat transfer is closely tied to the over-tip leakage (OTL) flow and aerodynamic loss. Any examination should consider both heat transfer and aerodynamic loss when determining the overall effectiveness of a blade design.

It is acknowledged that this study is not entirely engine-realistic as the blades are in a linear cascade, there is no blade rotation or moving endwall, and the coolant temperature ratio is not realistic. In addition, other issues have not been considered, such as turbulence intensity, realistic inlet temperature profiles and surface roughness (e.g. "rocks" on tips). However, it is argued that with a validated CFD code with transonic exit flow condition, some of these issues can be further considered.

The Oxford High-Speed Linear Cascade (HSLC) was developed to investigate the aero-thermodynamics of unshrouded blade tips under engine-realistic aerodynamic conditions. This thesis provides the details of the facility, including the instrumentation, the test section, the test blades and the coolant feed system. The rig is capable of sustaining steady inlet pressures under high-speed aerodynamic conditions. The test section is engine realistic with $M_{exit} = 1.0$, $Re_{exit} = 1.27 \times 10^6$, and a blade loading that matches the design (with peak Mach number of approximately 1.2). Though not entirely realistic for an operating engine, the turbulence intensity at the inlet is 1.0 percent and the inlet has a 4 mm boundary layer thickness on the casing wall.

Transient infrared (IR) thermography was used to obtain spatially-resolved heat transfer measurements on the blade tips and the near-tip sidewalls. A qualification of the heat flux reconstruction approach with the Impulse method was performed and this technique was determined to be well-suited to obtain detailed heat transfer results. Measurement uncertainty in heat transfer coefficient was calculated to be within 10 percent, though this did not consider the uncertainty near the edges or from run-to-run differences. Multiple experimental runs are analysed with the Impulse method and the results were very consistent, with pixel-to-pixel differences of less than 10 percent. Also, the Impulse method was shown to be computationally efficient, making it ideal for obtaining detailed, spatially-resolved heat transfer results.

Following the qualification of the heat transfer measurement technique, heat transfer tests of different blade geometries were undertaken. The thermal performance of a flat blade tip at three different tip gaps was experimentally investigated. As initial results differed from those in the published literature (mostly at low-speed conditions), a heat transfer study under low-speed flow conditions was performed and results from this study were compared to the high-speed results. The low-speed results show consistency with the low-speed and subsonic tests reported in the literature. A subsequent computational study reveals that an over-tip shock system over the aft region of the blade has a direct relationship to a series of heat transfer stripes, which would not be observed under low-speed test conditions. A plot of the circumferentially-averaged Nusselt number shows not only quantitative differences (partly due to the differences in Reynolds number), but qualitative differences as well, highlighting the importance of testing at high-speed engine-realistic conditions.

A tip gap survey of a flat blade tip was investigated and results are presented in this thesis. Increases in tip clearance generally show an increase in Nusselt number over the tip. An analytical study of the adiabatic wall temperature reveals supersonic flow over the tip. These heat transfer results validated the HYDRA CFD model and a subsequent examination of the effect of a moving casing was considered. The moving casing results show a large change to the heat transfer at the frontal (subsonic) part of the blade, but less change at the aft part of the blade, where the flow over the tip remains choked.

A tip gap survey of the uncooled and cooled Environmentally-Friendly Engine (EFE) winglet was then examined. The results revealed some of the flow structures over a complex tip design, many of which also occur over the flat blade tip. Like the flat blade tip, the recovery temperature-derived Mach number over the tip shows that the flow over the winglet tip is supersonic, though the size of the supersonic region is reduced compared to the flat tip. These results validated CFD code and were used to examine the effect of a moving casing, which had similar conclusions to the flat blade tip results. Lastly, contours of Nusselt number, with and without cooling injection, and film cooling effectiveness are presented. Coolant injection generally enhances

heat transfer on the tip and a decrease in tip clearance shows that the film cooling effectiveness increases.

Aerodynamic loss was also investigated in this present study. The calibration and experimental setup for the aerodynamic loss measurement are described. A 2-D traversing system was used to obtain a spatially-resolved map of the exit flow conditions one axial chord downstream of the blade row. A tip gap survey calculating the total pressure loss was examined for a flat blade tip and kinetic energy loss (which considers the pressure and temperature of the cooling flow) was obtained for the uncooled and cooled EFE winglet tip. The flat blade tip and uncooled winglet results separately validated complimentary CFD code, which helped to explain both the heat transfer and pressure loss on the suction-side sidewall and also the OTL vortex downstream of the blade row. The flat blade tip CFD results show the passage vortex that is somewhat less observed in the experimental results. In addition, aerodynamic loss results of the winglet show a decrease in loss with coolant injection.

Finally, a computational study investigated the effect of corner conduction on heat transfer measurements. Results show very high uncertainty on the corner when using the semi-infinite 1-D conduction assumption. A lateral corner conduction technique is developed to correct the heat transfer coefficient results. This technique was computationally verified for varying heat transfer coefficient boundary conditions and later applied to experimental heat transfer results.

9.3 Conclusions

The main conclusions of this thesis are:

1. To the best of the author's knowledge, there has been no published experimental research for detailed, spatially-resolved heat transfer over blade tips under transonic conditions. The present study is the first time that heat transfer on either an uncooled or cooled winglet has been experimentally investigated under transonic flow conditions. Finally, the present author has found no studies in

which spatially-resolved aerodynamic loss experimental results have been determined for a winglet with tip cooling injection. In these aspects, the present work is the first of its kind.

2. High-speed and low-speed results show large qualitative differences. Even using Reynolds number to scale the results, the heat transfer trends for the frontal and aft portions of the blade tip are very different.
3. The frontal region of the flat tip blade is subsonic and the tip Nusselt numbers decrease as tip gaps get smaller (from 1.3 to 0.4 percent of span). The aft portion of the blade is largely transonic and changes in tip gap have less of an effect on the Nusselt number.
4. On the suction side of the flat blade tip, an increase in tip gap results in a decrease in Nusselt number and the heat transfer signature shows the location of the attached OTL vortex, which is at a lower span position for an increased tip gap. On the pressure side of the flat blade tip, the peak heat transfer occurs at the tip near the trailing edge corner.
5. HYDRA CFD predictions are in good agreement with the flat blade tip experimental results. The CFD results help explain the flow physics over the tip. A local shock structure is associated with heat transfer striping on the tip. In addition, with a moving casing endwall, the supersonic region on the tip is smaller. The heat transfer at the frontal part of the blade is significantly affected by the moving casing, whereas the aft, transonic region is not significantly affected.
6. As on the flat blade tip, a large portion of the winglet tip experiences supersonic flow. This is consistently shown by both experimental and CFD results. The winglet also contains high and low heat transfer stripes around the aft region of the winglet tip surface which appear to be directly linked to transonic flow and over-tip shock structures.
7. On the suction surface near-tip region, the winglet has a region of high Nusselt number close to the tip, whereas the flat tip has a region of high Nusselt number at a lower span-wise position than the winglet. CFD results on the suction-side

surface relate these heat transfer signatures to the OTL vortex pressure loss core.

8. The winglet tip Nusselt number increases with coolant injection consistently for both tip clearances, consistently shown under two different tip gaps tested.
9. The tip film cooling effectiveness is generally lower for the larger tip gap. This may be due to weaker cooling films as a result of the increased OTL flow.
10. As with the flat tip, the heat transfer distribution on the winglet tip is largely affected by a moving casing endwall, except in the supersonic region towards the aft part of the blade. The moving endwall leads to a smaller supersonic region.
11. Aerodynamic loss data for the flat blade tip, uncooled winglet and cooled winglet show that the size of the loss core decreases as the tip gap decreases, as expected. In addition, the centre of the vortex is located further away from the blade suction side as the tip gap increases.
12. Magnitudes of the pitch-wise flow angle increase with increased tip gap. The pitch-wise flow angle for the winglet tip with 0.9 percent tip gap is similar in magnitude to the flat blade tip with 1.3 percent tip gap, indicating a reduction of the over-turning and under-turning of the flow with the winglet tip for equivalent tip clearances.
13. Cooling injection appears to reduce tip aerodynamic loss, possibly due to an aerodynamic sealing effect created by the films.
14. The numerical aerodynamic loss results contain a passage vortex signature that is not observed in the experimental results.
15. With relative casing movement, the size of the loss core does not change much for the larger tip gaps and the vortex is "*pushed away*" from the casing wall.
16. The corner conduction effect leads to high errors in calculating the heat transfer coefficient when using the semi-infinite 1-D conduction assumption.
17. A simple, computationally efficient approach has been developed to correct the corner conduction using a lateral corner correction coefficient.
18. When applied to experimental data, the correction approach shows a reasonable reduction in experimental h in the tip corner regions.

9.4 Recommendations for Future Work

This section presents a list of recommendations for future work. Some recommendations are important, but would be very challenging to implement. One such recommendation is to adapt the HSLC to test with a moving endwall. This can then be used to validate the CFD model with a moving casing endwall, however it is very difficult to measure tip heat transfer with a moving casing endwall under transonic conditions as optical access would be difficult.

The author recommends further work on the PID controller. A good optimisation requires many experimental runs, which was a limitation for the HSLC due to noise concerns. Alternatively, a new controller can be obtained or a PC-based PID algorithm can be developed to improve the valve control.

A recommendation that makes the HSLC more engine-representative and is easier to implement includes using a turbulence grid to increase the turbulence intensity to engine-realistic values. An additional test involves increasing surface roughness, to test concepts such as blade deposition.

One of the flat blade tips has 8 static pressure taps located on the mean camber line. A future test to measure the static pressure and calculate the isentropic Mach number could help explain the speed of the leakage flow and to further validate the CFD study.

In relationship to the work performed in the present thesis, there are several recommendations for future work. For heat transfer tests, recommendations include

1. Use multiple experimental runs to determine heat transfer coefficient. On occasion, some runs provided heat transfer coefficient results that were significantly higher or lower than others. This was typically due to the fluctuations in the control valve that regulates the mainstream air. Increased number of tests (on the order of 10 runs per test condition) would help determine the true range of heat transfer coefficient.

2. Test with an engine-realistic temperature ratio, which is quite challenging. One way to increase the temperature ratio is by increasing the mainstream temperature. However, the power required to raise the mainstream temperature is limited by the 100 V and 1000 A DC power supply. Also, as this is a transient test using a low-conductivity material, there is the possibility of melting the blade tip material if the mainstream temperature is raised much higher than it already is. The other way to increase the temperature ratio is by lowering the coolant temperature. For example, CO_2 can provide -40° gas. This is challenging as the cooling holes in the epoxy material have a tendency to freeze and block the coolant flow. Even with near-perfect conditions, the maximum temperature ratio that can be achieved is estimated to be less than 1.3.
3. Apply coolant to all three blades to ensure periodicity during heat transfer tests. During the present investigation, there was not enough volume of low-temperature air to cool all three blades. However, the rig can be modified to allow for higher-pressure air or even multiple cylinders of foreign gas.

For aerodynamic loss tests, recommendations include

1. Obtain pitch-wise flow angle results by either rotating the 3-hole probe or calibrating and testing with a 4-hole probe.
2. Obtain results at finer spatial resolution to see if the passage vortex can be observed.
3. Test with higher mainstream to coolant temperature ratios to determine its effect on loss. For the choked region, the mass flow capacity is governed by the both the mainstream and coolant flow's pressures and temperatures.

For corner conduction corrections, recommendations include

1. Improve the lateral corner correction coefficient to see if there is an equation that can be used to smooth out the correction, especially for relatively "sparse" experimental results (compared to CFD results using finer meshes).

2. Test with a higher-resolution camera not only to improve heat transfer measurements, but to bring the camera resolution closer to the mesh spacing for the lateral corner correction coefficient.
3. Apply this correction to the entire blade tip to see if circumferentially-averaged or area-averaged h changes.
4. Apply this correction to the uncooled winglet, not only with all of the outer corners, but also the edges of the pressure-side recess and the gutter.

References

Abhari, R. S. and Epstein, A. H., 1994, "Experimental Study of Film Cooling in a Rotating Transonic Turbine," *ASME Journal of Turbomachinery*, vol. 116, no. 1, pp. 63–70.

Acharya, S., Yang, H., Prakash, C. and Bunker, R., 2003, "Numerical Study of Flow and Heat Transfer on a Blade Tip with Different Leakage Reduction Strategies," *ASME Paper Number GT-2003-38617*.

Allen, H. W. and Kofskey, M. G., 1955, "Visualization Study of Secondary Flows in Turbine Rotor Tip Regions," *Tech. Rep. TN-3519*, NACA.

Amecke, J., 1970, "Anwendung der Transsonischen Ähnlichkeitsregel auf die Strömung Durch Ebene Schaufelgitter," *VDI Forschungsheft*, vol. 540, pp. 16–28, as reported in Day (1997).

Ameri, A. A. and Bunker, R. S., 2000, "Heat Transfer and Flow on the First-Stage Blade Tip of a Power Generation Gas Turbine: Part 2—Simulation Results," *ASME Journal of Turbomachinery*, vol. 122, no. 2, pp. 272–277.

Ameri, A. A., Steinthorsson, E. and Rigby, D. L., 1998, "Effect of Squealer Tip on Rotor Heat Transfer and Efficiency," *ASME Journal of Turbomachinery*, vol. 120, no. 4, pp. 753–759.

Anderson, J. D., 1989, *Introduction to Flight*, McGraw-Hill, New York, USA.

Anthony, R. J., Oldfield, M. L. G., Jones, T. V. and LaGraff, J. E., 1999, "Development of High-Density Arrays of Thin Film Heat Transfer Gauges," *Proc. of the 5th*

ASME/JSME Thermal Engineering Joint Conference, San Diego, CA. AJTE99-6159.

Azad, G. S., Han, J. C. and Boyle, R. J., 2000a, "Heat Transfer and Flow on the Squealer Tip of a Gas Turbine Blade," *ASME Journal of Turbomachinery*, vol. 122, no. 4, pp. 725–732.

Azad, G. S., Han, J. C., Teng, S. and Boyle, R. J., 2000b, "Heat Transfer and Pressure Distributions on a Gas Turbine Blade Tip," *ASME Journal of Turbomachinery*, vol. 122, no. 4, pp. 717–724.

Baldauf, S., Schulz, A. and Wittig, S., 2001, "High-Resolution Measurements of Local Effectiveness From Discrete Hole Film Cooling," *ASME Journal of Turbomachinery*, vol. 123, no. 4, pp. 758–765.

Behr, T., Kalfas, A. I. and Abhari, R. S., 2008, "Control of Rotor Tip Leakage Through Cooling Injection from the Casing in a High-Work Turbine," *ASME Journal of Turbomachinery*, vol. 130, no. 3, pp. 1–12.

Bindon, J. P., 1989, "The Measurement and Formation of Tip Clearance Loss," *ASME Journal of Turbomachinery*, vol. 111, no. 3, pp. 257–263.

Booth, T. C., Dodge, P. R. and Hepworth, H. K., 1982, "Rotor-Tip Leakage: Part I—Basic Methodology," *Journal of Engineering for Power*, vol. 104, no. 1, pp. 154–161.

Brunner, M. H., Rose, M. G., Mhlbauer, K. and Abhari, R. S., 2007, "In-Engine Turbine Heat Transfer Measurement," *Proc. Institution of Mechanical Engineers, Part A: Journal of Power and Energy*, vol. 221, no. 5, pp. 727–734.

Bunker, R. S., 2001, "A Review of Turbine Blade Tip Heat Transfer," *Annals of the New York Academy of Sciences*, vol. 934, no. 1, pp. 64–79.

Bunker, R. S., Bailey, J. C. and Ameri, A. A., 2000, "Heat Transfer and Flow on the First-Stage Blade Tip of a Power Generation Gas Turbine: Part 1—Experimental Results," *ASME Journal of Turbomachinery*, vol. 122, no. 2, pp. 263–271.

Chyu, M. K., Metzger, D. E. and Hwan, C. L., 1987, "Heat Transfer in Shrouded Rectangular Cavities," *AIAA Journal of Thermophysics*, vol. 1, no. 3, pp. 247–252.

Chyu, M. K., Moon, H. K. and Metzger, D. E., 1989, "Heat Transfer in the Tip Region of Grooved Turbine Blades," *ASME Journal of Turbomachinery*, vol. 111, no. 2, pp. 131–138.

Coleman, H. W. and Steele, W. G., 1989, *Experimentation and Uncertainty Analysis for Engineers*, Wiley, New York.

Day, C. R. B., 1997, "Aerodynamics of an Annular Film-Cooled Turbine Cascade," DPhil thesis, University of Oxford.

Day, C. R. B., Oldfield, M. L. G. and Lock, G. D., 1999, "The Influence of Film Cooling on the Efficiency of an Annular Nozzle Guide Vane Cascade," *ASME Journal of Turbomachinery*, vol. 121, no. 1, pp. 145–151.

Day, C. R. B., Oldfield, M. L. G. and Lock, G. D., 2000, "Aerodynamic Performance of an Annular Cascade of Film Cooled Nozzle Guide Vanes under Engine Representative Conditions," *Experiments in Fluids*, vol. 29, no. 2, pp. 117–129.

Deckers, M., 1996, "The Influence of Trailing Edge Coolant Ejection on the Loss of Transonic Turbine Blades," Ph.D. thesis, University of Cambridge.

Deluca, L., Cardone, G., Delachevalerie, D. A. and Fonteneau, A., 1995, "Viscous Interaction Phenomena in Hypersonic Wedge Flow," *AIAA Journal*, vol. 33, no. 12, pp. 2293–2298.

Denton, J. D., 1993, "Loss Mechanisms in Turbomachines," *ASME Journal of Turbomachinery*, vol. 115, no. 4, pp. 621–656.

Dey, D. and Camci, C., 2001, "Aerodynamic Tip Desensitization of an Axial Turbine Rotor using Pressure Side Tip Platform Extensions," *ASME Paper Number 2001-GT-0484*.

Dominy, R. G. and Hodson, H. P., 1993, "An Investigation of Factors Influencing the Calibration of 5-Hole Probes for 3D Flow Measurements," *ASME Journal of Turbomachinery*, vol. 115, no. 3, pp. 513–519.

Dunn, M. G. and Haldeman, C. W., 2000, "Time-Averaged Heat Flux for a Recessed Tip, Lip, and Platform of a Transonic Turbine Blade," *ASME Journal of Turbomachinery*, vol. 122, no. 4, pp. 692–698.

Dunn, M. G., Rae, W. J. and Holt, J. L., 1984a, "Measurement and Analysis of Heat Flux Data in a Turbine Stage: Part I—Description of Experimental Apparatus and Data Analysis," *Journal of Engineering for Gas Turbines and Power*, vol. 106, no. 1, pp. 229–233.

Dunn, M. G., Rae, W. J. and Holt, J. L., 1984b, "Measurement and Analysis of Heat Flux Data in a Turbine Stage: Part II—Discussion of Results and Comparison with Predictions," *Journal of Engineering for Gas Turbines and Power*, vol. 106, no. 1, pp. 234–240.

Dzung, L. S., 1971, "Konsistente Mittelwerte in der theorie der Turbomaschinen für Kompressible Medien," *BBC-Mitt*, vol. 58, pp. 485–492, as reported in Day (1997).

Ekkad, S. V., Ou, S. and Rivir, R. B., 2004, "A Transient Infrared Thermography Method for Simultaneous Film Cooling Effectiveness and Heat Transfer Coefficient Measurements from a Single Test," *ASME Journal of Turbomachinery*, vol. 126, no. 4, pp. 597–603.

FLIR Systems, Inc., 2008, *A320 and A325 User's Manual*, FLIR Systems, Inc., Thermography Center, 16 Esquire Road, North Billerica, MA 01865, USA.

Friedrichs, S., 2004, "Turbine Heat Transfer," *Cambridge Turbomachinery Course Notes*, Whittle Laboratory, Department of Engineering, University of Cambridge, UK.

Garg, V. K. and Abhari, R. S., 1997, "Comparison of Predicted and Experimental Nusselt Number for a Film-Cooled Rotating Blade," *International Journal of Heat and Fluid Flow*, vol. 18, no. 5, pp. 452–460.

Giel, P. W., Boyle, R. J. and Bunker, R. S., 2004, "Measurements and Predictions of Heat Transfer on Rotor Blades in a Transonic Turbine Cascade," *ASME Journal of Turbomachinery*, vol. 126, no. 1, pp. 110–121.

Gillespie, D. R. H., Wang, Z. and Ireland, P. T., 1995, "Heating Element," British Patent No. PCT/GB96/2017.

Guenette, G. R., Epstein, A. H., Giles, M. B., Haimes, R. and Norton, R. J. G., 1989, "Fully Scaled Transonic Turbine Rotor Heat Transfer Measurements," *ASME Journal of Turbomachinery*, vol. 111, no. 1, pp. 1–7.

Haldeman, C. W., Mathison, R. M., Dunn, M. G., Southworth, S., Harral, J. W. and Heitland, G., 2006a, "Aerodynamic and Heat Flux Measurements in a Single Stage Fully Cooled Turbine - Part II: Experimental Approach," *ASME Paper Number GT2006-90968*.

Haldeman, C. W., Mathison, R. M., Dunn, M. G., Southworth, S., Harral, J. W. and Heitland, G., 2006b, "Aerodynamic and Heat Flux Measurements in a Single Stage Fully Cooled Turbine - Part II: Experimental Results," *ASME Paper Number GT2006-90966*.

Haller, B. R. and Camus, J. J., 1984, "Aerodynamic Loss Penalty Produced by Film Cooling Transonic Turbine Blades," *Journal of Engineering for Gas Turbines and Power*, vol. 106, pp. 198–205.

Hartsel, J. E., 1972, "Prediction of Effects of Mass-Transfer Cooling on the Blade-Row Efficiency of Turbine Airfoils," *AIAA, 10th Aerospace Sciences Meeting, San Diego, Paper Number AIAA-72-11*, as cited in Young and Horlock (2006).

Harvey, N. W., Newman, D. A., Haselbach, F. and Willer, L., 2006, "An Investigation into a Novel Turbine Rotor Winglet. Part 1: Design and Model Rig Test Results," *ASME Paper Number GT2006-90456*.

Harvey, N. W. and Ramsden, K., 2001, "A Computational Study of a Novel Turbine Rotor Partial Shroud," *ASME Journal of Turbomachinery*, vol. 123, no. 3, pp. 534–543.

He, L. and Oldfield, M. L. G., 2011, "Unsteady Conjugate Heat Transfer Modelling," *ASME Journal of Turbomachinery*, vol. 133, no. 3, p. 031022.

Heyes, F. J. G., Hodson, H. P. and Dailey, G. M., 1992, "The Effect of Blade Tip Geometry on the Tip Leakage Flow in Axial Turbine Cascades," *ASME Journal of Turbomachinery*, vol. 114, no. 3, pp. 643–651.

Hodson, H. P. and Dominy, R. G., 1993, *Annular Cascades*, pp. 73–85, AGARD AG 328, Advanced Methods for Cascade Testing, North Atlantic Treaty Organisation.

Hofer, T. and Arts, T., 2009, "Aerodynamic Investigation of the Tip Leakage Flow for Blades with Different Tip Squealer Geometries at Transonic Conditions," *ASME Paper Number GT2009-59909*.

Holman, J. P., 2002, *Heat Transfer*, McGraw-Hill, New York, USA, 9th Edition.

Ireland, P. T. and Jones, T. V., 2000, "Liquid Crystal Measurements of Heat Transfer and Surface Shear Stress," *Measurement and Scientific Journal*, vol. 11, no. 7, pp. 969–986.

Ito, S., Eckert, E. R. and Goldstein, R. J., 1980, "Aerodynamic Loss in a Gas Turbine Stage with Film Cooling," *Journal of Engineering for Power*, vol. 102, pp. 964–970.

Jin, P. and Goldstein, R. J., 2003, "Local Mass/Heat Transfer on Turbine Blade Near-Tip Surfaces," *ASME Journal of Turbomachinery*, vol. 125, no. 3, pp. 521–528.

Key, N. L. and Arts, T., 2004, "Comparison of Turbine Tip Leakage Flow for Flat Tip and Squealer Geometries at High Speed Flow," *ASME Paper Number GT2004-53979*.

Kim, Y. W. and Metzger, D. E., 1995, "Heat Transfer and Effectiveness on Film Cooled Turbine Blade Tip Models," *ASME Journal of Turbomachinery*, vol. 117, no. 1, pp. 12–21.

Kingsley-Rowe, J. R., Lock, G. D. and Owen, J. M., 2005, "Transient Heat Transfer Measurements using Thermochromic Liquid Crystal: Lateral-Conduction Error," *International Journal of Heat and Fluid Flow*, vol. 26, no. 2, pp. 256–263.

Kiock, R., Hoheisel, H., Dietrichs, H. J. and Holmes, A. T., 1985, *The Boundary Layer Behaviour of an Advanced Gas Turbine Rotor Blade under the Influence of Simulated Film Cooling*, AGARDograph no. 390, Heat Transfer and Cooling in Gas Turbines, North Atlantic Treaty Organisation, Paper 42).

Kline, S. J. and McClintock, F. A., 1953, "Describing Uncertainties in Single-Sample Experiments," *Mechanical Engineering (ASME)*, vol. 75, no. 1, pp. 3–8.

Köllen, O. and Koschel, W., 1985, *Effect of Film Cooling on the Aerodynamic Performance of a Turbine Cascade*, AGARDograph no. 390, Heat Transfer and Cooling in Gas Turbines, North Atlantic Treaty Organisation, Paper 39).

Kost, F. and Nicklas, M., 2001, "Film-Cooled Turbine Endwall in a Transonic Flow Field: Part I—Aerodynamic Measurements," *ASME Journal of Turbomachinery*, vol. 123, no. 4, pp. 709–719.

Kost, F. H. and Holmes, A. T., 1985, *Aerodynamic Effect of Coolant Ejection in the Rear Part of Transonic Rotor Blades*, AGARDograph no. 390, Heat Transfer and Cooling in Gas Turbines, North Atlantic Treaty Organisation, Paper 41).

Krishnababu, S. K., Dawes, W. N., Hodson, H. P., Lock, G. D., Hannis, J. and Whitney, C., 2007a, "Aero-Thermal Investigation of Tip Leakage Flows in Axial Flow Turbines. Part II—Effect of Relative Casing Motion," *ASME Paper Number GT2007-27957*.

Krishnababu, S. K., Hodson, H. P., Booth, G. D., Lock, G. D. and Dawes, W. N., 2008, "Aero-Thermal Investigation of Tip Leakage Flow in a Film Cooled Industrial Turbine Rotor," *ASME Paper Number GT2008-50222*.

Krishnababu, S. K., Newton, P. J., Dawes, W. N., Lock, G. D., Hodson, H. P., Hannis, J. and Whitney, C., 2007b, "Aero-Thermal Investigation of Tip Leakage Flows in Axial Flow Turbines. Part I—Effect of Tip Geometry and Tip Clearance Gap," *ASME Paper Number GT2007-27954*.

Kwak, J. S. and Han, J. C., 2003a, "Heat Transfer Coefficients and Film-Cooling Effectiveness on a Gas Turbine Blade Tip," *Journal of Heat Transfer*, vol. 125, no. 3, pp. 494–502.

Kwak, J. S. and Han, J. C., 2003b, "Heat Transfer Coefficients and Film-Cooling Effectiveness on the Squealer Tip of a Gas Turbine Blade," *ASME Journal of Turbomachinery*, vol. 125, no. 4, pp. 648–657.

Lakshminarayana, B., 1996, *Fluid Dynamics and Heat Transfer of Turbomachinery*, John Wiley & Sons, Inc., New York, NY, USA.

Langston, L., 2007, "Fahrenheit, 3,600," *Mechanical Engineering (ASME)*, vol. 129, no. 4, pp. 34–37.

Langston, L. S., Nice, M. L. and Hooper, R. M., 1977, "Three-Dimensional Flow in a Turbine Cascade Passage," *ASME Journal of Engineering for Power*, vol. 99, no. 1, pp. 21–28.

Lekakis, I., 1996, "Calibration and Signal Interpretation for Single and Multiple Hot-Wire/Hot-Film Probes," *Measurement Science and Technology*, vol. 7, pp. 1313–1333.

Licu, D. N., Findlay, M. J., Gartshore, I. S. and Salcudean, M., 2000, "Transient Heat Transfer Measurements using a Single Wide-Band Liquid Crystal Test," *ASME Journal of Turbomachinery*, vol. 122, no. 3, pp. 546–552.

Lin, M. and Wang, T., 2002, "A Transient Liquid Crystal Method using a 3-D Inverse Transient Conduction Scheme," *International Journal of Heat and Mass Transfer*, vol. 45, pp. 3491–3501.

Ling, J. P. C. W., Ireland, P. T. and Turner, L., 2002, "Full Coverage Film Cooling for Combustor Transition Sections," *ASME Paper Number 2002GT-30528.*

Ling, J. P. C. W., Ireland, P. T. and Turner, L., 2004, "A Technique for Processing Transient Heat Transfer, Liquid Crystal Experiments in the Presence of Lateral Conduction," *ASME Journal of Turbomachinery*, vol. 126, no. 2, pp. 247–258.

Main, A. J., Day, C. R. B., Lock, G. D. and Oldfield, M. L. G., 1996, "Calibration of a Four-Hole Pyramid Probe and Area Traverse Measurements in a Short-Duration Transonic Turbine Cascade Tunnel," *Experiments in Fluids*, vol. 21, no. 4, pp. 302–311.

Main, A. J., Oldfield, M. L. G., Lock, G. D. and Jones, T. V., 1997, "Free Vortex Theory for Efficiency Calculations from Annular Cascade Data," *ASME Journal of Turbomachinery*, vol. 119, no. 2, pp. 247–255.

Matsunuma, T., 2006, "Effects of Reynolds Number and Freestream Turbulence on Turbine Tip Clearance Flow," *ASME Journal of Turbomachinery*, vol. 128, no. 1, pp. 166–177.

Mattingly, J. D., 2005, *Elements of Gas Turbine Propulsion*, AIAA, Reston, VA, USA.

Mayle, R. E. and Metzger, D. E., 1982, "Heat Transfer at the Tip of an Unshrouded Turbine Blade," U. Grigull, E. Hahne, K. Stephan and J. Straub (Eds.), *Heat Transfer 1982—Proceedings of the Seventh International Heat Transfer Conference, Volume 3*, pp. 87–92, 6th–10th September 1982, Munich, Fed. Rep. Of Germany.

McCarter, A. A., Xiao, X. and Lakshminarayana, B., 2001, "Tip Clearance Effects in a Turbine Rotor: Part II—Velocity Field and Flow Physics," *ASME Journal of Turbomachinery*, vol. 123, no. 2, pp. 296–304.

Mee, D. J., 1992, "Techniques for Aerodynamic Loss Measurement of Transonic Turbine Cascades with Trailing-Edge Region Coolant Ejection," *ASME Paper Number 92-GT-157.*

Mee, D. J., Baines, N. C., Oldfield, M. L. G. and Dickens, T. E., 1992, "An Examination of the Contributions to Loss on a Transonic Turbine Blade in Cascade," *ASME Journal of Turbomachinery*, vol. 114, no. 1, pp. 115–162.

Mee, D. J., Chiu, H. S. and Ireland, P. T., 2005, "Techniques for Detailed Heat Transfer Measurements in Cold Supersonic Blowdown Tunnels using Thermochromic Liquid Crystals," *International Journal of Heat and Mass Transfer*, vol. 45, no. 16, pp. 3287–3297.

Meech Static Eliminators Limited, 2010, "Vortex Tube," http://www.meech.com.

Metzger, D. E., Dunn, M. G. and Hah, C., 1991, "Turbine Tip and Shroud Heat Transfer," *ASME Journal of Turbomachinery*, vol. 113, no. 3, pp. 502–507.

Metzger, D. E. and Rued, K., 1989, "The Influence of Turbine Clearance Gap Leakage on Passage Velocity and Heat Transfer. Part I: Sink Flow Effects on Blade Pressure Side," *ASME Journal of Turbomachinery*, vol. 111, no. 3, pp. 284–292.

Mischo, B., Behr, T. and Abhari, R. S., 2006, "Flow Physics and Profiling of Recessed Blade Tips: Impact on Performance and Heat Load," *ASME Paper Number GT2006-91074.*

Mischo, B., Burdet, A., Behr, T. and Abhari, R. S., 2007, "Control of Rotor Tip Leakage through Cooling Injection from Casing in a High-Work Turbine: Computational Investigation using a Feature-Based Jet Model," *ASME Paper Number GT2007-27669.*

Moffat, R. J., 1988, "Describing the Uncertainties in Experimental Results," *Experimental Thermal and Fluid Science*, vol. 1, pp. 3–17.

Moore, J. and Elward, K. M., 1993, "Shock Formation in Overexpanded Tip Leakage Flow," *ASME Journal of Turbomachinery*, vol. 115, pp. 392–399.

Moore, J., Moore, J. G., Henry, G. S. and Chaudhry, U., 1989, "Flow and Heat Transfer in Turbine Tip Gaps," *ASME Journal of Turbomachinery*, vol. 111, no. 3, pp. 301–309.

Nasir, H., Ekkad, S. V., Bunker, R. S. and Prakash, C., 2004, "Effects of Tip Gap Film Injection from Plain and Squealer Blade Tips," *ASME Paper Number GT2004-53455*.

Newton, P. J., Lock, G. D., Krishnababu, S. K., Hodson, H. P., Dawes, W. N., Hannis, J. and Whitney, C., 2006, "Heat Transfer and Aerodynamics of Turbine Blade Tips in a Linear Cascade," *ASME Journal of Turbomachinery*, vol. 128, no. 2, pp. 300–309.

Newton, P. J., Lock, G. D., Krishnababu, S. K., Hodson, H. P., Dawes, W. N., Hannis, J. and Whitney, C., 2007, "Aero-Thermal Investigation of Tip Leakage Flows in Axial Flow Turbines. Part III: Tip Cooling," *ASME Paper Number GT2007-27368*.

Oates, G. C., 1985, *Aerothermodynamics of Aircraft Engine Components*, AIAA, New York, New York, USA.

Ochs, M., Schulz, A. and Bauer, H. J., 2006, "Design and Commissioning of a Transonic Test Section for the Investigation of Shock Wave-Film Cooling Interactions," *ASME Paper Number GT2006-90468*.

Ochs, M., Schulz, A. and Bauer, H. J., 2007, "Investigation of the Influence of Trailing Edge Shock Waves on Film Cooling Performance of Gas Turbine Airfoils," *ASME Paper Number GT2007-27482*.

O'Dowd, D. O., Zhang, Q., He, L., Ligrani, P. M. and Friedrichs, S., 2011, "Comparison of Heat Transfer Measurement Techniques on a Transonic Turbine Blade Tip," *ASME Journal of Turbomachinery*, vol. 133, no. 2, pp. 021028 (also ASME Paper Number GT2009–59376).

O'Dowd, D. O., Zhang, Q., He, L., Oldfield, M. L. G., Ligrani, P. M., Cheong, B. C. Y. and Tibbott, I., 2010a, "Aero-Thermal Performance of a Winglet at Engine Representative Mach and Reynolds Numbers," *ASME Journal of Turbomachinery*, to be published, (also ASME Paper Number GT2010-22794).

O'Dowd, D. O., Zhang, Q., Usandizaga, I., He, L. and Ligrani, P. M., 2010b, "Transonic Turbine Blade Tip Aero-Thermal Performance with Different Tip Gaps: Part II—Tip Aerodynamic Loss," *ASME Paper Number GT2010-22780.*

Oetiker, T., Partl, H., Hyna, I. and Schlegl, E., 2007, "The Not So Short Introduction to LaTeX 2_ε," Version 4.22.

Oldfield, M. L. G., 2008, "Impulse Response Processing of Transient Heat Transfer Gauge Signals," *ASME Journal of Turbomachinery*, vol. 130, no. 2, p. 021023.

Oldfield, M. L. G., Jones, T. V. and Schultz, D. L., 1978, "On-Line Computer for Transient Turbine Cascade Instrumentation," *IEEE Transactions on Aerospace and Electronic Systems*, vol. AES-14, no. 5, pp. 738–749.

Oldfield, M. L. G., Schultz, D. L. and Nicholson, J. H., 1981, "Loss Measurements Using a Fast Traverse in an ILPT Transient Cascade," *Symposium on Measuring Techniques for Transonic and Supersonic Flow in Cascades and Turbomachines, Oxford, UK.*

Palafox, P., Oldfield, M. L. G., Ireland, P. T., Jones, T. V. and LaGraff, J. E., 2006, "Blade Tip Heat Transfer and Aerodynamics in a Large Scale Turbine Cascade with Moving Endwall," *ASME Paper Number GT2006-90425*, to be published in Journal of Turbomachinery.

Palafox, P., Oldfield, M. L. G., LaGraff, J. E. and Jones, T. V., 2008, "PIV Maps of Tip Leakage and Secondary Flow Fields on a Low Speed Turbine Blade Cascade with Moving Endwall," *ASME Journal of Turbomachinery*, vol. 130, no. 1, p. 011001.

Papa, M., Goldstein, R. J. and Gori, F., 2003, "Effects of Tip Geometry and Tip Clearance on the Mass/Heat Transfer from a Large-Scale Gas Turbine Blade," *ASME Journal of Turbomachinery*, vol. 125, no. 1, pp. 90–96.

Patel, K. V., 1980, "Research on a High Work Axial Gas Generator Turbine," *Tech. rep.*, SAE 800618, as reported by Schabowski and Hodson (2007).

Payne, S. J., Ainsworth, R. W., Miller, R. J., Moss, R. W. and Harvey, N. W., 2003, "Unsteady Loss in a High Pressure Turbine Stage," *International Journal of Heat and Fluid*, vol. 24, no. 5, pp. 698–708.

Polanka, M. D., Clark, J. P., White, A. L., Meininger, M. and Praisner, T. J., 2003, "Turbine Tip and Shroud Heat Transfer and Loading Part B: Comparisons between Prediction and Experiment including Unsteady Effects," *ASME Paper Number GT2003-38916*.

Porreca, L., Behr, T., Schlienger, J., Kalfas, A. I., Abhari, R. S., Ehrhard, J. and Janke, E., 2005, "Fluid Dynamics and Performance of Partially and Fully Shrouded Axial Turbines," *ASME Journal of Turbomachinery*, vol. 127, no. 4, pp. 668–678.

Porreca, L., Kalfas, A. I. and Abhari, R. S., 2009, "Aerothermal Analysis of a Partially Shrouded Axial Turbine," *Journal of Propulsion and Power*, vol. 25, no. 1, pp. 181–190.

Povey, T., M. L. G. Oldfield, M. and Haselbach, F., 2008, "Transonic Turbine Vane Tests in a New Miniature Cascade Facility," *Proceedings of the Institution of Mechanical Engineers, Part A: Journal of Power and Energy*, vol. 222, no. 5, pp. 529–539.

Rao, N. M. and Camci, C., 2004, "A Flow Visualization Study of Axial Turbine Tip Desensitization by Coolant Injection from a Tip Trench," *Proceedings of ASME International Mechanical Engineering Congress and RD&D Expo 2004*, 13th-19th November 2004, Anaheim, California, USA (IMECE2004-60943).

Rao, N. M., Gumusel, B., Kavurmacioglu, L. and Camci, C., 2006, "Influence of Casing Roughness on the Aerodynamic Structure of Tip Vortices in an Axial Flow Turbine," *ASME Paper Number GT2006-91011.*

Reagle, C., Newman, A., Xue, S., Ng, W. and Ekkad, S., 2010, "A Transient Infrared Technique for Measuring Surface and Endwall Heat Transfer in a Transonic Turbine Cascade," *ASME Paper Number GT2010-22975.*

Rolls-Royce, 1973, *The Jet Engine*, Rolls-Royce plc., Derby, UK, 3rd Edition.

Rolls-Royce, 2005, *The Jet Engine*, Rolls-Royce plc., Derby, UK, 5th Edition.

Rued, K. and Metzger, D. E., 1989, "The Influence of Turbine Clearance Gap Leakage on Passage Velocity and Heat Transfer. Part II: Source Flow Effects on Blade Pressure Side," *ASME Journal of Turbomachinery*, vol. 111, no. 3, pp. 293–300.

Saha, A. K., Acharya, S., Prakash, C. and Bunker, R., 2003, "Blade Tip Leakage Flow and Heat Transfer with Pressure Side Winglet," *ASME Paper Number GT2003-38620.*

Sargison, J. E., Guo, S. M., Oldfield, M. L. G., Lock, G. D. and Rawlinson, A. J., 2002, "A Converging Slot-Hole Film-Cooling Geometry—Part 2: Transonic Nozzle Guide Vane heat Transfer and Loss," *ASME Journal of Turbomachinery*, vol. 124, no. 3, pp. 461–471.

Schabowski, Z. and Hodson, H., 2007, "The Reduction of Over Tip Leakage Loss in Unshrouded Axial Turbines using Winglets and Squealers," *ASME Paper Number GT2007-27623.*

Schabowski, Z., Hodson, H., Giacche, D., Power, B. and Stokes, M. R., 2010, "Aeromechanical Optimisation of a Winglet-Squealer Tip for an Axial Turbine," *ASME Paper Number GT2010-23542*.

Schneider, P. J., 1955, *Conduction Heat Transfer*, Addison-Wesley Publishing Company, Reading, MA, USA.

Schreiber, H. A., Starken, H. and Steinert, W., 1993, *Transonic and Supersonic Cascades (including Turbines)*, pp. 35–59, AGARD AG 328, Advanced Methods for Cascade Testing, North Atlantic Treaty Organisation.

Schultz, D. L. and Jones, T. V., 1973, *Heat-Transfer Measurements in Short-Duration Hypersonic Facilities*, AGARDograph no. 165, North Atlantic Treaty Organisation.

Schulz, A., 2000, "Infrared Thermography as Applied to Film Cooling of Gas Turbine Components," *Measurement Science and Technology*, vol. 11, no. 7, pp. 948–956.

Sen, B., Schmidt, D. L. and Bogard, D. G., 1996, "Film Cooling with Compound Angle Holes: Heat Transfer," *ASME Journal of Turbomachinery*, vol. 118, no. 4, pp. 800–806.

Shyam, V., Ameri, A. and Chen, J.-P., 2010, "Analysis of Unsteady Tip and Endwall Heat Transfer in a Highly Loaded Transonic Turbine Stage," *ASME Paper Number GT2010-23694*.

Sjolander, S. A. and Cao, D., 1995, "Measurements of the Flow in an Idealized Turbine Tip Gap," *ASME Journal of Turbomachinery*, vol. 117, no. 4, pp. 578–584.

Srinivasan, V. and Goldstein, R. J., 2003, "Effect of Endwall Motion on Blade Tip Heat Transfer," *ASME Journal of Turbomachinery*, vol. 125, no. 2, pp. 267–273.

Staubach, J. B., Sharma, O. P. and Stetson, G. M., 1996, "Reduction of Tip Clearance Losses Through 3-D Airfoil Designs," *ASME Paper Number 96-TA-13*, as reported in Harvey and Ramsden (2001).

Tallman, J. A. and Lakshminarayana, B., 2001a, "Numerical Simulation of Tip Leakage Flow in Axial Flow Turbines, With Emphasis on Flow Physics: Part II—Effect of Outer Casing Relative Motion," *ASME Journal of Turbomachinery*, vol. 123, no. 2, pp. 324–333.

Tallman, J. A. and Lakshminarayana, B., 2001b, "Numerical Simulation of Tip Leakage Flows in Axial Flow Turbines, With Emphasis on Flow Physics: Part I—Effect of Tip Clearance Height," *ASME Journal of Turbomachinery*, vol. 123, no. 2, pp. 314–323.

Tang, B. M. T., Palafox, P., Gillespie, D. R. H., Oldfield, M. L. G. and Cheong, B. C. Y., 2010, "Computational Modelling of Tip Heat Transfer to a Super-Scale Model of an Unshrouded Gas Turbine Blade," *ASME Journal of Turbomachinery*, vol. 132, no. 3, p. 031023.

Teng, S., Han, J. C. and Azad, G. M. S., 2001, "Detailed Heat Transfer Coefficient Distributions on a Large-Scale Gas Turbine Blade Tip," *Journal of Heat Transfer*, vol. 123, no. 4, pp. 803–809.

Thomas, G. A., 2006, "The Effect of a Casing Geometry Modification on Blade Tip-Gap Aero-Thermodynamics in a Transonic, High-Pressure Turbine," DPhil thesis, University of Oxford.

Thorpe, S. J., Yoshino, S., Ainsworth, R. W. and Harvey, N. W., 2004a, "An Investigation of the Heat Transfer and Static Pressure on the Over-Tip Casing Wall of an Axial Turbine Operating at Engine Representative Flow Conditions. (I). Time-Mean Results," *International Journal of Heat and Fluid Flow*, vol. 25, no. 6, pp. 933–944.

Thorpe, S. J., Yoshino, S., Ainsworth, R. W. and Harvey, N. W., 2004b, "An Investigation of the Heat Transfer and Static Pressure on the Over-Tip Casing Wall of

an Axial Turbine Operating at Engine Representative Flow Conditions. (II). Time-Resolved Results," *International Journal of Heat and Fluid Flow*, vol. 25, no. 6, pp. 945–960.

Thorpe, S. J., Yoshino, S., Thomas, G. A., Ainsworth, R. W. and Harvey, N. W., 2005, "Blade-Tip Heat Transfer in a Transonic Turbine," *Proceedings of the Institution of Mechanical Engineers, Part A: Journal of Power and Energy*, vol. 219, no. 6, pp. 421–430.

Treaster, A. L. and Houtz, H. E., 1986, "Fabricating and Calibrating Five-Hole Probes," *American Society of Mechanical Engineers, Fluids Engineering Division (Publication) FED*, vol. 34, pp. 1–4.

Vass, P. and Arts, T., 2009, "Advanced Aero-Thermal Investigation of High Pressure Turbine Tip Flows," *International Centre for Heat and Mass Transfer*, presented at the International Symposium on Heat Transfer in Gas Turbine Systems.

Vedula, R. J. and Metzger, D. E., 1991, "Method for the Simultaneous Determination of Local Effectiveness and Heat Transfer Distributions in Three-Temperature Convection Situations," *ASME Paper Number 91-GT-345*.

Vedula, R. P., Metzger, D. E. and Bickford, W. B., 1988, "Effects of Lateral and Anisotropic Conduction on Determination of Local Convection Heat Transfer Characteristics with Transient Tests and Surface Coatings," *ASME Heat Transfer Division Publication*, vol. 104, pp. 21–27.

von Wolfersdorf, J., 2007, "Influence of Lateral Conduction due to Flow Temperature Variations in Transient Heat Transfer Measurements," *International Journal of Heat and Mass Transfer*, vol. 50, no. 5-6, pp. 1122–1127.

Wadia, A. R. and Booth, T. C., 1982, "Rotor-Tip Leakage: Part II—Design Optimization through Viscous Analysis and Experiment," *Journal of Engineering for Power*, vol. 104, no. 1, pp. 162–169.

Wheeler, A. P. S., Atkins, N. R. and He, L., 2009, "Turbine Blade Heat Transfer in Low Speed and High Speed Flows," *ASME Paper Number GT2009-59404*, to be published in Journal of Turbomachinery.

Willer, L., Haselbach, F., Newman, D. A. and Harvey, N. W., 2006, "An Investigation into a Novel Turbine Rotor Winglet: Part 2—Numerical Simulation and Experimental Results," *ASME Paper Number GT2006-90459*.

Xiao, X., McCarter, A. A. and Lakshminarayana, B., 2001, "Tip Clearance Effects in a Turbine Rotor: Part I—Pressure Field and Loss," *ASME Journal of Turbomachinery*, vol. 123, no. 2, pp. 296–304.

Xu, L. and Denton, J. D., 1988, "The Base Pressure and Loss of a Family of Four Turbine Blades," *ASME Journal of Turbomachinery*, vol. 110, no. 1, pp. 9–17.

Yamamoto, A., 1989, "Endwall Flow/Loss Mechanisms in a Linear Turbine Cascade with Blade Tip Clearance," *ASME Journal of Turbomachinery*, vol. 111, pp. 264–275.

Yamamoto, A., Kondo, Y. and Murao, R., 1991, "Cooling-Air Injection into Secondary Flow and Loss Fields with a Linear Turbine Cascade," *ASME Journal of Turbomachinery*, vol. 113, no. 3, pp. 375–383.

Yan, Y. and Owen, J. M., 2002, "Uncertainties in Transient Heat Transfer Measurements with Liquid Crystal," *International Journal of Heat and Fluid Flow*, vol. 23, no. 1, pp. 29–35.

Yang, H., Acharya, S., Ekkad, S. V., Prakash, C. and Bunker, R., 2002a, "Flow and Heat Transfer Predictions for a Flat-Tip Turbine Blade," *ASME Paper Number GT2002-30190*.

Yang, H., Acharya, S., Ekkad, S. V., Prakash, C. and Bunker, R., 2002b, "Numerical Simulation of Flow and Heat Transfer past a Turbine Blade with a Squealer-Tip," *ASME Paper Number GT2002-30193*.

Yang, H., Chen, H. C. and Han, J. C., 2004, "Numerical Prediction of Film Cooling and Heat Transfer with Different Film-Hole Arrangements on the Plane and Squealer Tip of a Gas Turbine Blade," *ASME Paper Number GT2004-53199*.

Yang, H., Chen, H. C. and Han, J. C., 2006, "Turbine Rotor with Various Tip Configurations Flow and Heat Transfer Predictions," *Journal of Thermophysics and Heat Transfer*, vol. 20, no. 1, pp. 80–91.

Yang, T. T. and Diller, T. E., 1995, "Heat Transfer and Flow for a Grooved Turbine Blade Tip in a Transonic Cascade," *ASME Paper Number 95-WA/HT-29*, as reported in Bunker (2001).

Yaras, M., Yingkang, Z. and Sjolander, S. A., 1989, "Flow Field in the Tip Gap of a Planar Cascade of Turbine Blades," *ASME Journal of Turbomachinery*, vol. 111, no. 3, pp. 276–283.

Yaras, M. I. and Sjolander, S. A., 1992a, "Effects of Simulated Rotation on Tip Leakage in a Planar Cascade of Turbine Blades: Part I—Tip Gap Flow," *ASME Journal of Turbomachinery*, vol. 114, no. 3, pp. 652–659.

Yaras, M. I. and Sjolander, S. A., 1992b, "Prediction of Tip-Leakage Losses in Axial Turbines," *ASME Journal of Turbomachinery*, vol. 114, no. 1, pp. 204–210.

Yaras, M. I., Sjolander, S. A. and Kind, R. J., 1992, "Effects of Simulated Rotation on Tip Leakage in a Planar Cascade of Turbine Blades: Part II—Downstream Flow Field and Blade Loading," *ASME Journal of Turbomachinery*, vol. 114, no. 3, pp. 660–667.

Yoshino, S., 2002, "Heat Transfer in Rotating Turbine Experiments," DPhil thesis, University of Oxford.

Young, J. B. and Horlock, J. H., 2006, "Defining the Efficiency of a Cooled Turbine," *ASME Journal of Turbomachinery*, vol. 128, no. 4, pp. 658–667.

Zhang, Q., 2007a, "Drawings of HSLC," Deptartment of Engineering Science, University of Oxford.

Zhang, Q., 2007b, "Thermal Property Transient Measurement," Deptartment of Engineering Science, University of Oxford.

Zhang, Q., 2010, "HSLC CFD Results," Deptartment of Engineering Science, University of Oxford.

Zhang, Q., Lee, S. W. and Ligrani, P. M., 2004, "Effects of Surface Roughness and Turbulence Intensity on the Aerodynamic Losses Produced by the Suction Surface of a Simulated Turbine Airfoil," *ASME Transactions-Journal of Fluids Engineering*, vol. 126, pp. 257–265.

Zhang, Q., O'Dowd, D. O., He, L., Oldfield, M. L. G. and Ligrani, P. M., 2010a, "Transonic Turbine Blade Tip Aero-Thermal Performance with Different Tip Gaps: Part I—Tip Heat Transfer," *ASME Journal of Turbomachinery*, to be published (also ASME Paper Number GT2010-22779).

Zhang, Q., O'Dowd, D. O., He, L., Wheeler, A. P. S., Ligrani, P. M. and Cheong, B. C. Y., 2010b, "Over-Tip Shock Wave Structure and its Impact on Turbine Blade Tip Heat Transfer," *ASME Journal of Turbomachinery*, to be published.

Zhang, Q., Sandberg, D. and Ligrani, P. M., 2005, "Influence of Mach Number and Freestream Turbulence Intensity on the Aerodynamic Losses of a Turbine Vane," *AIAA Journal of Propulsion and Power*, vol. 21, no. 6, pp. 988–996.